Design and fabrication of nanostructures for light-trapping in ultra-thin solar cells

Inès Massiot

UNIVERSITÉ PARIS SUD

Comprendre le monde, construire l'avenir®

cnrs dépasser les frontières

LABORATOIRE DE PHOTONIQUE ET DE NANOSTRUCTURES

THÈSE DE DOCTORAT
Spécialité Physique

ÉCOLE DOCTORALE 422:
Sciences et technologies de l'information des télécommunications et des systèmes

Présentée par

Inès MASSIOT

pour l'obtention du
Diplôme de Docteur de l'Université Paris Sud

Sujet de la thèse:

Design and fabrication of nanostructures for light-trapping in ultra-thin solar cells

soutenue le 22/10/2013

Composition du jury :

M. PELOUARD Jean-Luc	**LPN**	**Directeur de thèse**
M. COLLIN Stéphane	**LPN**	**Encadrant**
M. SEASSAL Christian	**INL**	**Rapporteur**
M. SLAOUI Abdelillah	**iCUBE**	**Rapporteur**
M. BALLIF Christophe	**EPFL-PVLab**	**Examinateur**
M. KLEIDER Jean-Paul	**LGEP**	**Examinateur**
M. ROCA i CABARROCAS Pere	**LPICM**	**Membre invité**
M. SAUVAN Christophe	**IOGS**	**Membre invité**

UNIVERSITÉ PARIS SUD

Comprendre le monde, construire l'avenir®

cnrs

LABORATOIRE DE PHOTONIQUE ET DE NANOSTRUCTURES

THÈSE DE DOCTORAT
Spécialité Physique

ÉCOLE DOCTORALE 422:
Sciences et technologies de l'information des télécommunications et des systèmes

Présentée par

Inès MASSIOT

pour l'obtention du
Diplôme de Docteur de l'Université Paris Sud

Sujet de la thèse:

Conception et réalisation de nanostructures pour le piégeage optique dans des cellules photovoltaïques ultra-minces

soutenue le 22/10/2013

Composition du jury :

M. PELOUARD Jean-Luc	LPN	Directeur de thèse
M. COLLIN Stéphane	LPN	Encadrant
M. SEASSAL Christian	INL	Rapporteur
M. SLAOUI Abdelillah	iCUBE	Rapporteur
M. BALLIF Christophe	EPFL-PVLab	Examinateur
M. KLEIDER Jean-Paul	LGEP	Examinateur
M. ROCA i CABARROCAS Pere	LPICM	Membre invité
M. SAUVAN Christophe	IOGS	Membre invité

RÉSUMÉ

Diminuer l'épaisseur de la couche d'absorbeur est une solution attractive pour produire des cellules photovoltaïques à coût réduit. Cela permet également de réduire la quantité de matériau actif utilisé ainsi que d'améliorer la collection du courant dans la cellule. Cette thèse s'est focalisée sur la conception de nanostructures pour exalter l'absorption de la lumière dans des couches de semiconducteur d'épaisseur réduite et ainsi proposer des cellules ultraminces efficaces. Dans un premier temps, nous avons proposé une approche originale pour piéger la lumière dans une cellule ultra-fine ($\leq$ 100 nm) en silicium amorphe. Un réseau métallique est placé en face avant de la cellule déposée sur un miroir métallique afin d'obtenir une absorption multi-résonante large bande pour les deux polarisations de la lumière. Nous proposons aussi d'utiliser le réseau métallique comme une électrode transparente alternative afin de réduire les pertes optiques dans le contact avant de la cellule. Une analyse numérique approfondie des mécanismes résonants en jeu a été menée ainsi que la fabrication et la caractérisation optique de démonstrateurs. Dans un deuxième temps, nous avons appliqué ce concept de contact avant multirésonant à des couches ultra-fines en arsenure de gallium (GaAs). Nous avons montré numériquement et expérimentalement le potentiel d'une nanogrille métallique bi-dimensionnelle pour le confinement efficace de la lumière dans 25 nm de GaAs. Enfin, nous avons étudié la possibilité de réduire l'épaisseur de cellules en silicium cristallin d'un facteur 10 à 100 par rapport à l'état de l'art. Nous avons développé un procédé pour transférer des couches de silicium cristallin de quelques microns d'épaisseur épitaxiées par PECVD sur un substrat hôte bas coût. Nous avons également travaillé à la structuration contrôlée de nanopyramides en vue d'un piégeage optique efficace dans ces couches minces.

Mots-clefs: Photovoltaïque, Couches minces, Piégeage optique, Photonique, Plasmonique

ABSTRACT

Reducing the absorber thickness is an attractive solution to decrease the production cost of solar cells. Furthermore, it allows to reduce the amount of material needed and improve the current collection in the cell. This thesis has been focused on the design of nanostructures to enhance light absorption in very small semiconductor volumes in order to achieve efficient ultra-thin solar cells. First, we have proposed an original light-trapping concept for ultra-thin ($\leq$ 100 nm) amorphous silicon (a-Si:H) solar cells. A one-dimensional metallic grating is patterned on the front surface of the cell deposited on a metallic mirror. Broadband multi-resonant absorption has been demonstrated for both light polarizations. The metallic grating is also used as an alternative transparent electrode in order to reduce optical losses in the front contact. A detailed analysis of the multi-resonant absorption mechanism has been carried out through numerical calculations. The fabrication and optical characterization of ultra-thin a-Si:H solar cells with metallic gratings have validated the multi-resonant approach. Second, we have proposed a design with a two-dimensional metallic grid as a resonant front contact for very thin (25 nm) gallium arsenide (GaAs) layers. We have shown through the design and fabrication of a proof-of-concept structure the potential of metallic nanogrids to confine efficiently light absorption with an ultra-thin GaAs layer. Finally, advanced light-trapping structures could also allow a thickness reduction of crystalline silicon wafers of a factor 10 to 100 with respect to state-of-the-art cells. We have developed a process to transfer micron-thick epitaxial crystalline silicon (c-Si) layers onto a low-cost host substrate. Inverted nanopyramids have also been fabricated in crystalline silicon in order to achieve a broadband anti-reflection effect. It opens promising perspectives towards the realization of double-sided nanopatterned ultra-thin c-Si cells.

Keywords: Photovoltaics, Thin films, Light trapping, Photonics, Plasmonics

REMERCIEMENTS

L'hérédité a certainement joué un rôle, mais ce sont plus certainement la curiosité et l'amour des sciences et de la physique en particulier qui m'ont amenée au Laboratoire de Photonique et de Nanostructures par une belle journée d'avril. Je suis arrivée au LPN en tant que stagiaire et j'en ressors maintenant en tant que docteur mais surtout future chercheuse. Je me dois de remercier ici les personnes sans qui cette transformation n'aurait pu avoir lieu. Tout d'abord, merci à Jean-Luc Pelouard et Stéphane Collin de m'avoir proposé un sujet de stage d'abord puis de thèse. Jean-Luc, je te remercie d'avoir dirigé ma thèse mais aussi pour ton soutien, tes lettres de recommandation et les nombreuses discussions sur mon devenir. Stéphane, merci pour tout ce que tu m'as apporté. Merci pour nos discussions scientifiques, pour la liberté que tu m'as offerte dans mon projet et pour ta confiance qui m'a poussée à aller toujours plus loin.

Je tiens à remercier Christian Seassal et Abdelillah Slaoui pour m'avoir fait l'honneur de rapporter ma thèse. Je remercie les autres membres du jury, Christophe Ballif, Jean-Paul Kleider, Christophe Sauvan et Pere Roca i Cabarrocas d'avoir accepté de faire partie de mon jury de thèse malgré leur emploi du temps surchargé.

J'aimerais remercier mes collègues du LPN qui m'ont accompagnée durant cette aventure. Je pense très fort à mes compagnons de thèse: Clément, Benjamin, Emilie, Christelle, Florian et Nicolas. Clément, nous avons partagé ce bureau pendant trois ans et demi sans nous entretuer (même pendant la rédaction) et cela est un exploit en soi. Merci pour ce qu'on a partagé au quotidien (l'entretien des plantes, la musique, les paquets de Haribo, les innovations de Colin MatlabTech Inc.) et pour tout le reste. J'espère sincèrement que nos routes se recroiseront, scientifiquement ou pas. Nicolas, je ne saurais te remercier assez pour ta gentillesse et ton enthousiasme à toute épreuve.
Je tiens aussi à saluer l'aide que j'ai pu recevoir en salle blanche durant ma thèse. Merci à Christophe Dupuis, dit Cricri l'ancien, pour toutes ces belles images au Magellan et les conseils en tout genre en techno. Mais surtout merci pour ces belles séances de discussion sur la musique, le cinéma, ta jeunesse tout en contemplant des nanogrilles! Nathalie, merci pour ton aide en lithographie électronique et plus globalement en salle blanche, pour les séances à la piscine et les discussions du midi. Merci à Andrea pour son travail sur le projet Nathisol, ses idées à profusion et son sens de la décontraction très italien. Merci à Laurence Ferlazzo, Christophe Roblin, Laurent Couraud, Xavier Lafosse, David Chouteau et Stéphane Guilet pour leur aide technologique mais aussi pour les magnifiques photos souvenirs que je garde précieusement.

Je souhaite remercier les personnes du groupe Phydis que j'ai cotoyées durant ces trois ans: dans le désordre Gulnar, Nicolas Péré-Laperne, Grégory, Petru, Patrick, Ha, Charlie, Myriam, Sylvain, Simon, Quentin, Paul, Michaël, Clément

Tardieu et Benoît. Je garde un très bon souvenir des moments que nous avons partagés au labo et en dehors.

Enfin, ma troisième année de thèse aurait été beaucoup plus morne sans mes "rivaux": merci au groupe Nanoflu et Kleria et en particulier à Anne-Claire et Hugo pour tous nos échanges.

J'aimerais remercier les collaborations qui ont permis à mon projet d'exister. Merci à Pere Roca i Cabarrocas du LPICM non seulement pour ses échantillons mais également pour sa réactivité malgré son emploi du temps surchargé et la relecture attentive de mes publications. Merci à Romain Cariou pour son aide dans le cadre du projet Nathisol. Ce fut un plaisir de créer des paillettes ensemble! Je tiens également à remercier Philippe Lalanne et Christophe Sauvan de l'Institut d'Optique. J'ai pu apprécier non seulement votre aide pour les calculs numériques mais aussi votre implication déterminante dans mes publications.

La thèse a aussi été l'occasion pour moi d'assouvir mon désir d'enseigner. Je remercie l'équipe pédagogique du département GEII2 de l'IUT Cachan pour m'avoir accueillie et en particulier Sylvie Dugard avec qui ce fut un plaisir de mener à bien mon monitorat.

Enfin, je remercie les personnes qui m'ont entourée à l'extérieur. A mes amis de l'ENS Lyon: merci à Antoine, Phil, Marie-Blandine, Scu, Agnès, Jordane et Laurence pour les moments partagés à Paris, Lyon, Fribourg, qui furent autant d'escapades salutaires! A Thibaud, co-stagiaire autrefois et maintenant ami, merci pour les petits moments de folie qu'on a partagés en attendant qu'on sauve le monde avec nos cellule solaires! A Fanny, merci pour ton soutien en toutes circonstances. A ma famille, je vous dois tellement. Merci à ma mère pour m'avoir inspirée, pour m'avoir donné de l'ambition et m'avoir soutenue depuis si longtemps. Merci à mon père pour me pousser à me surpasser et pour avoir toujours une oreille attentive. Merci à mes grands-parents. Marie, tu m'as transmis tellement de choses, ta curiosité, ton ouverture et surtout ton amour de l'enseignement. Claude, merci pour ces week-ends à la Gilardière qui ont été une respiration dans ma vie agitée. Merci à mes compagnes de toujours, mes petites soeurs, Aude et Livia, pour tous nos souvenirs et tous ceux à venir encore.

CONTENTS

GENERAL INTRODUCTION

One of the main challenges of our time is to handle the growing energy demand due to the global population increase and the development of emerging countries. The current energy market is dominated by fossil-fuel energies (oil, coal and gas) which still represent more than 80 % of power generation in 2012 [1]. Redrawing the energy market is a necessity in order to address both the limited resources of fossil fuel energies and the climate change due to greenhouse-gases emissions. Solar photovoltaics arises as a promising solution to deliver an abundant, reliable and clean energy. Despite the discovery of the photoelectric effect, i.e the conversion from photon energy to electricity, in 1839 by Edmond Becquerel [2], no large scale applications have been developed before the oil crises in the 1970s. In the last decade, the photovoltaic market has shown a very impressive growth rate of 40 % on average [3] in order to reach a cumulative capacity of 65 GW in 2011. According to the International Energy Agency, solar energy is expected to have an important share in the new energy map: one third of global energy demand could be provided by solar energy in 2060 [3].

Several photovoltaic technologies are already developed at a commercial scale but research in each technology is still driven by the reduction of the production cost and the increase of the conversion efficiency of the device. In particular, reducing the absorber thickness is of main importance for several technologies because of the material cost (crystalline silicon or gallium arsenide), its scarcity (for materials with indium, tellurium or selenium) or stability issues (amorphous silicon). However, thinner solar cells suffer from poor light absorption at long wavelengths due to the decrease in the amount of absorbing material. Over the last few years, many strategies have been proposed to trap photons within ultra-thin absorber layers in order to increase light absorption in the solar cell. Some designs have already shown their ability to confine light in very thin layers (thickness $= 100 - 200$ nm) with photonic crystals [4] or a patterned metallic back contact [5–7]. In both cases, the active layer is structured thereby leading to increased surface recombination and the creation of defective areas in the junction, respectively. The impact of the increase of the short-circuit current density on the conversion efficiency is limited by the degradation of both the open-circuit voltage and the fill factor. In this thesis, our approach is to propose novel light-trapping designs using metallic nanostructures while keeping a flat active layer in order to prevent the problems mentioned above. In addition, metallic light-trapping nanostructures have extraordinary optical properties but are also attractive because of their conductivity. The originality of our designs also relies on this double functionality of metallic nanostructures that act both as a scheme to confine light and as an alternative electrode.

During this thesis, we have worked on three different photovoltaic materials (amorphous silicon, gallium arsenide and crystalline silicon) with the same purpose to reduce the absorber thickness toward ultra-thin layers: thickness of 100 nm for thin film materials and $2-5$ µm for crystalline silicon. The manuscript is structured in four parts.

PART 1 includes four chapters providing an introduction to the study. In *chapter 1*, a general introduction on photovoltaics is given in order to motivate our study. In particular, we show that ultra-thin solar cells are a promising solution to obtain more efficient and cheaper solar cells. *Chapter 2* provides an overview of the strategies proposed in literature to trap light within ultra-thin solar cells. In *chapter 3*, we introduce the concept of nanopatterned resonant front contact after giving a review of transparent electrodes with metallic films. During my thesis, I have worked on the setup of characterization tools adapted to the study of nanopatterned solar cells as described in *chapter 4*.

PART 2 is dedicated to the design of ultra-thin amorphous silicon solar cells with a thickness below 100 nm. We first introduce the general properties of amorphous silicon material as well as its intrinsic limitations for the realization of solar cells in *chapter 5*. In *chapter 6*, we present an original light-trapping approach based on a one-dimensional metallic grating placed in the front surface of the cell. Design rules for the conception of resonant solar cells are given and applied to design a realistic amorphous silicon solar cell. We also propose to use the metallic grating as an alternative transparent electrode in order to reduce optical losses in the front contact of the cell. The realization and optical characterization of demonstrators are presented in *chapter 7*.

In PART 3, we aim at showing the potential of metallic nanostructures to enhance light absorption in very thin (25 nm) semiconductor layers. We propose an original design which couples a two-dimensional metallic grid with an ultra-thin gallium arsenide absorber and a back mirror. We study the optimization of the design through numerical calculations and discuss the theoretical performances of the structure in *chapter 8*. In *chapter 9*, the experimental demonstration of ultra-thin Au/GaAs/Au broadband absorbers is presented.

Finally, PART 4 of the thesis is focused on monocrystalline silicon solar cells. This work has been done within the ANR project NATHISOL, which aims at using nanophotonic strategies to design ultra-thin ($2-5$ µm) crystalline silicon solar cells based on epitaxial silicon films deposited at low temperature. *Chapter 10* introduces the motivations and global context of the project by reviewing the existing technologies to obtain micron-thick monocrystalline silicon films and the adapted light-trapping solutions. In *chapter 11*, we present the processes developed in collaboration with LPICM to i) transfer micron-thick epitaxial crystalline silicon films and ii) fabricate upright and inverted nanopyramids. This work validates the first milestone of the project and opens promising perspectives for the realization of double-sided nanopatterned ultra-thin crystalline silicon solar cells.

I would like to precise here my contribution to the work presented in this manuscript. The numerical calculations for PARTS 2 and 3 have been performed

by myself with the Reticolo code supplied by Philippe Lalanne from LP2N and Christophe Sauvan from Laboratoire Charles Fabry, IOGS (Institute of Optics Graduate School). Some of the numerical results presented in *chapter* 8 have been obtained with the help of Nicolas Vandamme (LPN).

As for the experimental work shown in PART 2, the deposition of a-Si:H, ZnO:Al and ITO have been carried out at LPICM. The rest of the fabrication process has been done at LPN by myself, except from the electron beam lithography step (Nathalie Bardou, LPN). I have performed the other steps of the nanopatterning (resist development, metal deposition and resist lift-off). The AFM measurements have been done by Gulnar Dagher (LPN). All the SEM measurements in my thesis have been performed at LPN by coworkers (Christophe Dupuis, Andrea Cattoni, Clément Colin). I have carried out all the optical measurements presented in *chapter 7* on the setup described in PART 1, *chapter 4*. An important part of my thesis has been devoted to the setup of this experimental platform for the optical and electrical characterization of nanopatterned solar cells.

Regarding the fabrication of the demonstrators presented in PART 3, the epitaxy of the GaAs layers as well as the SiN_x deposition have been done by coworkers at LPN (Aristide Lemaitre and David Chouteau, respectively). I did the deposition of the back mirror, layer transfer by anodic bonding and patterning of the gold grid (except from the electron beam lithography step as already mentioned above). The substrate removal was performed by Nicolas Vandamme (LPN). I also carried out the optical characterizations presented in *chapter 9*.

Finally, for PART 4, the experimental work was done in collaboration with LPICM. The ellipsometry, AFM and Raman measurements were performed at LPICM as well as the I-V measurements. I have developed the patterning process of nanoinverted pyramids with the help of Andrea Cattoni (LPN) for the electron beam lithography of the HSQ resist. The development of the etching process of random pyramids on epi crystalline silicon was done at LPN by myself with the help of Romain Cariou, from LPICM. I have developed the thermal lift-off process at LPN, with Andrea Cattoni (LPN) and Romain Cariou (LPICM). I have carried out the reflectivity measurements on the patterned samples as displayed in *chapter 11*.

Part I

INTRODUCTION

1

MOTIVATIONS TOWARDS ULTRA-THIN SOLAR CELLS

Contents

1.1 OUTLOOK OF THE ENERGY MARKET

The first challenge faced by the energy market is the growth of energy demand to meet social and economic development. The global energy consumption per year reported by the International Energy Agency (IEA) for 2010 is 150.000 TWh[1] with a predicted value of 175.000 TWh for 2020. How will we fulfill this energy demand? The current energy market combines different sources of energy (the market share in 2012 taken from Ref. 1 is given in brackets):

- fossil-fuel energies (oil (32.4 %), coal (27.3 %), gas (21.4 %))
- nuclear energy (5.7 %)
- renewable energy sources (13.2 %) (wind energy, solar energy, biomass, geothermal, hydropower, ocean energy).

In 2012, fossil-fuel energies still represent more than 80 % of the global energy consumption [1]. One major concern of the 21st century is the global climate change due to human activities. As reviewed in the last report of the IPCC

1 TWH=terawatt-hours

(Intergovernmental panel on climate change) [8], scientific studies have already reported the first consequences of the climate change: increase of the average air and ocean temperatures, melting of snow and ice and rising of sea level ($15-20$ cm on average over the last century [9]). Limiting the temperature increase is crucial for the future of wildlife as well as mankind.

During the United Nations Framework Convention on Climate Change Conference (Cancun, 2010), the international community has decided to limit the average global temperature increase to 2°C with respect to pre-industrial levels. However, the IEA has suggested in their report of june 2013 [10] that the effective value of the temperature increase is likely to be between 3.6°C and 5.3°C. The global climate change is driven by greenhouse-gas emissions due to human activities. The increase of the atmospheric concentrations of greenhouse-gases and aerosols affects the absorption, scattering and emission of radiations within the atmosphere and at the Earth's surface. The most important greenhouse-gases are carbon dioxide (CO_2) and methane (CH_4). Two thirds of global greenhouse-gas emissions come from energy production, according to the IEA [10]. Despite encouraging decrease trends in several countries (European Union and the United States), the energy-related carbon dioxide emissions have increased by 1.4 % in 2012 [10]. In order to stay within the initial objective of a 2°C increase, strong political decisions have to be taken.

IEA presents four energy policies to stop the increase of energy-related emissions by 2020 at non net economical cost in their scenario called the "4 for 2°C" [10]. One of their conclusions is that renewable energy sources should have a more important share in the global energy mix (27 % in 2020). In particular, non-OECD[2] countries currently account for 60 % of global greenhouse-gas emissions. Developing countries should invest early in low-carbon energy sources in order to avoid future expenses due to the sector decarbonisation.

As a matter of fact, renewable power generation is the fastest-growing power generation sector. In spite of the difficult economic context, global renewable generation has shown an impressive growth of 8 % in 2012, reaching a total renewable power generation of 4860 TWh [10]. In particular, the emerging markets (China, India, Brazil) see accelerated investment and deployment of renewable sources. The non-OECD countries are expected to represent two thirds of the increase in renewable power generation between 2013 and 2018. The global conclusion of the IEA is that renewable energies do have a bright future but long-term policies and support incentives are required in order to increase the investment in technologies and infrastructures.

1.2 SOLAR ENERGY: A POWERFUL RESOURCE

Solar energy is the largest energy resource on Earth. In 90 min, the amount of sun light striking the earth is enough to provide the planet energy needs

2 The OECD is the Organization for Economic Co-operation and Development [11]. Its mission is to promote political actions to improve the economical and social well-being of people worldwide.

for a whole year [3]! The solar radiation is emitted from its outer surface, the photosphere, and strikes earth under two forms:

- the direct radiation: photons coming directly from the Sun
- the diffuse radiation: part of solar radiation is attenuated when passing through the atmosphere because of Rayleigh scattering by molecules and absorption by atmospheric gases.

There are two main types of solar energy[3]:

- Solar photovoltaics (PV)
- Concentrating solar power (CSP).

Solar PV relies on the direct conversion of sun energy into electricity. As for CSP, sunbeams are concentrated with optics (mirrors or lenses) in order to heat a receiver to high temperature. The heat is then converted into mechanical energy through a heat engine and finally into electricity. It is also called solar thermal electricity. CSP only uses the direct sun radiation while solar photovoltaic systems convert direct and diffuse sunlight.

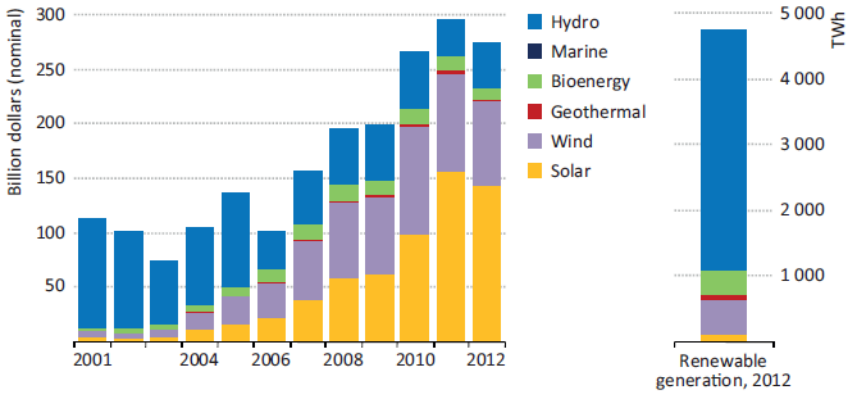

Figure 1: (left) Repartition of world investment by renewable-based energy sector. (right) Renewable total generation in 2012. Figure extracted from Ref. 10.

Figure 1 (right) shows the repartition of renewable power generation in 2012. We see that most of the electricity produced by renewable energy sources comes from hydro generated power (almost 80 %). Electricity coming from solar energy (PV and CSP) represents a very small fraction of the global electricity generation. However, solar PV is the fastest-growing renewable power market. Figure 1 (left) shows the world investment in renewable-based energy sectors. We see that investments in solar energy have dramatically grown since 2001. In 2012, the solar energy sector represented more than half of the world investments. Consequently, the PV market has shown a very impressive growth since 2003 with an average 40 % growth rate until 2009 [3]. As shown in Fig. 2, a production capacity over 40 GW has been reached in 2010 with a deployment in

3 Note that other renewable energy sources such as wind, hydropower or biomass also exploit solar resources but indirectly.

several countries, Germany being the 1st PV market since 2001. This growth has been confirmed these last years with a cumulative capacity of 65 GW reached in 2011. As for CSP, it is a re-emerging market. Concentrating solar power was first developed in the United States in the 1980s. A new development wave has occurred in 2005 led by the United States and Spain. The global CSP installation is currently 1.5 GW.

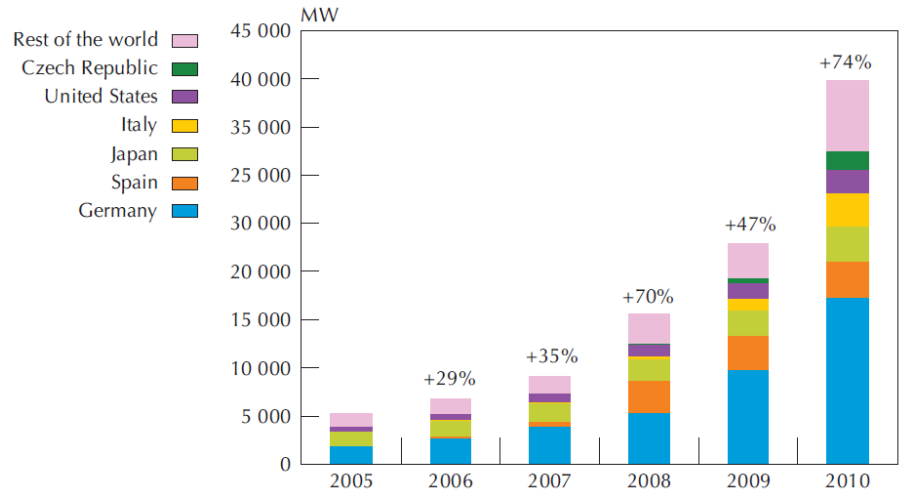

Figure 2: Evolution of cumulative solar PV installation between 2005 and 2010. Figure extracted from Ref. 3.

One of the challenges faced by solar PV is that it must be cost-competitive with other sources of energy and in particular with fossil fuel energies and nuclear energy. Because of increased production capacities, the price of PV produced electricity has dropped dramatically in the last decade. Grid parity has already been reached in several countries in Europe (Italy, Spain, Portugal, Germany, Denmark) [12]. It means that electricity generated by PV installations has the same price as the one bought from the grid. Electricity production with solar PV is now an achievable goal for most countries in the world. According to the IEA [3], solar energy (solar PV and CSP) could provide one third of global energy demand in 2060. Support incentives are still required in order to extend the deployment of solar energy power installations.

Last but not least, solar energy is a renewable, secure and clean source of energy. Those advantages are of main importance to be competitive over the other alternative to fossil fuel energies that is nuclear energy. Beside the crucial issue of the disposal of nuclear wastes which still remains unanswered, the Fukushima nuclear disaster of March 2011 has raised awareness about the safety of nuclear power plants. As a consequence, nuclear energy is currently questioned as a reliable energy source. Besides, as stated by the IPCC [8], "*renewable energies may, if implemented properly, contribute to social and economic development, energy access, a secure energy supply, and reducing negative impacts on the environment and health*". Let us take the case of Solar Aid [13], a leading international charity that provides access to clean and affordable solar lights

since 2006. In Africa, 85 % of the population do not have access to electricity. In particular, they use mostly kerosene lamps which are expensive and toxic not to mention the fire hazard they represent. Solar Aid's action relies on replacing kerosene lamps by solar lights that can be charged during the day in order to provide light in the night. Another charity, Renewable World [14] has centered its action on using renewable energies, mainly solar PV but also wind and hydropower, to improve the living conditions of people in developing areas (East Africa, Southern Asia and Central America). Renewable energies and in particular, solar PV, can overcome geographical and financial boundaries and provide electricity in off-grid communities. Solar electricity can give access to a clean source of light but also to drinkable water thanks to solar pumping and purification systems and to healthcare facilities. Solar PV is therefore an essential part of sustainable development.

1.3 PRINCIPLE OF PHOTOVOLTAIC CONVERSION

The photovoltaic effect has been discovered by Edmond Becquerel in 1839 [2]. Photovoltaic conversion is the conversion of solar energy into electrical energy. The photovoltaic conversion consists of three steps: carrier generation by photon absorption, charge separation and collection.

1.3.1 *Photogeneration of carriers*

The basis of a photovoltaic device is a two band system (Fig. 3), in which the absorption of photons can give rise to electron-hole pairs and generate a current. The existence of an energy bandgap is required so that the carriers could stay in their excited states long enough to be separated. In the case of inorganic semiconductors, the ground state is the valence band and the excited state is the conduction band. The energy gap between the two states is therefore the bandgap energy E_g of the semiconductor. Note that there is an equivalent structure in the case of organic solar cells. The characteristic bandgap is the energy gap between the highest occupied molecular orbital (HOMO) of the donor material and the lowest unoccupied molecular orbital (LUMO) of the acceptor.

Let us consider a photon with an energy $E = h\nu$ (h is Planck's constant and ν the photon frequency) hitting the active material. It can be reflected with a probability that depends on the refractive index of the semiconductor material. If the photon enters the material, several situations are possible as described in Fig. 3. If the photon energy is lower than the bandgap energy, the photon can pass through the material without being absorbed (case A). If $h\nu \geq E_g$, the photon can be absorbed, promoting an electron to an excited state within the conduction band (cases B and C). It results in the creation of an electron-hole pair. As shown in Fig. 3 (case C), when the photon energy is higher than the bandgap, the carriers relax rapidly towards the band edges and the excess energy is lost as heat. It is noteworthy that because of this thermalisation process, all the generated carriers have an energy equal to the bandgap energy whatever

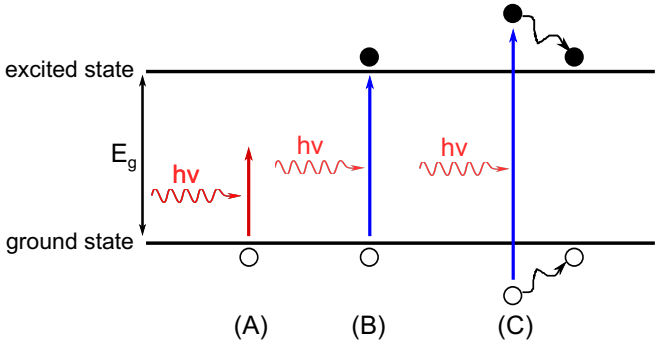

Figure 3: Simplified schematic of a system with two energy states. (A) If the incoming photon has an energy $h\nu < E_g$, it is not absorbed in the material. (B, C) If $h\nu \geq E_g$, the photon can be absorbed and give rise to an electron-hole pair. The carriers can then be separated and collected. (C) If $h\nu > E_g$, the excess energy is quickly lost by relaxation of the carriers to the band edges.

the energy of the absorbed photon. Therefore, photogeneration depends on the incident photon flux but not on the photon energy density.

The efficiency of the photogeneration process is limited by several channel losses:

- *Reflection losses:* incident photons can be reflected on the surface of the cell. A simple way to reduce reflection losses is to use an anti-reflection coating layer.
- *Non absorption:* photons with an energy $E < E_g$ cannot be absorb in the material.
- *Thermalisation losses:* electrons with an energy $E > E_g$ relax quickly towards the energy level E_g. The excess energy is lost as heat through electron-phonon interactions.

1.3.2 *Charge separation*

Once the carriers (electron and hole) are generated, they have to be separated. The separation mechanism may vary depending on the solar cell. In the case of inorganic semiconductores, the most widely used structure is the p-n homojunction, which we describe briefly in this subsection.

The p-n homojunction is made of two layers of the same semiconductor material (hence the term homojunction) which are doped in order to increase their conductivity. The n-type doped layer is obtained by the introduction of electron donor atoms and has a higher electron density. The p-type doped layer is based on acceptor atoms and has a higher hole density. As a consequence, the Fermi level of the n-doped (p-doped) layer is closer to the conduction (valence) band than the Fermi level of the intrinsic semiconductor. In the p-n junction at equilibrium, the Fermi level must be the same in the entire junction. It leads to a bending of the energy band at the junction and the creation of a potential barrier. The height of the potential barrier is equal to $q\,V_{bi}$, with V_{bi} the built-in

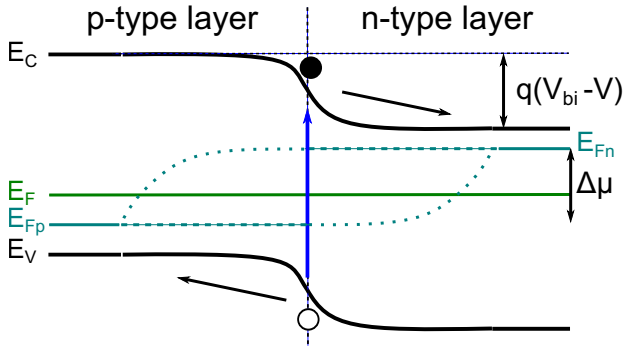

Figure 4: Simplified energy band diagram of a p-n homojunction after illumination.

potential of the junction. V_{bi} is a function of the doping levels N_a (density of acceptor atoms), N_d (density of donor atoms) and n_i (intrinsic doping):

$$V_{bi} = \frac{k_b T}{q} ln(\frac{N_a N_d}{n_i^2}), \tag{1}$$

where k_b is the Boltzmann constant, q the electron charge and T the temperature.

Figure 4 gives a schematic view of a p-n homojunction after illumination. When the solar cell is illuminated, electron-hole pairs are created in the whole junction. It increases the carrier densities above their equilibrium values. It the disturbance is not too important, we can assume that carriers are in quasi thermal equilibrium. Their distribution can thereby be modeled as new apparent Fermi levels called Quasi-Fermi levels (QFL) of electrons and holes. At equilibrium, the Fermi level is the same in the whole semiconductor: $E_{Fn} = E_{Fp}$, with E_{Fn} and E_{Fp} the quasi-Fermi levels for the electrons and holes respectively. Upon illumination, the Fermi level splits, giving rise to a chemical potential $\Delta\mu$ defined by:

$$\Delta\mu = E_{Fn} - E_{Fp}\,, \tag{2}$$

as illustrated in Fig. 4. As developed by Würfel [15, 16], the driving force of charge separation is the gradient in the quasi-Fermi levels of the carriers, or in other words, the chemical potential $\Delta\mu$. A more intense light excitation increases the separation in the QFL. The output voltage of the cell is related to the electrical potential energy of the photogenerated carriers by: $\Delta\mu = q\,V$. The electrical work extracted depends on the quasi-Fermi level splitting and thus on the semiconductor material used and the doping level.

As shown in Fig. 4, the separation of the carriers is done through selective contacts. The potential barrier is a selective barrier to charge carrier flow: electrons can only travel to the n contact and holes to the p contact. The p-n junction thus enables to spatially separate electron and holes in order to prevent carrier recombinations. The p-n junction is the building block of the solar cell: it allows the current flow and it is the source of the chemical potential.

1.3.3 *Carrier collection*

The last step of photovoltaic conversion is the collection of the carriers through charge transport towards the electrical contacts. The contacts are usually made of a transparent conductive oxide on the front side of the cell and a metallic contact on the rear side. The efficiency of the collection process is limited by recombination losses. As illustrated in Fig. 5, there are three possible recombination mechanisms:

A. *Radiative recombination*: the electron-hole pair recombines radiatively through spontaneous emission of a photon ($h\nu = E_g$). This process is unavoidable in light absorbing materials and is most important for strong light absorption.

B. *Non-radiative recombination*: the electron and holes relax to a localised trap state due to impurities or defects in the material. The energy lost is given up as heat.

C. *Auger recombination*: one carrier (an electron in Fig. 5) interacts with a similar carrier. It results in the relaxation of one of the carriers towards the valence band and the increase in kinetic energy of the second carrier. This recombination mechanism is important for high carrier densities.

In a real material, non-radiative recombination losses are the dominant mechanism. Trap assisted recombination is particularly important at surfaces and interfaces (for multicrystalline materials and heterostructures) because of the high density of surface defects. Localised defect states at surfaces can be crystal defects due to broken bonds or extrinsic impurities. Surface recombination via trap states is characterized by the surface recombination velocity which is proportional to the density of traps per unit area. These recombination losses degrade the conversion efficiency of the photovoltaic device. Surface recombinations can be limited by the use of surface passivation. For instance, in monocrystalline silicon solar cells, the front surface is passivated using a thin layer of silicon oxide. It prevents carriers from reaching the surface and thereby reduces the surface recombination velocity.

1.3.4 *I-V curve of a solar cell*

The generated photocurrent I_{SC} for an applied voltage V_p is modeled as an ideal current generator. The collection efficiency of the photovoltaic conversion process is limited by several sources of losses that can be taken into account in the electric circuit equivalent to a realistic cell as shown in Fig. 6:

1. *Recombination losses:* despite the p-n junction, photogenerated electrons and holes can recombine before being collected. Recombination losses are taken into account through the dark current I_d, which is the current in the solar cell under applied bias without illumination. The dark current I_d can be modeled by a diode in parallel with the current generator, as shown in Fig. 6.

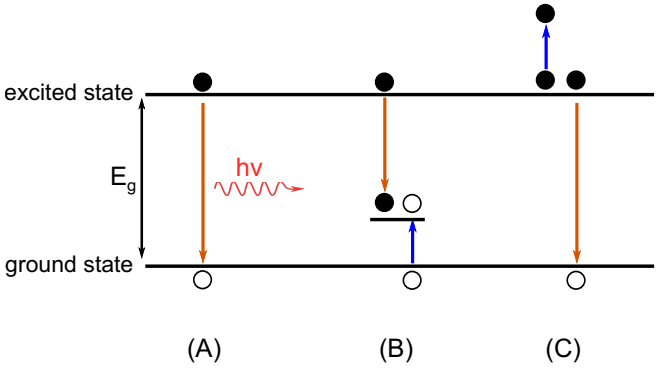

Figure 5: Sources of recombination losses: radiative recombination (A), non-radiative recombination via trap state (B) and Auger recombination (C).

2. *Shunt resistance:* leakage currents in the cell are modeled by a shunt resistance R_{sh} in parallel with the current generator (Fig. 6).

3. *Series resistance*: resistance arises from the semiconductor resistance when a current is flowing through the cell and from the contact resistances. It is modeled by a series resistance R_s. Series resistance is particularly important in the case of high injection levels, as for concentrated light.

As a consequence, the expression of the current of a solar cell as a function of the applied voltage can be approximated by [17]:

$$I = I_{SC} - I_d = I_{SC} - I_0 \, (exp(\frac{q\,V + I\,R_s}{m\,k\,T})) - \frac{V}{R_{sh}}, \tag{3}$$

in the one-diode model with:

- I_0 the saturation current
- q the electron charge
- V the applied voltage
- k the Boltzmann constant
- T the temperature.

m is the ideality factor of the diode. Its value, between 1 and 2, reflects the recombination mechanisms in the material. An ideal solar cell has an ideality factor equal to 1. Note that the contributions of the different recombination mechanisms can be taken into account more accurately with a two-diode model.

A standard characterization of photovoltaic devices is the current-voltage ($I - V$) curve. As the generated photocurrent I depends on the illuminated area, it is common to use the current density J, usually expressed in mA/cm^2. Figure 7 shows a typical $J - V$ curve. Three particular points are highlighted. The first one (0, J_{SC}) gives the photocurrent generated for no applied voltage, also called short-circuit current density of the cell J_{SC}. The second point (V_{OC}, 0) shows the voltage value for a photocurrent $J = 0$, also called the open-circuit

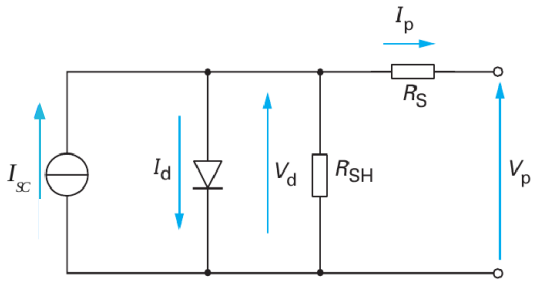

Figure 6: Equivalent circuit of a realistic photovoltaic device.

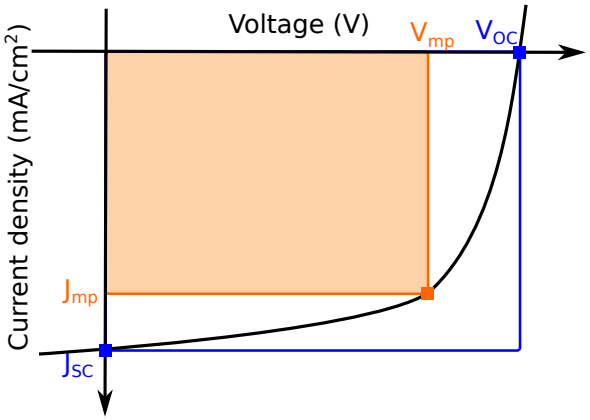

Figure 7: J-V curve of a typical solar cell. The orange area shows the maximum output power of the device.

voltage of the cell V_{OC}. These two points set the boundaries of the zone of the $J-V$ curve where electrical power can be extracted. The open-circuit voltage V_{OC} is limited by the bandgap of the material E_g:

$$V_{OC} < \frac{E_g}{q}.$$

The third point is the maximum power point (V_{mp}, J_{mp}) as highlighted in orange in Fig. 7. It corresponds to the operating point of the cell, which determines the conversion efficiency of the cell.

The power conversion efficiency of a solar cell is defined as the ratio of the generated electrical power over the incident light power:

$$\eta = \frac{P_{el}}{P_{in}}. \tag{4}$$

The electrical power at the operating point is given by:

$$P_{el} = J_{mp}\, V_{mp}. \tag{5}$$

We usually define the fill factor of the cell FF as:

$$FF = \frac{J_{mp}\, V_{mp}}{J_{SC}\, V_{OC}}. \tag{6}$$

The fill factor value is always below 1. The conversion efficiency can then be expressed as a function of J_{SC}, V_{OC} and FF:

$$\eta = \frac{FF\, J_{SC}\, V_{OC}}{P_{in}}. \tag{7}$$

We see that the conversion efficiency value depends on the incident power P_{in} which is given by the integrated solar spectrum. Standard illumination conditions must be defined in order to compare accurately the key characteristics (J_{SC}, V_{OC}, FF, η) of several solar cells.

1.3.5 *Standard solar spectrum*

The solar spectral irradiance is defined as the emitted energy flux density for each wavelength of the solar spectrum. Several solar spectra have been defined, each one is characterized by the air mass (AM) the sun light has to pass through before reaching the Earth's surface. The AM0 (Air Mass zero) spectrum corresponds to the sun irradiance outside the Earth's atmosphere. The AM0 solar spectrum resembles the spectral irradiance of a black body at 6000 K as displayed in Fig. 8. The black body radiation depends only on the temperature of the body and is described by Planck's law.

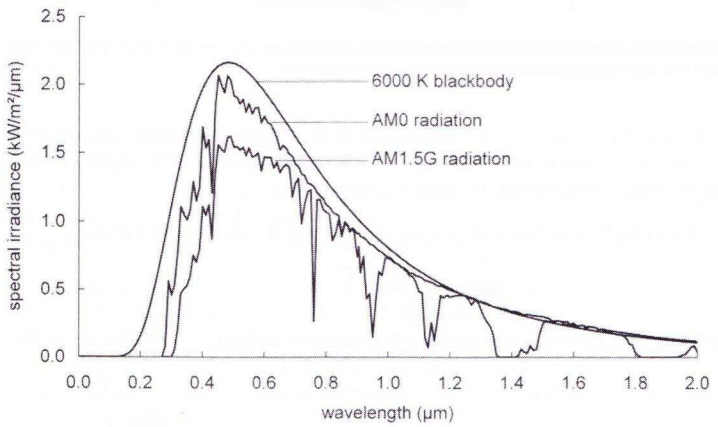

Figure 8: Spectral irradiance from a black body at 6000 K, the sun's photosphere as observed outside the atmosphere (AM0) and the sun's photosphere after passing through 1.5 times the thickness of the atmosphere (AM1.5G). Figure extracted from Ref. 18.

The standard solar spectrum used to determine the conversion efficiency of a solar cell is the AM1.5G spectrum. The AM1.5 solar spectrum is the sun spectral irradiance after having passed through 1.5 times the thickness of the atmosphere. As shown in Fig. 8, it is attenuated compared to the AM0 spectrum because of the light scattering and absorption by atmospheric gases (ozone, oxygen, water vapour or carbon dioxide). The air mass the solar radiation has to pass before reaching the Earth's surface depends on the sun's position. The zenith position corresponds to the AM1 radiation. The AM1.5 solar spectrum is equivalent to a sun angle of 41.8° with respect to the zenith position. The

attenuation due to the air mass 1.5 leads to a mean irradiance of 900 W/m^{-2}. For convenience, the standard terrestrial spectrum used for solar cells is the AM1.5G spectrum normalized in order to obtain a mean irradiance of 1000 W/m^{-2}.

It is the noteworthy that they are two AM1.5 solar spectra:

- AM1.5D which corresponds to the direct sun radiation
- AM1.5G which corresponds to the global sun radiation, i.e both direct and diffuse solar radiations.

In the following, we only use the normalized AM1.5G spectrum as the solar spectrum.

1.3.6 *Influence of the material bandgap*

The power conversion efficiency of the photovoltaic cell is a function of the energy bandgap of the semiconductor E_g. As explained previously, only the photons with an energy above the bandgap can be absorbed in the cell. Therefore, lowering the energy bandgap increases the number of absorbed photons and thereby the short-circuit current density of the cell. As for the open-circuit voltage of the cell, it depends on the saturation current density and the short-circuit current density:

$$V_{OC} = \frac{m\,k\,T}{q}\,\ln(\frac{J_{SC}}{J_0} + 1). \tag{8}$$

The limiting factor is the diode saturation current, which reflects the recombinations in the cell. The recombination current J_0 drops when the bandgap energy increases. Thus the open-circuit voltage increases for higher bandgaps. Therefore, there is an optimum bandgap energy achieving a trade-off between the short-circuit current density and the open-circuit voltage.

Schockley and Queisser published in 1961 a detailed balance in order to estimate the maximum efficiency of photovoltaic devices [19]. Figure 9 shows the limiting efficiency as a function of the material bandgap for a single-junction solar cell under one-sun AM1.5G illumination. Note that this calculation corresponds to an ideal case where the only recombination mechanism is radiative recombination. Real conversion efficiencies are expected to be lower because of non radiative recombination and resistive losses. The maximum efficiency predicted by Schockley and Queisser for a single-junction solar cell is 33 % for an optimum bandgap of $E_g = 1.4$ eV.

1.3.7 *Going beyond the Schockley-Queisser limit*

Several approaches have been developed to reach efficiencies beyond this limit. The main strategy to increase the conversion efficiency beyond the single-junction limit is to stack cells with different energy bandgaps [20], to obtain a so called

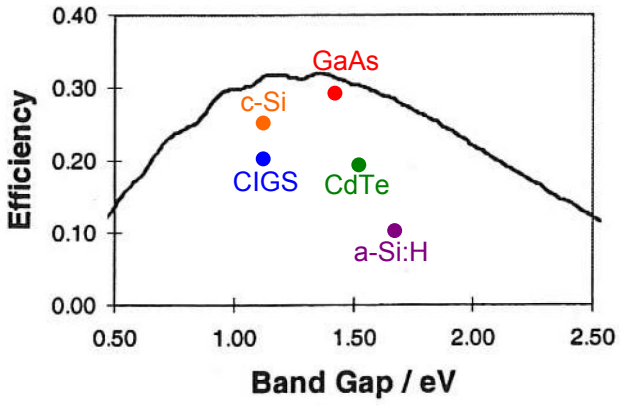

Figure 9: Limiting conversion efficiency (black curve) as a function of the material bandgap for a single-junction solar cell under one-sun AM1.5G illumination (figure extracted from Ref. 17). The current record efficiencies for several semiconductor materials are also shown.

multi-junction cell. As introduced previously (subsection 1.3.1), in a single-junction solar cell, photons with energies lower than the bandgap are not absorbed in the material, which limits the photogenerated current. In multi-junction designs, each cell converts a different energy range of the solar spectrum. It allows not only to increase the generated current because of the spectrum splitting but also to increase the open-circuit voltage. Indeed, as each junction converts photons in a specific energy range, it is possible to extract carriers generated by high energy photons at an energy closer to the bandgap.

The current efficiency record for a multi-junction solar cell is 44.4 % demonstrated by Sharp in April 2013 for triple junction InGaP/GaAs/InGaAs cells under concentrated light (302 suns) [21]. InGaP has a bandgap energy of 1.88 eV and InGaAs of 0.97 eV. Therefore, the InGaP junction absorbs high energy blue photons and InGaAs converts low energy photons in the infrared range that would not be absorbed in the single-junction GaAs cell ($E_g = 1.4$ eV). The multi-junction strategy has a short-term potential of 50 % conversion efficiencies. However, the most efficient multi-junction cells are based on III-V compounds semiconductor materials and require advanced growth techniques to achieve the lattice-matched multi-junction architecture. To date, this strategy is too expensive for wide-scale applications and limited to concentrator solar cells.

1.4 OVERVIEW OF THE PV TECHNOLOGIES

In this section, we give a brief overview of the existing technologies and their main characteristics. The latest record efficiencies for cells and modules are summarized in Table 1 for the main technologies. The energy bandgap of the different materials is shown in Fig. 9.

Material	Record cell efficiency	Record module efficiency
c-Si	25 % (UNSW)	22.9 % (UNSW)
a-Si:H	10.1 % (Oerlikon)	10.5 % (LG Electronics)
CdTe	19.6 % (GE Global Research)	16.1 % (First Solar)
GaAs	28.8 % (Alta Devices)	24.1 % (Alta Devices)
CIGS	20.4 % (EMPA)	17.8 % (SolarFrontier)
OPV	11.1 % (Mitsubishi Chemical)	-

Table 1: Values extracted from Ref. 21 and the latest efficiency chart from NREL (2013). It is noteworthy that the record module efficiency for a-Si:H technology is for tandem a-Si/Si-Ge/nc-Si cells. OPV stands for organic photovoltaics.

1.4.1 *Crystalline silicon*

At the present, 85 % of photovoltaic industry is based on crystalline silicon technology (monocrystalline or polycrystalline silicon). Silicon is an abundant and non toxic material and it has a nearly optimal bandgap energy ($E_g = 1.1$ eV) for solar cells as shown in Fig. 9. Most commercial silicon solar cells use single-crystal or poly-crystal silicon wafers with a thickness of $100 - 200$ µm. Purified silicon ingots are sawed to obtain wafers, that are then assembled into modules. Significant improvements have been done since the first 15 % efficiency reported in the eighties. In particular, contacts and surface passivation have been improved as well as light-trapping strategies. The latest efficiency record for a c-Si cell is 25 % achieved by the University of South Wales for a passivated emitter and rear, locally diffused cell [22]. Wafer silicon technology is limited by its cost: around 50 % of the module cost is due to the material cost and its processing. Furthermore, crystalline silicon has a low absorption coefficient because of its indirect bandgap and a thick semiconductor layer is required to achieve efficient absorption. Therefore, a second generation of solar cells based on direct bandgap materials has been developed with thin films with a thickness of a few microns.

1.4.2 *Thin film technologies*

1.4.2.1 *Amorphous silicon*

Hydrogenated amorphous silicon (a-Si:H) has an absorption coefficient α much higher than crystalline silicon ($\alpha_{aSi} \sim 6.25\,10^5 \mathrm{cm}^{-1}\mathrm{cm}^{-1}$ at 500 nm, to be compared to $\alpha_{cSi} \sim 10^4 \mathrm{cm}^{-1}$ [23]) which enables absorber thickness reduction towards a few hundred nanometers. In addition to the decrease of silicon material usage, amorphous silicon technology also uses PECVD (plasma enhanced chemical vapor deposition) technique that allows large area, low temperature and high throughput deposition on low-cost substrates. The possible use of roll-to-roll deposition technique leads to an overall reduction of the manufacturing cost compared to c-Si modules. Amorphous silicon is thus a material of choice

for large-area electronics applications such as liquid-crystal displays. As for the applications to thin film photovoltaics, its potential is limited by the intrinsic material properties. In particular, amorphous silicon solar cells suffer from the well-known Staebler-Wronski effect that leads to efficiency degradation when the cell is illuminated. As a consequence, the current cell record of 10.1 % (Oerlikon Solar) for a single-junction solar cell [24] is dramatically lower than for the other thin film materials (CdTe, GaAs, CIGS) as can be seen in Table 1 and Fig. 9. The future of amorphous silicon technology relies on stacked cells with microcrystalline or nanocrystalline silicon in order to reach conversion efficiencies over 10 %. For instance, Kaneka has reported a 12.3 % efficiency for a tandem a-Si:H/µc-Si cell and LG Electronics has shown a 13.4 % efficiency for a triple junction a-Si/µc-Si/µc-Si cell [21].

1.4.2.2 *CdTe*

Cadmium telluride (CdTe) is a II-VI compound semiconductor with a direct optical bandgap at $E_g = 1.45$ eV. It has a high absorption coefficient: 99 % of photons are absorbed within two microns of CdTe. Therefore, CdTe has very good properties for photovoltaic applications. CdTe is currently the most developed thin-film technology with over 1 GW of world PV cell production in 2009 [25]. It is a mature technology at the industrial scale with a development of CdTe cells and modules led mainly by First Solar and GE Global Research. The current cell efficiency record of 19.6 % for CdTe/CdS heterojunctions is held by GE Global Research [21]. CdTe modules efficiency is also increasing rapidly: First Solar has just reported a record 16.1 % module efficiency, which represents an increase of nearly 2 % over their prior record set in 2012 [21]. However, wide-scale commercialization of CdTe modules faces safety issues due to the cadmium toxicity. Managing Cd includes protecting the environment from contamination in the event of a mechanical failure as well as the recycling of the modules. CdTe also uses tellurium which is one of the rarest metals on earth.

1.4.2.3 *GaAs*

Gallium arsenide (GaAs) is a III-V compound with an optimal bandgap of 1.4 eV as shown in Fig. 9. The current world's highest conversion efficiency for a single-junction solar cell has been obtained with GaAs material by Alta Devices: 28.8 % have been reported for only 1 micron of GaAs [21]. The records for dual junctions and other multijunctions have also been obtained for III-V compounds, by Alta Devices and Sharp, respectively [21]. Furthermore, these record cells are achieved in lightweight and flexible thin-film cells that are compatible with wide-scale deployment. However, GaAs solar cells are not cost-competitive with other thin-film technologies and are limited for specific applications such as space devices or portable systems more generally.

1.4.2.4 *CIGS*

$Cu(In,Ga)Se_2$ (CIGS) is a compound chalcogenide semiconductor obtained from alloying copper, indium, gallium and selenide. The bandgap of CIGS can be tuned between 1.04 and 1.68 eV depending on the gallium content, the most efficient cells having a bandgap of $1.2 - 1.25$ eV [25]. CIGS technology also has a high potential for large-scale industrial applications thanks to several deposition techniques available, and in particular the possibility to use flexible substrates and roll-to-roll processes. A record 20.4 % efficiency has been obtained very recently at the laboratory scale by EMPA [21] for flexible films on polymide. However, the wide-scale development of the CIGS technology is likely to be limited by the scarcity of Indium. Alternative indium-free materials such as Cu_2ZnSnS_4 (CZTS) and CZTSSe are currently developed with lower but still promising efficiencies so far: 8.5 % for CZTS and 11.1 % for CZTSSe [21]. Another strategy could be to reduce the amount of CIGS material used through ultra-thin CIGS absorber layers [26] or microscaled CIGS cells [27].

1.4.3 *Organic photovoltaics*

Other technologies have been developed (organic photovoltaics, dye-sensitized solar cells, quantum dot solar cells) with limited performances so far. Among the emerging technologies, organic photovoltaics (OPV) has shown an impressive growth over the last decade. 11.1 % efficiency has been demonstrated by Mitsubishi Chemical in 2012 [21] and Heliatek is currently claiming a record over 12 %, yet to be confirmed. Organic PV relies on applying technologies already developed for the OLED (organic light-emitting diodes) industry. It has a high potential for large-scale applications because of its low fabrication cost [28] and the already mature technology. The major challenge currently faced by OPV is long-term stability, yet to be demonstrated for commercial modules. It should be noted that in the framework of the thesis, the concept of nanopatterned transparent front electrodes, which is developed further in *chapter 3*, has been mainly inspired by works done on alternative electrodes for organic solar cells.

1.5 THE FUTURE OF PV: GOING THINNER?

This thesis is focused on ultra-thin solar cells. As already mentioned, thin film technologies have been the first step towards more efficient and cheaper photovoltaic devices. What could be the advantages of going thinner towards ultra-thin devices?

First, reducing the amount of raw material needed is still a key issue for several technologies because of the material cost (c-Si) or its scarcity (Te, Se, In). For c-Si technology, recent research is aimed at reducing the absorber thickness from 200 µm to nearly 10 µm[4]. For thin film technologies such as GaAs

4 The existing technologies to obtain thin c-Si films are developed in *chapter 10* of the thesis.

or a-Si:H, the goal is to reach 100 nm. In the following, the notion of *ultra-thin* solar cells will refer to a thickness reduction of a factor *at least* 10 compared to the standard commercial thickness for the technology considered. A clear consequence of the decrease of material usage is a drop in light absorption and thereby of the short-circuit current density of the ultra-thin photovoltaic device. As the absorber thickness is reduced, a smaller part of long-wavelength photons will be absorbed in a single pass in the solar cell. Light-trapping techniques are required to increase the effective optical path in the cell and thus, the short-circuit current density. For instance, performing a tenfold thickness reduction of CIGS cells while maintaining the same efficiency could relieve the limitations on Indium and Selenium scarcity. At the module scale, reducing further the thickness of solar cells also enables lightweight and flexible solar panels.

Second, the collection efficiency could benefit from thickness reduction. The lifetime of carriers depends on the quality of the semiconductor material but also on the thickness of the junction. Reducing the thickness of the junction decreases the number of recombination centers. It thereby leads to a decrease of non radiative bulk recombinations. This effect is particularly important in the case of materials with a low carrier diffusion length such as organic polymers or amorphous semiconductors. For instance, for amorphous silicon, thinner p-i-n junctions exhibit an improved stability upon light-induced degradation. It is worth noticing that thinner solar cells are more sensible to interfaces. The reduction of volume recombinations may be compensated by the increase of surface recombinations. The issue of surface passivation is therefore crucial for ultra-thin solar cells in particular in the case of structured cells where the area is increased, as in the case of nanowire solar cells for instance.

Third, as previously displayed in Eq. (8), the open-circuit voltage is a function of J_0, the dark current density or saturation current density. The dark current depends on the material volume, thereby decreasing the absorber layer thickness should also lead to a drop in the dark current. If the same value of the generated photocurrent J_{SC} is maintained, for instance using light-trapping techniques, the open-circuit voltage may be improved compared to thicker devices. Ultrathin solar cells with an increased conversion efficiency could be obtained.

To conclude this section, in a very recent article [29], Bernardi et al. from MIT have pushed the concept of ultra-thin solar cells towards the nanometer limit. They have studied the feasibility of nanometer-thin solar cells based on MoS_2/graphene systems. They suggest that a stacking of three graphene monolayers and three MoS_2 monolayers with a back metallic contact (for light trapping purposes) could reach 10 % efficiency with a 3 nm-thick active layer! Even if this design is only a concept so far, it shows that research on optoelectronics is currently bursting with proposals of novel architectures for ultra-thin solar cells.

In this thesis, we will concentrate on ultra-thin solar cells as defined above. Advanced strategies are required to compensate drop in light absorption due to thickness reduction. In *chapter* 2, we give a selected state-of-the-art of light-trapping approaches for absorption enhancement in ultra-thin semiconductor layers.

1.6 SUMMARY

The redrawing of the current energy market is driven by the necesity to meet global energy demand while reducing greenhouse-gas emissions. Solar photovoltaics is an attractive candidate to supply renewable and clean energy provided that it is competitive for large scale applications.

Ultra-thin solar cells have the potential to reduce production cost while increasing the conversion efficiency. The design of ultra-thin solar cells still require advanced strategies to confine light absorption within very thin absorber layers in order to increase the short-circuit current density.

2

STATE-OF-THE-ART: LIGHT-TRAPPING IN ULTRA-THIN LAYERS

Contents

As explained in *chapter* 1, ultra-thin solar cells are attractive only if high photocurrent can be achieved in very thin absorber layers. Therefore, research on light-trapping strategies for ultra-thin layers has drawn a lot of attention in the past few years. The aim of this section is not to give an extensive review of the works published so far but to give an overview of the different approaches in order to place this thesis within the research field. The integration of strategies to enhance light absorption is particularly important for a-Si:H solar cells because of their low conversion efficiency, as will be further discussed in PART 2, *chapter* 5. As a consequence, most light-trapping approaches presented in this chapter have been developed for a-Si:H devices.

2.1 TEXTURING OF INTERFACES

Standard light-trapping schemes rely on texturing of interfaces. Light is scattered at the interface, thereby increasing the optical path length in the cell. Texturing approaches have been developed for both thick solar cells (as c-Si) and thin film solar cells.

2.1.1 *Ergodic limit for thick films*

For thick films in the ergodic limit, light is not coherent over the thickness of the film and light trapping can be described with ray optics. Yablonovitch and Cody have defined the limit of the path length enhancement due to light scattering on a textured surface in an article published in 1982 [30]. In a structure

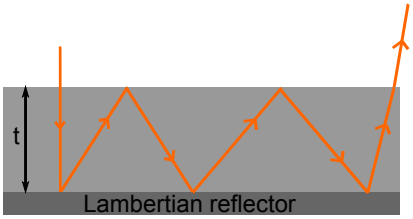

Figure 10: Lambertian surface used as a back reflector. In this case, after three reflections on the Lambertian surface, the ray has an angle lower than the critical angle for total internal reflection and thereby, escapes the cell.

without any light trapping structure, photons incoming at a normal incidence on a semiconductor film with a thickness t travel an average distance equal to t. One approach to enhance the path length is to use a randomising surface. Figure 10 illustrates the case of a Lambertian surface used as a back reflector. A Lambertian surface is a perfectly randomising surface that scatters light isotropically, which means that all reflected angles have the same probability. Let us consider incident light at normal incidence as pictured in Fig. 10. After reflection on the rear surface, if the ray strikes the front surface with an angle wider than the critical angle, it is internally reflected for another double pass within the cell. Only rays which are reflected within the escape cone come out of the cell. In the case illustrated in Fig. 10, it occurs after three reflections on the Lambertian surface. The average path length for the reflected ray to strike back the front surface is twice the cell thickness. If we add up the path lengths of the rays taking into account the number of times they scattered, we find the ideal path length due to Lambertian scattering [30]:

$$< l >= 4\,n^2 t\,, \tag{9}$$

where n is the refractive index of the solar cell material. It represents a path length enhancement with respect to a planar semiconductor of $4\,n^2$, well known as the Yablonovitch limit. This limit is valid only for semiconductor films with a thickness $t \gg \frac{\lambda}{2n}$, with λ the incoming wavelength and therefore, is not valid for thin film solar cells. The upper limits of path length enhancement for different nanophotonic strategies have been summarized in a recent review article [31].

The most widely used strategy to texture thick films is random surface texturing, which is easy to fabricate with standard wet etching techniques and offer effective light trapping over a wide angular and spectral range. In particular, random pyramidal texturing obtained with anisotropic wet etching is a well known light-trapping strategy for c-Si solar cells [32–34]. An overview of light-trapping approaches for c-Si cells is presented in PART 4, chapter 10.

2.1.2 *Texturing of interfaces in thin film silicon solar cells*

The current world-record for single-junction a-Si:H solar cells has been obtained with transparent ZnO electrodes with random pyramidal texture as shown in Fig. 11a [24]. The size and shape of the random textures have to be carefully optimized in order to achieve the highest performances. Scattering textures

with larger features are favorable to high short-circuit current density values because of increased light scattering. However, the growth of amorphous silicon on rough substrates leads to defective active layers [35, 36]. Some works have proposed designs that decouple the textured interface for light scattering from the growth substrate which should be flat in order to achieve high open-circuit voltage and fill factor [37, 38].

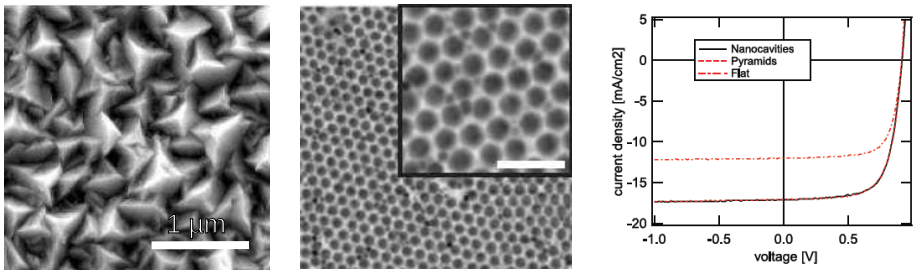

(a) (b) (c)

Figure 11: Random versus periodic surface texturing: (a) SEM image of a LPCVD-ZnO substrate with a random pyramidal texture (Figure extracted from Ref. 24); (b) AFM image of periodic nanocavities fabricated by nanosphere lithography (Figure extracted from Ref. 39). The scale bar is 1 µm; (c) J-V curves for a-Si:H cells deposited on a periodic nanocavity array, a random pyramidal texture and a flat substrate (Figure extracted from Ref. 39).

Periodic textures have also been developed [40–42] with the possibility of using low-cost and large-area patterning processes such as nanoimprinting and nanomoulding [43, 44]. The question of whether periodic structures are more efficient than random textures is still unresolved in spite of theoretical [45] and experimental [39, 46, 47] studies. For instance, Battaglia et al. [39] have processed a-Si:H solar cells (thickness $=$ 250 nm) on a scattering substrate with periodic arrays of nanocavities on glass, as displayed in Fig. 11b. They have shown that the periodic nanocavities achieve an initial conversion efficiency of 10.9 % which is the same as for a random textured substrate (Fig. 11c). So far, no experimental studies have demonstrated unambiguously that periodic structures could outperform random structures. However, as the range of shapes and sizes of random textures available is limited, periodic structures offer the possibility to design morphologies with a large-angle scattering while avoiding V_{OC} and FF losses.

2.2 PERIODIC NANOPHOTONIC STRUCTURES

More complex structures have been proposed to control light propagation in thin-film solar cells such as photonic crystals [4, 48–55], diffraction gratings [40, 41] or nanowires [56, 57]. All these approaches have already shown promising results. However, a major problem of structured cells is the high surface recombination that may be encountered because of the higher surface area and the etching of the active layer.

Photonic crystals have been proposed as a promising approach to enhance light absorption in ultra-thin solar cells a few years ago [58]. A photonic crystal is a structure with a periodical modulation of the refractive index. The lattice constant of the photonic crystal is of the order of the incoming wavelength. Photonic crystals allow to control light propagation and in the case of ultra-thin solar cells, to confine light in very thin layers. 1D [48, 52, 54], 2D [4, 53] and 3D [51, 55] geometries have been proposed. Figure 12a presents the schematic view of an ultra-thin amorphous silicon solar cell with 2D photonic crystals. A periodic array of holes is etched within the active a-Si:H layer (thickness = 100 nm) and the top ITO layer. Meng et al. have fabricated such structures using holographic lithography and shown an absorption enhancement of 28 % compared to an unpatterned cell [4]. Incident light is coupled onto Bloch modes that propagate in the plane of the a-Si:H layer. As for diffraction gratings, they can be used either on the front side of the cell to decrease reflection and enhance the coupling of incoming light or on the back side as advanced back reflectors. Double-sided designs have recently been proposed to obtain a broadband absorption enhancement [49, 59].

Thickness reduction towards ultra-thin solar cells is partly motivated by the idea of improving carrier collection in the device. To do so, the cell has to be electrically thin but optically thick in order to achieve efficient light absorption. 3D nanostructured geometries with nanowires, nanorods or nanocones have been proposed to decouple the optical path from the electrical path. For instance, Vanecek et al. [56] have implemented a "swiss cheese" design in a micromorph a-Si/µc-Si tandem cell. As shown in Fig. 12b, an hexagonal array of holes has been patterned in a ZnO substrate using UV-photolithography and RIE process in order to obtain a nanostructured solar cell. A short-circuit current density enhancement of 40 % has been demonstrated for such a cell compared to a cell with flat ZnO layers [56].

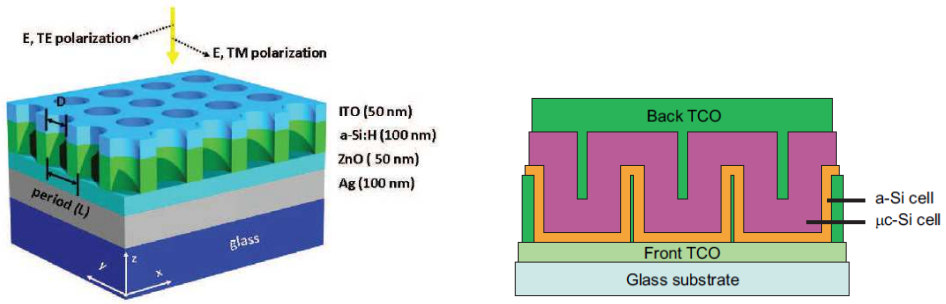

(a) (b)

Figure 12: Advanced nanophotonic designs for thin-film silicon solar cells. (a) Ultra-thin amorphous silicon solar cell with a 2D array of photonic crystals (Figure extracted from Ref. 4). (b) "Swiss cheese" design: the micromorph tandem cell is folded in an array of holes patterned in the TCO substrate (Figure extracted from Ref. 56).

2.3 PLASMONICS FOR PHOTOVOLTAICS

2.3.1 *Introduction to plasmonics*

Even if the bases of plasmonics have been already described at the beginning of the 20th century [60], the field of plamonics has started to expand mainly since 1998 thanks to newly developed fabrication and modelisation tools at the nanoscale. The ability of plasmonic structures to confine and control light at the nanoscale has opened novel applications in applied physics [61]. In particular, the possible enhancement of light absorption using metallic nanostructures has driven many works on the application of plasmonics to photovoltaic devices as reviewed in some recent articles [62–66]. Three main strategies have been developed to integrate plasmonic nanostructures in photovoltaic devices [62]. In this section, after introducing the properties of surface plasmons, we address the potential and limitations of plasmonic structures for photovoltaic applications.

Plasmonics relies on interactions between electromagnetic radiation and conduction electrons in metal. The two forms of plasmonic interactions are *surface plasmon polaritons* (SPP) and *localized surface plasmon resonances* (LSPR) as described in the following.

2.3.1.1 *Surface plasmon polaritons*

Surface plasmon polaritons are propagating waves localized at the interface between a metal and a dielectric as depicted in Fig. 13. They arise from the coupling of an electromagnetic field to the collective oscillations of conducting electrons in the metal. SPP modes exist at wavelengths above the surface plasmon resonance wavelength, which is 600 nm for silver. SPPs are evanescent waves: they are strongly confined at the metal/dielectric interface. The dispersion relation of a surface plasmon at the dielectric/metal interface is given by:

$$k_x = k_0 \sqrt{\frac{\epsilon_d \times \epsilon_m}{\epsilon_d + \epsilon_m}}\,, \tag{10}$$

with ϵ_d and ϵ_m the dielectric functions of the dielectric and the metal respectively. k_x is the wavector along the x axis and k_0 is the incident momentum. k_{zi} the component of the wavector along z in the material i is given by:

$$k_{zi} = \sqrt{(\epsilon_i k_0^2 - k_x^2)}\,, \tag{11}$$

with ϵ_i the dielectric function of the material i (ϵ_d for the dielectric and ϵ_m for the metal). The wave amplitude along z axis decays exponentially with the distance from the interface as shown in Fig. 13. The decay length δ_i of the surface plasmon polariton, i.e the penetration depth of the evanescent wave, characterises the confinement of the surface plasmon in the material i along the z axis (see Fig. 13). It depends on the dielectric function of the material i:

$$\delta_i = \frac{1}{|\mathrm{Im}(\mathrm{k_{zi}})|}\,, \tag{12}$$

with k_{zi} the component of the wavevector along z in the material i, which can be determined from Eq. (11). The wave is more confined in the metal than in the dielectric. For SPPs at a GaAs/Ag interface, at 700 nm, we calculate $\delta_{Ag} = 14$ nm and $\delta_{GaAs} = 24$ nm from Eq. (12). Thanks to SPPs, field confinement below the diffraction limit is achieved in the dielectric material. It also means that in a metal/dielectric/metal structure, if the dielectric layer is sufficiently thin, the SPPs at the metal/dielectric interfaces can be coupled. This point is discussed further in the case of Ag/GaAs/Ag structures in PART 3, *chapter 8*.

The damping of surface plasmon polaritons is characterized by their propagation length along the x direction. The surface plasmon propagation length δ_{SP} (intensity decay length), characteristic from the wave intensity attenuation along the x axis, can be expressed as:

$$\delta_{SP} = \frac{1}{2 \times \mathrm{Im}(k_x)}, \tag{13}$$

and therefore can be determined from Eq. (10). In the case of SPPs at a GaAs/Ag interface, the propagation length is $\delta_{SP} = 87$ nm at 700 nm. The propagation length and the decay length are interrelated: stronger field confinement (smaller decay length) leads to an increased damping (smaller propagation length).

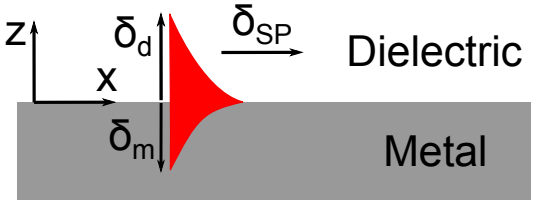

Figure 13: Surface plasmon polariton propagating at a dielectric/metal interface. The vertical confinement of the surface plasmons is characterized by δ_d and δ_m, the decay lengths of the plasmon mode in the dielectric and in the metal, respectively. The attenuation of the surface wave along the x axis is characterized by δ_{SP}.

2.3.1.2 *Localized surface plasmons*

On the other hand, localized surface plasmons are non-propagating excitations of the electrons in the metal [60]. The simplest structure to study LSPR is a metallic sphere (size $d \ll \lambda$) placed in an electromagnetic field. Upon application of an electromagnetic field (in the case of photovoltaics, the incoming solar radiation), a resonant dipole moment is induced inside the nanoparticle. The resonance of the nanoparticle dipole induces a field enhancement in the vicinity of the particle as well as an enhancement of the scattering and absorption efficiencies. The scattering and absorption cross-sections can be expressed as follows [60, 67]:

$$C_{sca} = \frac{k^4}{6\pi}|\alpha|^2 \propto d^6. \tag{14}$$

$$C_{abs} = k\,\mathrm{Im}(\alpha) \propto d^3. \tag{15}$$

k is the wavevector $k = \frac{2\pi}{\lambda}$ and α the polarizability of the nanoparticle. We see from Eqs. (14) and (15) that the dominant mechanism (scattering or absorption) depends on the size d of the nanoparticle.

2.3.2 *Light scattering by metal nanoparticles*

Metal nanoparticles have enhanced scattering cross sections near their plasmon resonance wavelength. As illustrated in Fig. 14, two main geometries have been proposed to use scattering metal nanoparticles to enhance absorption in solar cells. For both approaches, several large-area patterning processes have been developed such as self-assembly of metal islands [68–70], imprint lithography [71] and hole-mask colloidal lithography [72, 73].

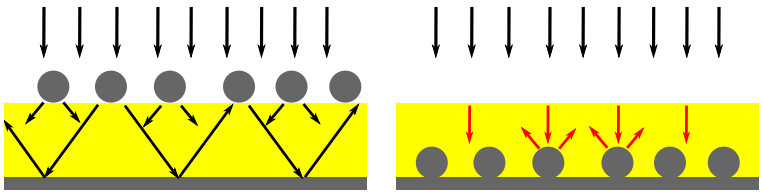

Figure 14: Light trapping by scattering from metal nanoparticles placed on (a) the front and (b) the rear surface of the solar cell.

In the first geometry (Fig. 14a), metal nanoparticles are placed on the front surface of the cell and in most cases, associated with a metallic mirror as a back contact. The incoming photons are scattered by the nanoparticles and they acquire an angle in the semiconductor. The optical path length of the photons in the cell is thereby increased. Furthermore, long-wavelength photons that are weakly absorbed in a single pass can be reflected on the back mirror and be scattered back in the semiconductor layer by the nanoparticles. The front scattering approach has already been applied to a-Si:H [74–76], GaAs [77, 78] and quantum well [79] solar cells. Most works have used silver nanoparticles but a recent numerical study by Hylton et al. [78] on GaAs solar cells suggests that aluminium nanoparticles could lead to higher efficiency enhancements. Al has a higher k value, which using Eqs. (14) and (15) leads to a higher scattering cross-section and lower parasitic absorption losses in the nanoparticles than Ag and Au.

In order to limit the parasitic absorption in the front metal nanoparticles, a second geometry has emerged with metal scatterers integrated in the back contact. So far, this approach has been mainly used in thin film silicon cells (a-Si:H [70] or µc-Si:H [71]). As shown in Fig. 14b, in this approach, the fonction of the back reflector is to scatter and reflect long-wavelength photons (in the red spectral range) that are weakly absorbed in a single pass. For instance, Tan et al. [70] have reported a gain of 2 $\mathrm{mA/cm^2}$ in the short-circuit current density

of an a-Si:H (thickness = 300 nm) solar cell with a back reflector made of self-assembled silver nanoparticles with respect to a flat back mirror. They have also shown that the silver back scatterers lead to improved performances compared to standard textured Asahi glass.

The front approach offers the major advantage of depositing the metal nanoparticles at the end of the fabrication process. Indeed, the rear side geometry assumes that the active material is grown on the metal nanoparticles which can induce defects that can be detrimental for the V_{OC} and FF [35, 36]. This technical advantage has to be balanced with the higher metal losses associated to the front approach.

2.3.3 *Near-field enhancement*

A second way to take advantage of localized plasmon resonances is to use the strong local field enhancement near metal nanoparticles. In a standard antenna problem, the optical antenna couples the energy of the incoming radiation into the receiver. Small metal nanoparticles ($20 - 50$ nm) can be considered as subwavelength optical antennas that boost the efficiency of the photovoltaic conversion process [62, 80]. To do so, metal nanoparticles are embedded within the active material. Close to the plasmon resonance wavelength, the effective absorption cross-section is increased (see Eq.(15)). It enhances the efficiency of the creation of electron-hole pairs in the vicinity of the metallic particles.

This approach has been particularly developed in organic [66] and dye-sensitized [81] solar cells. The embedding of metal nanoparticles in the active layer is quite easy in OPV but it may be more difficult in inorganic photovoltaics technology. The near-field approach is also limited by the parasitic absorption in the metal particles. The optical antennas are efficient only if the absorption process in the semiconductor is faster than the plasmon decay in the particles [62]. Otherwise, all the incoming energy is lost within the metal particles.

2.3.4 *Excitation of guided SPP modes*

The third approach relies on the coupling of incident photons to surface plasmon polariton modes at the rear surface of the solar cell. This approach has been particularly developed for a-Si:H solar cells with 1D [5, 59, 82, 83] or 2D [6, 7, 47] metallic arrays. Photocurrent enhancement has been experimentally demonstrated in ultra-thin (thickness $= 100 - 200$ nm) amorphous silicon solar cells for 1D [5] and 2D [6, 7] silver gratings integrated in the back contact. The absorption enhancement is attributed to the excitation of guided modes thanks to the metal grating. The light then propagates horizontally within the semiconductor layer. Another approach with a double sided design has been proposed [59]. As for GaAs, Ferry et al. [84] have proposed subwavelength ridges in the metallic back mirror to enhance the performances of GaAs solar cells thickness $= 50 - 200$ nm). They have predicted numerically an absorption enhancement factor between 1.4 and 1.6 near the band edge (880 nm) with respect to absorption in a identical film without a groove.

So far, this third approach seems the most promising for solar cells with absorber layers below 100 nm. However, the design of plasmonic back contacts for photovoltaic devices has to take into account the intrinsic limitations of surface plasmon modes:

- SPPs do not exist for a transverse electric polarization
- part of the SPP wave decays in the metal, inducing parasitic losses
- SPP modes are dispersive and thereby sensitive to incident light angles.

Regarding the first point, one-dimensional structures (gratings or ridges) are often used to spare calculation time in the numerical studies. It is also a valuable tool to analyze in detail the absorption mechanism because of its selectivity to polarization. However, in order to integrate efficiently plasmonic back reflectors in solar cells, the design has to be insensitive to the polarization (TE or TM). A common solution is to use a 2D geometry (square particles or crossed grating) which is by definition independent from the incident polarization at normal incidence. In PART 2 of this thesis, we will show that a broadband absorption spectrum can be achieved in both TE and TM polarizations with one-dimensional structures by combining multiple resonances.

As for the second point, a main limitation of plasmonic structures is parasitic absorption losses in the metallic parts. By definition of the SPP modes, the propagating wave decays in both the semiconductor and the metal. The absorption in the semiconductor contributes to the generated photocurrent whereas the photons absorbed in the mirror lead to ohmic losses. SPP losses in the metal can be engineered with a spacer layer between the semiconductor and the back mirror [82, 85]. This point is further developed in PART 2, *chapter* 6 along with the full design of an ultra-thin plasmonic amorphous silicon solar cell.

About the third point, another key issue is to achieve a broadband and omnidirectional response. Resonant phenomena are intrinsically characterized by a small absorption bandwidth. Multiple electromagnetic modes can be combined to broaden the absorption spectra such as SPP resonances, waveguide mode resonances and Fabry-Perot resonances. In a recent article, Aydin et al. [86] have proposed an ultrathin (260 nm) super absorber made of a metal-insulator-metal stack. The top metal film is patterned with crossed trapezoidal arrays in order to achieve an omnidirectional and polarization-independent absorption. Broadband resonant absorption is maintained for an incident angle up to 70°. However, in this design, power is mainly absorbed in the top and bottom silver films. In a similar configuration, Cattoni et al. [87] have fabricated two-dimensional metal/insulator/metal cavities with nanoimprint lithography performing nearly perfect omnidirectional total absorption at the resonance wavelength. The square metal nanoparticles play the role of Fabry-Perot resonators for SPPs propagating at both top and bottom metal/insulator interfaces. In PARTS 2 and 3 of this thesis, we propose designs to implement this multi-resonant approach in order to achieve high absorption within an ultrathin semiconductor layer.

2.4 CONCLUSION

The starting point of this thesis is to design efficient ultra-thin solar cells. For thin film materials, our objective is to go below 100 nm for the absorber layer thickness. In this chapter, we have presented the existing approaches for light-trapping in thin and ultra-thin film solar cells. Most of the proposed strategies have not been implemented for 100 nm-thick absorber layers yet. Photonic crystals show promising results [4] but imply to etch the active layer which may increase surface recombinations. As for plasmonic structures, designs with a patterned back contact have already shown their ability to confine light in very thin layers (thickness $<$ 100 nm). However, growing the active layer on a patterned substrate creates defective areas (cracks and voids) that induces shunt currents in the solar cells [35, 36].

In this thesis, we have chosen to focus on plasmonic nanostructures integrated in the front side of the solar cell. This approach offers the advantage of keeping a flat active layer which prevents the problems mentioned above. The light-trapping structure can be patterned at the end of the fabrication process. Last but not least, our idea is to give the metallic light-trapping structure an additional functionality. A metallic grating can be used to confine light absorption in the absorber layer but also to ensure carrier collection at the front side of the cell. In next chapter, we give an outlook of transparent conductive electrodes with metallic films before introducing the concept of resonant nanostructured front contact that we have used in this thesis.

2.5 SUMMARY

The research field of light-trapping solutions for thin film solar cells has been very fertile over the past few years. Among the proposed strategies, plasmonic nanostructures show a strong potential to enhance light absorption in very thin absorber layers.

In this thesis, our approach is based on an ultra-thin (thickness $<$ 100 nm) absorber layer with a plasmonic nanostructure placed on the front side of the absorber. The plasmonic structure has a double functionality: it plays the role of a light-trapping structure to confine light absorption and an alternative electrode to ensure carrier collection on the front contact.

3

TRANSPARENT CONDUCTIVE ELECTRODES WITH METALLIC FILMS

Contents

3.1 STATE-OF-THE-ART OF TRANSPARENT ELECTRODES

Transparent conductive electrodes (TCE), i.e electrodes that combine optical transparency and high conductivity, are of main importance for photovoltaics technologies. $In_2O_3 : SnO_2$, commonly abbreviated as *indium tin oxide* (ITO), is the most used *transparent conductive oxide* (TCO) material because of its high optical transmission in the visible range and low sheet resistance. However, since 2005, with the increasing demand of indium for both photovoltaics and flat-panel display industries, many research works have focused on the replacement of ITO. Research on alternative TCEs is mainly driven by the cost of ITO sputtering deposition and the scarcity of indium. Recently, in the particular field of organic photovoltaics, ITO-free electrodes have drawn attention due to the chemical incompatibility of ITO with organic devices [66, 83, 88–95]. ITO has been identified as a source of oxygen leading to a degradation of the devices [96]. For more general applications, in a review article published recently in Nature Photonics, Ellmer summarizes the different approaches developed to replace ITO [97]. In the following, the main TCEs reviewed in this article will be presented briefly before focusing on transparent electrodes with metallic films.

3.1.1 *Indium-free transparent conductive oxide materials*

Good alternatives to ITO are *zinc oxide* (ZnO) or *tin oxide* (SnO_2) which are non toxic, inexpensive and abundant materials but too resistive to be used as a front contact. One solution to improve their conductivity is to use dopants to increase the carrier concentration. For instance, SnO_2:F or ZnO:Al are TCO materials commonly used in electronics. However, increasing the carrier concentration comes at the expense of transparency because of absorption of light

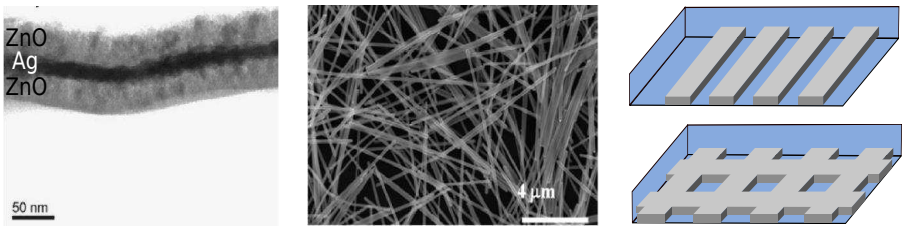

(a) (b) (c)

Figure 15: Different geometries of TCEs with metallic films. (a) Transmission electron microscopy (TEM) picture of the cross section of a ZnO/Ag/ZnO structure with a 14 nm-thick Ag layer [99]. (b) Scanning electron microscopy (SEM) image of Ag nanowires [100]. (c) Schematic of TCEs with a one-dimensional or two-dimensional silver grid (grey) embedded in a TCO material (blue).

by free carriers. Another strategy to increase the conductivity without loss of transparency relies on embedding a metallic film (uniform or patterned) in the TCO material. This multilayer approach is developed in the following.

3.1.2 *Carbon alternatives*

Another class of transparent contacts is based on carbon: single-walled carbon nanotubes networks [88], graphene [89] or conductive polymer films [90]. Hecht et al. [98] gave an overview of these carbon-based strategies in a recent article. In particular, graphene electrodes are a very promising candidate for ITO replacement because of their very high electron mobility and high optical transmittance (higher than conventional ITO layers). Yet, large-area production and long-term stability of graphene-based electrodes have still to be demonstrated.

3.1.3 *Transparent conductive electrodes with metallic films*

Figure 15 presents several geometries proposed for TCEs with metallic films:

- multilayer TCO/metal/TCO electrodes (Fig. 15a)
- metal nanowire networks (Fig. 15b)
- metal nanogrids (Fig. 15c).

The first approach, based on combining thin metal films (Ag, Cu, Au,...) with TCO materials (ITO, ZnO, SnO_2), is inspired from low-emissivity coatings on glass [101]. The idea was to control the heat passing through glass windows using the optical properties of thin metal films: high transmittance in the visible range and high reflectivity in the infrared.

In the case of TCEs, both optical and electrical properties of metallic layers are used. Among the metals, silver (Ag) is preferred [1] because of its very low bulk resistivity $\rho_{Ag} = 1.6\,\mu\Omega.\text{cm}$.

Let us consider a TCO/Ag/TCO three-layer structure (Fig. 15a). The resistances of the single layers (top and bottom TCO layers, silver layer) are connected in parallel. The equivalent resistance of this system can be expressed as:

$$\frac{1}{R_{eq}} = \frac{1}{R_{TCO\,top}} + \frac{1}{R_{Ag}} + \frac{1}{R_{TCO\,bottom}}\,. \tag{16}$$

The TCO material is much more resistive than silver ($\rho_{TCO} \sim 100\,\mu\Omega.\text{cm}$ [104]). If we take a TCO thickness of 30 nm, and a silver film of 10 nm, Eq. (16) leads to:

$$\frac{1}{R_{eq}} = \frac{1}{R_{Ag}} \times \left(1 + \frac{6 \times 1.6}{100}\right) \sim \frac{1}{R_{Ag}}\,. \tag{17}$$

Integrating a thin metal film in a TCO material thus reduces greatly the resistance of the electrode. Several works have focused on the optimization of TCO/Ag/TCO multilayer electrodes for various TCO materials: ITO [91, 105], ZnO [99] and ZnO:Al [106]. The optimum thickness of the silver film is chosen to achieve both high optical transmittance and good electrical conductivity. For instance, Crupi et al. [106] showed that the electro-optical properties of the tri-layer electrode were optimized upon insertion of an ultra-thin 9.5 nm-thick silver layer between two layers of ZnO:Al (20 and 30 nm). They have reported an average transmittance of 75 % in the visible range and a sheet resistance of $6\,\Omega/\square$ (to be compared to $10^6\,\Omega/\square$ without any silver layer) [106]. Besides, the bi-layer TCO material allows to prevent both the degradation of the metal optical properties because of oxidation and the diffusion of metal atoms in the active layer of the solar cell as reported by [106]. Hence, these ZnO:Al/Ag/ZnO:Al multilayer structures offer better durability and enhanced thermal stability compared to single-layer metal electrodes.

In order to enhance the optical transparency of the electrode, the ultra-thin metal film can be replaced by a patterned film. Two geometries have been proposed: random metal nanowire networks (Fig. 15b) and periodic one-dimensional (1D) or two-dimensional (2D) metallic nanogrids (Fig. 15c). The apertures in the metallic film enable a better light transmittance and the conduction is ensured along the grid or the percolating nanowires network. Scalable and low-cost fabrication processes have been developed for these two geometries: spin coating [107], air spraying [108], inkjet printing [109] or nanoimprint [92, 93]. All these approaches may enable significant cost reductions compared to sputtered deposition of ITO and are suitable for flexible applications. Note that these approaches can be combined with other strategies presented previously: silver nanowires (AgNW) can be embedded in a TCO material [107] or in graphene

1 Several recent works have focused on the design of copper-based nanostructures for transparent electrodes [102, 103]. Copper could be a good alternative to silver: it has a similar conductivity and is cheaper and more abundant.

sheets [100] in order to enhance the conductivity and the flexibility of the transparent contact. However, the nanowire approach may have drawbacks compared to metal nanogrids: i) optimization of the nanowires density is required to ensure the existence of a percolating network [107] and ii) nanowire networks are more likely to encounter degradation due to junction resistances between the nanowires [102].

Very recently, Kim et al. [107] reported an indium-free transparent electrode composed of a ZnO/AgNW/ZnO multilayered system integrated in a CIGSSe thin film solar cell. They showed that the composite electrode exhibited higher V_{OC} and J_{SC} compared to a CIGSSe solar cell with a sputtered ITO transparent electrode, resulting in a 20 % increase in the power conversion efficiency [107]. This work shows the potential of nanostructured metallic transparent contacts to improve the efficiency of thin-film photovoltaic devices. For now, these novel TCE strategies have been limited to organic and CIGS devices, but they are suitable for any photovoltaic material. In this PhD thesis, we propose to apply such concepts to amorphous silicon (PART 2) and GaAs (PART 3) cells.

3.2 COMPARISON OF TRANSPARENT CONDUCTIVE NANOSTRUCTURED ELECTRODES FOR SOLAR CELLS

In the previous section, the properties of different transparent electrodes were presented qualitatively. If we want to choose the proper TCE given a specific photovoltaic system (absorber material, device configuration,...), an accurate *figure of merit* (FoM) is required. In Ref. 110, Barnes et al. review the existing figures of merit in order to determine the most adequate metrics to evaluate the benefits of novel TCE approaches for photovoltaics applications. In this section, I will first define the most useful FoMs and then compare the potential of TCE with metallic films using the different FoM.

The simplest figures to evaluate the potential of a TCE are its visible transmittance T and electrical sheet resistance $R_\square$. The transmittance $T(\lambda)$ is defined as the fraction of incident light passing through the material at a specific wavelength. The sheet resistance $R_\square$ of a uniform film (thickness h, bulk resistivity ρ) is given by[2]:

$$R_\square = \frac{\rho}{h} \tag{18}$$

and is expressed in $\Omega/\square$.

If we consider a nanostructured metallic film as the ones depicted in Fig.15c (thickness h_m, grating period p, width of the wires w, bulk resistivity ρ), the sheet resistance for a current flow along the wires is [112]:

$$R_\square = \frac{\rho}{h_m} \times \frac{p}{w}\,. \tag{19}$$

A relevant FoM must take into account the two main properties of transparent contacts: high transmittance and low sheet resistance. A first FoM has been

2 This expression assumes a thickness-independent resistivity ρ. For metal films thinner than 30 nm, the sheet resistance increases due to electron scattering at the surfaces and grain boundaries. A more accurate value for R_s can be calculated using Fuchs–Sondheimer and Mayadas–Shatzkes models [111].

introduced by Haacke [113] in 1976 following the work of Fraser and Cook [114] who first proposed to assess the performances of ITO films using the ratio of the transmission over the sheet resistance. The maximum value of this ratio is obtained for a transmittance $T = 37\,\%$, which is too low for applications to transparent electrodes. As a consequence, Haacke redefined a FoM in order to achieve a better balance between transmittance and sheet resistance:

$$\phi_H = \frac{T^x}{R_\square}\,, \tag{20}$$

where $x > 1$ [113]. If we take $x = 10$ in this expression, the maximum value ϕ_H is reached for a 90 % transparency of the material. This is suitable for most transparent conductive oxide applications. Haacke's FoM is thereby given in its usual form by:

$$\phi_H = \frac{T^{10}}{R_\square}\,. \tag{21}$$

Another widely used FoM, called Jain's FoM, is defined by [104, 115]:

$$\phi_J = \frac{\sigma}{\alpha} = -\frac{1}{R_\square\, ln(T+R)}\,, \tag{22}$$

with σ and α the bulk conductivity and absorption coefficient of the material, respectively. R is the optical reflectance of the transparent electrode. ϕ_H and ϕ_J are both expressed in Ω^{-1}.

In several publications, ϕ_H and ϕ_J are determined using the value of the transmittance and reflectance at 550 nm. For photovoltaics applications, the optical properties of the transparent contact must be known on the whole visible range. As a consequence, Barnes et al. [110] defined the weighted transmittance:

$$WT = \frac{Transmitted\ power}{Incident\ power} = \frac{\int_{\lambda_1}^{\lambda_2} P(\lambda)T(\lambda)d\lambda}{\int_{\lambda_1}^{\lambda_2} P(\lambda)d\lambda}\,. \tag{23}$$

$P(\lambda)$ is the AM1.5G solar flux and $[\lambda_1, \lambda_2]$ the spectral range of interest. Eq. (23) can be adapted to define the weighted reflectance WR. In the following, the calculation of Haacke's and Jain's FoMs is done using the weighted transmittance and reflectance instead of $T(\lambda = 550\text{ nm})$ and $R(\lambda = 550\text{ nm})$.

Let us compare the three different approaches of transparent electrodes with metallic films using the standard figures of merit of Haacke and Jain. The structures considered here are:

A. a multilayer electrode ZnO:Al/Ag/ZnO:Al

B. a nanowires network ZnO/AgNW/ZnO

C. a multilayer TCO/Ag nanogrid/TCO system.

Conventional TCO electrodes will be taken as references: ITO (from Ref. 110 and from LPICM) and ZnO:Al (LPICM) layers[3]. In the case of the ZnO/AgNW/ZnO structure, the values of WT , WR , ϕ_H, ϕ_J have been calculated with

3 The optical constants of the materials from LPICM are given in Appendix **??**.

Material	Bulk resistivity (Ω.m)	Reference
ITO	100×10^{-8}	[104]
ZnO:Al	150×10^{-8}	[104]
ZnO	1×10^{-2}	[99]
Ag	1.58×10^{-8}	[112]

Table 2: Values of the bulk resistivity used for the sheet resistance calculations.

Material	$R_\square$ ($\Omega/\square$)	WT	WR	ϕ_H ($m\Omega^{-1}$)	ϕ_J (Ω^{-1})
ITO (Ref. 110)	12.5	0.8260	0.1721	11.8	41.8
ITO (LPICM)	16.7	0.7601	0.2307	3.9	6.48
ZnO:Al (LPICM)	25.0	0.7142	0.2550	1.4	1.28
ZnO:Al/Ag/ZnO:Al	0.775	0.5004	0.3813	1.3	10.2
ZnO/AgNW/ZnO	8.0	0.8315	0.2045	19.7	3.53
ZnO:Al/Ag 1D/ZnO:Al	1.82	0.6212	0.2645	4.7	4.53
ZnO/Ag 1D/ZnO	2	0.6785	0.2367	10.3	5.64
ZnO/Ag 2D/ZnO	2	0.5878	0.2187	2.5	2.32

Table 3: Comparison of the performance of transparent contacts with metallic films or nanostructures using different metrics: sheet resistance, weighted transmittance and reflectance, Haacke's and Jain's figures of merit.

data extracted from Ref. 107. For the geometries A and C, the FoM have been determined using the following procedure:

1. Numerical calculation of the optical transmittance and reflectance
2. Calculation of WT and WR using Eq. (23)
3. Calculation of $R_\square$ using Eq. (16) and Eq. (18) (uniform film) or (19) (grid)
4. Calculation of ϕ_H and ϕ_J using Eqs. (21) and (22), respectively.

In step 1 of the procedure, the calculations are done with Reticolo code[4]. The optical constants of silver are taken from Ref. 116. The values of bulk resistivity used in the calculation of the sheet resistance (step 3) for all geometries are summarized in Table 2 with the references. For both geometries A and C, the TCO layer thickness is 30 nm and the metal layer thickness is 20 nm. The geometrical parameters of the silver grids are the following: 1D (grating period = 200 nm, width of the wires = 160 nm) and 2D grids (grating period = 200 nm, width of the wires = 80 nm).

The final results of the above procedure are shown in Table 3. In the case of 1D silver grids, the values are calculated for TE polarized light for the sake of

4 More information about the Reticolo code can be found in Appendix A.

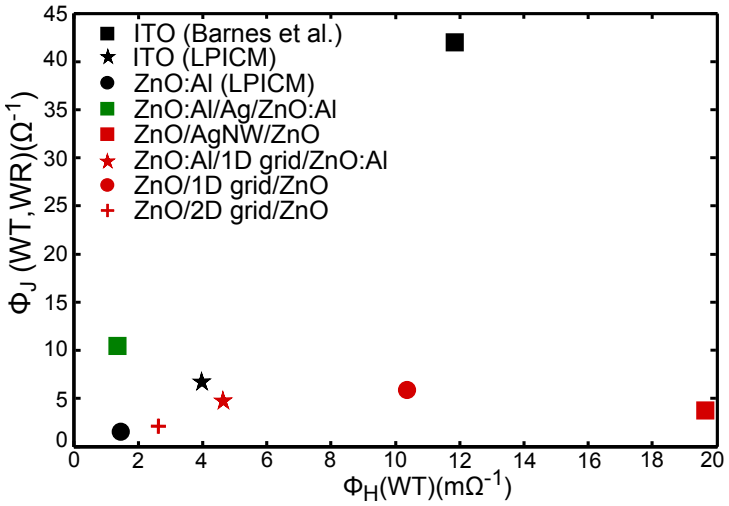

Figure 16: $\phi_J(WT, WR)$ versus $\phi_H(WT)$ for different geometries of TCEs with metallic films. Conventional ITO and ZnO:Al electrodes are also shown for comparison.

simplicity[5]. For more clarity, we have also plotted $\phi_J(WT, WR)$ as a function as $\phi_H(WT)$ for all the geometries considered. The resulting graph is displayed in Fig. 16.

The best material for transparent electrodes should be in the top right corner of the graph ϕ_J versus ϕ_H. First, among the conventional TCO materials, we can see that the commercial ITO has much better properties than the ITO and ZnO:Al materials we use. It is probably due to the influence of the deposition conditions and doping level of the material on both the transmittance and the sheet resistance.

According to Barnes et al. [110], Haacke's FoM reflects the performance of the transparent contact when integrated in a photovoltaic device better than Jain's FoM. Here, the multilayer ZnO/AgNW/ZnO fabricated by Kim et al. [107] seems to have the best performance. Note that we obtain $\phi_H = 19.7$ mΩ^{-1} for this electrode whereas, in Ref. 107, they published a value of 54 mΩ^{-1} obtained calculating the transmittance at $\lambda = 550$ nm. We see here the importance of using the weighted transmittance to evaluate more accurately the FoM.

If we consider the geometries with silver grids, this study leads to three main results:

- 1D grids are more favorable than 2D grids (lower metal coverage ratio) and uniform metal films (better transmittance).
- Replacing ZnO:Al by undoped ZnO material leads to a two-fold increase of ϕ_H despite the increase in $R_\square$.
- The ZnO/1D grid/ZnO geometry can compete with conventional ITO electrodes: ϕ_H(1D grid)=10.3 and ϕ_H(ITO)=11.8.

5 The dependence of the optical properties of the transparent electrode on light polarization (TE or TM) is studied in detail in *chapter* 6.

It is worth noticing that for TCEs made of metallic films or nanostructures, it is shown (see Table 3) that the sheet resistance reaches very low values so that $R_\square$ is no longer a limiting factor for the cell performance. The main factor to assess the potential of TCEs with nanopatterned metallic films is their optical transparency as a function of the wavelength.

3.3 APPLICATION TO RESONANT NANOSTRUCTURED FRONT CONTACTS

Recent works have studied the optical properties of nanopatterned metallic films. In particular, Catrysse and Fan [112] and van de Groep et al. [117] have shown that the optical transmittance through nanopatterned metallic films involves propagating modes and surface plasmon resonances. This optical behavior can be used to improve light absorption in solar cells owing to light trapping effects.

We propose to use a periodic metallic grating embedded in a transparent material as the front electrode of an ultra-thin solar cell. Figure 17 shows the proposed designs with a 1D or 2D nanostructured metallic layer (period p, width of the wires w and metal thickness h_m) patterned on the semi-conductor absorbing layer. A back metallic mirror is used to avoid light transmission through the substrate. We will describe further the optical properties of these designs in PARTS 2 and 3 of this thesis. The main idea of the design is that the metallic grid plays the role of both an alternative front contact and a resonant light-trapping scheme.

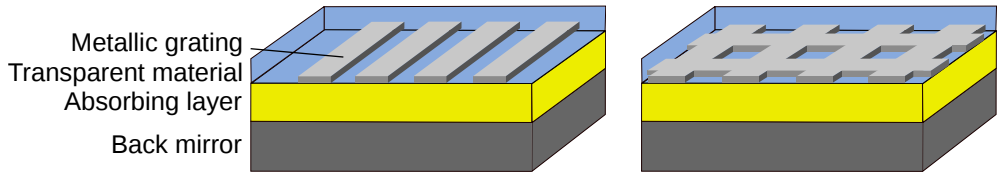

Figure 17: Schematics of the proposed nanopatterned front contacts: a metallic grating (period p, width of the wires w, metal thickness h_m) is embedded in a transparent material.

In the previous subsection, we have assessed the performances of transparent conductive nanostructured electrodes using ϕ_H and ϕ_J, that is to say the standard figures of merit for transparent electrodes. However, we have seen the weaknesses of these figures of merit for applications to solar cells. First, both FoM ϕ_H and ϕ_J consider the properties of the electrode alone, i.e independently from the rest of the solar cell. Indeed, the optical properties of the electrode are estimated without considering the influence of the refractive index and roughness of the cell. Second, these metrics do not take into account the spectral response of the cell, which depends on the absorber material.

In order to correct this last assumption, Barnes et al. [110] have proposed to use the current density loss in the transparent electrode J_{loss} as a more accurate FoM. In particular, they have shown that J_{loss} is a valuable tool to estimate the performances of TCEs integrated in CIGS and organic solar cells [110]. Nevertheless, J_{loss} only accounts for optical losses due to absorption and reflectance

in the TCE. If we use J_{loss} as a figure of merit, we may underestimate the final performances of solar cells with nanostructured metallic transparent electrodes.

In our design, the metallic nanogrid is optically coupled with the back reflector in order to achieve multi-resonant absorption. Therefore, a more accurate FoM should take into account the benefit of using the TCE on the optical absorption as well as the parasitic absorption losses already considered in the calculation of J_{loss}. In order to estimate the optical performances of the nanostructured metallic electrode presented in Fig. 17, we propose to calculate:

$$\Delta J = J_{SC} - J_{SC\,ref}\,, \tag{24}$$

with J_{SC} the short-circuit current density of the patterned cell and $J_{SC\,ref}$ the current density of a reference cell. ΔJ is the current density gain with respect to a reference cell, for instance a conventional cell without any light-trapping scheme. It should be noted that the reference cell should be defined very carefully in order to provide an accurate estimation of the performances of the transparent electrode. This figure of merit takes into account:

- the current density loss in the contact J_{loss}
- the current density gain due to light-trapping effects.

As mentioned previously, ΔJ should only be used when the optical transmittance is the main factor limiting the performance of the TCE, i.e to compare transparent contacts with similar sheet resistance values. We have used this figure of merit to discuss the performances of the nanopatterned front electrode we have proposed for ultra-thin solar cells, as explained in PART 2, *chapter* 6, subsection 6.4.3.

3.4 SUMMARY

Transparent conductive electrodes with patterned metallic films are good alternatives to conventional TCO electrodes. They combine optical transparency and a low sheet resistance and offer possible applications in the flexible photovoltaics market.

Standard figures of merit (Haacke and Jain) used to assess transparent conductors are not suitable for applications to solar cells because they consider the properties of the electrode independently from the solar cell.

In the case of resonant nanostructured front contacts, we propose to use the short-circuit current density gain ΔJ with respect to a reference cell as a more accurate FoM in order to account for the beneficial light trapping effects of the metallic electrode.

4

SETUP FOR ELECTRO-OPTICAL CHARACTERIZATION OF SOLAR CELLS

Contents

The optical response of the ultra-thin solar cells we want to design should satisfy: i) a broad absorption band, ii) no polarization dependence and iii) low angle dependence. In order to verify these points, we need a setup which allows us to measure the absorption in nanopatterned cells for different light polarizations (transverse magnetic or transverse electric) and angles of incidence. Figure 18 shows the experimental setup we have used to characterize the fabricated devices. Our platform for electro-optical characterization is made of two complementary setups devoted to angle-resolved reflection and transmission measurements (GonioVISIR) and micro-scaled optical and electrical characterization (MicroVISIR), each one being presented in this chapter. The optical paths corresponding to the angle-resolved and microscaled reflectivity measurements are shown in red and orange respectively in Fig. 18.

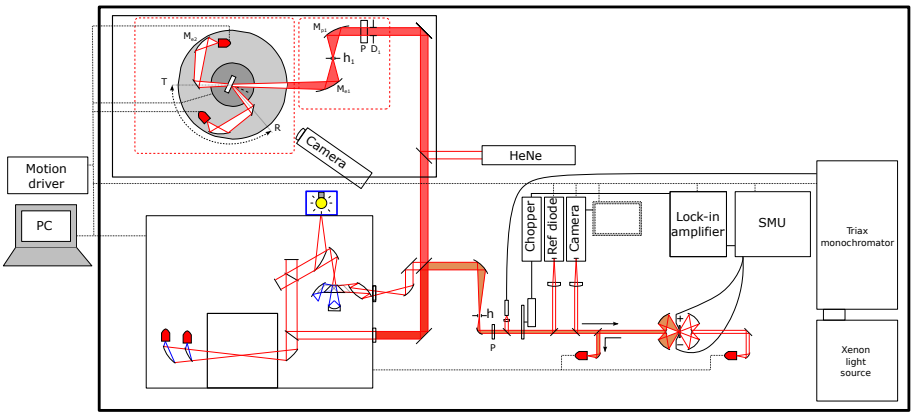

Figure 18: Schematic of the platform for electro-optical characterization of solar cells. The optical paths corresponding to the angle-resolved and microscaled reflectivity measurements are shown in red and orange respectively.

4.1 ANGLE-RESOLVED REFLECTION AND TRANSMISSION MEASUREMENTS

The GonioVISIR setup is aimed at measuring transmission and reflection spectra under polarized light and a variable angle of incidence. It was first developed by Cyrille Billaudeau during his PhD thesis [118]. As depicted in Fig. 19, it can be divided in threee blocks:

A. *Light source:* We use a commercial Fourier Transform Infra Red (FTIR) spectrometer (Brüker Equinox 70) with two internal sources (near and medium IR) and an external source that allow us to carry experiments in the $0.3 - 17$ µm range. The principle of the FTIR spectrometer is based on a broadband light source coming through a Michelson inteferometer before exciting the sample. The interferogram obtained contains the intensity measured (reflection or transmission in our case) for the different values of retardation. A Fourier Transform is then performed by the software to obtain the final spectrum. FTIR spectrometers allow to achieve a much higher spectral resolution than standard dispersive spectrometers. In our case, the highest spectral resolution possible is $\delta\sigma_{min} = 0.5\,\mathrm{cm}^{-1}$ but we used a spectral resolution of $\delta\sigma = 20\,\mathrm{cm}^{-1}$ for the experiments presented in the following.

B. *Focusing system:* The light coming from the FTIR has a beam diameter around 4 cm and thereby has to be focused on the sample. We use a homemade achromatic optical focusing system made of a pinhole h_1 (diameter 250 µm) placed between a parabolic mirror M_{p_1} (focal length 69 mm) and an elliptic mirror M_{e_1} (focal lengths 40 and 250 mm). The pinhole controls the size of the probe, which is $\varnothing = 1.7$ mm in this configuration. Note that an additional diaphragm D_1 allows us to tune the angular resolution between $\pm 0.3°$ and $\pm 1°$. The light polarization is controlled with a Glan-Taylor polarizer P, suitable on the wavelength range $0.25 - 2.3$ µm.

C. *Measurement and detection platform:* We use two coaxial motorized rotation stages to perform angle-resolved measurements in either transmission (T) or reflection (R) configurations as shown in Fig. 19. It should be noted that the excitation and detection angles can be varied independently. Thanks to four detectors working on different spectral ranges (Gallium Phosphide (GaP), Silicon (Si), Indium antimonide (InSb), Mercury Cadmium Telluride (MCT)), we can achieve measurements on a wide spectral range ($0.3 - 17$ µm as mentioned previously). The excitation beam is focused on the detector using a second elliptic mirror M_{e_2} (focal lengths 40 and 250 mm). A camera is used to see the sample and focus precisely the excitation beam on the desired area.

Note that this setup is based on a FTIR spectrometer and was initially devoted to the characterization of devices in the infrared spectral range ($0.7 - 16$ µm). We have adapted it to the visible range using new detectors (Si and GaP) and achromatic mirrors in the focusing system.

The main limitation of the GonioVISIR setup is the probe size which allows us to characterize only samples with areas larger than 2 mm^2. Therefore, during

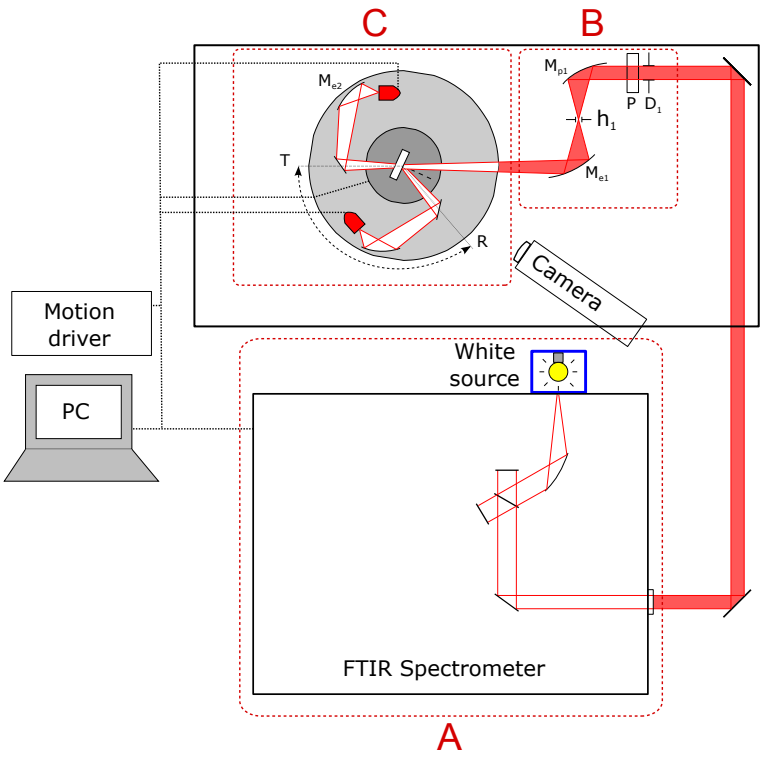

Figure 19: Schematic of the GonioVISIR setup for angle-resolved reflection and transmission measurements; A: Light source; B: Focusing system; C: Measurement and detection platform.

this thesis, we have developed a complementary setup which is described in the following section.

4.2 MICRO-SCALED OPTICAL AND ELECTRICAL CHARACTERIZATION OF SOLAR CELLS

The MicroVISIR setup has been developed for two main purposes:

1. Optical characterization: reflection and transmission measurements at a micrometer scale
2. Electrical characterization: I-V and EQE measurements.

4.2.1 *Optical characterization*

The structure of the MicroVISIR setup devoted to optical characterization is very similar to the GonioVISIR setup, as can be seen in Fig. 20. The excitation comes from the external white light source of the FTIR. The beam is focused with a home-made achromatic focalising system using two parabolic mirrors M_{p_3} and M_{p_4} and a pinhole with a diameter that can be varied between 0.1 and 1 mm. The pinhole is placed in the image focal plane of M_{p_3} (focal length 180 mm) and the object plane of M_{p_4}(focal length 43 mm). The excitation light then goes through a microscope objective onto the sample. The size of the beam is

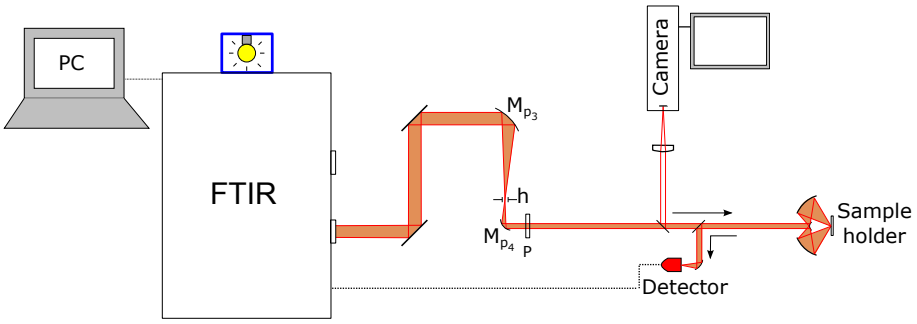

Figure 20: Schematic of the MicroVISIR setup dedicated to microscaled reflection measurement of solar cells.

chosen by varying the size of the pinhole and the magnification of the objective used.

For instance, a 200 µm-large pinhole can be combined with a $\times 20$ objective (Nachet, focal length 10 mm): the resulting beam size is $\varnothing \sim 50$ µm. The reflected light is deflected and focused on an external detector with a beamsplitter and a parabolic mirror. The detector is connected to the FTIR spectrometer, the measurements have the same spectral resolution as for the GonioVISIR setup. We use an imaging system made of a CCD camera to control the position of the excitation spot. Note that Fig. 20 shows the optical path corresponding to reflectivity measurements but the setup can also be used to measure transmission spectra with an additional microscope objective. In the framework of this thesis, we have used a silicon diode as a detector. Another configuration could be to combine the internal near infrared source of the FTIR with the InSb detector in order to characterize other types of solar cells with a higher bandgap wavelength such as CIGS or c-Si.

In our case, we have used the MicroVISIR setup to perform only reflection measurements. The reflectivity (or reflectance) is defined as the ratio of the reflected energy over the incident energy. In order to obtain accurate reflectivity measurements, we have normalized the spectra with respect to a reference taken on a gold mirror deposited on the side of the sample. The optical data used for gold were taken from Palik [116].

The MicroVISIR setup combines the advantages of the measurements with a FTIR and the possibility to have an excitation beam focused at a micrometer scale. The main specifications of the MicroVISIR setup are summarized in Table 4 and compared to the GonioVISIR setup described previously. In the case of the measurements carried out during this thesis, we have used a Cassegrain achromatic objective to focus the excitation light on the sample. It is a $\times 15$ Reflx objective from Edmund Optics, working on the $200 - 1100$ nm spectral range with a working distance of 23.2 mm. The external diameter is 29 mm and the diameter of the small mirror is 11 mm. Using this objective, we measure the light reflected from the sample between the angles $\theta = 13°$ and $\theta = 26°$.

Specifications	GonioVISIR	MicroVISIR
Maximal spectral resolution	$\delta\sigma = 0.5\,\mathrm{cm}^{-1}$	$\delta\sigma = 0.5\,\mathrm{cm}^{-1}$
Maximal angular resolution	$\delta\theta = \pm 0.3^\circ - \pm 1^\circ$	$\delta\theta = 13^\circ - 26^\circ$
Probe diameter	$\varnothing = 1.7$ mm	$\varnothing = 20$ µm -1 mm

Table 4: Specifications of the GonioVISIR and MicroVISIR setups. The maximal angular resolution value for the MicroVISIR setup corresponds to the Cassegrain objective and can be decreased by using other microscope objectives.

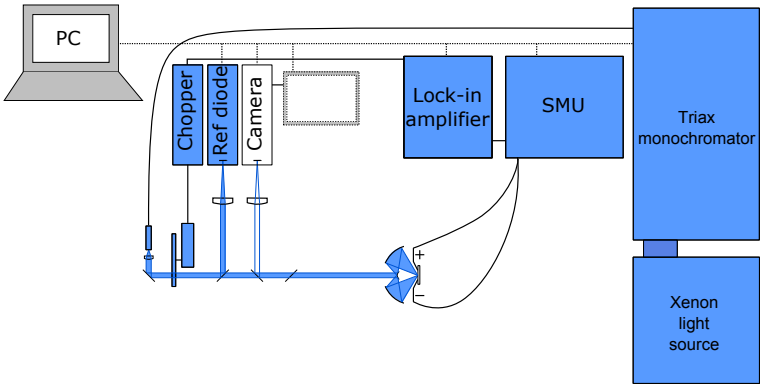

Figure 21: Schematic of the MicroVISIR setup for opto-electrical characterization of solar cells.

4.2.2 *Electrical characterization*

We have extended the MicroVISIR setup in order to measure I-V characteristics and EQE spectra (see Fig. 21). The principle of I-V measurements is to measure the current produced in the device (with and without illumination) as a function of the applied voltage. The sample is excited with a Xenon light source (Horiba) connected to a monochromator (Horiba TRIAX 180). We use an optical fiber with a collimator to bring light from the exit of the monochromator to the optical axis of the setup. A source monitoring unit (SMU) delivers the voltage and measures the current generated in the cell. A four point-probe ensures the electrical contact between the device and the SMU. Note that the use of a four point-probe removes the effect of the random resistance between the probe and the contact.

The dark I-V measurements are a valuable tool to assess the sources of losses in the cell. In particular, we can use the dark I-V curve to determine the shunt and series resistances as well as the ideality factor of the diode. The ideality factor m corresponds to the slope of the dark I-V curve and gives information on the recombination mechanisms in the cell.

Another physical quantity that can be used to assess the performances of solar cells is the external quantum efficiency. The EQE (external quantum efficiency) is the probability to collect a photogenerated electron at each wavelength. In an ideal solar cell, EQE should be equal to 1. In particular, the EQE spectrum allows us to assess the optical losses in the cell due to reflection on

the front surface or absorption in the other materials (front window, buffer layers or contacts). The EQE value is also affected by the recombination losses in the cell.

The EQE is the ratio of the number of electrons collected in the device over the number of incident photons. In other words, EQE measurements are done in two steps:

1. Measurement of the current delivered at zero voltage as a function of the incident wavelength
2. Measurement of the number of incident photons.

The first step is carried out with the same setup as for I-V measurements but with a monochromatic source. The excitation wavelength is selected by the diffraction grating of the TRIAX monochromator (spectral range $400 - 1200$ nm). The spectral width of the source is controlled by the size of the entrance and exit slits of the monochromator.

The second step is based on two calibrated diodes. The first one (the reference diode) is placed perpendicularly to the optical axis and measures the incident photon flux at every moment thanks to a beamsplitter. The second one is used to calibrate the signal. It is placed in the focal plane of the microscope objective, i.e at the exact place of the sample when we measure the current. We deduce from this measurement the number of incident photons defined as the ratio of the energetic flux over the energy of a single photon. We can then calculate the EQE value as a function of the excitation wavelength.

Within this PhD project, we have performed mainly optical characterizations on the nanopatterned ultra-thin a-Si:H devices fabricated. Yet, this "in-house" setup has already been used to carry out EQE measurements on GaAs solar cells in the framework of another PhD project. The spectral responses obtained were consistent with similar characterizations done at IRDEP.

4.3 SUMMARY

We have developed a platform adapted to electro-optical characterizations of nanopatterned solar cells. This platform includes two complementary setups with different aims:

- the GonioVISIR setup dedicated to angle-resolved reflection and transmission measurements
- the MicroVISIR setup devoted to micron-scaled optical and electrical characterization.

Within this thesis, we have used the complementarity of these setups to characterize optically ultra-thin a-Si:H solar cells with one-dimensional metallic gratings, as presented in *chapter 7*, section 7.2.

Part II

DESIGN OF ULTRA-THIN AMORPHOUS SILICON SOLAR CELLS

5 INTRODUCTION TO AMORPHOUS SILICON SOLAR CELLS

Contents

As introduced in *chapter* 1, monocrystalline silicon is the dominant technology for solar cells. Yet, its amorphous form is more flexible in its applications because it can be deposited in thin films at low temperature onto a wide range of substrates. It is also often used as a low-cost material to test advanced light management concepts. In PART 2 of my thesis, we focus on the design of metallic nanostructures to enhance light absorption in ultra-thin amorphous silicon solar cells. The characteristics of the proposed light-trapping structure are strongly related to the physical properties of the photovoltaic material (refractive index, bandgap wavelength, absorption coefficient,...). This chapter is thus devoted to give a brief insight on the properties of amorphous silicon material. In the following, the main characteristics of standard amorphous silicon solar cells are presented and we close this chapter with a discussion on the potential and limitations of amorphous silicon as a photovoltaic material.

5.1 HISTORICAL OVERVIEW OF AMORPHOUS SILICON SOLAR CELLS

In the 1970s, the works of Chittick et al. [119] followed by Le Comber and Spear [120] showed that discharge-produced amorphous silicon had better electronic properties than a-Si obtained by sputtering or evaporation. This amorphous silicon material is obtained by applying a radio frequency voltage between two electrodes across a silane (SiH_4) gas[1]. This deposition method is now called *plasma enhanced chemical vapor deposition* (PECVD). The improvement of the electronic properties of plasma-deposited amorphous silicon is attributed to the

1 See *chapter* 7, subsection 7.1.3 for more details on PECVD.

presence of hydrogen atoms (about 10%) bonded into the a-Si structure. This gave rise to the material called *hydrogenated amorphous silicon* and often referred as a-Si:H. In 1975, Spear and Le Comber [121] reported the possibility to dope the a-Si material using phosphine (PH_3) for n-type doping or diborane (B_2H_6) for p-type doping mixed with silane during plasma deposition. Consequently, they obtained the first a-Si:H p-n junction [122]. The same year, Carlson and Wronski fabricated the first solar cell based on a discharge-produced a-Si p-i-n junction [123] deposited on ITO coated glass. They demonstrated a conversion efficiency of 2.4 % for an intrinsic a-Si:H layer thickness of 1 µm. The current record for amorphous silicon solar cells is a stabilized efficiency over 10 % for a 250 nm-thick intrinsic layer demonstrated in 2009 by Benagli et al. from Oerlikon [24]. In this work, a short-circuit current density over 17 mA/cm^2 is achieved using a textured ZnO substrate obtained by LPCVD (*low-pressure chemical vapor deposition*) in order to trap light efficiently in the a-Si:H active layer.

5.2 PROPERTIES OF AMORPHOUS SILICON MATERIAL

5.2.1 *Atomic structure and defects*

Silicon is a tetravalent atom. Hence, in monocrystalline silicon, all the silicon atoms are linked to four other silicon atoms by covalent bonds in a tetrahedral configuration. In the case of amorphous silicon, there is no long range order in the material. The disorder is induced through small variations in the distances and the angles of the covalent bonds between two neighbouring silicon atoms.

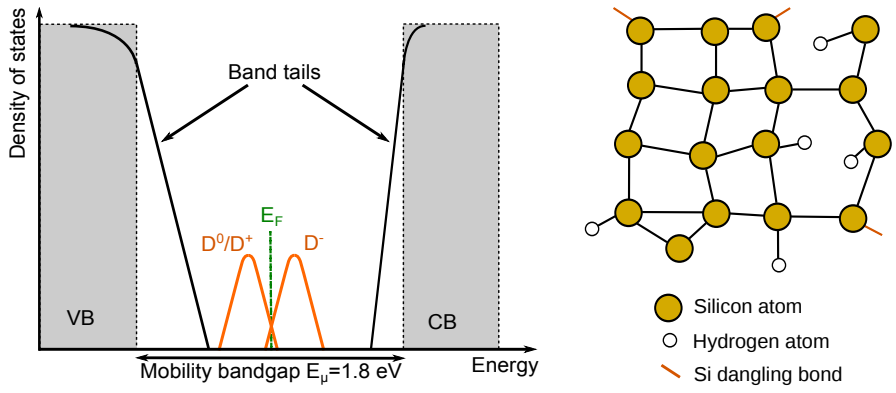

(a) (b)

Figure 22: (a) Density of electronic states in undoped hydrogenated amorphous silicon (adapted from Ref. 23). The valence and conduction bands (noted VB and CB) are displayed in grey. Due to disorder, exponential band tails reduce the optical energy bandgap. The defect states due to silicon dangling bonds are localized close to the Fermi level. (b) Atomic structure of hydrogenated amorphous silicon. The introduced hydrogen atoms passivate some of the silicon dangling bonds by bonding with the vacant orbital.

Figure 22a shows the distribution of the density of states in undoped a-Si:H, adapted from Ref. 23. The first effect of disorder is exponential energy distributions of localized states close to the edges of the conduction and valence bands. These band tails are asymmetric: the width of the valence band tail is $0.3 - 0.4$ eV whereas the width of the conduction tail states is 0.2 eV [120]. The exponential band tails reduce the optical bandgap E_g which is lower than the mobility bandgap E_μ defined as the gap between the valence and conduction bands: $E_\mu \sim E_g + 0.15$ eV [124].

Second, because of the disappearance of the lattice structure, some silicon atoms have only three electrons bonded to other silicon atoms. The missing covalent bond is called a dangling bond, also referred as D-center. As shown in Fig. 22a, the dangling bonds lead to two Gaussian distributions (width $= 0.2 - 0.3$ eV [125]) of defect states localized in the middle of the bandgap: D^+/D^0 at 0.9 eV above E_v and D^0/D^- at 1.1 eV above E_v. In undoped a-Si:H, the main defects are the neutral dangling bonds D^0 but two charged states exist: D^+ (zero electron) and D^- (two electrons). The silicon D-centers are recombination centers for carriers (D^+ for electrons and D^- for holes) thereby altering the electronic properties of amorphous silicon. Moreover, the defect density in amorphous silicon is too high to allow any extrinsic doping. Most of the excess charges introduced by doping would be trapped in the dangling-bond defect states. The problem is partially solved for plasma-deposited hydrogenated amorphous silicon. The hydrogen atoms introduced can bond with the silicon dangling bonds as shown in Fig. 22b. Adding 5 to 10% of hydrogen during plasma deposition allows a reduction of the defect density from 10^{19} to 10^{15} cm^{-3} [25]. This passivation process explains the improved electronic properties exhibited by amorphous silicon once hydrogenated.

5.2.2 *Doping of amorphous silicon*

The purpose of doping is to increase the electrical conductivity of the material by adding a controlled amount of impurity atoms. The main doping elements for a-Si:H are boron for p type doping and phosphorus for n type doping. Let us consider the case of n-doped a-Si:H. Phosphorus is a pentavalent atom. In monocrystalline silicon, the incorporated phosphorus atoms are fourfold coordinated (P_4^0) and thus are electron donors. In amorphous silicon, the most stable configuration for the phosphorus atom in the random network is to be in a threefold configuration P_3^0. Phosphorus atoms in this configuration do not contribute to doping. The main doping mechanism in a-Si:H is the creation of defect-compensated donors P_4^+. In this configuration, the phosphorus atom is positively charged and has a coordination 4: P_4^+. Its formation is accompanied by the creation of a negatively charged dangling bond $Si_3^- = D^-$, hence the name defect-compensated donor. Likewise, for boron doping, the doping is driven by the formation of defect-compensated acceptors B_4^- and positively charged defect states $Si_3^+ = D^+$.

Furthermore, doping of a-Si:H leads to the increase of the defect density in the material. It has been shown that the dangling bond density increases as

$\sqrt{N_d}$, with N_d the concentration of dopants [126]. Different models have been proposed to explain the creation of new dangling bonds upon doping. The first one, proposed by Street [127], assumes that the insertion of dopant atoms requires the creation of new dangling bond defects. The model proposes that there is a chemical equilibrium between threefold and fourfold coordinated atoms following the equation $P_3^0 + Si_4^0 = P_4^+ + Si_3^-$ in the case of n type doping. In another model by Stutzmann et al. [126], the increase of the dangling bond density is explained independently from the formation of dopant sites. On a microscopic scale, the dangling bonds would result from a rearrangement of the silicon network. This increase of the dangling bond density can also be triggered by light exposure as in the case of the Staebler-Wronski effect (see section 5.4).

Another important difference with crystalline silicon is the fact that increased concentration of phosphorus and boron atoms do not shift the Fermi level closer to the valence and conduction band mobility edges. The full shift of the Fermi level towards band edges is not allowed by the presence of tail states and defect states in the material bandgap. Therefore, the shift of the Fermi level towards the conduction band due to n-type doping is limited ($E_C - E_F \sim 0.2$ eV for high doping level) [128]. p-doping with boron atoms has a slightly lower doping efficiency ($E_F - E_V \sim 0.3$ eV) because of the wider valence band tail [128].

In summary, doping of hydrogenated amorphous silicon is possible (typical doping level $= 10^{18}$ cm^{-3}). However, it has several drawbacks:

1. the doping efficiency, which can be defined as the fraction of active dopants, in this case fourfold coordinated atoms, is low. It is typically $10^{-2} - 10^{-3}$ in amorphous silicon, to be compared to a doping efficiency close to 1 for crystalline silicon at ambient temperature [129]. High concentrations of dopant atoms are needed to obtain a-Si:H material with high conductivity.

2. the defect density in doped a-Si:H is several orders of magnitude larger than for intrinsic amorphous silicon material [129]. The diffusion length of photogenerated carriers is thus very short in doped a-Si:H material. In an a-Si:H p-n junction, the carriers would all recombine in the doped layers before reaching the depletion region of the junction. A p-i-n structure with an intrinsic layer with a low defect density is therefore required as described in subsection 5.3.1.

3. The internal built-in potential is limited by the restricted shift of the Fermi level upon doping. It thereby leads to an open-circuit voltage value much lower than expected from the value of the energy bandgap. For instance, the value for the current single-junction a-Si:H record is $V_{OC} = 0.88$ V [24] whereas the bandgap of a-Si:H is typically equal to $E_g = 1.7$ eV.

5.2.3 *Absorption in amorphous silicon*

As reminded in Fig. 23a, crystalline silicon is a semi-conductor with an indirect bandgap. The maximum of the valence band and the minimum of the conduc-

tion band do not occur in the same point of the k space. It means that the absorption of a photon in c-Si requires the absorption of a phonon with a momentum q. Absorption close to the band edge of c-Si is thus limited by the quantity of phonons available. In the case of amorphous silicon, the loss of crystalline order leads to a relaxation of the momentum conservation rule. Amorphous silicon behaves as a direct bandgap semiconductor (see Fig. 23b) and thus has a higher absorption coefficient α than crystalline silicon (at $\lambda = 500$ nm, $\alpha_{aSi} > 10\,\alpha_{cSi}$). Passivation with hydrogen also increases the amorphous silicon bandgap leading to a typical value of $E_g = 1.7$ eV. Note that it is higher than the optimum for photovoltaic applications ($E_{g\,opt} \sim 1.4$ eV as presented in Fig.9 in *chapter* 1). The bandgap and absorption coefficient can be tuned by changing the hydrogen content. However, amorphous silicon materials with low hydrogen dilution exhibit higher defect densities. In the following, we discuss the use of solar cells with ultra-thin absorber layers to circumvent the intrisinc limits of amorphous silicon.

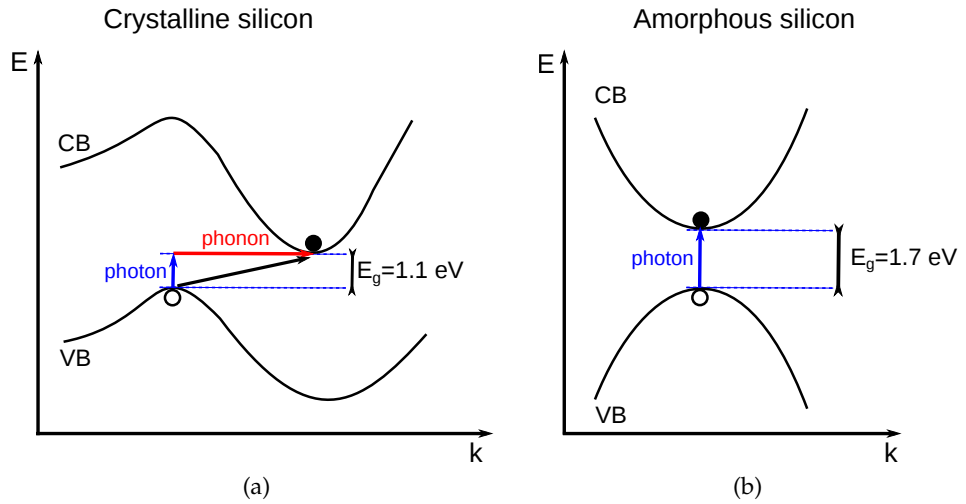

Figure 23: Simplified energy band structure of a semi-conductor with (a) an indirect bandgap (crystalline silicon) and (b) a direct bandgap (amorphous silicon). In the case of c-Si, the excitation of an electron in the conduction band requires the absorption of a phonon (momentum q$\neq$ 0) in order to ensure the conservation of the momentum.

5.3 STRUCTURE OF A STANDARD AMORPHOUS SILICON SOLAR CELL

5.3.1 *Description of a p-i-n junction*

Because of the high defect density, the lifetime of minority carriers is short in doped a-Si:H. Electrons and holes generated by photons absorbed in the doped layers are very likely to recombine before reaching the contacts and being collected. Therefore, it is generally assumed that the carriers generated in the doped layers do not contribute to the generation of photocurrent in the solar cell. Doped a-Si:H layers are very thin layers with a typical thickness of

$10 - 20$ nm and the active absorber layer of the solar cell is an intrinsic a-Si:H layer much larger than the doped layers (typical i $-$ layer thickness $=200 - 500$ nm).

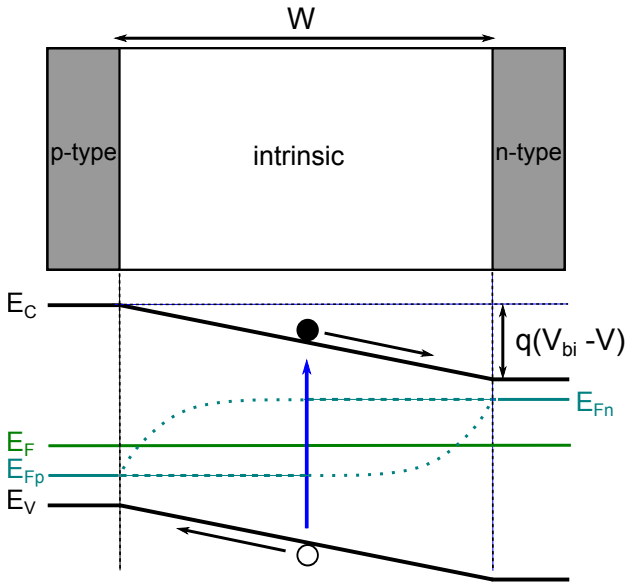

Figure 24: Simplified energy band diagram of a p-i-n junction.

Figure 24 shows a very simplified energy band diagram of a p-i-n junction. The first function of the doped layers is to create an internal electric field E across the intrinsic layer. The strength of E depends on the built-in potential V_{bi} and the thickness of the i layer t:

$$E = \frac{V_{bi} - V}{t}. \tag{25}$$

The built-in potential is mainly determined by the position of the Fermi levels in the doped materials at equilibrium, i.e by the doping level. As described previously, a-Si:H is characterized by a low doping efficiency with a reduced shift of the Fermi level in the doped material. Hence, the built-in potential is limited compared with solar cells based on crystalline semi-conductors and much lower than $E_g/q = 1.7$ V.

When a photon is absorbed in the intrinsic layer, an electron-hole pair is generated and separated due to the internal electric field. The second function of the doped layers is to establish ohmic electrical contacts between a-Si:H and the external electrodes. The photogenerated carriers are collected in the n type doped layer for the electrons and the p type doped layer for the holes.

The main transport mechanism in a p-i-n junction is the drift of the carriers in the internal electric field. The collection efficiency thus depends on the magnitude of the electric field and on the mobility and lifetime of the carriers. In Eq. (25), the electric field E is assumed to be uniform in the junction. In reality, the electric field in the i-layer of an a-Si:H junction is non uniform, due to charged dangling bonds and bandtail states [130]. In particular, the field is deformed in the interface regions: D^+ (D^-) defects accumulate at the p/i (n/i) interface. The distribution of the space charge in the intrinsic layer has a major influence

on the collection efficiency and should therefore not be neglected in the case of amorphous silicon. This non uniformity is emphasized by light-soaking (see section 5.4).

5.3.2 *Substrate and superstrate designs*

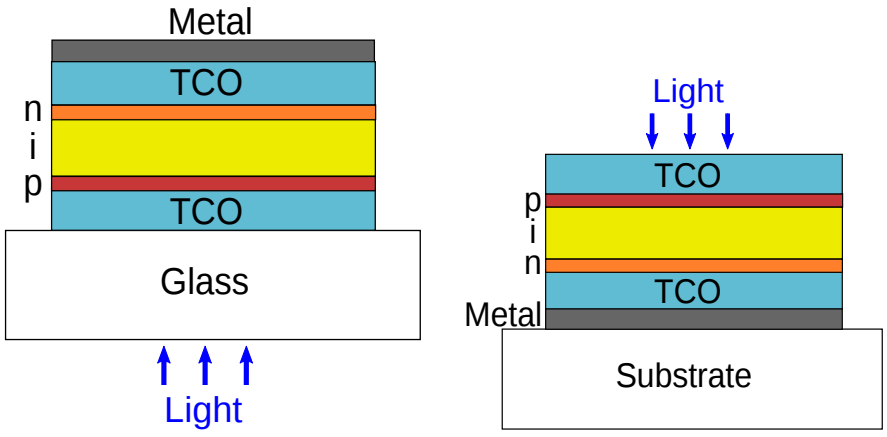

Figure 25: Amorphous silicon solar cell in a (a) superstrate p-i-n and (b) substrate n-i-p configuration.

One of the main advantages of amorphous silicon compared with crystalline silicon technology is the ability to deposit the absorber material on any substrate. As shown in Fig. 25, two designs are possible: the superstrate and substrate configurations. Note that in this subsection the order in which the layers are deposited matters: the p-i-n sequence corresponds to the cell grown starting by the p-layer followed by the i- and n- layers.

In the superstrate configuration (see Fig. 25a), the p-i-n junction is deposited on a transparent substrate (usually glass). Light enters the cell through the glass substrate and a TCO layer is used as a front contact layer. The back contact combines a TCO layer for the electrical conductivity and a metallic mirror to reflect light in the intrinsic absorber layer. In this configuration, the choice of the TCO substrate material is critical, it has to be stable during the PECVD process. Doped ZnO is conventionally used, ITO is not suitable because it could be chemically reduced during the silane decomposition [130].

In the substrate configuration (see Fig. 25b), the a-Si:H cell is grown starting by the n-layer which is deposited on a metallic back contact. The advantage of the substrate configuration is the possibility to use opaque substrates such as metallic back mirrors or plastic substrates. It opens up novel possibilities for integrating light trapping strategies in a-Si:H solar cells. In the framework of my PhD project, we want to use metal/semiconductor/metal cavities. Therefore, in the following, we consider only a-Si:H solar cells in the substrate configuration.

Note that in both designs, incident light enters the solar cell through the p-layer. This design is motivated by two reasons:

1. the mobility of holes is lower than the mobility of electrons. Because of the small absorption depth of amorphous silicon (below 20 nm for a wavelength of 500 nm), most of photogenerated carriers are created in the front part of the cell. Placing the p type doped layer in the front surface means that the holes travel on average a shorter distance than the electrons, thereby leading to a better hole collection.

2. carriers photogenerated in the p-doped layer do not contribute to current generation because of their very short lifetime. The absorption in the p layer should therefore be minimized. As a consequence, high bandgap energy materials are preferably chosen such as silicon carbide alloys (aSiC:H) that have a typical energy bandgap of $E_g = 2$ eV. Using a front p-doped layer allows a better utilization of the solar spectrum.

5.4 LIGHT-INDUCED DEGRADATION

The main problem encountered by amorphous silicon solar cells is the decrease of the efficiency with light exposure. Indeed, in the first 100 hours of illumination, the conversion efficiency of an amorphous silicon device suffers from a reduction going up to 30 %. In 1977, Staebler and Wronski experimentally demonstrated the decrease of photoconductivity and dark conductivity upon light exposure [131]. They showed that this degradation process, called the *Staebler-Wronski effect* (SWE), had the following characteristics:

- The conductivity drops until a saturation value is reached. This stabilized value depends on the light intensity and the sample temperature.

- The initial conductivity can be recovered after annealing of the sample at a temperature above 150°C.

As a consequence, the efficiency of the a-Si:H modules varies depending on the seasons. In particular, an improved efficiency is exhibited in summer [23]. It shows that at high temperatures, the increase of the stabilized efficiency due to a limited impact of SWE overcompensates the degradation of the conversion efficiency that is usually observed for solar cells.

Extensive studies have been done in order to understand the mechanism of the SWE. Several microscopic models have been proposed to explain this light-soaking degradation, all of them assuming that the hydrogen atoms incorporated in amorphous silicon are involved [125, 132, 133]. Light excitation could break weak Si-Si bonds leading to the increase of the D-centers density with light exposure, which has been observed experimentally. The creation of new dangling-bond defects competes with carrier recombinations in the already existing D-centers. The Staebler-Wronski effect is therefore a self-limiting phenomenon. It is consistent with the saturation of the conductivity drop observed by Staebler and Wronski in 1977. As a result, a-Si:H solar cells are characterized by two values of the conversion efficiency: the initial value and the stabilized efficiency after light exposure. The standard light-soaking experiments are carried out under one-sun light intensity at T= 50°C during 1000 h and at open-

circuit voltage.

The SWE is a problem intrinsic to a-Si:H solar cells but its effects on the performances can be limited. Developing solutions to improve the stability to light-soaking is a driving force of research on a-Si:H solar cells. Several strategies have been proposed so far:

1. The easiest way to improve the stability of the a-Si:H cell is to use thinner intrinsic layers [24, 128]. It reduces the distance crossed by the carriers before being collected and thus the probability that they recombine. It also enhances the electric field in the junction thereby ensuring a good collection in spite of the increase of the recombination centers. Benagli et al. [24] showed that the stabilized fill factor of the cell increases with a decreased thickness of the i-layer (see Fig. 26a). They have demonstrated a record conversion efficiency of 10.09 % [21, 24] with an i-layer thickness of 250 nm but their results show that reducing further the i-layer thickness may lead to higher conversion efficiencies.

2. Another solution to limit the SWE is the a-Si/a-Si stacked cell design [25, 128]. When two solar cells are stacked, the main requirement is to achieve current matching between the two cells. The top cell absorbs more photons and thus, has to be much thinner than the bottom cell. Typical thicknesses for the top and bottom a-Si:H p-i-n junctions are 80 and 300 nm respectively. The top cell is more stable than usual single-junction a-Si:H solar cells because of the lower i-layer thickness. Besides, the incident light is partially absorbed in the first junction. The light exposure of the bottom cell is reduced, thereby leading to a limited degradation of its efficiency. The stabilized fill factor of the stacked cell should be higher than for a single-junction a-Si:H cell with the equivalent i-layer thickness.

3. Stacking multiple cells also enables a better utilization of the solar spectrum if we use absorber materials with different bandgaps. Germanium alloy of a-Si:H, called a-SiGe:H, has an energy bandgap between 1.1 eV (a-Ge:H) and 1.7 eV (a-Si:H), depending on the fraction of germanium. a-SiGe:H is thereby an ideal material to be used as the bottom cell of a multi-junction structure. For the top cell, a wide-band-gap a-Si:H material is obtained by increasing the hydrogen content or using an amorphous silicon carbide (a-SiC:H) alloy. Figure 26b displays the quantum efficiency of an a-Si:H/a-Si:H/a-SiGe:H triple-junction solar cell, which achieves an efficient spectral splitting of the solar spectrum [128]. A stabilized conversion efficiency of 10.5 % was obtained in 2012 for a multi-junction a-Si:H/a-SiGe/nc-Si module by LG Electronics [21]. It represents a significant improvement to achieve a higher efficiency than the single junction record of Benagli et al. at the module scale (total area $> 1\,m^2$).

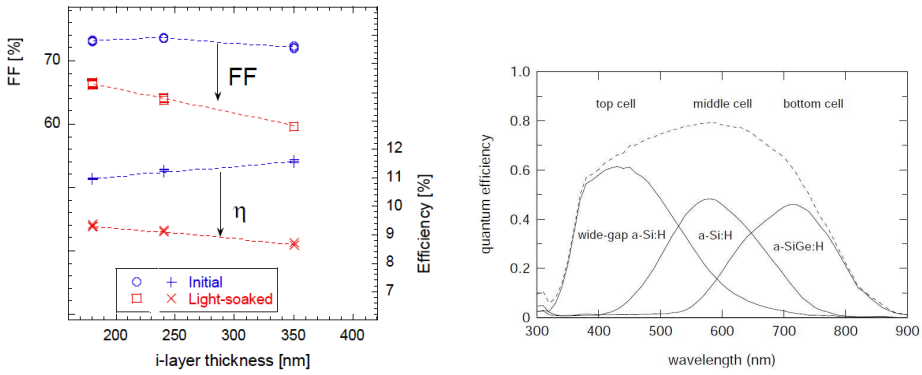

(a) (b)

Figure 26: Strategies to improve the stabilized efficiency of amorphous silicon solar cells. (a) FF–values and efficiency as a function of the i-layer thickness for a single-junction a-Si:H solar cell in the initial and light-soaked state. The stabilized FF and efficiency increase with reduced i-layer thickness (Figure extracted from Ref. 24). (b) Quantum efficiency of an a-Si:H/a-Si:H/a-SiGe:H triple-junction solar cell. The bandgaps of the three materials are engineered in order to optimize the utilization of the solar spectrum (Figure extracted from Ref. 128).

5.5 AMORPHOUS SILICON SOLAR CELLS: POTENTIAL AND WAYS OF IMPROVEMENT

Since the fabrication of the first a-Si:H solar cell in 1976, amorphous silicon has shown a potential to be an alternative to crystalline silicon. The main drawback of crystalline silicon technology is the cost of the cell fabrication which requires in particular expensive substrates and costly purification processes. Let us summarize the advantages of amorphous silicon material with respect to crystalline silicon technology:

1. a higher absorption coefficient than c-Si, thereby allowing a thickness reduction of the absorber layer

2. a PECVD deposition technique (large area, low temperature, low-cost substrate) leading to an overall decrease of the manufacturing cost.

Therefore, many research works have been carried out to improve the efficiency of 2.4 % exhibited by the first a-Si:H solar cell [123]. Figure 27 displays the I-V curves of the first amorphous silicon solar cell [123] (red) and the current record for a single-junction a-Si:H solar cell [24] (green). The values of the characteristics of the two cells (J_{SC}, V_{OC}, FF, η) are also shown. This comparison highlights the technological developments made in 20 years to increase the performance and stability of amorphous silicon solar cells.

The first improvement has been to reduce the thickness of the i-layer from 1 µm down to 250 nm, leading to an increase of the fill factor and the open-circuit voltage. Besides, as can be seen in Fig. 27, the current record single-junction a-Si:H solar cell is deposited in a substrate configuration which allowed the Oerlikon group to use a textured ZnO substrate combined with a white reflector. A

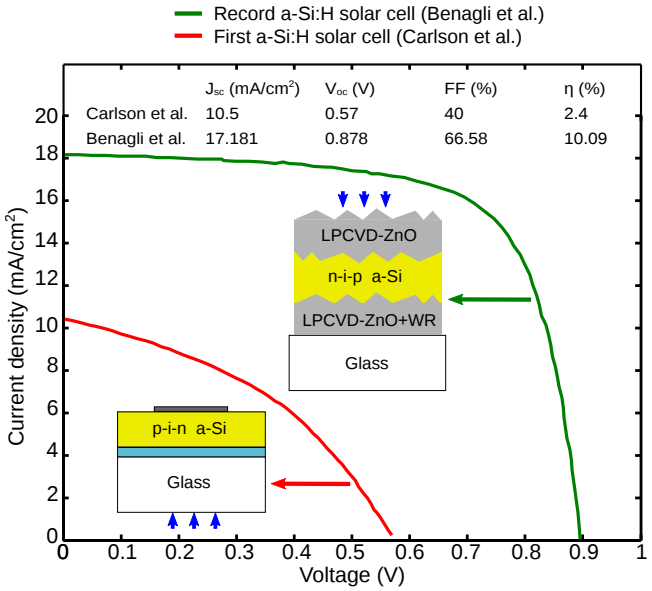

Figure 27: Comparison of the performances of the first amorphous silicon solar cell (1 µm) [123] and the current record for a single-junction a-Si:H solar cell (250 nm) [24]. Inset: the structures of the two cells are shown as well as their main characteristics (J_{SC}, V_{OC}, FF, η). The values given for the record a-Si:H cell have been measured after light-soaking. As for Carlson's cell, they are assumed to be unstabilized values. The current record a-Si:H solar cell has been deposited on a LPCVD-ZnO layer with a white reflector (WR).

similar texturation of the ZnO front window leads to an increase of the short-circuit current density of 70 % with respect to the cell of Carlson and Wronski in spite of the fivefold thickness reduction.

To conclude this chapter, we would like to give an outlook of the future of amorphous silicon solar cells. As developed in sections 5.2 and 5.4, a-Si:H is a material with a high defect density. The degradation of the device efficiency due to the Staebler-Wronski effect restrains its use at a commercial scale. However, as mentioned previously, successful solutions such as stacked cells designs have been developed to achieve better efficiency and stability.

The main perspectives for a-Si:H based solar cells relies in the multi-junction cells. In particular, a promising solution is to use microcrystalline or nanocrystalline silicon as a low-bandgap material. The use of a-Si:H/µc-Si:H solar cells, also called *micromorph cells*, were first proposed by IMT (Neuchâtel, Switzerland) in 1994 [130]. The top cell is made of a thin a-Si:H ($\sim 200 - 300$ nm) cell with a gap of 1.7 eV and the bottom cell is made of µc-Si:H ($1 - 2$ µm) with a gap of 1.1 eV. An intermediate reflector layer is needed to increase the absorption in the top cell in order to achieve current matching. At the industry level, the current record for a-Si/nc-Si solar cells is a conversion efficiency of 12.3 % hold by Kaneka [21]. LG Electronics have reported last year a higher conversion efficiency ($\eta = 13.4\,\%$) for a triple-junction a-Si/nc-Si/nc-Si [21].

The advantages of micromorph solar cells compared with other multi-junction devices described in section 5.4 are the following:

- the whole cell can be deposited in the same PECVD reactor. The transition between amorphous and microcrystalline silicon is controlled by varying the hydrogen dilution during the deposition process.
- the microcrystalline bottom cell does not suffer from light-induced degradation.

Current developments of this technology focus on increasing the short-circuit current density with efficient intermediate reflectors [134] and textured substrates [36–38, 43, 46, 56, 135–137] or electrodes [44, 138] for advanced light trapping. It reflects the current trends in photovoltaics industry: *thinner absorber layers* and *efficient light trapping strategies*. In the next chapter, we will present a novel design using a metallic grating in order to improve light absorption in ultra-thin amorphous silicon solar cells.

5.6 SUMMARY

Amorphous silicon technology offers non negligible advantages despite lower electronic performances than crystalline silicon. Low-cost and large area deposition processes such as PECVD lead to higher throughput and lower manufacturing cost.

However, the conversion efficiency of amorphous silicon solar cells is limited by the intrinsic properties of the material such as the Staebler-Wronski light-induced degradation. A main solution to limit the negative effects of the Staebler-Wronski effect is to reduce the thickness of the intrinsic amorphous silicon layer.

The main perspectives of amorphous silicon technology rely on tandem and multi-junction designs with promising results such as stabilized efficiencies over 10 %.

6

DESIGN OF A RESONANT FRONT CONTACT FOR ULTRA-THIN AMORPHOUS SILICON SOLAR CELLS

Contents

The potential and intrinsic limits of amorphous silicon material for solar cell applications were presented in the previous chapter. In particular, we have shown that the stability against light-induced degradation could be improved by reducing the a-Si:H absorber layer thickness. As developed in *chapter 2*, recent research works have proposed advanced light trapping strategies for ultra-thin (< 100 nm) a-Si:H layers. Our approach is based on a nanopatterned metallic layer embedded in the top layers at the front surface of the cell to achieve a multi-resonant absorption spectrum. We have defined several conditions that our design should fulfill:

1. a flat and ultra-thin (< 100 nm) absorber layer
2. a broad absorption band (absorption $> 80\,\%$ on $400 - 700$ nm)
3. no polarization dependence
4. low angle dependence.

In this chapter, we will present the proposed design fulfilling all these criteria. We will first define the simplified model structure used to provide a detailed analysis of the light trapping mechanism at stake. We will then show how this work can be extended to fully design an ultra-thin a-Si:H solar cell. As a conclusion, the performances of the light-trapping concept proposed will be discussed. The results presented in this chapter have been published in two articles [139, 140].

6.1 DESCRIPTION OF THE 1D PATTERNED MODEL STRUCTURE

6.1.1 *Definition of the three-layer model*

In order to fulfill the requirements defined above, the first challenge is to answer the following question: how can we absorb light efficiently in an ultra-thin intrinsic a-Si:H layer (< 100 nm)? To do so, let us consider a simplified three-layer model as depicted in Fig. 28. The structure is made of a grating of metallic wires (period p, width of the wires w and metal thickness h_m) deposited on an amorphous silicon absorber layer[1] (thickness h_s) and a metallic mirror used as a back contact. The top ZnO:Al layer (thickness h_1) is used both as an anti-reflection coating layer and as a front contact. We use silver as the metal for the wires and the back mirror because of its high reflectivity.

The optical response of this structure is studied through numerical calculations with the Reticolo code developed by Philippe Lalanne and co-workers at IOGS. It is based on a Rigorous Coupled Wave Analysis (RCWA) method and is devoted to determine the optical response of stacks of lamellar structures. The inputs of the calculations are:

- the thicknesses of the different layers of the stack (h_s, h_1, h_m)
- the geometrical parameters of the grating (w, p)
- the optical constants (n, k) of each material (here, ZnO:Al, a-Si:H and Ag).

Several outputs are available: the total absorption in the structure, the absorption fraction in each layer, the reflectivity and the electric and magnetic fields amplitude in each point. We mainly use the absorption spectra combined with the electric and magnetic fields maps to understand the absorption mechanism. The refractive index of silver (n_{Ag}) is taken from Ref. 116, p. 350-357. The a-Si:H

1 For the sake of simplicity, the difference between the refractive indices of the intrinsic and doped layers is not taken into account here. The absorption losses in the doped layers will be discussed in section 6.5.

material is deposited by PECVD at LPICM, see subsection 7.1.3 for more details. The refractive indices of a-Si:H (n_S) and ZnO:Al (n_1) are taken from ellipsometry measurements on layers deposited at LPICM. Further details on Reticolo code as well as the optical constants used for each material are provided in Appendix.

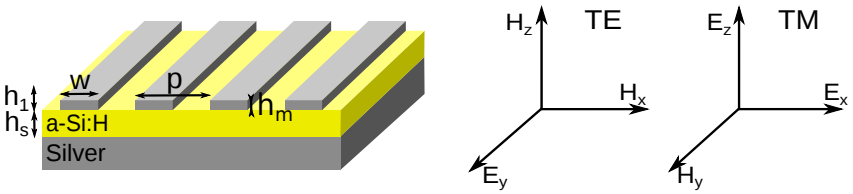

Figure 28: Schematic of the ZnO:Al/a-Si:H/Ag model structure. A 1D silver grating (width w, pitch p, metal thickness h_m) is deposited on the a-Si:H layer (thickness h_s) and embedded in a ZnO:Al anti-reflection coating layer (thickness h_1). The definition of transverse electric (TE) and magnetic (TM) modes are displayed.

The parameters of the structure (h_s, h_1, w, p, h_m) are chosen to satisfy the above defined requirements (broadband absorption, low polarization dependency, low angular dependency, absorber thickness < 100 nm). An optimized geometry (refered further as the model structure) has been found with an a-Si:H absorber layer with a thickness $h_s = 90$ nm and a patterned silver layer ($h_m = 20$ nm) embedded in a ZnO:Al layer ($h_1 = 60$ nm). The metallic grating consists of silver wires with $w = 80$ nm and $p = 200$ nm.

6.1.2 *Definition of an unstructured reference stack*

As a first step towards the study of the design depicted in Fig. 28, we consider an unstructured ZnO:Al/a-Si:H/Ag stack, with a 90 nm-thick a-Si:H absorber layer and a 50 nm-thick ZnO:Al layer. Figure 29a displays the total absorption spectrum (black curve) in the ZnO:Al/a-Si:H/Ag reference stack.

In order to assess the ligh-trapping effect of the back silver mirror, the single-pass absorption in a 90 nm-thick a-Si:H layer is plotted in Fig. 29a (red curve). For an absorber layer with a thickness h and an absorption coefficient α, the single-pass absorption is defined as the fraction of photons absorbed after a single pass through the layer. It is given by:

$$A_{single} = 1 - e^{-\alpha h}, \tag{26}$$

assuming a perfect anti-reflection coating layer. At short wavelengths ($\lambda < 430$ nm), the use of ZnO:Al as a front contact layer results in absorption losses compared to single-path absorption. Above 430 nm, the absorption in the ZnO:Al/a-Si:H/Ag stack is higher than the single-pass absorption due to light trapping effects. The spectrum exhibits two remarkable features: a broad absorption resonance in the $450 - 550$ nm wavelength range and a sharp resonance at 660 nm. In particular, at 660 nm, it leads to a twelve-fold absorption enhancement compared to single-pass absorption.

To study the resonances independently from the effect of the ZnO:Al coating layer, we consider a simple Air/a-Si:H/Ag system. As shown in Fig. 29a (green curve), the absorption spectrum of such a structure exhibits two absorption peaks at 460 nm and 640 nm. The Air/a-Si:H/Ag system can be modeled by a Fabry-Perot resonator depicted in Fig. 29b and characterized by:

- the cavity thickness h
- the phase shift ϕ_1 induced by reflection at the a-Si/Air interface
- the phase shift ϕ_2 induced by reflection at the a-Si/Ag interface.

The phase shifts ϕ_1 and ϕ_2 are determined using the Fresnel reflection coefficients: $\phi_1 = arg\,(\frac{n_s-1}{n_s+1})$ and $\phi_2 = arg\,(\frac{n_s-n_{Ag}}{n_s+n_{Ag}})$. In the Fabry-Perot model, the resonance condition in such a cavity can be written as

$$h = \frac{\lambda}{2n_s}(q - \frac{\varphi}{2\pi}) \tag{27}$$

with q an integer. The total phase shift φ due to reflection on cavity bounds is defined by $\varphi = \phi_1 + \phi_2$. In Fig. 29b, the Fabry-Perot cavity thickness h obtained with Eq. (27) is plotted as a function of the resonance wavelength λ for $q = 1$ (blue curve) and $q = 2$ (red curve). The curve $h = f(\lambda)$ is non linear because of the spectral dependence of the refractive index $n_s(\lambda)$. We see that for a cavity thickness of $h = 90$ nm, there are two resonances at $\lambda_1 = 640$ nm and $\lambda_2 = 440$ nm corresponding to $q = 1$ and $q = 2$; respectively. It agrees well with the absorption spectrum displayed in Fig. 29a (green curve)[2]. For the first-order resonance, perfect absorption is obtained at the resonance wavelength: the critical coupling condition is achieved for $\lambda_1 = 640$ nm [87]. We can conclude that in the simple Air/a-Si:H/Ag system defined above, absorption is enhanced thanks to first-order and second-order Fabry-Perot resonances in the Air/a-Si:H/Ag cavity.

If we add a ZnO:Al coating layer to obtain the unstructured reference cell, i.e the ZnO:Al/a-Si:H/Ag stack, the Fabry-Perot resonance at 640 nm described previously still exists but shifts spectrally towards long wavelengths. Indeed, the change of refractive index from 1 (air) to 1.9 (ZnO:Al) at 640 nm leads to an increase of the phase shift ϕ_1 due to reflection on the top interface. The new value of the resonance wavelength given by Eq. (27) is thus higher than λ_1. At short wavelengths, the addition of ZnO:Al leads to a dramatic increase of the absorption compared to the Air/a-Si:H/Ag system due to the anti-reflection effect of the ZnO:Al coating.

It is noteworthy that the ZnO:Al thickness in the reference stack ($h_1 = 50$ nm) is different from the value used for the patterned design ($h_1 = 60$ nm) (Fig. 28). The reference structure parameters have been chosen to optimize the

2 Note that the wavelength noted λ_2 in Fig. 29a (460 nm) is slightly different from the theoretical resonance wavelength of the second-order Fabry-Perot mode in the Air/a-Si:H/Ag cavity (440 nm). In this wavelength range, light absorption in a-Si:H is very strong, the absorption depth at 440 nm is 16 nm, which means that photons do not do a complete single pass in the absorber layer. Therefore, it is difficult to define a resonant mode at short wavelengths, which may explain the discrepancy between the two wavelength values.

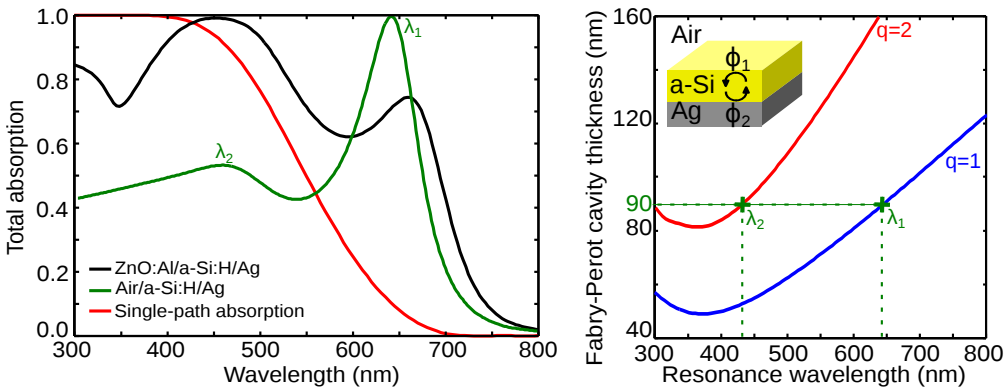

(a) (b)

Figure 29: (a) Absorption spectrum of the reference stack ZnO:Al/a-Si:H/Ag (black curve) compared with a simple a-Si:H layer deposited on a silver mirror (green curve) and the single-pass absorption in a 90 nm-thick a-Si:H layer (red curve). (b) Plot of the Fabry-Perot Air/a-Si:H/Ag cavity thickness as a function of the resonance wavelength for $q = 1$ (blue curve) and $q = 2$ (red curve).

short-circuit current density value of the cell. We integrate the absorption in the a-Si:H active layer to calculate the theoretical short-circuit current density of the cell J_{th}, assuming that all photogenerated carriers are collected. J_{th} is expressed in $\mathrm{mA/cm^2}$ and defined by:

$$J_{th} = \frac{q}{hc} \int_{300}^{\lambda_g} A(\lambda)\, P(\lambda)\, \lambda\, d\lambda \tag{28}$$

with the incident power $P(\lambda)$ corresponding to the normalized AM1.5G solar illumination, $A(\lambda)$ the absorption fraction in the a-Si:H layer and λ_g the bandgap wavelength. Figure 30 displays the evolution of J_{th} when the ZnO:Al and a-Si:H thicknesses vary. A maximum value of $J_{th} = 15.3\,\mathrm{mA/cm^2}$ is found for $h_1 = 50$ nm and $h_s = 90$ nm. Once the metallic grating is added on the absorber layer, the ZnO:Al thickness is varied again in order to find the optimal value ($h_1 = 60$ nm for the design displayed in Fig. 28).

In this subsection, we have shown that in a simple non structured ZnO:Al/a-Si:H/Ag stack, we can trap light efficiently close to the bandgap of the material ($600 - 800$ nm) thanks to Fabry-Perot resonances. However, the plain ZnO:Al layer used as a front contact in this case induces parasitic optical losses at short wavelengths. In subsection 6.4.3, we show that transparent electrodes integrating metallic grids can compete with conventional TCO electrodes. We first focus on the three-layer design with a 1D grating as defined in Fig. 28. The non structured ZnO:Al/a-Si:H/Ag stack will be considered as the reference cell.

6.1.3 *Optical response of the 1D patterned structure*

Figure 31 shows the optical response of the ZnO:Al (Ag)/a-Si:H/Ag structure depicted in Fig. 28 calculated at normal incidence. The one-dimensional metal-

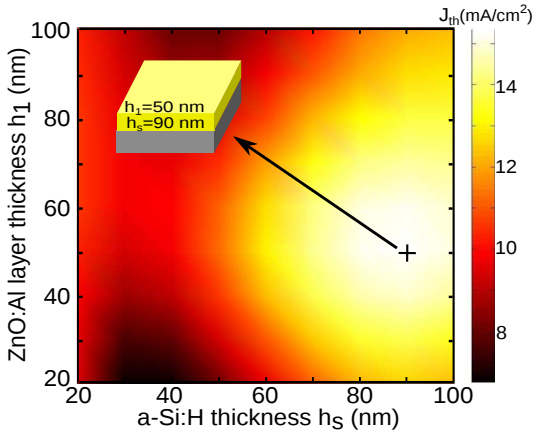

Figure 30: Theoretical short-circuit current density J_{th} (in mA/cm^2) as a function of h_1 (thickness of the ZnO:Al layer) and h_s (thickness of the a-Si:H layer) for a ZnO:Al/a-Si:H/Ag stack. Inset: schematic of the optimized structure ($h_1 =$ 50 nm and $h_s = 90$ nm).

lic grating is polarization dependent, thereby the absorption spectra are displayed for both TE (green curve) and TM (orange curve) polarizations. The definition of transverse electric (TE) and transverse magnetic (TM) polarizations is reminded in Fig. 28.

Remarkably, despite the strong anisotropy of the structure, broadband absorption (absorption $> 70\%$ on the $400 - 700$ nm range) is achieved for both TE and TM light polarizations. This is due to the presence of six resonances (three for each polarization) that are judiciously combined by the design. The main absorption peaks identified in this structure are $\lambda_{A_E} = 476$ nm, $\lambda_{B_E} = 631$ nm, $\lambda_{C_E} = 687$ nm for TE and $\lambda_{A_M} = 430 - 550$ nm, $\lambda_{B_M} = 649$ nm, $\lambda_{C_M} = 770$ nm for TM light polarizations.

At first sight, if we compare the TE and TM absorption spectra to the response of the reference cell, we recognize the broad absorption band at short wavelengths attributed to the Fabry-Perot resonances in the ZnO:Al/a-Si:H/Ag stack (A_E and A_M peaks). At longer wavelengths, the spectra are more complex and polarization dependent. A detailed analysis of the resonances is provided in the following section.

6.2 ANALYSIS OF THE RESONANCES

In this section, we provide a physical analysis of the multi-resonant mechanism. To do so, we numerically study the evolution of the total absorption spectrum as a function of four important design parameters (ZnO:Al thickness h_1, a-Si:H thickness h_s, grating period p and thickness h_m). In the following, for each spectral range, we identify the main parameter having an effect on the resonance peaks and propose a simple analytical model to fit the numerical results.

For the sake of simplicity, only the total absorption spectrum is analyzed. Note that it enables to show resonances that do not contribute to the generation of current because they are below the energy bandgap (in this case, the

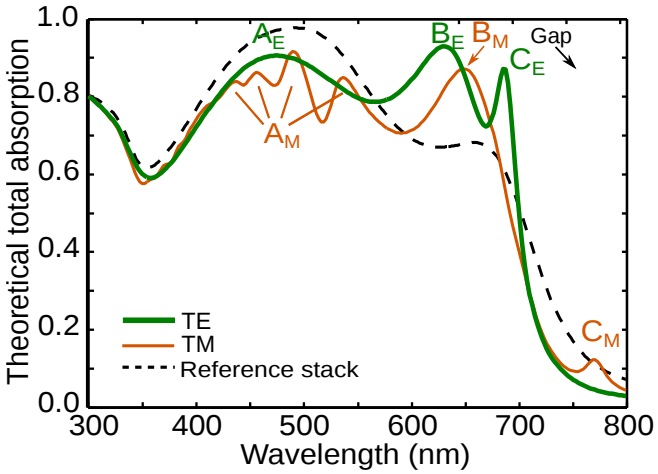

Figure 31: Spectra of the numerically computed total absorption of the model structure under TM (orange) and TE (green) polarized light at normal incidence. The parameters of the 1D metallic grating are $p = 200$ nm, $w = 80$ nm and $h_m = 20$ nm. The total absorption spectrum of the reference stack (ZnO:Al (50 nm)/a-Si:H (90 nm)/Ag) is shown for the sake of comparison (black dashed curve). The bandgap of the a-Si:H material is displayed in grey ($E_g \sim 1.63$ eV here).

absorption peak C_M). It is clear that for application to solar cells, we are only interested in the useful photons, i.e the ones absorbed in the intrinsic a-Si:H layer. The absorption fraction in each layer of the stack is detailed for a complete amorphous silicon cell in subsection 6.3. We show that the absorption only in the a-Si:H active layer exhibits the same peak positions as the total absorption spectrum.

6.2.1 *Absorption resonances at short wavelengths: resonances A_E and A_M*

Let us consider the absorption peaks observed at short wavelengths (resonances A_E and A_M). We first study the evolution of the absorption spectrum when the thickness h_1 of the ZnO:Al layer varies from 20 to 170 nm. For $h_1 = 20$ nm, there is ZnO:Al material in the grooves but not on the nanowires (metal thickness $h_m = 20$ nm). Figure 32b displays the evolution of the total absorption intensity as a function of the ZnO:Al layer thickness h_1 and the excitation wavelength for TE (left) and TM (right) polarizations. The color scale represents the intensity of the absorption in the structure.

It is noteworthy that at long wavelengths ($\lambda > 600$ nm), absorption bands independent of h_1 are attributed to resonances B_E, C_E, B_M and C_M as shown with orange dashed lines in Fig. 32b. At shorter wavelengths ($\lambda < 600$ nm), the TE and TM absorption diagrams exhibit two absorption bands (black dashed curves) that strongly depend on the ZnO:Al layer thickness. The shape of the two bands is very similar to the plot $h = f(\lambda)$ obtained for the cavity Air/a-Si:H/Ag discussed previously (see Fig. 29b). Therefore, we have fitted the evolution of h_1 as a function of the resonance wavelength with a Fabry-Perot model.

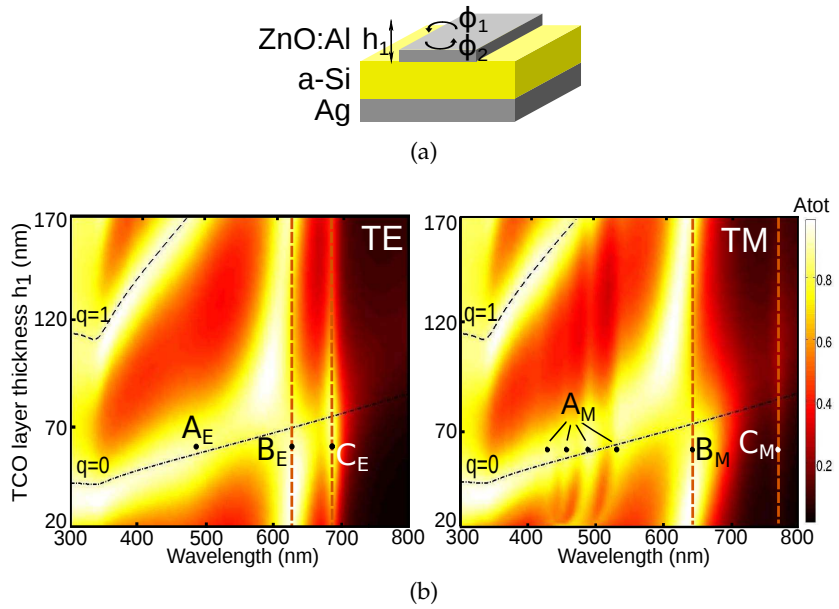

Figure 32: Study of the short-wavelength resonances A_E (TE) and A_M (TM). (a) Sketch of the Air/ZnO:Al/a-Si Fabry-Perot model used to fit the numerical calculations. (b) Total light absorption spectrum in the model structure (defined in Fig. 28) as a function of the ZnO:Al layer thickness h_1 and the wavelength λ for an excitation at normal incidence in TE (left) and TM (right) polarizations. The position of the absorption bands with low dependence on h_1 can be attributed to resonances B_E, C_E, B_M and C_M as shown with orange dashed lines. The resonance position $h_1 = f(\lambda)$ given by the Fabry-Perot model (Eq. (27)) is shown with black dashed curves for $q = 0, 1$.

We consider the ZnO:Al layer as an asymmetric Fabry-Perot resonator with ϕ_1 and ϕ_2 the phase shifts induced by reflection at the ZnO:Al/Air and ZnO:Al/a-Si:H interfaces as depicted in Fig. 32a. In the Fabry-Perot model, the resonance condition in such a cavity can be obtained from Eq. (27) with $h = h_1$ and $n_s = n_1(\lambda)$. Because of the presence of the metallic grating, the calculation of the phase shifts ϕ_1 and ϕ_2 is not straightforward as in the case of the unpatterned reference stack. If the metallic grating is neglected in a rough approximation, the total phase shift φ_0 in the cavity Air/ZnO:Al/a-Si varies slowly in the vicinity of the resonances A_E and A_M (on the $400 - 550$ nm range) and has a mean value of $\varphi_0 \sim -2.91$ rad on this spectral range. In order to take into account the influence of the grating, we consider the total phase shift φ as the fitting parameter to adjust the Fabry-Perot model from Eq. (27) to the numerical calculations displayed in Fig. 32b. The corresponding curves $h_1 = f(\lambda)$ obtained from Eq. (27) with $q = 0, 1$ and $\varphi \sim -1.89$ rad are shown in Fig. 32b with black dashed curves. The latter show a good agreement with the absorption bands of the structure and in particular, the fit with the Fabry-Perot model gives a good approximation of the position of the resonance peaks called A_E and A_M. We see that the absorption mechanism is the same as without a grating, the influence of the grating is limited to the variation of the total phase shift in the resonator. Therefore, we attribute the main absorption mechanism

of resonances A_E and A_M to the lowest order mode ($q = 0$) of the Fabry-Perot resonances in the cavity Air/ZnO:Al(Ag)/a-Si:H.

Note that the Fabry-Perot resonance occurs in the ZnO:Al layer but leads to absorption in the active a-Si:H layer. For resonances A_E and A_M, the absorption intensity in the amorphous silicon layer is 85 % and 75 % respectively. The performances of the patterned device are further developed in the case of a full a-Si:H cell in subsection 6.4.2.

Assuming that the influence of the metallic grating is neglegible at short wavelengths gives a good approximation of the spectral position of the resonance peaks. However, in TM polarization, the metallic grating affects the optical response giving rise to a splitting of the resonance A_M on the $430 - 550$ nm spectral range. The effect of the grating is further discussed in subsection 6.2.4.

6.2.2 *Absorption resonances in the a-Si:H layer: resonances B_E and B_M*

The nature of resonances B_E and B_M is now investigated. Figure 33 displays the evolution of the predicted total absorption as a function of the absorber layer thickness h_s and the excitation wavelength for TE (Fig. 33a) and TM (Fig. 33b) polarizations. We first note that at short wavelengths ($\lambda < 550$ nm), h_s has a low influence on the absorption spectrum. In particular, the spectral position of the absorption bands A_E and A_M discussed previously is independent from the a-Si thickness as shown with vertical orange dashed lines. In TM polarization, we see that the four resonances with the denomination A_M have a different behaviour as a function of h_s: in particular, the peaks at 490 and 540 nm show higher absorption intensity for certain thickness ranges ($40 - 70$ nm, $90 - 130$ nm and $150 - 190$ nm). As already shown for the unpatterned ZnO:Al/a-Si:H/Ag structure, there is a Fabry-Perot resonance in the a-Si:H layer in this wavelength range (peak λ_2 in Fig. 29a). This could explain the dependence of the intensity on the a-Si:H layer thickness. The absorption mechanism at short wavelengths seems to be a combination of several effects with a dominant effect of the Fabry-Perot Air/ZnO:Al/a-Si:H resonances discussed in the previous subsection.

On the contrary, according to Figs. 33a and 33b, the absorption peaks corresponding to resonances B_E and B_M have a spectral position and an intensity that both strongly depend on h_s. We thereby consider an asymmetric ZnO:Al/a-Si:H/Ag Fabry-Perot resonator (see Fig. 34a) and we can adapt the resonance condition of Eq. (27) with $h = h_s$. As in the previous subsection, we use a constant value of φ to fit the numerical calculations over the spectral range of interest ($500 - 700$ nm): $\varphi \sim -1.82$ rad in this case. The corresponding curves $h_s = f(\lambda)$ are plotted in Figs. 33a and 33b with black dashed lines for different values of the integer q. For both B_E and B_M resonances, the Fabry-Perot model is in qualitative agreement with the RCWA calculations. Both absorption peaks can thereby be attributed to Fabry-Perot resonances within the a-Si:H layer (mode with $q = 1$).

Figures 34b and 34c display the spatial distribution of the electric field intensity in the structure when it is excited at $\lambda = 649$ nm (TM, resonance B_M) and

$\lambda = 631$ nm (TE, resonance B_E), respectively. We note that for both TE and TM polarizations there is a field maximum localized within the a-Si:H layer between the metallic wires. This lateral confinement of the field is due to the metallic grating. The low field intensity in the metal for TE polarization confirms that the metallic grating has a low effect on the resonance. In TM polarization, there is a field exaltation at the edges of the silver wires. Consistently, there is a larger difference between λ_{B_M} and the wavelength predicted by the Fabry-Perot model than for TE polarization. As discussed below in subsection 6.4.2, it also induces higher absorption losses in the metallic parts in TM polarization.

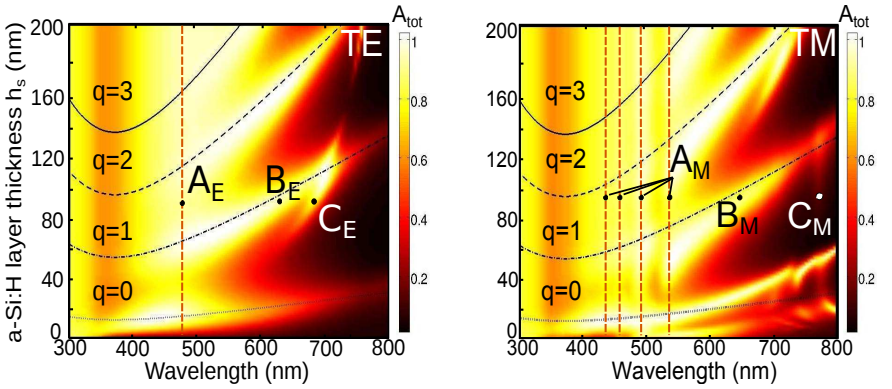

Figure 33: Total light absorption spectrum in the model structure as a function of the absorber layer thickness h_s and the wavelength λ for an excitation at normal incidence in TE (Fig. 33a) and TM (Fig. 33b) polarizations. The resonance position $h_s = f(\lambda)$ given by the Fabry-Perot model (Eq. (27)) with $h = h_s$, is shown for $q = 0, 1, 2, 3$ (black dashed lines).

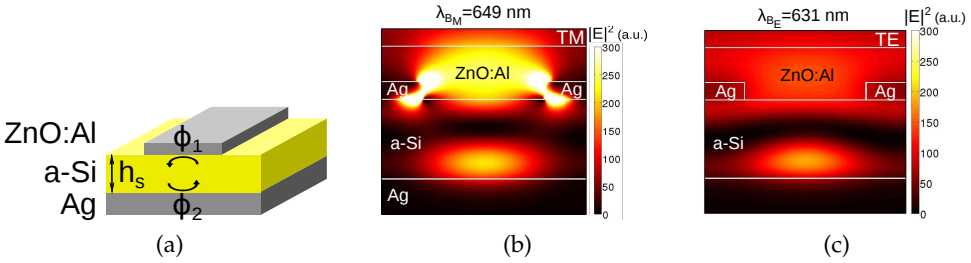

Figure 34: (a) Sketch of the ZnO:Al/a-Si:H/Ag Fabry-Perot resonator model. (b, c) Electric field intensity maps for a 1D silver grating with $w = 80$ nm, $p = 200$ nm, $h_m = 20$ nm for an excitation at (b) $\lambda_{B_M} = 649$ nm under TM polarized light and (c) $\lambda_{B_E} = 631$ nm under TE polarized light.

6.2.3 *Absorption resonances induced by guided modes: resonances C_E and C_M*

In order to study the last resonance contributing to the absorption in the a-Si:H layer, called C_E, we have investigated the influence of the grating period p on the absorption spectrum of the structure for TE polarization. The results

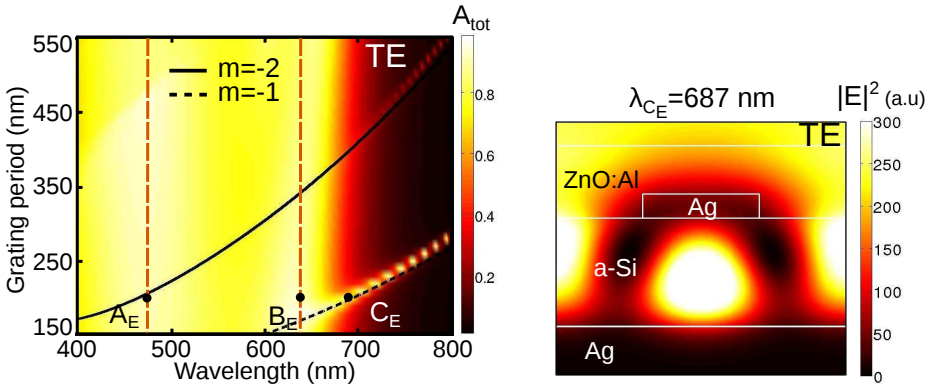

(a) (b)

Figure 35: (a) Total light absorption spectrum of the model structure as a function of the grating period at normal incidence. Orange dashed lines: absorption bands corresponding to resonances A_E and B_E. Dark lines: plot of $p = f(\lambda)$ obtained from Eq. (32) for $m = -1$ (dashed line) and $m = -2$ (plain line) at normal incidence. (b) Electric field intensity map for an excitation at $\lambda_{C_E} = 687$ nm for a TE polarization at normal incidence.

are shown in Fig. 35a. The absorption peak corresponding to the resonance C_E is the only one exhibiting a dispersive character as p varies. The spectral position of resonances A_E and B_E does not depend on p as shown with orange dashed lines. Figure 35b displays the spatial distribution of the electric field intensity for an excitation at wavelength $\lambda_{C_E} = 687$ nm in TE polarization. The electric field is confined in the a-Si:H layer with two maxima along x axis below and between the silver wires. The grating efficiently traps light because of the excitation of a waveguide mode supported by the a-Si:H layer as shown in previous studies on a-Si:H solar cells with periodic patterns [5, 6, 141].

The angle of incidence θ is defined in the plane of incidence perpendicular to the wires (xz plane), as shown in Fig. 36. The in-plane incident momentum is then given by:

$$k_{0x} = k_0 \sin\theta = \frac{2\pi}{\lambda} \sin\theta. \tag{29}$$

The in-plane momentum k_{wg} of a waveguide eigenmode with an effective index n_{eff} can be expressed as:

$$k_{wg} = \frac{2\pi}{\lambda} Re(n_{eff}), \tag{30}$$

thus $k_{0x} < k$. The coupling of incident light into a waveguide can only happen if the 1D metallic grating supplies the extra momentum required to satisfy the conservation of the in-plane momentum:

$$k_{wg} = k_{0x} + k_{gr}^{(m)}. \tag{31}$$

The incident photon gains or looses a momentum $k_{gr}^{(m)}$ which must be a multiple of the reciprocal lattice vector, hence $k_{gr}^{(m)} = m\frac{2\pi}{p}$, with m a relative integer [82].

Therefore, the incident light can couple with a diffracted mode of order m and excite an eigenmode of the ZnO:Al/a-Si:H/Ag waveguide if:

$$\frac{2\pi}{\lambda_{C_E}} Re(n_{eff}) = \frac{2\pi}{\lambda_{C_E}} sin\,\theta + m\,\frac{2\,\pi}{p}. \tag{32}$$

First, we have calculated the effective index $n_{eff}(\lambda)$ of the waveguide modes in a ZnO:Al/a-Si:H/Ag stack with $h_1 = 60$ nm and $h_s = 90$ nm. Figure 35a displays the curves $p = f(\lambda_{C_E})$ obtained from Eq. (32) at normal incidence ($\theta = 0$) for $m = -1$ (dashed line) and $m = -2$ (plain line). It fits well with the spectral positions predicted by the numerical calculations. Resonance C_E can be attributed with the mode resulting from the coupling to the diffracted orders $m = \pm 1$ and guided in the ZnO:Al/a-Si:H/Ag waveguide. An additional peak resulting from the coupling to a higher order diffracted mode ($m = \pm 2$) appears in the $730 - 800$ nm wavelength range for a grating period $p > 425$ nm with a lower absorption intensity. As can be shown in Fig. 35a, this mode should also lead to an absorption peak at short wavelengths close to the resonance A_E. However, its effect on the total absorption is difficult to discuss since absorption in this wavelength range is really strong. In particular, we cannot observe the dispersion with the period grating (see Fig. 35a) or the angle of incidence (see Fig. 36). This mode appears to have a low contribution in the absorption mechanism compared to the resonance A_E in the Air/ZnO:Al/a-Si cavity.

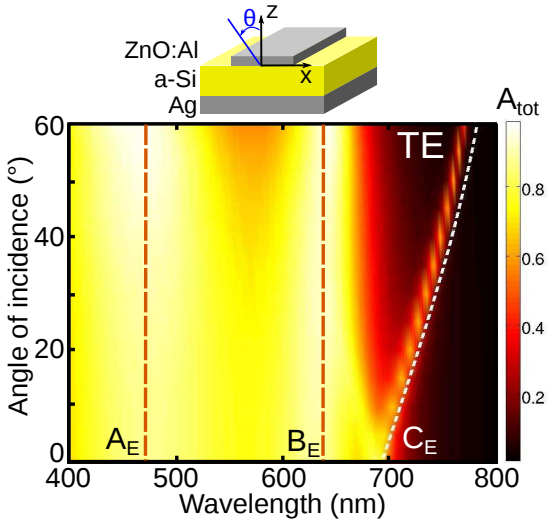

Figure 36: Total light absorption spectrum of the model structure as a function of θ. Orange dashed lines: absorption bands corresponding to resonances A_E and B_E. White dashed line: plot of $\theta = f(\lambda)$ obtained with Eq. (32) for $m = -1$ and $p = 200$ nm. Inset: definition of the angle of incidence θ (plane of incidence perpendicular to the wires).

Second, according to Eq. (32), the resonance wavelength of C_E should depend strongly on the angle of incidence θ. We have investigated the angular dependence of the total absorption (Fig. 36) and plotted the $\theta = f(\lambda_{C_E})$ curve for the model structure ($p = 200$ nm) (white dashed line). Eq. (32) agrees well with the

shift of λ_{C_E} predicted by the RCWA calculations as θ increases. Note that the resonance wavelengths λ_{A_E} and λ_{A_M} do not depend on the angle of incidence, which is consistent with the attribution to Fabry-Perot resonances in the stack.

The attribution of the resonance C_E to the coupling of diffracted light to an eigenmode of the ZnO:Al/a-Si:H/Ag waveguide also explains the evolution of the total absorption spectrum when the a-Si:H layer thickness h_s varies. Indeed, the effective index of the guided mode increases with the thickness of the guiding layer, leading thereby to a shift of λ_{C_E} towards higher wavelengths. This is consistent with the spectral shift of the resonance C_E when h_s increases (see Fig. 33a).

Third, the absorption peak at $\lambda = 770$ nm for TM polarization, labelled C_M, can also be attributed to a guided mode supported by the a-Si:H layer. The plot $p = f(\lambda_{C_M})$ exhibits the same dispersive behavior as resonance C_E (not shown here). This resonance involves surface plasmons propagating at the a-Si:H/Ag interface thereby leading to parasitic absorption in the metallic mirror. As shown in Fig. 31, it leads to an absorption peak at an energy below the electronic bandgap of the absorber material. In the following, we show that this resonance can be shifted towards shorter wavelengths by adding a ZnO:Al buffer layer between the absorber layer and the back mirror and hence contribute to the generation of photocurrent in the structure (see subsection 6.3.2).

6.2.4 *Influence of the metallic layer thickness*

For now, the numerical analysis of the absorption spectrum was performed for a fixed metallic layer thickness $h_m = 20$ nm. We have also studied the evolution of the absorption spectrum when h_m varies from 0 to 20 nm as displayed in Fig. 37. Note that in this subsection, we study the absorption only in the a-Si:H layer. For both TE (Fig. 37a) and TM (Fig. 37b) polarizations, the metal thickness has non negligible effects on the intensity and the spectral position of the absorption peaks.

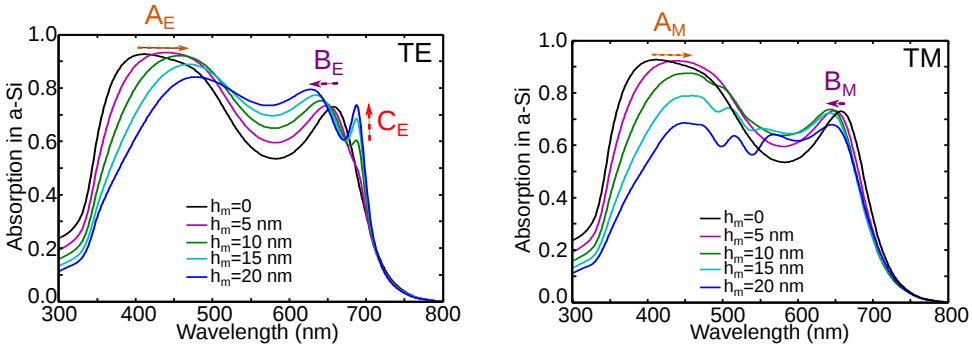

(a) (b)

Figure 37: Influence of the metal layer thickness h_m on the absorption in the a-Si:H layer for TE (a) and TM (b) polarizations.

The first striking effect of increasing the metallic grating thickness is a decrease of absorption intensity at short wavelengths because of parasitic absorp-

tion losses in the metal. These losses are particularly important for a TM polarization as shown in Fig. 37b. Indeed, the electric field is confined in the vicinity of the metallic wires because of surface plasmons (see Fig. 34b), leading to increased absorption in the metallic grating.

Second, for $h_m = 0$, the absorption spectrum exhibits two broad peaks corresponding to Fabry-Perot resonances in the Air/ZnO:Al/a-Si cavity ($\lambda \sim 350 - 500$ nm) and ZnO:Al/a-Si/Ag cavity ($\lambda \sim 600 - 650$ nm). For both polarizations, a higher value of the metal thickness induces a spectral shift of these resonances. The absorption peaks corresponding to resonances A_E and A_M ($\lambda \sim 400 - 500$ nm) have been attributed to resonances in the Air/ZnO:Al/a-Si cavity (see subsection 6.2.1). Silver has a lower refractive index than amorphous silicon: $n_{Ag} \sim 0.13$ to be compared to $n_{aSi} \sim 4.9$ at 500 nm. Therefore, the addition of the metallic grating leads to an increase of the phase shift ϕ_2 induced by reflection on the bottom interface of the cavity, thereby redshifting the peak. Note that for TM polarization, thicker metallic layers also lead to an increased splitting of the resonance peak A_M. It confirms that the existence of several absorption peaks in this wavelength range is due to the grating. We suggest that the splitting stems from surface plasmons at the surface of the wires since this phenomenon is observed only for a TM polarization.

Likewise, for resonances B_E and B_M (Fabry-Perot resonances in the ZnO:Al/a-Si/Ag cavity, $\lambda \sim 600 - 650$ nm), the presence of the metallic grating decreases the phase shift ϕ_1 induced by reflection on the top interface of the cavity, hence blueshifting the peak. These two spectral shifts result in a narrower absorption band for both TM and TE polarizations. However, for a transverse electric field, the absorption reduction at short wavelengths is compensated by an increase in the $500 - 600$ nm spectral range due to the B_E absorption peak.

Finally, for TE polarized light, at long wavelengths ($\lambda \sim 700$ nm), the peak corresponding to resonance C_E appears for $h_m \geq 10$ nm. As expected, C_E does not exist for $h_m = 0$. A thicker metal grating leads to stronger coupling to guided modes. As a consequence, the overall performance of the structure is improved for TE polarized light with a thicker silver grating.

To sum up, the thickness of the metallic grating should be chosen so that the absorption losses in the metal are minimized. A maximum theoretical short-circuit current density of 14.9 mA/cm^2 is obtained for $h_m = 10$ nm. We have fixed h_m to 20 nm so that the structure would be technologically feasible.

6.2.5 *Conclusion and design rules*

In section 6.2, we have studied the absorption mechanism in the ZnO:Al/a-Si:H/Ag model structure. We have shown that a broad absorption band is achieved with a combination of multiple resonances in different spectral ranges. The parameters of the structure (ZnO:Al thickness h_1, a-Si:H thickness h_s, grating period p and metal thickness h_m) are chosen to obtain the absorption peaks in the desired spectral range. The results of the analysis performed through numerical simulations are summarized in Table 5. In the following section, we

will present the application of this analysis to design a complete a-Si:H solar cell with a 1D patterned metallic grating.

Geometrical parameter	Resonance type	Spectral range
ZnO:Al thickness h_1	F-P resonance in the top layer	$450 - 500$ nm
a-Si:H thickness h_s	F-P resonance in the a-Si layer	$600 - 650$ nm
Grating period p	Excitation of guided modes	$650 - 750$ nm

Table 5: Summary of the analysis of the absorption resonances developed in section 6.2. "F-P resonance" stands for "Fabry-Perot resonance".

6.3 DESIGN OF A COMPLETE A-SI:H SOLAR CELL

6.3.1 *Description of the complete solar cell design*

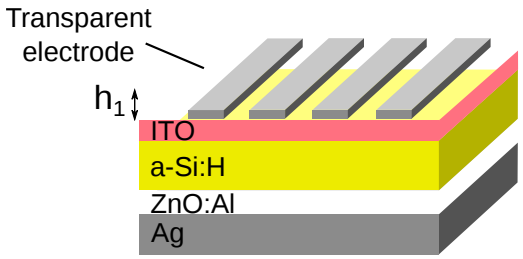

Figure 38: Schematic of the a-Si:H solar cell investigated: Si_3N_4(Ag)/ITO/a-Si:H/ZnO:Al/Ag stack with a 90 nm-thick p-i-n a-Si:H absorber layer. The front transparent electrode is made of a 1D silver grating (metal thickness = 20 nm, width = 80 nm and period = 200 nm) embedded in a layer of a non absorbing material. Other geometrical parameters are $h_1 = 60$ nm, $h_{ITO} = 10$ nm, $h_{ZnO:Al} = 15$ nm.

A complete a-Si:H photovoltaic cell is illustrated in Fig. 38. The active layer is composed of a p-i-n a-Si:H junction, the influence of the doping on the refractive index of the material is neglected in the numerical calculations. Two additional spacing layers are inserted above (ITO) and below (ZnO:Al) the a-Si:H layer in order to prevent metal diffusion in the absorbing layer. Contamination of the a-Si:H layer by silver could create carrier recombination traps in the absorber layer. Even at low temperature ($T = 50°C$), the diffusion coefficient of silver in a-Si:H is $D = 10^{-18}$ cm^2/s [142]. It means that during a silver deposition process supposed to last $t = 3$ minutes, the vertical diffusion length of the metal within a-Si:H is $L = 2\sqrt{D \times t} = 2\sqrt{(10^{-18} \times 180)} \sim 3.6$ nm, and thereby non negligible with respect to the thickness of the doped layers (typically $10 - 20$ nm). A very thin ($10 - 15$ nm) spacing layer is sufficient to act as a diffusion barrier layer [106].

We propose to use the metallic grid to act as a transparent conductive electrode on the front contact of the cell. The top ZnO:Al layer of the model struc-

ture is replaced by a non-absorbing material. The top contact is then formed by the thin ITO[3] spacing layer and the metallic grating, resulting in a reduction of optical absorption in the top layers of the structure at short wavelengths. In the numerical calculations, we consider silicon nitride (Si_3N_4) as the transparent material of the front electrode, the refractive index of Si_3N_4 is taken from Palik [116]. In this section, the refractive index used for silver is taken from Johnson and Christy [143].

We have used the results of the analysis presented in section 6.2 as guidelines for the design of the complete a-Si:H solar cell. The top anti-reflection silicon nitride layer thickness is set at 60 nm in order to obtain a resonance at $450 - 500$ nm. The thickness of the a-Si:H layer is 90 nm and contributes to the absorption enhancement in the $600 - 650$ nm wavelength range. With a period $p = 200$ nm, the grating leads to the excitation of guided modes for both TE and TM polarizations at a wavelength close to 700 nm.

6.3.2 *Influence of the spacing layers*

Adding spacing layers in the stack has a non negligible effect on the localization of the electric field and therefore on the absorption intensity in the a-Si:H layer. The thicknesses of the two spacing layers have to be chosen carefully. Besides, the optimization of the spacing layer thicknesses is more critical for a transverse magnetic field because of the field confinement close to the metal. We have therefore investigated the influence of h_{ITO} and $h_{ZnO:Al}$ on the absorption spectrum considering the effect of each thickness on the response for a TM polarization.

6.3.2.1 *Influence of the ITO spacing layer*

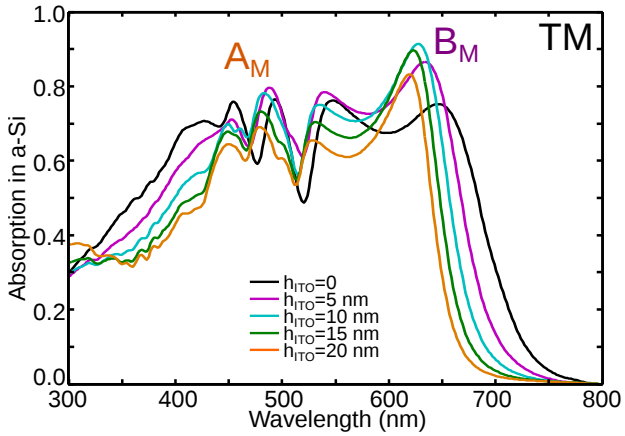

Figure 39: Influence of the ITO spacing layer thickness on the absorption in the a-Si:H layer for the structure depicted in Fig. 38 with $h_{ZnO:Al} = 0$ for a TM polarized excitation at normal incidence.

3 The choice of ITO for this spacing layer is discussed in subsection 6.3.2.1.

Figure 39 displays the evolution of the absorption in the a-Si:H layer when the ITO layer thickness varies from 0 to 25 nm. The structure considered is the design depicted in Fig. 38 with $h_{ZnO:Al} = 0$. The absorption spectrum for $h_{ITO} = 0$ (black curve) corresponds to a Si_3N_4/a-Si:H/Ag stack with $h_1 = 60$ nm and $h_s = 90$ nm. We see different trends on the absorption spectrum when h_{ITO} increases.

First, there is a drop of intensity at short wavelengths ($350 - 450$ nm) due to parasitic absorption losses in the ITO layer. Furthermore, the resonances A_M in the Air/ZnO:Al/a-Si cavity exhibit a blue shift when the ITO thickness increases.

Second, the absorption peak at 650 nm (resonance B_M) blueshifts partly due to the lower phase shift on the a-Si:H/ITO interface ($\phi_1 = 0.034$ rad at 650 nm) compared to a-Si:H/SiN_x ($\phi_1 = 0.044$ rad at 650 nm). This shift comes with an increase of the absorption intensity corresponding to the peak B_M: for $h_{ITO} = 10$ nm, the absorption in the whole stack (not shown here) is total ($A_{tot} = 1$) at the resonance wavelength. For $h_{ITO} > 10$ nm, this trend is reversed: the absorption intensity drops for thicker ITO layers.

We see that the influence of the ITO layer is not clear yet. Adding the ITO layer modifies the phase shift induced by reflection at the interface but also changes the effective index of the resonant mode. Understanding the role of this layer in the absorption mechanism requires further analyses.

The main consequences of the increase of h_{ITO} is a decrease of the total width of the multi-resonant absorption band and a reduction of the absorption intensity. As a consequence, if we consider the calculated short-circuit current density, the optimal ITO layer thickness is $h_{ITO} = 0$ nm. As discussed previously (subsection 6.3.1), this spacing layer is needed to prevent metal diffusion in the a-Si:H layer. The thickness of the ITO spacing layer is therefore chosen to be $h_{ITO} = 10$ nm to i) minimize the absorption decrease at short ($350 - 450$ nm) and long ($650 - 700$ nm) wavelengths and ii) maximize the absorption gain in the $600 - 650$ nm spectral range.

The first idea of having this ITO layer was to begin with a good electrical contact ITO/a-Si:H, which is already well known in a-Si:H technology. If ITO could be replaced by a non doped layer (for instance intrinsic ZnO), the absorption losses in this layer due to free carrier absorption could be strongly reduced. There are two resistances to account for:

- the resistance to the vertical current i.e the series resistance R_s
- the resistance to the lateral conduction, i.e the sheet resistance $R_\square$.

As already shown in *chapter* 3, the sheet resistance of a trilayer ZnO/Ag/ZnO is approximately $2\,\Omega$/sq, which is very low (commercial ITO layers have a sheet resistance higher than $10\,\Omega$/sq, see *chapter* 3). Regarding the series resistance, let us consider a spacing layer with a thickness of 10 nm. Given a current density J, the voltage drop due to series resistance in this layer is then:

$$\Delta V = R \times I = (\rho \times \frac{h}{S})(J \times S) = J \times \rho \times h\,, \tag{33}$$

Material	Bulk resistivity (Ω.m)	Voltage drop (V)
ITO	100×10^{-8} [104]	1.5×10^{-12}
i-ZnO	1×10^{-2} [99]	1.5×10^{-8}

Table 6: Effect of the vertical resistance of the spacing layer on the voltage.

with ρ the material resistivity and h the layer thickness. We have considered a current density $J = 15$ mA/cm^2 and we have calculated the voltage drop as well as the relative efficiency drop due to series resistance in the spacing layer as shown in Table 6. We see that because the spacing layer is very thin, the effect of the series resistance on the voltage is negligible. As a consequence, we could imagine using a non doped material such as intrinsic zinc oxide to reduce the absorption losses in this layer. Note that the doping level of the spacing layer material has also an impact on the quality of the Ag/ZnO/a-Si:H ohmic contact.

6.3.2.2 *Influence of the ZnO:Al spacing layer*

We have investigated the influence of the ZnO:Al spacing layer thickness on the absorption in the a-Si:H layer for TM polarization, as displayed in Fig. 40a. The calculations are done for a thickness of the ITO spacing layer fixed to $h_{ITO} = 10$ nm. Since the ZnO:Al spacing layer is placed on the rear of the a-Si:H absorber layer, the ZnO:Al thickness has an influence mostly in the long wavelength range ($\lambda > 550$ nm). We see that adding a spacing layer between the amorphous silicon absorbing layer and the metallic back mirror introduces a new absorption peak below the bandgap wavelength, labelled G (see Fig. 40a).

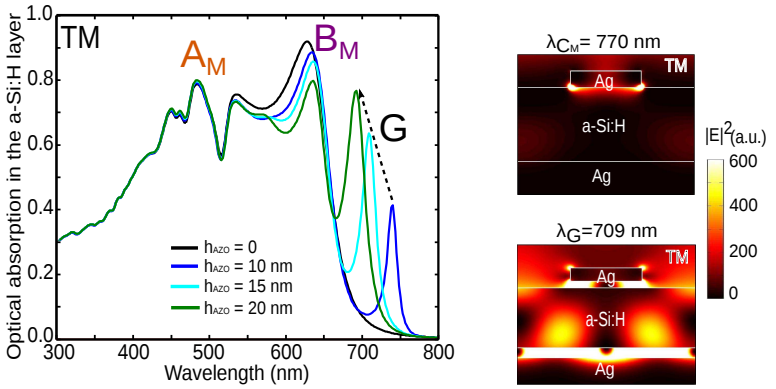

(a) (b)

Figure 40: (a) Absorption spectrum in the a-Si:H layer for a ZnO:Al layer thickness $h_{ZnO:Al}$ varying from 0 to 20 nm for a TM polarized light at normal incidence. (b) Electric field intensity $|E|^2$ maps for an excitation at λ_{C_M}= 770 nm (three-layer model structure, Fig. 28) (top) and λ_G= 709 nm (complete cell with $h_{ZnO:Al}$= 15 nm , Fig. 38) (bottom) at normal incidence for a TM polarization. Both electric field maps have the same color scale, which leads to a saturation of the bottom figure.

Let us compare this peak to the resonance labelled C_M for the simplified three-layer model (see Fig. 31). Figure 40b displays the electric field intensity maps corresponding to these two peaks (top: resonance C_M in the simplified three-layer model; bottom: resonance G in the complete cell with $h_{ZnO:Al} = 15$ nm). In the first case (resonance C_M), the electric field is confined at the a-Si:H/Ag interface below the metallic wires. As for the complete cell (resonance G), the maxima of the electric field are localized in the spacing layers. Secondary maxima are observed within the absorber layer with a much higher intensity for the structure with spacing layers. This agrees with the attribution of these peaks to a low energy guided mode observed under TM polarization.

We see in Fig. 40a that the resonance G shifts towards shorter wavelengths when $h_{ZnO:Al}$ increases. This is consistent with the decrease of the effective index of the guided mode when we add a low index buffer layer ($n_{ZnO:Al} \sim 1.8$ to be compared to $n_{aSi} \sim 4.2$ at 700 nm) below the a-Si:H layer. The thickness of the buffer layer allows us to tune the spectral position of the peak corresponding to the guided mode G so that it could contribute to the photogeneration of current. It is consistent with the work of Haug et al. [82] which reported that the buffer layer between the a-Si:H absorber layer and the back silver mirror could have a beneficial effect on the absorption in the active layer. The total absorption in the cell (not shown here) is perfect ($A_{tot} = 1$) at the resonance wavelength and the absorption intensity in the a-Si:H layer is limited by the parasitic losses in the ZnO:Al layer and the metallic substrate. When $h_{ZnO:Al}$ varies from 10 to 20 nm, absorption losses in the silver back mirror are reduced from 20 % to 6 % leading to an absorption maximum over 75 % at 690 nm.

However, increasing $h_{ZnO:Al}$ induces a decrease of the absorption intensity at $\lambda = 635$ nm (resonance B_M) as evidenced in Fig. 40a. Therefore, the buffer ZnO:Al layer thickness is fixed to the value of $h_{ZnO:Al} = 15$ nm in order to achieve an optimal broadband absorption spectrum favored by a lower spectral position of the peak while limiting the absorption drop at 635 nm.

6.3.3 *Optical response of the complete solar cell*

The optical response of the complete structure is shown in Fig. 41 for TE (green) and TM (orange) polarizations. The multi-resonant absorption spectra are very similar to those obtained for the simplified model structure described in section 6.1. The combination of the multiple resonances leads to a broad absorption band for both TE and TM polarizations.

We define a new reference structure for the study of the complete cell. The design is similar but in spite of the alternative $Si_3N_4(Ag)$ electrode, the front contact is made of a standard TCO material. Therefore, the unpatterned reference structure is a TCO[4]/a-Si:H/ZnO:Al/Ag stack with the same a-Si:H and ZnO:Al thicknesses and a top TCO layer thickness $h_{TCO} = h_1 + h_{ITO} = 70$ nm. The absorption spectra of the complete cell are compared to the response of the reference structure (dashed black curve). Introducing the alternative transpar-

4 Here, the transparent conductive oxide is ZnO:Al. The conclusion of the calculations is valid for other TCO materials such as ITO.

ent electrode made of the metallic grating embedded in a Si_3N_4 layer results in an absorption enhancement in the short wavelength ($300 - 380$ nm) and long wavelength ($600 - 700$ nm) regions as shown in Fig. 41. At short wavelengths, the replacement of the front TCO by a non absorbing material (Si_3N_4) reduces the absorption losses in the front electrode. In the case of the reference structure with a conventional TCO electrode (ZnO:Al or ITO), there is a trade-off between the conductivity required and the transparency of the electrode. Using a highly doped TCO layer leads to parasitic absorption losses due to free carrier absorption. The use of the alternative electrode relieves this trade-off, thereby allowing lower losses at short wavelengths while keeping a high conductivity (sheet resistance $\sim 2\,\Omega/\text{sq}$). In the red part of the spectrum, absorption improvement is due to the light trapping effects (resonances C_E (TE) and G (TM)) close to the bandgap of amorphous silicon.

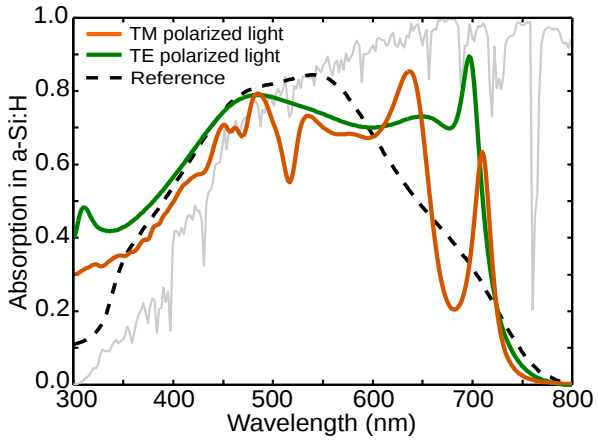

Figure 41: Absorption in the a-Si:H layer of the complete solar cell (see Fig. 38) for TE (green) and TM (orange) polarizations at normal incidence. The normalized AM1.5G solar spectrum is shown as a reference (grey curve). Dashed curve: absorption spectrum of a TCO/a-Si:H/ZnO:Al/Ag reference structure (same a-Si:H and ZnO:Al thicknesses, $h_{TCO} = h_1 + h_{ITO} = 70$ nm, no grating). The bandgap of the a-Si:H material is shown in grey.

6.4 THEORETICAL PERFORMANCES OF THE DEVICE

6.4.1 *Theoretical short-circuit current density and angular dependence*

	No grating	TE	TM	Unpolarized light
J_{th} (mA/cm^2)	14	15.8	13.4	14.6

Table 7: Theoretical short-circuit current density values of the complete cell at normal incidence for TE, TM polarizations and unpolarized light. The value obtained for the reference structure is given for comparison.

We have calculated the theoretical short-circuit current density J_{th} using Eq. (28). Table 7 summarizes the short-circuit current density values of the design for different light polarizations at normal incidence. The J_{th} value for an excitation with unpolarized light is calculated as the average of the J_{th} values for TE and TM polarizations. We show that the use of the 1D metallic grating as a transparent front electrode leads to a theoretical short-circuit density J_{th} of 14.6 mA/cm^2 for 90 nm of a-Si:H. As shown in Table 7, a value of 14 mA/cm^2 has been calculated for the reference structure. This improvement of the short-circuit current density can be attributed to:

- the reduction of absorption losses at short wavelengths ($300 - 400$ nm) due to the replacement of the TCO by silicon nitride
- the absorption enhancement close to the bandgap of a-Si:H ($600 - 700$ nm) due to Fabry-Perot resonances in the a-Si layer (resonances B_E and B_M) and coupling to guided modes (resonances C_E and G).

As displayed in Fig. 42, we have also investigated the dependence of the theoretical short-circuit current density J_{th} on the angle of incidence θ (plane of incidence perpendicular to the wires). The maximum value of J_{th} occurs for $\theta = 10°$, this may be due to a better coupling to guided modes. For higher incident angles, the short-circuit current density decreases. However, up to 60°, the short-circuit current density depends weakly on for both TE and TM polarizations. For instance, at $\theta = 60°$, the J_{th} is still equal to 80 % of the value at normal incidence.

It is noteworthy that we have not studied the influence of the angle of incidence ϕ in the plane of incidence parallel to the stack. In order to assess the real angular dependence for incident sunlight, we should study the influence of both θ and ϕ. As a matter of fact, the complete calculation should lead to better performances at high angles than we have predicted because the modes attributed to the excitation of eigenmodes of the waveguide (C_E and C_M) are the only dispersive modes and they do not depend on the angle ϕ.

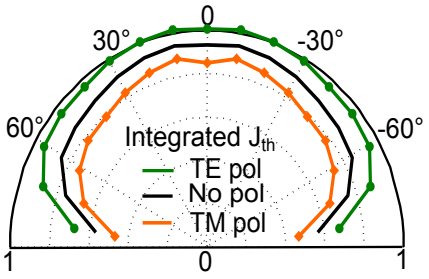

Figure 42: Angular dependence of the integrated short-circuit current for the structure depicted in Fig. 38. The values of J_{th} are normalized with respect to the maximum value of J_{th} under TE polarization (equal to 15.97 mA/cm^2 for $\theta = 10°$).

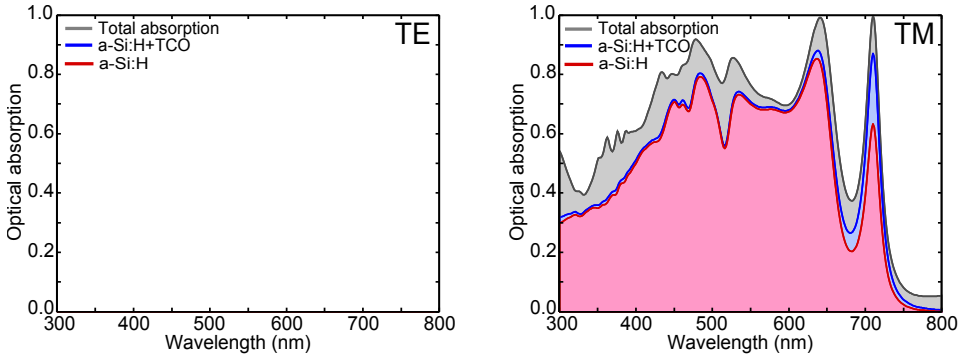

Figure 43: Numerically computed optical absorption in each material of an ultra-thin a-Si:H solar cell for an excitation under TE (a) and TM (b) polarizations at normal incidence (red curve: absorption only in a-Si:H; blue curve: absorption in a-Si:H and the ITO and ZnO:Al spacing layers; grey curve: total absorption). The bandgap of amorphous silicon is shown in grey.

6.4.2 *Balance of the optical losses in the cell*

Only the photons absorbed in the 90 nm-thick a-Si:H layer contribute to the generation of photocurrent. The remaining part of the impinging photons are either reflected or absorbed in the metal (grating + back mirror) or the buffer layers. In Figs. 43a and 43b, we show the absorption fractions in each material constituting the solar cell for TE and TM polarizations.

A main issue addressed by the use of a silver grating as a front contact is the significant absorption losses expected in the metallic wires. We have evaluated the fraction of photons absorbed in both metallic contacts defined as the ratio of the absorption in the metal (grating + mirror) (grey area in Figs. 43a and 43b) over the total absorption in the structure. Both absorption values are integrated on the $300 - 800$ nm spectral range. We have found that the parasitic losses in the metal are below 10 % of incident photons (for an excitation with unpolarized light at normal incidence). Note that losses are more important for a transverse magnetic field because of the strong field exaltation close to the grating and the back mirror surface.

In Fig. 43, we also see that there is still room for improvement of the optical response. In particular, a better engineering of the anti-reflection coating layer should lead to reduced reflection losses. Furthermore, it is noteworthy that the optical response displayed in Fig. 43 shows a drop of absorption for wavelengths between 700 nm and $\lambda_g = 760$ nm, which unfortunately corresponds to a spectral range with high solar power intensity. Shifting the long wavelength resonances (C_E and G) closer to the bandgap could improve the short-circuit current density. However, as shown in Fig. 40a, the intensity of the absorption peak drops when it gets closer to the bandgap because the absorption coefficient of the a-Si:H material decreases drastically in this wavelength range. We see here that the optimization of the light-trapping structure is limited by the intrinsic properties of amorphous silicon such as its bandgap wavelength.

6.4.3 *Discussion of the performances of the alternative contact*

In *chapter* 3, we have discussed the necessity to define a figure of merit in order to assess accurately the performances of nanopatterned resonant front contacts. We have used a figure of merit ΔJ expressed as the theoretical current density gain with respect to a reference structure (see *chapter* 3, subsection 3.3). With this definition, the figure of merit accounts both for the parasitic absorption losses due to the metallic grating and the beneficial light-trapping effect. The reference structure is the TCO/a-Si:H/ZnO:Al/Ag stack defined in subsection 6.3.3. It results in $\Delta J = 0.6$ mA/cm^2 for the structure presented here with a 1D grating (period = 200 nm, width = 80 nm).

In order to discuss our contribution to the research field, we have compared our results with two state-of-the-art works on a nanopatterned back contact for thin amorphous silicon solar cells. In Ref. 47, Ferry et al. have reported the fabrication and characterization of patterned ultra-thin a-Si:H solar cells. The a-Si:H junction (i layer thickness $= 90 - 150$ nm) is conformally grown on a substrate with rounded hemiellipsoidal nanostructures. The patterning thus provides light-trapping effects both on the front and back sides of the cell. The calculated absorption spectrum for a 90 nm-thick i-layer thickness is shown in Fig. 44 (blue curve). The integration of the curve gives a value of $J_{SC} = 13.3$ mA/cm^2. In Ref. 144, Naqavi et al. studied the photocurrent enhancement due to 1D back gratings in thin a-Si:H solar cells, the total thickness of the p-i-n junction being 230 nm in their designs. They predicted a short-circuit current density of 12.62 mA/cm^2 for an unpolarized light (green curve in Fig. 44) and demonstrated an experimental value of 12.36 mA/cm^2 for the same structure. According to Fig. 44, we find that our approach allows us to combine more resonances and achieve an overall better performance with a thinner absorber layer (a total thickness of 90 nm instead of 90 nm for the i layer [47] and 230 nm [144]).

6.5 ABSORPTION LOSSES IN THE DOPED LAYERS

To discuss further the performances of our design, we have used state-of-the-art values [5] for the open-circuit voltage ($V_{OC} = 0.88$ V) and fill factor (FF = 0.7) in order to predict the global performances of the modeled device. We have obtained a theoretical conversion efficiency of 9%, using the value $J_{th} = 14.6$ mA/cm^2 calculated for 90 nm of a-Si:H at normal incidence. The predicted conversion efficiency is to be discussed because so far, we have not taken into account the absorption in the doped layers for the sake of simplicity. As already mentioned in *chapter* 5, carriers generated in the a-Si:H doped layers are very likely to recombine before being collected.

In order to predict more accurately the performances of our design, let us assess the absorption losses in the doped layers. We have considered standard thicknesses of the doped layers (15 nm for p layer and 10 nm for n layer). Figure 45 displays the calculated absorption fraction in the doped layers for both TE

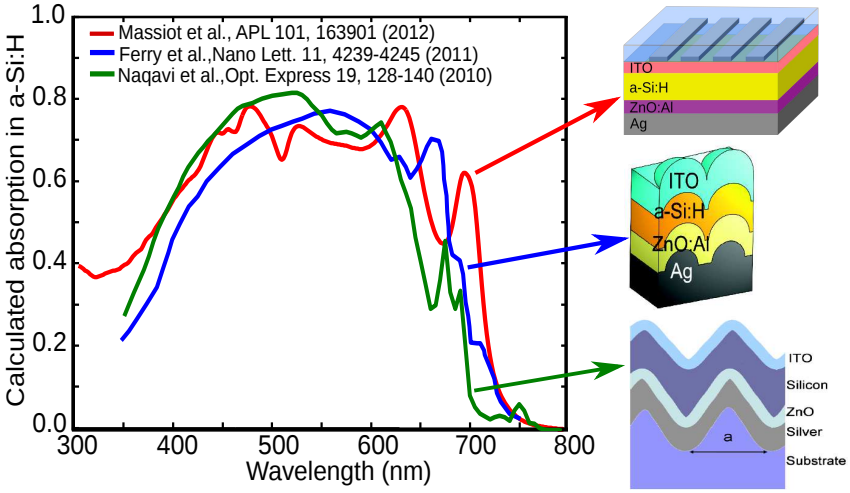

Figure 44: Comparison with state-of-the-art works (Ferry et al. [47] (blue) and Naqavi et al. [144] (green)). Inset: Schematic of the designs extracted from Refs. 47 and 5.

(Fig. 45a) and TM (Fig. 45b) polarizations. The red and orange areas represent the losses in the p and n layers respectively.

For $\lambda < 450$ nm, there is no absorption losses in the n doped layer because the photons are strongly absorbed in the p and i layers. For instance, at 300 nm, the absorption depth in a-Si:H is around 7 nm which is lower than the p layer thickness. Most of the photons at this wavelength are lost in the p layer.

Regarding the Fabry-Perot resonances ($450 - 650$ nm), around 20 % of photons are lost in the p layer, and 10 % in the n layer. If we consider the case of the resonances in the a-Si:H layer (peaks B_E and B_M), the maxima of the electric field within the a-Si:H layer are confined close to the wires and the metallic mirror, as can be seen in Figs. 34b and 34c. Photons are preferentially absorbed within the doped layers, which explains the important losses in both the p and n doped layers.

In both TE and TM polarizations, losses in the doped layers are lower for the long wavelength resonances (C_E and G) that we attributed to coupling to guided modes. This is due to the confinement of the field within the i layer. Near-field effects are limited for this kind of resonances leading to a lower absorption fraction in the p and n layers.

We have calculated the theoretical short-circuit current density from integrating the green area in Figs. 45a and 45b. We find an average value of $J_{th} = 8.7$ mA/cm^2 for an unpolarized light excitation. It represents a 40 % current density loss compared to our previous estimation. In order to do another assessment of the advantage of the patterned resonant front contact, we have also taken into account the doped layers for the TCO/a-Si:H/ZnO:Al/Ag reference structure. With a 15 nm-thick p-doped layer and a 10 nm-thick n-doped layer, the theoretical current density is equal to $J_{th} = 8.2$ mA/cm^2. The current density gain with respect to the reference structure is 0.5 mA/cm^2, which is slightly lower than our first estimation ($\Delta J = 0.6$ mA/cm^2).

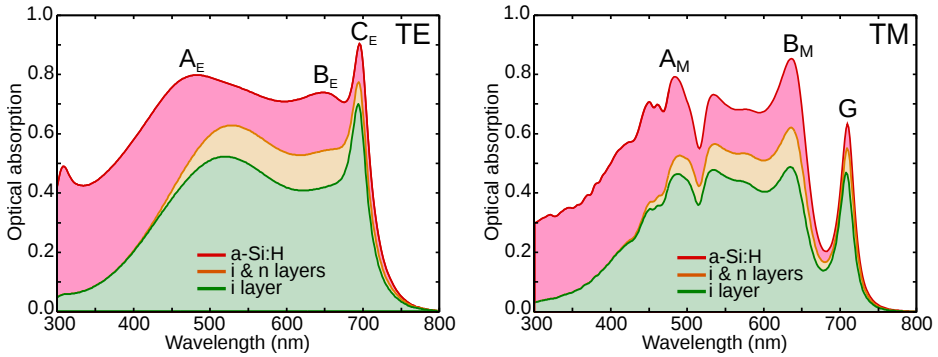

(a) (b)

Figure 45: Absorption losses in the doped layers for an excitation under TE (a) and TM (b) polarizations at normal incidence (red curve: absorption fraction in the junction; orange curve: absorption fraction in the i and n layers; green curve: absorption fraction in the i layer). The bandgap of the modeled a-Si:H material is shown in grey.

6.6 CONCLUSION

In this chapter, we have proposed a design for a-Si:H ultra-thin solar cells with a nanopatterned resonant front contact in order to achieve efficient light-trapping. We have numerically shown that this design combines multiple resonances with various absorption mechanism. From an optical point of view, our design achieves similar performances to state-of-the-art works. Yet, the overall performance of the optimized a-Si:H cells is not as promising as expected because of important losses in the doped layers. We have already shown that the ZnO:Al layer between the a-Si:H layer and the back mirror could be used to reduce parasitic losses in the metal. Karin Söderström has shown in her PhD thesis that the ZnO:Al layer could also decrease the absorption losses in the n-doped layer [145]. Further optimization of both spacing layers (above and below the a-Si:H layer) could enable a reduction of the absorption losses in the doped layers and thus increase the performances of the cell.

However, even if this concept is not to be applied at the industrial scale for the amorphous silicon technology, our approach has important benefits compared to previous works. Most light-trapping strategies proposed for amorphous silicon cells have been focused on nanopatterned back contacts as the works already mentioned [47, 144]. Growing the junction on a patterned substrate can lead to an increase of surface recombination as well as the creation of cracks which induce shunt currents through the cell [35, 146]. In our front-side approach, efficient light-trapping is achieved while keeping a flat absorber layer. Besides, our design is based on an ultra-thin (thickness = 90 nm) a-Si:H p-i-n junction. The open-circuit voltage and fill factor values we have used to estimate the conversion efficiency were extracted from a work on a patterned back contact approach. We expect an increased open-circuit voltage compared to this value as well as a better stability to light-induced degradation because of the thinner intrinsic layer. Last but not least, our approach uses the patterned

metallic layer both as a light-trapping scheme and as an alternative front contact. It allows us to use non doped front layers (SiN_x in our study) and therefore reduce optical losses due to free carrier absorption. As for the optical design of the cell, it offers an additional degree of freedom for the choice of the embedding layer.

In my PhD, we have only considered single-junction a-Si:H solar cells for the sake of simplicity but the proposed designs could be applied to more complex devices with additional optimization. For instance, let us consider a tandem a-Si:H/µc-Si:H device. The standard solution to achieve current matching is to use an intermediate reflecting layer between the top a-Si:H and the bottom µc-Si:H cells. Higher performances could be reached with a light-trapping structure in the front surface of the a-Si:H cell in order to increase the short-circuit current density in the top cell. In this case, the light-trapping scheme will be seen only by the top cell since the bottom cell absorbs long wavelength photons that are transmitted through the a-Si:H top cell. The grating would act mainly on the blue photons. First, the parameters of the metallic grating as well as the thickness of the a-Si:H junction have to be optimized to achieve the desired value of J_{SC}. Then, the thickness of the microcrystalline junction is chosen to match the current.

The nanopatterned resonant front contact concept can also be applied to other thin film materials. In the framework of this thesis, we have worked on the extension of this design to GaAs ultra-thin layers. We present our proposal for 2D nanogrids for ultra-thin GaAs devices in PART 3.

6.7 SUMMARY

We have presented the design of an ultra-thin (thickness = 90 nm) a-Si:H solar cell with a 1D silver grating used as a front contact. We have shown that the combination of vertical Fabry-Perot resonances and coupling to guided modes in the a-Si:H layer leads to a broadband absorption spectrum with low polarization and angular dependence.

Our design is based on a patterned metallic layer which:

- strongly confine light in an ultra-thin and flat a-Si:H layer
- plays the role of an alternative front contact with reduced sheet resistance and similar transparency compared to conventional electrodes.

This versatile approach can be applied to different solar cells materials and geometries of the electrode. It opens new possibilities for transparent electrodes with high conductivity and optical transmittance.

7

EXPERIMENTAL RESULTS ON ULTRA-THIN AMORPHOUS SILICON SOLAR CELLS

Contents

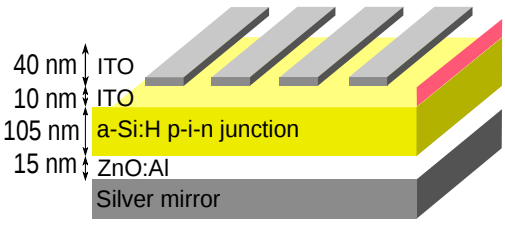

Figure 46: Schematic of the ultra-thin a-Si:H solar cells fabricated.

Ultra-thin amorphous silicon demonstrators with patterned metallic layers have been fabricated to validate experimentally the multi-resonant approach developed in *chapter 6*. The fabricated structure is depicted in Fig. 46. The experimental structures described in this chapter do not correspond exactly to the designs studied numerically in the previous chapter. In particular, the thicknesses and refractive indices are slightly different, and the collection in the front surface of the cell is ensured with a conventional ITO layer instead of the alternative Si_3N_4 (Ag) transparent electrode. The mismatch between modeled and fabricated structures will be discussed further in subsection 7.2.1.

7.1 FABRICATION PROCESS

7.1.1 *Overview of the process flow*

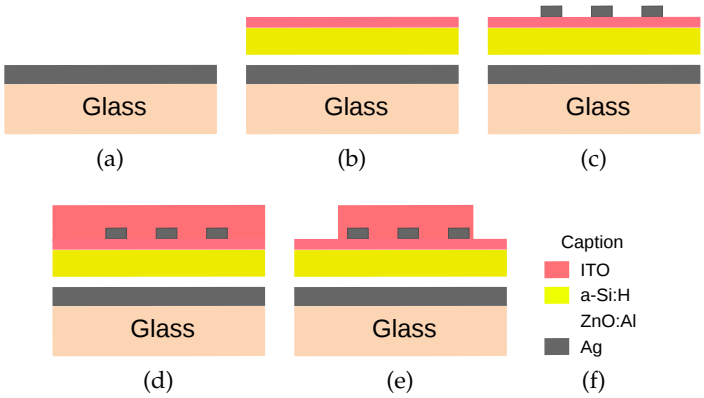

Figure 47: Overview of the fabrication process.

Figure 47 shows the main steps of the fabrication process:

A. Deposition of the back silver mirror on a glass substrate (Fig. 47a)

B. Deposition of the n-i-p junction and the spacing layers (Fig. 47b)

C. Nanopatterning of the metallic grating (Fig. 47c)

D. Deposition of the ITO front contact (Fig. 47d)

E. Insulation of the devices[1] (Fig. 47e).

Steps A, C and E were performed at LPN, steps B and D at LPICM. The different stages of the fabrication process are developed in detail in the following.

7.1.2 *Deposition of the back mirror*

In the design we proposed, the solar cells are in a substrate configuration. The first fabrication step is to place the back mirror, the metal chosen is silver because of its optimal reflectivity. The 400 nm-thick silver layer is deposited on a glass substrate (Corning) using an electron beam evaporator (PLASSYS MEB 550 SL). We use a 10 nm-thick chromium layer to improve the adhesion of silver on glass. We have studied the texture of the as-deposited silver surface through SEM and AFM (Atomic Force Microscopy) measurements as shown in Fig. 48. The surface roughness can be characterized by:

- the maximum peak-to-valley height of the profile R_t: difference between the highest peak and the lowest valley of the surface

1 Step E aims at insulating all the devices patterned on the same sample.

- the root mean squared roughness RMS: root mean squared average of the roughness profile.

Using the AFM measurements, we found $R_t \sim 14$ nm and RMS ~ 2.8 nm: the silver layers are flat with low surface roughness compared to the silver layer thickness. We coat a resist layer on the mirror shortly after silver plating in order to prevent formation of silver sulfides and oxides. This protective coating is removed in an acetone bath just before deposition of the ZnO:Al spacing layer.

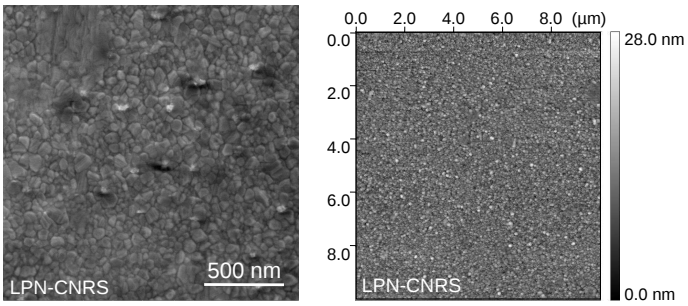

(a) (b)

Figure 48: SEM (a) and AFM (b) images of the surface of the silver back mirror.

7.1.3 *Amorphous silicon deposition technique*

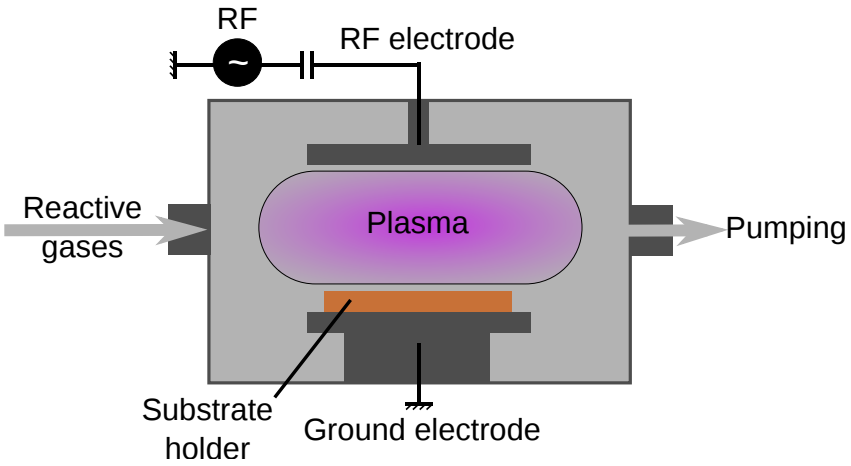

Figure 49: Schematic of the PECVD "ARCAM" reactor used for a-Si:H deposition (see Ref.147 for more details).

The most used technique for a-Si:H deposition is plasma enhanced chemical vapor deposition using a *radio frequency* (RF) glow discharge. The deposition of the a-Si:H junction is done at LPICM in the ARCAM reactor, described in Ref. 147. ARCAM is a multi-plasma monochamber capacitively-coupled RF-PECVD reactor. Figure 49 shows the structure of the reactor. A RF-voltage with a frequency of 13.56 MHz is applied between the RF and the ground electrodes,

creating an electric field in the deposition chamber. The electrical source is a Nextral RF generator coupled to the electrodes with a matching box. The RF power is between 0 and 25 W when matched with a 50 Ω load. The space between the two electrodes is filled with a mixture of the reacting gases, SiH_4 and H_2 in the case of hydrogenated amorphous silicon deposition. The dissociation of silane results in the deposition of a-Si:H material on the ground electrode where the substrate is placed.

The main advantages of the ARCAM reactor are:

1. a low temperature deposition ($< 200°C$)
2. a precise control of the deposition parameters: gas flow rates, gas pressure, RF power and substrate temperature
3. the possibility of doping (with phosphine or diborane) or alloying (a-SiGe:H, a-SiC:H) in the same plasma chamber.

Note that the hydrogen content has crucial consequences on the nature and the quality of the deposited material. Several works from LPICM showed that the formation of silicon clusters and nanocrystals in the plasma could be controlled in order to deposit various silicon materials from amorphous to microcrystalline or even epitaxial crystalline silicon [148–150].

In our case, the first deposited layer is the 10 nm-thick n-doped layer obtained by dissociation of a mixture of silane and diborane. The intrinsic a-Si:H layer (80 nm) is then deposited followed by a 15 nm-thick layer of a boron-doped silicon-carbide alloy (p-aSiC:H). The two spacing layers (15 nm of ZnO:Al and 10 nm of ITO) are deposited by sputtering at LPICM.

7.1.4 *Nanopatterning of the silver grating*

The nanopatterning of the silver grating is one of the most critical stages of the fabrication process. The size and period of the metallic grating must be controlled to ensure an optical response of the structure corresponding to the one modeled. The fabrication of the metallic array is done by lithography.

The word lithography comes from the Greek words *lithos* (= stone) and *graphein* (= write). In order to write patterns at a small scale, several lithography methods have been developed. In photolithography, a collimated beam of photons illuminates a photosensitive substrate through a mask. The replica of the mask appears onto the substrate after development of the resist. The photolithography technique used at LPN enables the realisation of patterns with a size down to 500 nanometers. To obtain 80 nm-wide nanostrips (as in our case), we need another technique. The main techniques yet used for nanopatterning are the electron beam lithography (EBL), nanoimprint lithography (NIL), and holographic lithography. Bottom-up techniques such as colloidal lithography are also used with good performances.

At LPN, the two sub-100 nm lithography techniques available are EBL and NIL. In the case of EBL, the pattern is created by controlling the electron beam as it scans the sample, the mask is virtual. The main disadvantage of EBL is the

time and cost of a single lithography run which limits the patterned area. NIL is a powerful nanolithography method which allows low-cost structuration on a large area with high resolution. However, if we want to imprint a new pattern, we have to make new master and mold. In our process, it is important to be able to adapt the pattern between two samples. Therefore, we have chosen e-beam lithography.

As shown in Fig. 50, the patterning process using EBL is done in four steps, which are described below:

A. Electron beam lithography of the PMMA resist (Fig. 50a)

B. Resist development (Fig. 50b)

C. Metal deposition (Fig. 50c)

D. Lift-off of the resist (Fig. 50d).

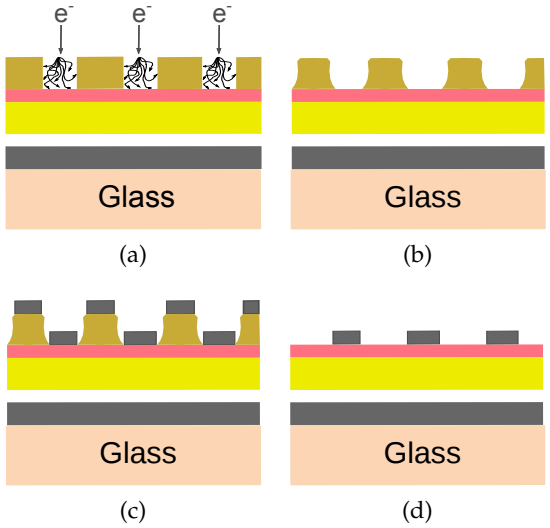

Figure 50: Schematic of the patterning of the metallic layer step by step.

7.1.4.1 *Electron beam lithography*

EBL relies on an energy transfer process between the electrons of the incident beam and the atoms of the material to be structured. Prior to electron-beam exposure, the sample is coated with an electron-sensitive resist. Two types of resist are distinguished:

- *positive:* in the areas exposed to the electron beam, the polymer breaks into smaller fragments that can be dissolved in a specific solvent called developer.
- *negative:* the polymer areas exposed to the electron beam become insoluble. The unexposed areas can be dissolved in the developer.

A side effect of the EBL process is the scattering of the electrons in the resist [151]. Two types of scattering occur in the material. First, elastic collisions between the incoming electrons and atoms lead to a continuous change of direction when passing through the exposed material. Second, after penetrating in the substrate, secondary electrons can travel back in the resist: this phenomenon is called back scattering. As a result, the profile of exposure dose combines two Gaussians:

- the first one due to primary electron flux is very intense and has a size close to the initial spot (initial size $\sim$ 20 nm)
- the secondary flux due to back scattering is less intense and much broader (a few microns).

The initial flux has to be set so that the incoming electron flux is mostly due to primary electrons. A main consequence of the secondary electron flux is the so-called proximity effect. The exposure dose of a specific pattern may be affected by the scattering of secondary electrons coming from the exposure of a neighbouring pattern. As a consequence, the effective exposure dose can be higher in the centre of the exposed area than on the edges. Several techniques have been developed to correct the proximity effect such as the dose correction. As for our process, we resize the patterns to a value lower than the nominal size in order to take into account the broadening of the beam.

There is a large number of parameters controlling the EBL process: exposure dose, resist material, resist thickness, developer, development temperature and time[2]. In our process, we use PMMA (polymethylmethacrylate), a high-resolution positive electron-sensitive resist. We have fixed the developer as well as the development temperature. Several tests were made varying the other parameters. It is noteworthy that the exposure and development parameters are interrelated. For higher exposure doses, the average fragment size decreases as the solubility in the developer increases [152].

A preliminary study was done to choose the optimal exposure dose following two criteria: the shape and size of the patterns. In Fig. 51, examples of metallic particles patterned on an a-Si:H layer with EBL are shown after metal deposition and lift-off of the resist. Fig. 51a corresponds to a dose of 1200 $\mu C/cm^2$, Fig. 51b to 500 $\mu C/cm^2$ and Fig. 51c to 350 $\mu C/cm^2$. When the exposure dose is too high, the exposed area is much larger than desired, hence the resulting patterns[3] are bigger and have a lower resolution (see Fig. 51a). On the contrary, if the sample is underexposed (see Fig. 51c), the lack of resolution in the pattern shape leads to a continuous metal deposition in some parts of the metal lines making thereby the lift-off of the resist impossible. In our case, the nanoparticles had a nice square shape for doses between 500 and 700 $\mu C/cm^2$. We have finally chosen an exposure dose of 500 $\mu C/cm^2$ in order to obtain the right dimensions for the patterns.

2 See Ref. 152 for a detailed explanation about the importance of all the parameters.

3 In the case of overexposure, the pattern is defined by the Gaussian distribution of secondary electrons, hence the round shape oberved in Fig. 51a.

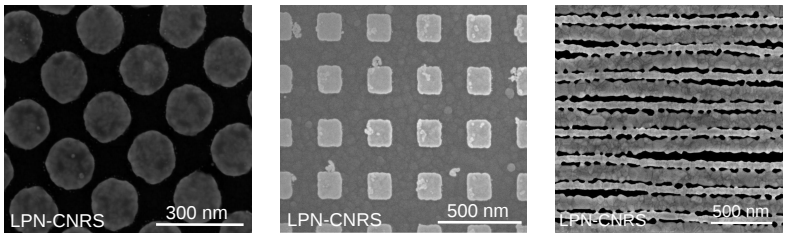

(a) (b) (c)

Figure 51: SEM images of 2D (a, b) and 1D (c) metallic nanoparticles patterned on a-Si:H with EBL for a varying exposure dose: 1200 $\mu C/cm^2$ (a), 500 $\mu C/cm^2$ (b) and 350 $\mu C/cm^2$ (c).

We use a commercial PMMA resist (A5 from MicroChem), spin coated at 4000 rpm during 30 s and prebaked in an oven at 160°C during 80 min. In these conditions, the resist layer has a thickness around 250 nm. The e-beam lithography is done with a VISTEC EBPG 5000 equipment. The sample was exposed with a dose of 500 $\mu C/cm^2$. The mask used for EBL is made of arrays of 1D or 2D particles with varying period and size.

7.1.4.2 *Resist development*

We use a mix of methyl isobutyl ketone (MIBK) and isopropyl alcohol (IPA) solvents as a developer. The solution temperature is kept constant at 20° C with a thermostatically controlled water bath. The resist is developed by immersion in a 3 : 1 IPA:MIBK solution for 75 s and rinsed in IPA for 10 s. The sample is then blow dried with nitrogen. The development step duration is critical. The resist profile must be as sharp as possible to ensure a good lift-off of the resist at step D. The resist profile is the result of both optimal exposure and development conditions.

7.1.4.3 *Metal deposition*

The 20 nm-thick silver layer is deposited by electron beam evaporation (PLASSYS MEB 550 SL) with a Ge nucleation layer (1 nm deposited with a rate of 0.01 nm/s) to improve the surface texture. Indeed, Logeeswaran et al. [153] showed that thin silver films ($10-20$ nm) deposited with Ge nucleation layers ($1-2$ nm) exhibited over an order of magnitude improvement in the RMS roughness (from $6-8$ nm to 0.6 nm for a 1 nm-thick Ge layer). Before metal deposition, a short ion beam etching is done in situ to improve the adhesion of the metal on the substrate.

7.1.4.4 *Lift-off of the resist*

The last step of metal patterning is the removal of the resist and the metal deposited above. To do so, the sample is immersed in a trichloroethylene solution heated at 80°C with soft magnetic stirring for at least one hour. The sample

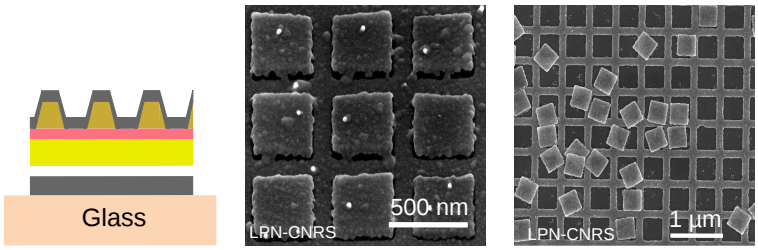

(a) (b) (c)

Figure 52: (a, b) Schematic (a) and SEM image (b) of a case where the lift-off of the resist is impossible because of a continuous metal deposition. (c) SEM image of a case where the lifted off particles (resist + metal) redeposited on the surface. The SEM images (b, c) presented here correspond to 2D silver grids patterned on ultra-thin GaAs layers (see PART 3, *chapter* 9).

is then rinsed with cold trichloroethylene, acetone and isopropyl alcohol and blow dried with nitrogen.

The resist thickness is a key parameter of the EBL process and in particular, of the lift-off step. The resist profile depends on the exposure dose and the development duration and in optimal cases, it looks like Fig. 50c. If the resist thickness is not sufficient, the metal deposition does not show abrupt interfaces at the edges of the resist patterns. In this case, the solvent cannot reach and dissolve the resist as shown in Figs. 52a and 52b. Usually, the resist layer is chosen to be at least $2-3$ times thicker than the metal layer. In our case, the PMMA thickness is around 250 nm, which is more than sufficient to lift off the 20 nm-thick silver layer. SEM images of successful patterning processes are shown in Figs. 53a and 53b.

Another major problem that can happen during the lift-off process is the redeposition of metal particles. As can be seen in Fig. 52c, the lifted off particles (resist + metal) can get reattached onto the surface. In this case, it is very difficult to wash them off once the sample has dried. To prevent redeposition, we have fixed vertically the sample with a clamp and the lift-off is done on a hot plate with a magnetic stirrer. Ideally, the sample should be placed horizontally with the side with the surface to be lifted upside down so that the resist fragments should fall at the bottom of the beaker.

7.1.5 *Sputtering deposition of the ITO front contact*

The ITO front contact layer (thickness $=$ 40 nm) is deposited by sputtering. Figure 54 displays SEM images of 1D (Fig. 54a) and 2D (Fig. 54b) gratings after ITO deposition. We see that the ITO layer is too thin to be planar. The structuration of ITO due to the nanopatterning of silver should impact the optical response of the structure at short wavelengths. We have studied further the ITO surface with AFM measurements. Let us consider the example of a 1D silver grating with a period of 500 nm and a width of 250 nm (see Fig. 55a). We have extracted the surface profile of the grating embedded in ITO from the AFM

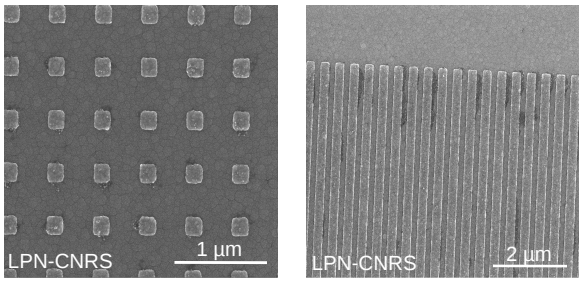

(a) (b)

Figure 53: SEM images of patterned metallic layers after lift-off of the resist: 2D silver particles (period = 500 nm, width = 150 nm) (a) and 1D silver wires (period = 400 nm, width = 200 nm) (b).

measurements as shown in Fig. 55b. The profile is quite regular with an average height of 40 nm between the baseline and the top of the nanostructures. The nanopatterns are slightly broadened compared to the metallic wires. Besides, as can be also seen on Fig. 54, the ITO layer is rough on the nanopatterns. AFM measurements were done on the ITO layer outside of the patterned areas to evaluate the surface roughness and we obtained a RMS roughness value around 10 nm.

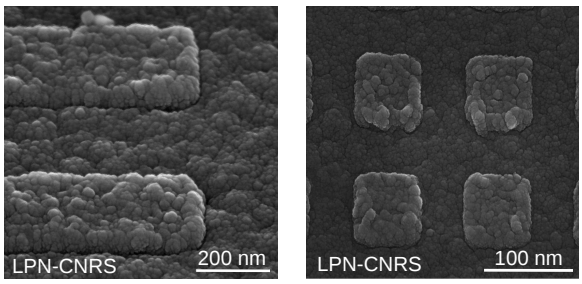

(a) (b)

Figure 54: SEM images of 1D (a) and 2D (b) patterned metallic layers after deposition of the ITO front contact.

7.1.6 *Insulation of the devices*

We patterned multiple cells with varying areas and grating parameters on the same sample and we needed therefore to insulate electrically the different devices. To do so, we chose to etch the ITO front layer between the patterned areas by ion beam etching (IBE). Figure 56 describes the insulation process step by step:

A. Spin coating of the photosensitive resist (AZ5214) (Fig. 56a)

B. UV photolithography (Fig. 56b)

C. Resist development with AZ MIF 726 developer (Fig. 56c)

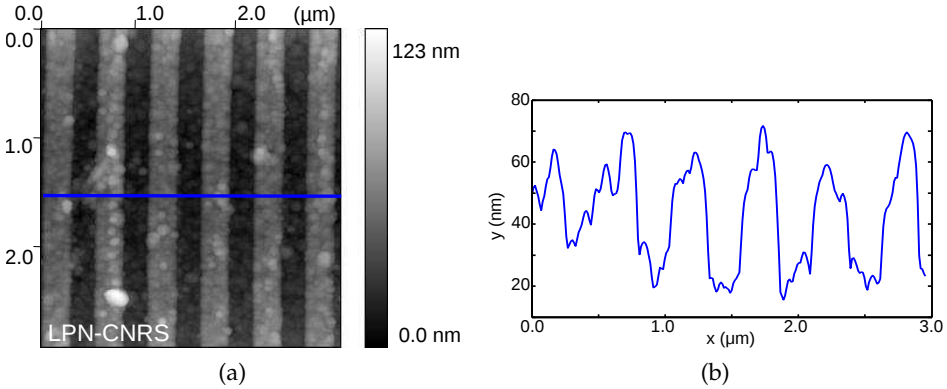

Figure 55: Study of the structure after ITO deposition: AFM image (a) and extracted profile (b) of a 1D pattern (period = 500 nm, width = 250 nm).

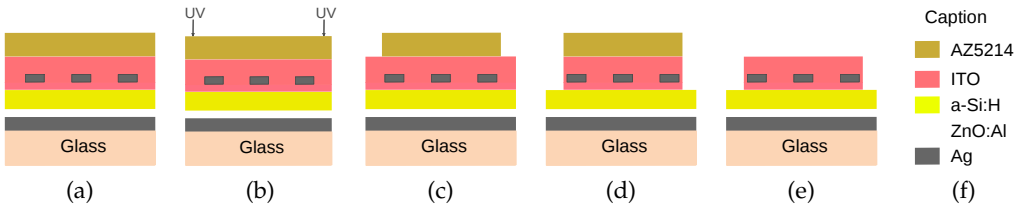

Figure 56: Description of the insulation of the devices step by step.

D. Ion beam etching of ITO (Fig. 56d)

E. Removal of the resist with acetone (Fig. 56e).

We use a photosensitive resist layer as an etching mask and the areas to be etched are defined by UV photolithography. We control the etching depth during the IBE process by following the composition of the etched layer with mass spectrometry. Figure 57 shows a SEM image of the etching profile. We see that we have etched down to the a-Si:H layer.

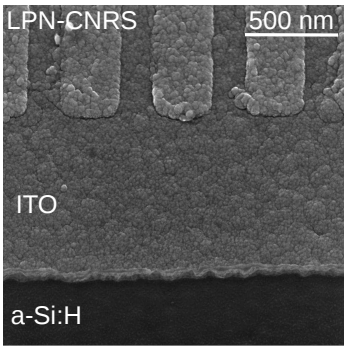

Figure 57: SEM image of the sample after etching of the ITO front contact.

7.2 OPTICAL CHARACTERIZATION OF THE FABRICATED DEVICES

At the end of the process described in section 7.1, we obtained 38 cells with varying areas (1, 4 or 16 mm^2) on the sample (total area: 2.5 cm $\times$ 2.5 cm). In the following, we will define each cell by the geometrical parameters of the metallic grating (grating period and fill factor). The fill factor ff is defined as the ratio of the particle width w over the grating period p[4]. Among the fabricated cells, only 12 cells could be optically characterized. In other cases, the lift-off of the resist was not successful in particular for patterns with a high fill factor. The geometrical parameters of the grating were measured by SEM. Two cells were not patterned in order to provide a reference to assess the effects of light trapping due to the grating.

7.2.1 *Modeling of the fabricated cells*

As already mentioned, the fabricated structures show several differences with respect to the design proposed in chapter 6. First, the total thickness of the deposited n-i-p junction is 105 nm instead of 90 nm for the structure optimized with numerical calculations. This thickness mismatch should have an influence on the absorption peaks attributed to Fabry-Perot resonances. A spectral redshift of the resonance wavelength is expected when the a-Si:H thickness increases.

Second, ellipsometry measurements were performed at LPICM to determine the optical constants and the thickness of the deposited a-Si:H material. Fig. 58 displays the real and imaginary parts of the a-Si:H index used in the calculations (from older LPICM data) (blue curve) compared to the measurements on the material deposited (green curve). We see that the two refractive index values differ significantly (Fig. 58a). For instance, the increase of n_s at short wavelengths should cause a redshift of the resonances. As for the extinction coefficient (Fig. 58b), the bandgap wavelength of the material deposited, i.e the wavelength value when $k = 0$, is lower than modeled in the calculations. We find that $\lambda_{g\,exp} \sim 720$ nm. On the whole spectral range ($300 - 800$ nm), $k_{exp} < k_{modeled}$ which means that the absorption coefficient of the deposited a-Si:H material is lower than expected.

In conclusion, the numerical calculations already done could not be directly compared to the experimental results. Therefore, a new structure had to be defined to model the experimental data. To do so, we have considered the response of the non structured cells. The thickness of the top ITO layer h_{ITO} and the total thickness of the a-Si:H junction h_s have been adjusted to fit the absorption curves starting from the nominal values $h_{ITO} = 50$ nm and $h_s = 105$ nm. The best curve fitting was obtained for the following structure: ITO/a-Si:H/ZnO:Al/Ag with the thicknesses $h_{ITO} = 50$ nm, $h_s = 100$ nm and $h_{ZnO:Al} = 15$ nm. The 400 nm-thick back mirror is considered as a semi-infinite silver layer

4 Note that the fill factor ff has the same definition for one-dimensional and two-dimensional patterns since it is a linear fill factor.

with optical constants taken from Johnson and Christy [143]. Ellipsometry measurements were done to determine the optical constants of the 15 nm-thick p-doped a-Si:H layer (see Appendix B). In the following, we present the results of optical measurements done on the fabricated cells and compare them to the calculations.

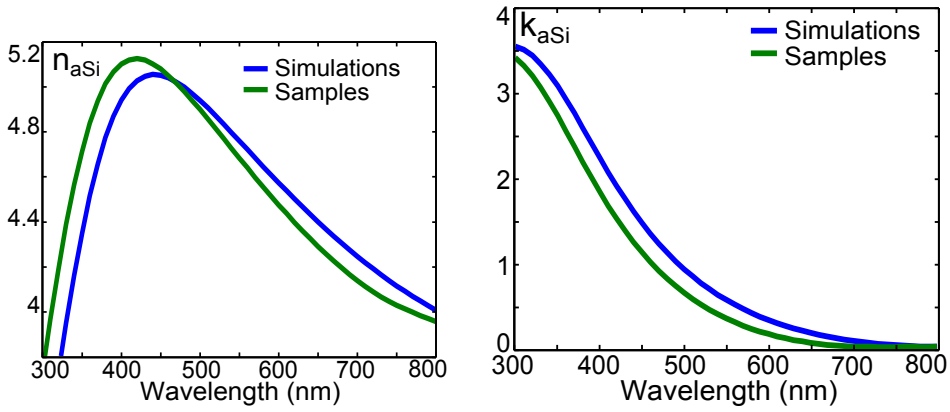

(a) (b)

Figure 58: Ellipsometry measurements of the refractive index Re(n) (a) and the extinction coefficient Im(n) (b) of amorphous silicon. The data used for the numerical calculations presented in *chapter* 6 (blue curve) are compared to the measurements done on the fabricated cells (green curve).

7.2.2 *Reflectivity measurements and comparison to the calculations*

The reflectivity R of the different cells has been measured using the experimental setup GonioVISIR described in *chapter* 4, section 4.1. Given that there is no light transmission through the silver mirror, the total absorption in the structure A is obtained by: $A = 1 - R$. Figure 59 displays the total absorption at $\theta = 5°$ (plane of incidence perpendicular to the wires) of a 4 mm^2 cell with an array of silver wires (thickness = 20 nm, period = 500 nm, fill factor = 0.38) for TE (green curve) and TM (orange curve) polarizations. The measured response of a non structured reference cell is shown in black dashed line for the sake of comparison.

Without any structuration, only two broad absorption peaks (P_1 and P_2) due to vertical Fabry-Perot resonances in the multilayer stack are exhibited. The response of the patterned cell also shows the absorption peaks P_1 and P_2 observed for the reference cell. In addition, the spectra of the patterned cell under both TE and TM polarizations exhibit multiple absorption peaks achieving light trapping in the high-wavelength range. Unfortunately, we see that most of these peaks are located above the bandgap wavelength (shown in grey in Fig. 59) and thereby do not contribute to the generation of carriers.

We have calculated the optical response of the corresponding model structure ITO(Ag)/a-Si:H/ZnO:Al/Ag with $h_{ITO} = 50$ nm, $h_m = 20$ nm, $h_s = 100$ nm and $h_{ZnO:Al} = 15$ nm (as defined in the previous subsection). As shown in

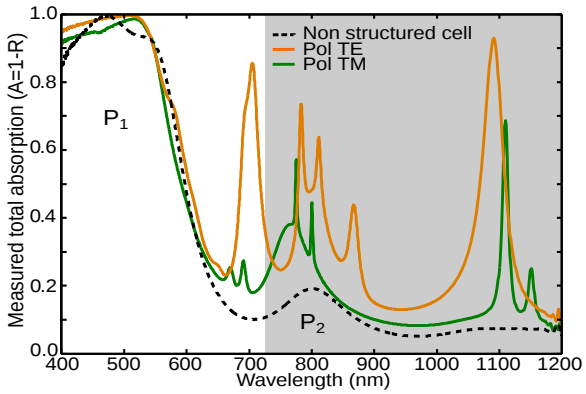

Figure 59: Measured total absorption ($A = 1 - R$) spectra of ultra-thin a-Si:H cells with a 1D silver grating ($p = 500$ nm, $ff = 0.38$) for an excitation at $\theta = 5°$ with a TE (green) and TM (orange) polarized light compared to the response of non structured cells (black dashed curve). The bandgap of the a-Si:H material is shown in grey.

subsection 7.1.5, sputtering leads to an ITO deposition conformal to the grating profile. However, for the sake of simplicity, we have assumed a planar top interface ITO/air. The measured absorption spectra are in good agreement with the calculations as shown in Fig. 60 (blue curve) for TE (Fig. 60a) and TM (Fig. 60b) polarizations.

In order to perform a more detailed analysis of the measured optical response, we have numbered all the absorption peaks exhibited on the experimental spectra (in addition to the broad P_1 and P_2 peaks already mentioned above), i.e 6 peaks for TE and TM polarizations. All peaks are in good agreement with the calculations with a slight spectral shift for TM polarization. The attribution of these peaks in both polarizations is further discussed in the following.

7.2.3 *Study of the angular dependence*

We have used the GonioVISIR setup described in *chapter* 4, section 4.1 to investigate the evolution of the absorption spectrum as a function of the angle of incidence. Reflectivity measurements were done on the same cell as in the previous subsection ($p = 500$ nm and $ff = 0.38$) for an angle of incidence θ varying from 5 to 60°, with a measurement every 5°. The results are shown in Fig. 61 for TE (Fig. 61a) and TM (Fig. 61b) polarizations. Different behaviors are evidenced. The first type of high absorption bands ($\lambda \sim 500$ nm and $\lambda \sim 700$ nm) does not depend on the angle of incidence. The spectral position of these peaks is shown with vertical black dashed lines in Fig. 61. These bands are attributed to vertical Fabry-Perot resonances in the stack (peaks P_1 and P_2). Note that the absorption band corresponding to P_2 does not appear clearly for both TE and TM polarizations because of its low intensity.

Second, several absorption peaks have a dispersive behavior as a function of the angle of incidence θ. As developed in chapter 6, subsection 6.2.3, it corre-

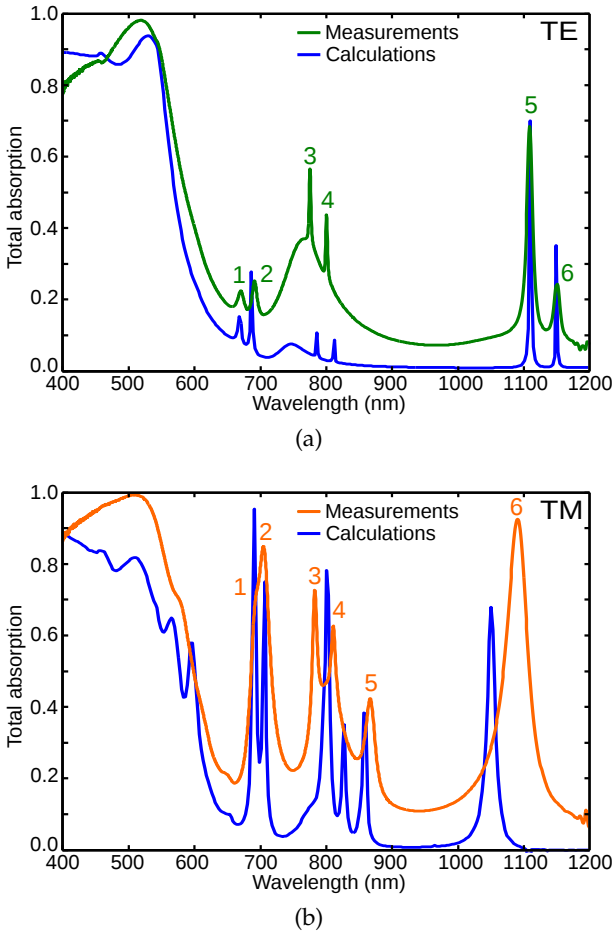

Figure 60: Measured absorption spectra of ultra-thin a-Si:H cells with a 1D silver grating (p = 500 nm, ff = 0.38) for an excitation at $\theta = 5°$ with a TE (a) and TM (b) polarized light compared to numerical calculations (blue curves).

sponds to the excitation of guided modes via grating coupling. We have considered an ITO (50 nm)/a-Si:H (100 nm)/ZnO:Al (15 nm)/Ag waveguide. Figure 62a displays the effective index real part of the guided mode for both polarizations. We find one mode for TE polarization (green curve) and two modes for TM polarization (blue and red curves). As displayed in Fig. 62, we have plotted the profiles of the electric field intensity $|E|^2$ (TE, Fig. 62b) and the magnetic field intensity $|H|^2$ (TM, Figs. 62c and 62d) in the structure[5]. The excitation wavelength is $\lambda = 1$ µm for transverse electric polarization and $\lambda = 600$ nm for transverse magnetic. For TE polarization, the electric field is clearly confined within the a-Si:H layer. This is consistent with the attribution of this mode to the coupling of incident light with diffracted modes. For TM polarization, we see that the two modes combine a guided mode localized in the a-Si:H layer and a surface plasmon mode at the Ag/ZnO:Al interface. The coupling between the guided mode and the surface mode seems weaker in the case of mode 2.

5 The electromagnetic fields intensity profiles are displayed for a different a-Si:H thickness value (h_S= 105 nm). The induced variation of the effective index does not change the observations about the nature of the modes.

We have also calculated the dispersion relation of the guided modes and plotted the curves $\theta = f(\lambda)$ shown in Fig. 61 (white plain and dashed lines for TE polarization; white plain and green dashed lines for TM polarization). It is in good agreement with the experimental results. Note that each guided mode gives rise to two absorption peaks because of the oblique incidence ($\theta \neq 0°$). We find that for a TE polarization, peaks 3 and 4 correspond to the coupling to the diffracted order $m = \pm 2$ and peaks 5 and 6 to $m = \pm 1$ (see Fig. 61a). Note that the intensity corresponding to the second-order diffraction is much lower than the first-order one as expected.

For a TM polarization, peaks 3 and 5 can be attributed to the mode 1 with $m = \pm 2$ (see Fig. 61b). The second mode also leads to two absorption peaks ($m = \pm 1$) at shorter wavelengths (peaks 1 and 2). It is noteworthy that for TM polarization, there are two additional absorption peaks with a slight dependence on the angle of incidence at $\lambda \sim 800$ nm (peak 4) and $\lambda = 1.1$ µm (peak 6). These resonances will be discussed in the following.

7.2.4 *Influence of the grating parameters for TE polarization*

Through the study of the angular dependence, we have already managed to identify the absorption mechanism corresponding to most of the absorption peaks as summarized in Table 8. In order to obtain additional information about the other peaks, we have investigated the influence of the grating parameters on the optical response of the cell as presented in this subsection.

Light polarization	Absorption peak	Attribution
TE and TM	P_1	Fabry-Perot resonance
TE and TM	P_2	Fabry-Perot resonance
TE	3, 4; 5, 6	Guided modes
TM	1, 2; 3, 5	Guided modes

Table 8: Summary of the analysis of the measured absorption spectra (see Fig. 60 for the peaks notations).

7.2.4.1 *Reflectivity measurements on the MicroVISIR setup*

We have measured the total absorption of 1D patterned cells with varying period and fill factor using the experimental setup MicroVISIR described in *chapter 4*, section 4.2. Some of the cells to be measured had a surface of 1 mm^2 and were therefore too small to be characterized on the GonioVISIR setup. In this section, we study the response only for a TE polarization for the sake of clarity.

The switch from GonioVISIR to MicroVISIR leads to a slight variation in the absorption intensity of the peaks and to a lower resolution of the peaks. For instance, let us consider the structure with a 1D silver grating with $p = 500$ nm and $ff = 0.38$. The measured absorption spectra of this structure are displayed in Fig. 60a (green curve) for the GonioVISIR setup and in Fig. 63a (purple curve)

for the MicroVISIR setup. If we consider the long wavelength range, we see that peaks 5 and 6, well defined in Fig. 60a, lead to a broad feature between 1 µm and 1.1 µm in Fig. 63a. Likewise, we cannot distinguish the peaks 3 and 4 from the broad Fabry-Perot peak P_2. As a matter of fact, because of the achromatic Cassegrain objective, we do not measure the response at normal incidence but the response corresponding to the convolution of angles between 12 and 26°. In the following, the denomination "at normal incidence" means that the sample is normal to the optical axis and not that $\theta = 0°$. Due to the low angular resolution, the results presented in this subsection are discussed only on a qualitative point of view.

Figure 63 shows the measurement results for two grating periods $p = 500$ nm (Fig. 63a) and $p = 400$ nm (Fig. 63b) and a varying fill factor. For $p = 500$ nm, for each fill factor value, dashed and plain lines show measurements done on two different cells with the same nominal grating parameters. The peaks positions are in very good agreement showing that the fabrication process is robust.

7.2.4.2 *Influence of the grating period*

We have extracted from Fig. 63 the measured spectral position of the different resonances in order to study their shift as a function of the grating parameters. The result is plotted in Fig. 64 for grating periods $p = 500$ nm and $p = 400$ nm. We find that there is a slight blueshift of the whole absorption spectrum when the fill factor increases. It is noteworthy that because of the few number of points (only three different fill factor values), we cannot extract accurate conclusions about the evolution of the spectrum as a function of the fill factor.

However, Fig. 64 also allows us to study the evolution of the absorption spectrum when the grating period varies while keeping a constant fill factor. There is no significant influence of the grating period for all peaks except peaks 5 and 6. The plots corresponding to peaks P_1 and P_2 for $p = 500$ nm (plain line) and $p = 400$ nm (dashed line) almost match perfectly, as expected for Fabry-Perot resonances.

For peaks 5 and 6, the resonance wavelength shifts dramatically ($\sim$ 100 nm shift) towards lower wavelengths when period decreases from 500 to 400 nm. This is consistent with Eq. (32) (see *chapter* 6, subsection 6.2.3) which implies that the wavelength resonance should decrease when the period decreases.

Besides, according to the same equation, the dependence of the resonance wavelength on the period is weaker in the case of coupling to higher diffracted orders. Peaks 1 and 2 exhibit only a slight blueshift when period decreases. In the previous subsection, we have attributed peaks 5 and 6 to coupling to diffracted orders $m = \pm 1$ and 3 and 4 to coupling to diffracted orders $m = \pm 2$. Peaks 1 and 2 should therefore correspond to higher diffracted orders ($m = \pm 3$ or higher). We have not been able to do a more detailed study of peaks 1 and 2 because of their low intensity.

7.2.5 *Long wavelength resonances for TM polarization*

We have not yet attributed peaks 4 ($\lambda \sim 800$ nm) and 6 ($\lambda \sim 1.05$ μm) exhibited on the absorption spectrum at long wavelengths in TM polarization (see Fig. 60b) (excitation at $\theta = 5°$). As shown in Fig. 61b, these peaks have a slight dependence on the angle of incidence but cannot be attributed to the coupling of incident light with diffracted orders. Let us look at the spatial distribution of the electric and magnetic fields in order to extract additional information about these two resonances.

Figure 65 displays the electric field $|E|^2$ and magnetic field $|H|^2$ maps for an excitation at $\lambda_4 = 800$ nm (Figs. 65a and 65b) and $\lambda_6 = 1.05$ µm (Figs. 65c and 65d) under TM polarization (excitation at $\theta = 5°$). The attribution of peak 4 is quite difficult since both the electric and magnetic field maps are complex. As shown in Fig. 61, this peak position has a clear dependence on the angle of incidence. However, it is difficult to distinguish from peaks P_2, 3 and 5.

As for peak 6, it shows only a slight angular dependence. The map of the magnetic field $|H|^2$ (Fig. 65d) shows a very strong field confinement below the silver wires. It is very similar to the magnetic field intensity profiles reported by Pala et al. [154] in the case of silver wires on a SiO_2/Si system. They have attributed this confinement to localized surface plasmon resonances of the wires.

Note that in our case, these resonances do not contribute to the generation of current since they are beyond the bandgap wavelength. They lead to absorption losses in the metallic parts (grating and back mirror) and the spacing layers (ITO and ZnO:Al).

7.3 CONCLUSION

In this chapter, we have presented the fabrication process successfully developed to fabricate nanopatterned a-Si:H cells with a one-dimensional silver grating. We have investigated the evolution of the measured absorption spectrum as a function of the angle of incidence and the geometrical parameters of the grating. This experimental study validates the multi-resonant approach proposed in *chapter* 6. Indeed, we have shown that this system exhibits resonances with very different absorption mechanisms:

- Fabry-Perot resonances
- Coupling to guided modes
- Localized surface plasmon resonances.

This approach based on the combination of multiple electromagnetic modes can be applied to other materials. In particular, within the silicon technology, resonant metallic nanostructures offer perspectives for light-trapping within tandem a-Si/µc-Si cells as discussed in *chapter* 6, section 6.6 but also silicon-based alloys such as SiGe or SiC.

Another important result is that the characterization of this particular system has highlighted the complementarity of the two experimental setups that we

have developed and presented in *chapter* 4. The GonioVISIR setup has enabled to evidence the coupling to diffracted orders thanks to the high resolution of the peaks. Despite its lower spectral resolution, the MicroVISIR setup allows to characterize even the smallest devices and in our case, to give information about the influence of the grating parameters on the optical response.

Finally, the fabricated structure did not match with the design optimized with numerical calculations and presented in *chapter* 6. In particular, the optical constants of the a-Si:H material were different. As a consequence, most of the observed resonances were localized above the bandgap wavelength. This work shows that controlling the properties of the material deposited is critical in order to achieve efficient light trapping. It is therefore crucial to perform optical simulations hand in hand with advanced material characterization.

It is noteworthy that we have not presented any electro-optical measurements in this chapter. As a matter of fact, we have managed to perform I-V measurements on only two cells. The obtained experimental data are not fully understood yet. Because of the difficulty to obtain a material with the good optical properties (as mentioned above), we have not worked further to obtain devices that would generate current.

7.4 SUMMARY

Ultra-thin a-Si:H solar cells with 1D patterned silver layers have been fabricated and characterized using the dedicated setup described in *chapter* 4. The measured absorption spectra have provided an experimental validation of the multi-resonant approach introduced in *chapter* 6.

The evolution of the optical response with the angle of incidence and the geometrical parameters of the grating have been investigated. We have attributed the absorption peaks to Fabry-Perot resonances as well as the excitation of guided modes propagating in the a-Si:H layer and localized surface plasmon resonances.

Most of the light-trapping effects in the fabricated cells occur above the bandgap wavelength. Controlling the a-Si:H deposition parameters is crucial to achieve the optimal optical properties (refractive index, bandgap wavelength, absorption coefficient). The conception of light-trapping strategies is deeply interrelated with a complete understanding of the material properties.

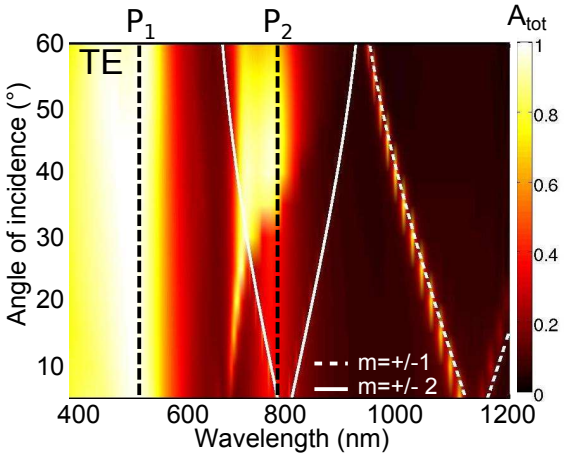

(a)

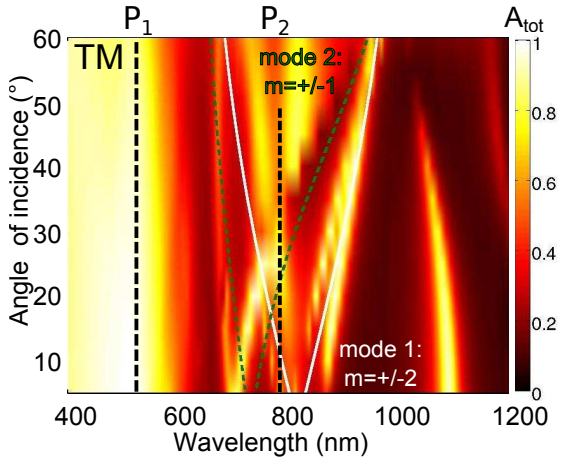

(b)

Figure 61: Measured total absorption ($A = 1 - R$) of a cell with a 1D silver grating ($p = 500$ nm, $ff = 0.38$) as a function of the excitation wavelength when the angle of incidence θ varies from 5 to 60° for an excitation with TE (a) and TM (b) polarized light. The main absorption peaks are attributed to Fabry-Perot resonances (black dashed line) and guided modes supported by the a-Si:H layer (white plain and dashed lines for TE polarization; white plain line and green dashed line for TM polarization).

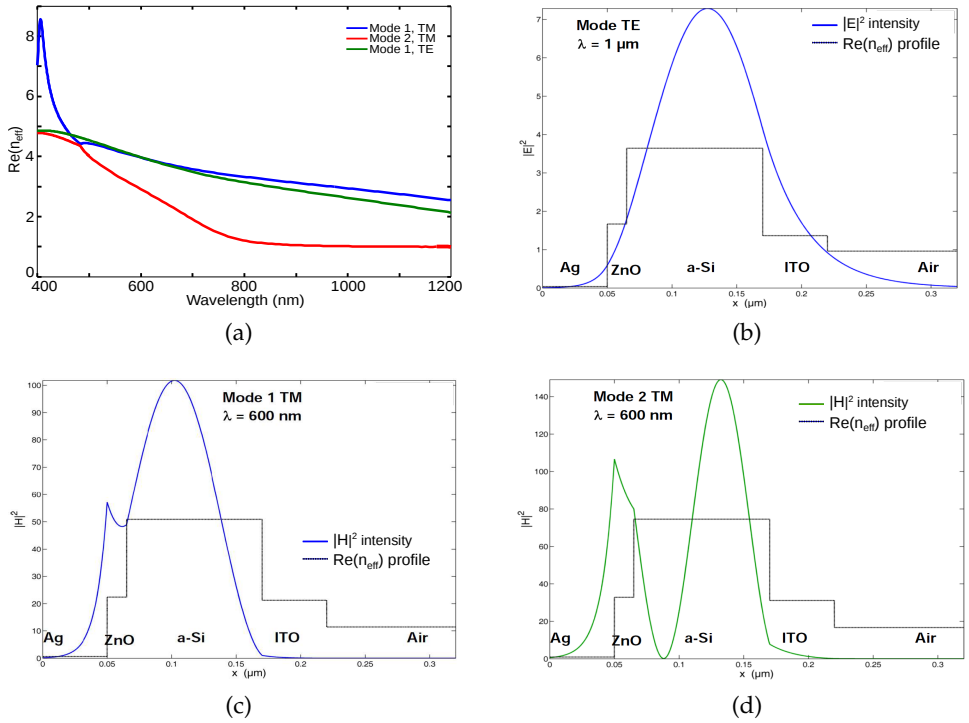

Figure 62: Modes of the ITO/a-Si:H/ZnO:Al/Ag waveguide. (a) Real part of the effective index for TE (green) and TM (blue, red) polarizations. (b) Electric field intensity profile for an excitation at $\lambda = 1$ µm for a TE polarization. (c, d) Magnetic field intensity profile corresponding to modes 1 and 2 for an excitation at $\lambda = 600$ nm for a TM polarization. In Figs. 62b, 62c and 62d, the $\mathrm{Re}(n_{\mathrm{eff}})$ profile is also displayed.

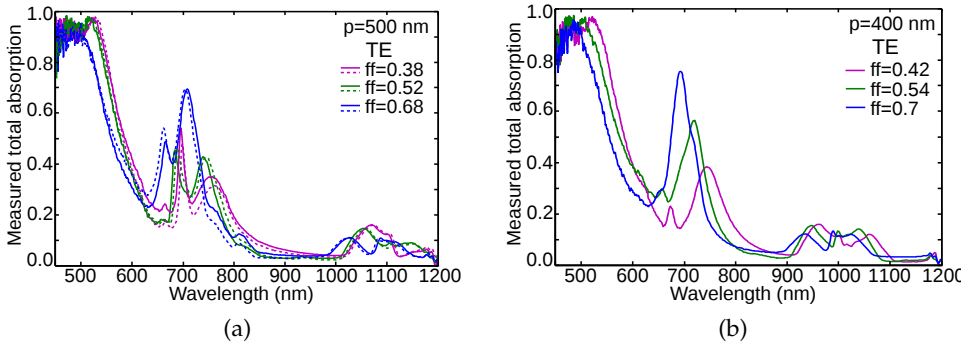

Figure 63: Measured total absorption spectra of a-Si:H structures with 1D silver gratings for a TE polarized excitation at normal incidence. (a) $p = 500$ nm, $ff = 0.38$; 0.52; 0.68. (b) $p = 400$ nm, $ff = 0.42$; 0.54; 0.7. For $p = 500$ nm, for each fill factor value, dashed and plain lines show measurements done on two different cells with the same nominal grating parameters.

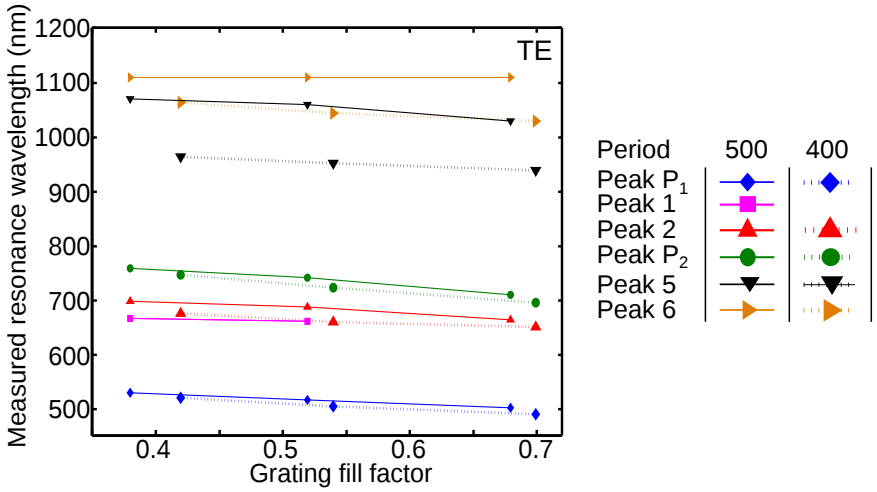

Figure 64: Evolution of the measured resonance wavelengths as a function of the grating fill factor for $p = 500$ nm (plain line) and $p = 400$ nm (dashed line). The structure is excited at normal incidence with a TE polarized light.

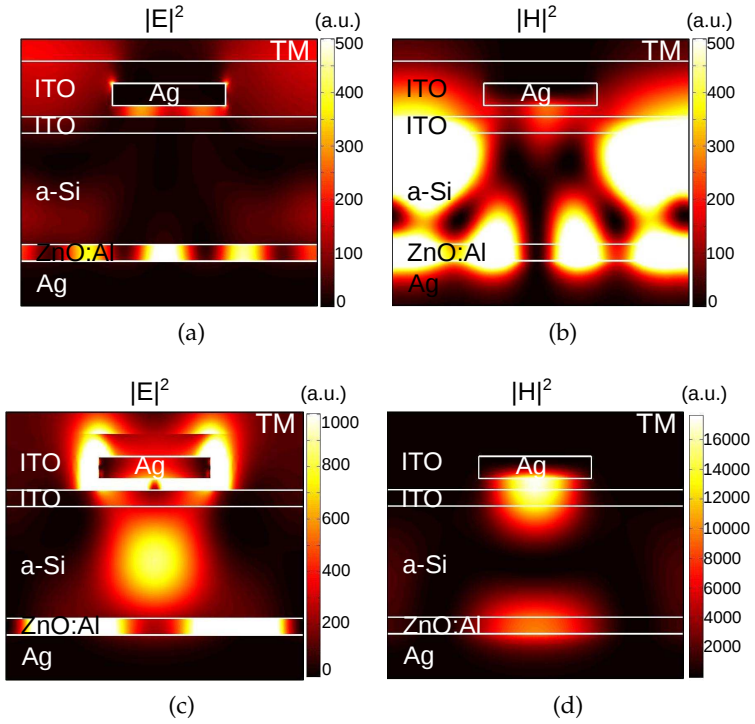

Figure 65: Calculated electromagnetic field intensity maps for a 1D silver grating ($p = 500$ nm, $ff = 0.38$) for an excitation at $\lambda_4 = 800$ nm (a, b) and $\lambda_6 = 1.05$ µm (c, d) and an incident angle $\theta = 5°$ under TM polarization. All the intensity maps have the same unit.

Part III

APPLICATION TO GALLIUM ARSENIDE : TOWARDS HIGH-EFFICIENT ULTRA-THIN SOLAR CELLS

8

DESIGN OF A TRANSPARENT METAL ELECTRODE FOR ABSORPTION ENHANCEMENT IN ULTRA-THIN GALLIUM ARSENIDE LAYERS

Contents

In PART 2 of the thesis, we have introduced the concept of nanopatterned resonant front contact. We have shown that ultra-thin a-Si:H solar cells could be beneficially designed using a one-dimensional metallic grating as a front contact. The metallic grating is also used to enhance light absorption in the cell thanks to multiple resonances. However, the potential of plasmonic nanostructures for single-junction a-Si:H solar cells is limited by the low bandgap wavelength of a-Si:H. In this third part of the thesis, we present the extension of the nanopatterned resonant front contact concept to another material which is gallium arsenide. GaAs is a semiconductor with an optimal bandgap for photovoltaic conversion ($E_g \sim 1.42$ eV thus $\lambda_g \sim 870$ nm).

In this chapter, we propose a design with a two-dimensional metallic grid as a front contact to enhance light absorption within a very thin (25 nm) GaAs layer. It should be noted that metallic films with periodic hole arrays have already been considered to enhance the performances of optoelectronic devices such as light-emitting devices [155] or c-Si solar cells [156]. As first reported by Ebbesen et al. [157], sub-wavelength holes in a metal film lead to extraordinary optical transmission (EOT). In other words, light transmission through the metallic hole array is possible at specific wavelengths depending on the size and geometry of the sub-wavelength apertures. The EOT phenomenon is attributed

to the coupling of incident light to surface plasmons propagating on the surface of the patterned metallic film [157–159]. In solar cells, the front metal electrodes could be structured in order to increase light absorption within the active layer thanks to surface plasmon resonances as proposed by Chi et al. [156]. However, the transmitted power is enhanced only on a limited spectral range ($\sim$ 200 nm) around the EOT wavelength [156].

In the following, we show that a two-dimensional metallic grid (that is to say a metallic film patterned with square holes) induces a broadband multi-resonant mechanism when coupled with an ultra-thin absorber and a back mirror. Contrary to the study presented in PART 2, we have not designed a full solar cell. Our work has been focused on the design of a proof-of-concept structure to demonstrate the potential of our light-trapping strategy.

8.1 INTRODUCTION: LIGHT ABSORPTION IN 25 NM OF GALLIUM ARSENIDE

8.1.1 *Absorption depth in GaAs*

The absorption depth is a valuable tool to describe how deeply light penetrates into a semiconductor before being absorbed. The absorption depth d is defined as the inverse of the absorption coefficient α:

$$d = \frac{1}{\alpha} = \frac{\lambda}{4\,\pi\,k}\,. \tag{34}$$

λ is the wavelength and k the extinction coefficient of the material. d gives the depth in the material where the fraction of non absorbed photons is equal to the incident intensity over e. We have calculated the absorption depth in GaAs using Eq. (34) and Palik's data [116] for k. The resulting $d = f(\lambda)$ curve is plotted in Fig. 66. It should be noted that in a standard GaAs solar cell with a thickness of 1 micron, 63 % of the photons at 840 nm are absorbed in a single pass.

Now let us consider the case of an ultra-thin GaAs layer with a thickness of 25 nm. As highlighted with a dashed red line in Fig. 66, photons with wavelengths longer than 430 nm are weakly absorbed in such a thin layer. Another way to picture the amount of photons absorbed in the ultra-thin layer is to calculate the single-pass absorption, i.e the fraction of photons absorbed after a single pass through the layer. Figure 67 displays the single-pass absorption in 25 nm of GaAs (blue curve) calculated using Eq. (26) (see *chapter 6*, subsection 6.1.2). At 500 nm, only 20 % of incident light is absorbed in the GaAs layer.

8.1.2 *Addition of a back mirror*

The simplest way to increase the number of photons absorbed in the GaAs layer is to add a metallic back mirror. Absorption in a 25 nm-thick GaAs layer on a silver mirror[1] is plotted in Fig. 67 (green curve). At short wavelengths

1 Optical constants for GaAs and Ag are taken from Palik [116] and Johnson and Christy [143], respectively.

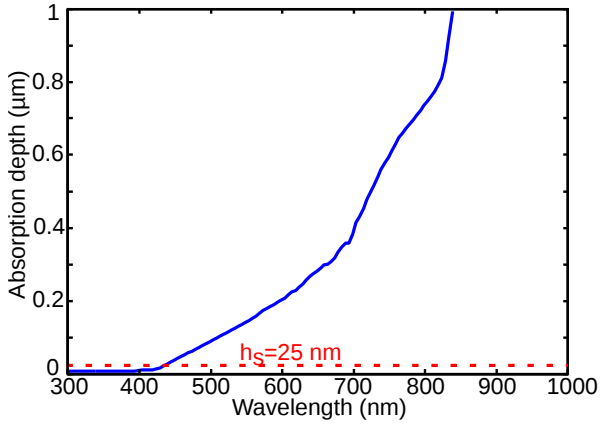

Figure 66: Absorption depth in GaAs as a function of the incident wavelength. The 25 nm value for GaAs thickness is highlighted with a dashed red line.

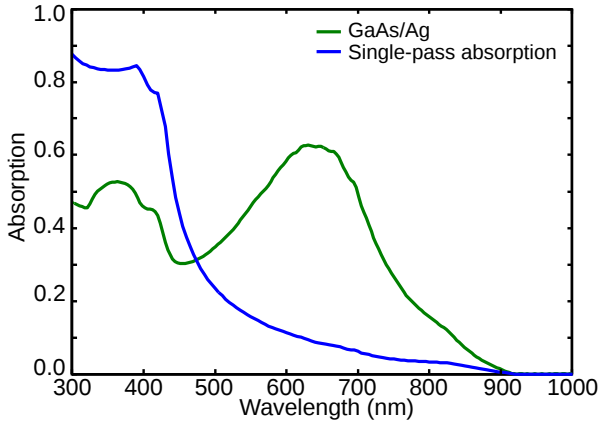

Figure 67: Single-pass absorption in 25 nm of GaAs (blue curve) and absorption in a GaAs/Ag structure with the same GaAs thickness (green curve).

($\lambda < 470$ nm), the absorption in the GaAs/Ag stack is lower than single-pass absorption because the single-pass absorption calculation assumes a perfect anti-reflection coating layer. In the long wavelength spectral range ($470 - 920$ nm), the absorption intensity is improved by the addition of the back mirror. In particular, a broad absorption peak is evidenced in the middle of the visible range with an intensity reaching 65 % at 620 nm.

This broad feature is due to Fabry-Perot resonances in the Air/GaAs/Ag cavity. The existence of such a thin Fabry-Perot resonator is unexpected. It is due to a particular phase shift condition. At 620 nm, the phase shift ϕ_2 due to reflection on the bottom GaAs/Ag interface is close to $-\pi/2$ as shown in Fig. 68. The phase shift ϕ_1 due to reflection on the top GaAs/Air interface is almost constant over the $300 - 900$ nm range and has a value close to zero. Therefore, the resonance condition for the lowest order Fabry-Perot mode ($q = 0$) gives a cavity thickness h of:

$$h = \frac{\lambda}{2n_{GaAs}}(q - \frac{\phi_1 + \phi_2}{2\pi}) \sim \frac{\lambda}{8\, n_{GaAs}},$$

where λ is the resonance wavelength and n_{GaAs} the refractive index of GaAs. At 620 nm, $n_{GaAs} \sim 3.8$, which leads to a minimum GaAs thickness of 21 nm. Note that the absorption peak corresponding to the first order ($q = 1$) Fabry-Perot resonance in the Air/GaAs/Ag cavity is also observed in Fig. 67 around 360 nm.

Yet, in spite of the broad Fabry-Perot feature, the absorption band is too narrow (full width at half maximum $\sim$ 250 nm) and the absorption maximum is only 65 % at 620 nm. We have shown in PART 1 of the thesis that arrays of metallic wires could be used to achieve a multi-resonant absorption spectrum in both polarizations. In the following, we present a design with a nanostructured metallic layer on top of the ultra-thin GaAs layer.

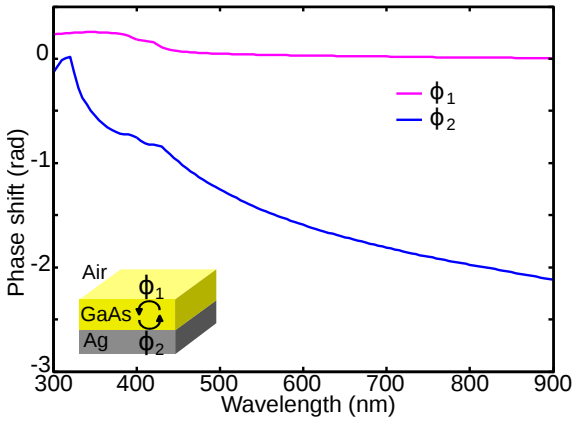

Figure 68: Phase shifts induced by reflection on the GaAs/Air (pink curve) and GaAs/Ag (blue curve) interfaces within the Air/GaAs/Ag Fabry-Perot cavity depicted in the inset. The phase shift values are obtained from the Fresnel reflection coefficients.

8.2 2D METAL NANOPARTICLES

In our group at LPN, we have already proposed a design for light-trapping in ultra-thin GaAs layers as presented in detail in Colin's PhD thesis [160]. In this section, we will briefly introduce this structure and its properties. A periodic array of two-dimensional metallic square nanoparticles is patterned on a 25 nm-thick GaAs layer. The proposed design is depicted in the inset of Fig. 70. Numerical calculations have been performed with the code Reticolo[2] in order to predict the optical response of the structure. The predicted absorption spectra are displayed in Fig. 70 for the optimized geometrical parameters of the metallic array (period = 200 nm, width = 100 nm, thickness = 20 nm). The absorption spectrum is multi-resonant and exhibits three main peaks at 560 nm (A), 675 nm (B) and 760 nm (C).

Peaks A and B correspond to the broad absorption peak observed in the case of the Air/GaAs/Ag system and attributed to vertical Fabry-Perot resonances in the GaAs layer. However, the phase shift induced by reflection on the top

2 See Appendix A for further details.

interface of the cavities is not the same below and between the particles because the refractive index of silver is lower than the Air index. The addition of the metallic particles induces thereby a splitting of the peak into peaks A (Ag/GaAs/Ag cavities) and B (Air/GaAs/Ag cavities).

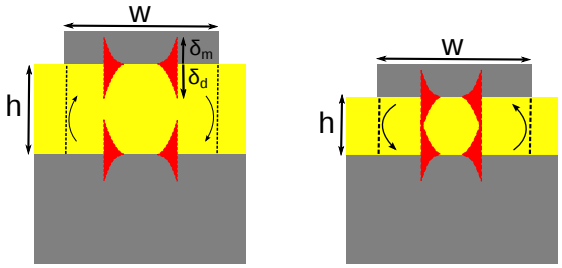

(a) $h > 2 \times \delta_d$ (b) $h < 2 \times \delta_d$

Figure 69: Schematics of two surface plasmons propagating at the Ag/GaAs and GaAs/Ag interfaces in the case where there is no coupling (a) and strong coupling (b) between the two surface waves.

Peak C is due to another kind of Fabry-Perot resonance. Surface plasmons can propagate along the x axis on the top Ag/GaAs and bottom GaAs/Ag interfaces. Figure 69 shows a schematic of two surface plasmons propagating at the top Ag/GaAs and bottom GaAs/Ag interfaces. At 760 nm, the propagation length of the surface plasmons along the x axis obtained from Eq. (13) (see *chapter* 2, section 2.3) is $\delta_{SP} = 200$ nm which is longer than the particle size ($w = 100$ nm). Thus the surface waves are confined by the particle edges. As a matter of fact, the areas of the GaAs layer below the silver particles play the role of Fabry-Perot cavities with a cavity size equal to the particle width w. Such a resonance can be considered as a 'horizontal' Fabry-Perot resonance. The cavity thickness is given by:

$$w = \frac{\lambda\, q}{2\, n_{eff}}\,, \tag{35}$$

with q the order of the resonant mode. The magnetic field intensity $|H|^2$ maps (not shown here, see Ref. 161) suggest that peak C is due to a third-order Fabry-Perot resonance ($q = 3$). If we take the GaAs index value at 760 nm ($n_{GaAs} \sim 3.7$), we should have a width cavity of 308 nm. In our case, this mode is observed within a 100 nm-wide cavity. How is it possible?

In Eq. (35), we see that increasing the effective index reduces the cavity width w. In our case, because of the very thin GaAs layer, the two surface plasmons are strongly coupled (case shown in Fig. 69b). Coupling of the two surface plasmons is possible when the thickness of the GaAs layer h is lower than twice the decay length of the plasmon mode in GaAs δ_d. At $\lambda_C = 760$ nm, the decay length of the surface plasmon mode in GaAs obtained from Eqs. (12) and (11) (see *chapter* 2, section 2.3) is 33 nm. It confirms that in our case, $h < 2 \times \delta_d$ and thereby that the two surface plasmons are coupled. It gives rise to a high effective index of the resonant mode ($n_{eff} > 10$ here) and allows us to reduce the cavity width down to 100 nm [161].

Figure 70 displays the total absorption (black curve) and the absorption fraction in the GaAs layer (red curve). The area between the two curves represents

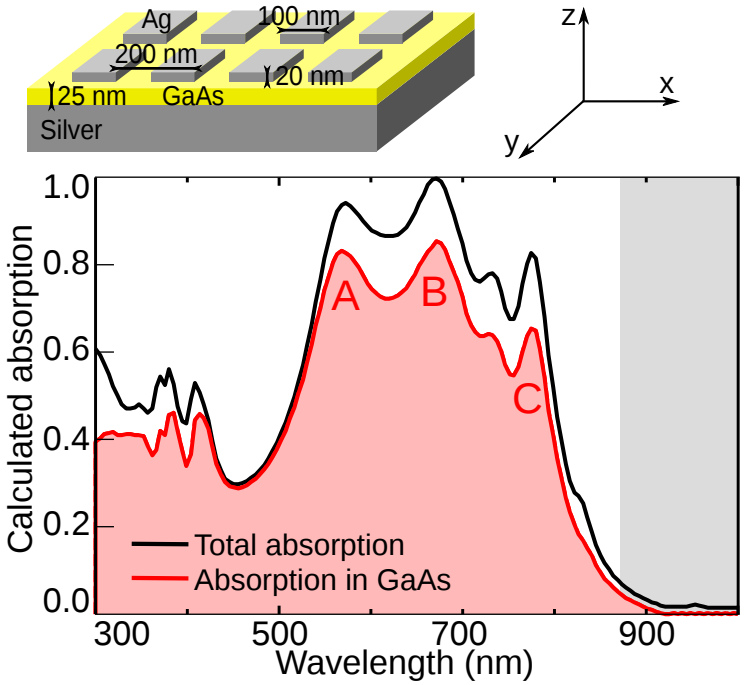

Figure 70: Calculated spectra of total absorption (black curve) and absorption in the GaAs layer (red curve) for the structure depicted in the inset. Inset: Schematic of an array of 2D silver nanoparticles (period = 200 nm, width = 100 nm, thickness = 20 nm) patterned on a 25 nm-thick GaAs layer on a silver back mirror.

the absorption losses in the metal (2D particles + mirror). For this structure, metal losses are estimated to be below 15 % over the whole absorption spectrum, which is unexpectedly low given the presence of the metallic structure on the front surface. The limited losses in the metal grating are due to the strong contrast between the refractive indices of GaAs ($n_{GaAs} \in [3.5 - 5.1]$) and silver ($n_{Ag} \in [0.04 - 1.3]$) that tends to confine the electro-magnetic field in the semi-conductor layer and also to the very thin (20 nm) metal used.

The performances of the 2D nanoparticles have been estimated by calculating the theoretical current density J_{th} as defined in Eq. (28) (see *chapter 6*, subsection 6.1.2). The absorption spectrum has been weighted by the AM1.5G solar spectrum and integrated over the whole spectral range ($300 - 900$ nm). We obtained a current density value of $J_{th} = 18\,mA/cm^2$ for only 25 nm of GaAs! Note that this value assesses only the potential of the proposed design for absorption enhancement in the cell and does not take into account the current collection efficiency.

It is still a very promising result. We have shown through this study that broadband absorption enhancement could be achieved with a polarization independent structure and overall, with low metal losses.

The new challenge here is to obtain the same results with the concept of nanopatterned resonant front contact. In order to ensure current collection in the front side, we consider a nanogrid structure as presented in the following.

The novel design should exhibit the same properties as the 2D particles array: broadband absorption, polarization independence and limited metal losses.

8.3 2D METAL NANOGRID

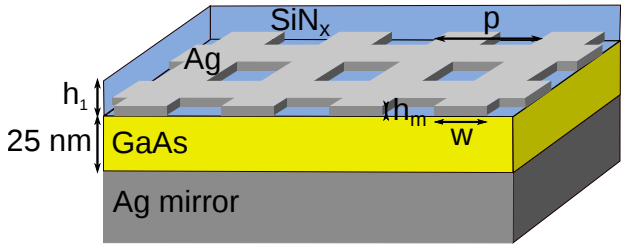

Figure 71: Schematic of our approach for a broadband ultra-thin GaAs absorber.

Our approach is described in Fig. 71. A 2D silver grid (period p, width w and metal thickness h_m) is patterned on a 25 nm-thick GaAs layer on a silver mirror. The silver grid is embedded in an anti-reflection coating layer with a total thickness h_1. When $h_1 = h_m$, the dielectric material fills exactly the holes in the metallic grid. We have chosen the silicon nitride as the dielectric material because of its suitable optical index ($n_{Si_3N_4} \in [2 - 2.15]$) which is between the GaAs ($n_{GaAs} \in [3.5 - 5.1]$) and Air indices.

As a first step towards the optimization of the structure presented in Fig. 71, we have first considered a Ag/GaAs/Ag structure, i.e without the silicon nitride material, as illustrated in the inset of Fig. 72a. We have investigated numerically the influence of the grid parameters (linear fill factor, period and metal thickness). All spectra displayed in this section are at normal incidence[3].

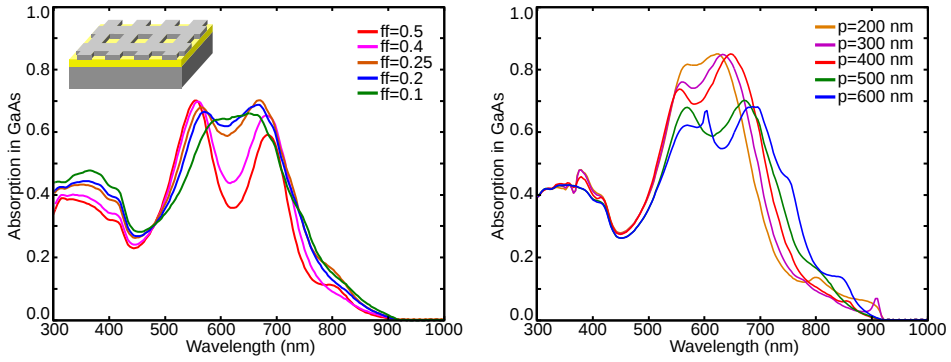

(a) Influence of the fill factor (b) Influence of the period

Figure 72: Absorption spectrum for a varying fill factor for $p = 500$ nm (a) and varying period for $ff = 0.25$ (b). The metal grid thickness is fixed to $h_m = 20$ nm.

3 Since the absorption mechanism in this structure relies mainly on Fabry-Perot resonances, the angle of incidence has a weak influence of the absorption spectra. In the case of the complete structure with a top anti-reflection coating layer described in the following, the study of the angular dependence is more important because surface plasmon modes are involved.

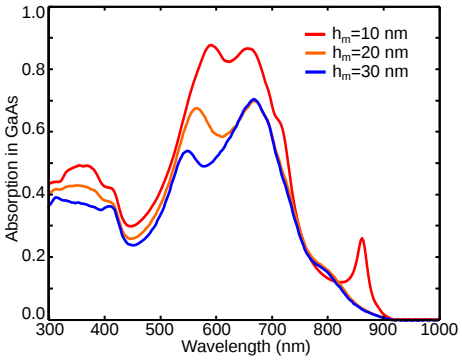

Figure 73: Absorption spectrum for a grid thickness h_m varying between 10 and 30 nm. The other grid parameters are: $p = 500$ nm and $w = 125$ nm.

The grid fill factor is defined as the ratio of the grid width w over the grid period p. Figure 72a shows the absorption in GaAs for a grid fill factor varying from 0.1 to 0.5. The grid period is constant and set to 500 nm. When the fill factor is equal to zero, the system corresponds to an Air/ GaAs/Ag stack, leading to a single Fabry-Perot resonance peak as already explained in section 8.1. For a higher fill factor, the peak is splitted in two because of the two different Fabry-Perot cavities Ag/GaAs/Ag and Air/GaAs/Ag, as already discussed in the previous section. When the fill factor increases, the spectral gap between the two peaks increases thereby widening the absorption band. However, the two absorption peaks are narrow (full width at half maximum $\sim$ 100 nm) and the fill factor increase leads to a drop in the absorption intensity at 600 nm.

We have also studied the influence of the grid period on the absorption spectrum as displayed in Fig. 72b. Let us consider the absorption spectrum for $p = 200$ nm (orange curve), which almost corresponds to the structure with 2D particles discussed in the previous section. The spectrum exhibits two main absorption peaks at 570 and 620 nm, which are attributed to Fabry-Perot resonances in the GaAs layer. Note that we also see a peak at 800 nm, with low intensity ($\sim$ 15 %), that should correspond to the resonance C of the complementary structure. The attribution of this peak to the coupling of surface plasmons propagating on the two GaAs/Ag interfaces is further discussed in *chapter* 9 from the experimental results. It is also noteworthy that the absorption in the GaAs drops when the grid period increases for a constant value of the fill factor. It reflects one paradox of plasmonic structures. Intuitively, one could think that larger grid period, that is to say larger aperture width, is favorable to an efficient light absorption in the semiconductor. In this structure, light absorption is also confined below the metallic grid and the efficiency of the incoupling light is higher for small period values.

Finally, Fig. 73 displays the absorption spectra of a structure with a 2D grid ($p = 500$ nm, $ff = 0.25$) and a varying metal thickness: $h_m = 10$ nm (red curve), $h_m = 20$ nm (orange curve) and $h_m = 30$ nm (blue curve). We see that the spectral position of the peak at longer wavelengths ($\lambda \sim 680$ nm) does not vary with the metal thickness. It is consistent with the attribution of this peak to a Fabry-Perot resonance in the Air/GaAs/Ag cavity. As for the feature at

$\lambda \sim 570$ nm corresponding to resonances in Ag/GaAs/Ag cavities, a metal thickness variation modifies the peak intensity and the resonance wavelength. For instance, an increase of the metal thickness from 20 to 30 nm leads to an intensity drop of 15 % as well as a spectral shift towards short wavelengths. We see that lower metal thicknesses are favorable to a high absorption intensity.

Through this study, we see that the design with the 2D silver grid, that is to say the structure complementary to the 2D metal particles, exhibits the same Fabry-Perot resonances. The position and intensity of the absorption peaks can be tuned by varying the grid parameters. However, the performances of the grid structure are limited. If we consider a structure with a period of 500 nm, a grid width of 125 nm and a metal thickness of 20 nm, the absorption spectrum exhibits two absorption peaks at 570 nm and 670 nm with a maximum absorption of 70 %. The absorption band is thus broader than in the case of a simple GaAs/Ag stack but is still not sufficient for applications to photovoltaic devices. One solution to add resonances and broaden the absorption band is to embed the metallic grid in a dielectric layer as shown in the following.

8.4 ADDITION OF AN ANTI-REFLECTION COATING LAYER: PERFORMANCES

We have calculated the integrated absorption in the GaAs layer over the visible range for varying values of the different parameters of the structure (h_1, p, w, h_m)[4]. Optical constants of the silicon nitride material, Si_3N_4 in our case, are taken from Palik [116]. The best result is obtained for $h_1 = 80$ nm, $p = 500$ nm, $w = 125$ nm and $h_m = 20$ nm. We have plotted the absorption spectrum corresponding to the optimal structure, as displayed in Fig. 74. For this particular silicon nitride thickness, we obtain five absorption peaks. A very broad absorption spectrum is shown thanks to these multiple resonances. Note that this response is independent from the polarization of incident light at normal incidence because of the square 2D structure.

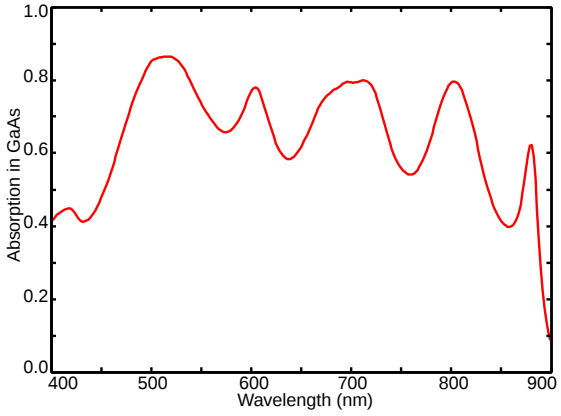

Figure 74: Calculated absorption spectrum for the structure: $h_1 = 80$ nm, $h_{GaAs} = 25$ nm, $p = 500$ nm, $w = 125$ nm and $h_m = 20$ nm.

4 We have chosen to optimize the structure by varying one parameter at a time. It enables a more physically intuitive optimization process and to avoid to explore the whole parameter space.

We have estimated the performances of the structure with the silicon nitride layer by calculating the theoretical current density J_{th} for the curve shown in Fig. 74. A value of $J_{th} = 21.6\,mA/cm^2$ has been obtained for an excitation at normal incidence. For the sake of comparison, the current experimental record for a single-junction GaAs solar cell is a conversion efficiency of 28.8 % under one sun demonstrated by Alta Devices in 2012 [162]. The measured short-circuit current density is $J_{SC} = 29.68\,mA/cm^2$ for a GaAs thickness of 1 µm. In our 2D silver grid design, the theoretical short-circuit current density is only 1.4 times lower than the experimental record value while the GaAs thickness has undergone a fortyfold reduction. Because of the thinner absorber layer, we also expect a better current collection and an improved open-circuit voltage.

8.5 INFLUENCE OF THE STRUCTURE PARAMETERS

As shown previously, the addition of the top silicon nitride layer leads to a broadening of the absorption spectrum thanks to five resonances. The absorption mechanism is more complex than in the case of a 2D grid patterned on a GaAs/Ag stack and understanding the effect of the silicon nitride layer is not trivial. The purpose of the work presented in this part (PART 3) has been to propose a design with optimal performances and to fabricate it (as developed in *chapter 9*). As presented previously, our optimal design is based on a $SiN_x(Ag)/GaAs/Ag$ stack with:

- 2D grid parameters: period = 500 nm, width = 125 nm, thickness = 20 nm
- GaAs layer thickness: 25 nm
- Silicon nitride layer thickness: 80 nm.

The detailed analysis of the absorption mechanism is still in progress. Nevertheless, in this section, we present preliminary results in order to understand the influence of each parameter of the structure. We have chosen to plot the total absorption (instead of the absorption only in the GaAs layer) in order to see the absorption peaks located beyond the GaAs bandgap wavelength.

8.5.1 *Influence of the anti-reflection coating layer thickness*

Figure 75 displays the total absorption in the $SiN_x(Ag)/GaAs/Ag$ stack as a function of the silicon nitride thickness and the excitation wavelength. We see seven high absorption intensity bands, called *a* to *g*. It is noteworthy that some of the absorption peaks exist only on a limited thickness range.

We see three main domains:

- for silicon nitride thicknesses lower than 60 nm, the absorption spectrum shows only three peaks corresponding to bands *b*, *d* and *f*. In this thickness range, absorption is low ($< 40\,\%$) on two wavelength ranges in the middle of the visible range ($420 - 550$ nm and $600 - 750$ nm).

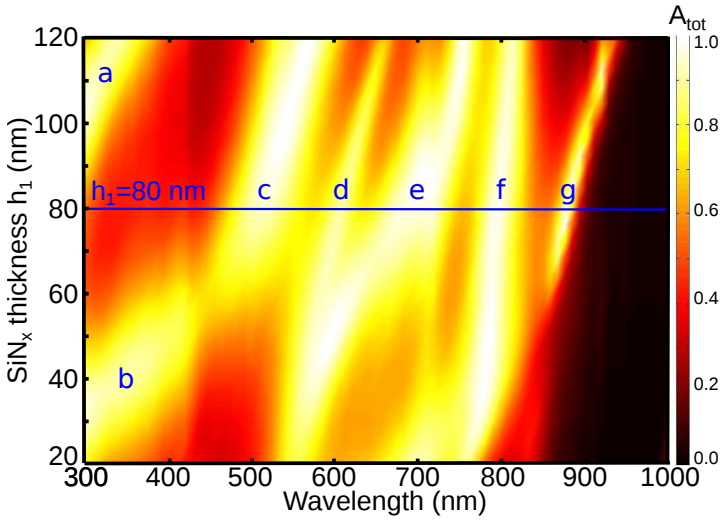

Figure 75: Total absorption for the structure defined in the inset of Fig. 74 as a function of the SiN_x layer thickness h_1 and the excitation wavelength at normal incidence. The grid parameters are: p= 500 nm, w= 125 nm and h_m= 20 nm.

- For 60 nm$< h_1 <$ 90 nm, the spectrum exhibits five absorption peaks (c, d, e, f and g). Our nominal structure belongs to this domain. In particular, the absorption peak g appears clearly ($A > 70\,\%$) only on this domain.
- For 90 nm$< h_1 <$ 120 nm, the spectrum exhibits six absorption peaks (a, c, d, e, f and g in this case). The peak d shows a drop in the intensity as well as a shrinking of its band width in this thickness range. The band a appears but at short wavelengths ($<$ 400 nm), thereby leading to a low increase in the short-circuit current density. For these two reasons, we see a drop of the calculated J_{th} for $h_1 >$ 90 nm.

8.5.2 *Influence of the grid parameters*

8.5.2.1 *Fill factor and grid period*

Figures 76a and 76b show the total absorption as a function of the fill factor (Fig. 76a)/the period (Fig. 76b) and the wavelength at normal incidence. The observed dependence is quite complicated to understand at this stage of the study. However, in both figures, we see that the absorption peak at 500 nm has a low dependence on the fill factor and the period. When the fill factor tends to zero, the structure is a SiN_x/GaAs/Ag stack with only one absorption peak at 500 nm due to Fabry-Perot resonances in the cavity.

In Fig. 76b, we have shown the limit corresponding to diffracted orders in air ($p = \lambda$) with a black dashed line. Above this limit, the absorption intensity drops because of diffraction losses. In spite of a wider absorption band, larger grid periods do not seem favorable to achieve high absorption intensity. The fitting of the curves $p = f(\lambda)$ should give more information about the absorption mechanism at stake.

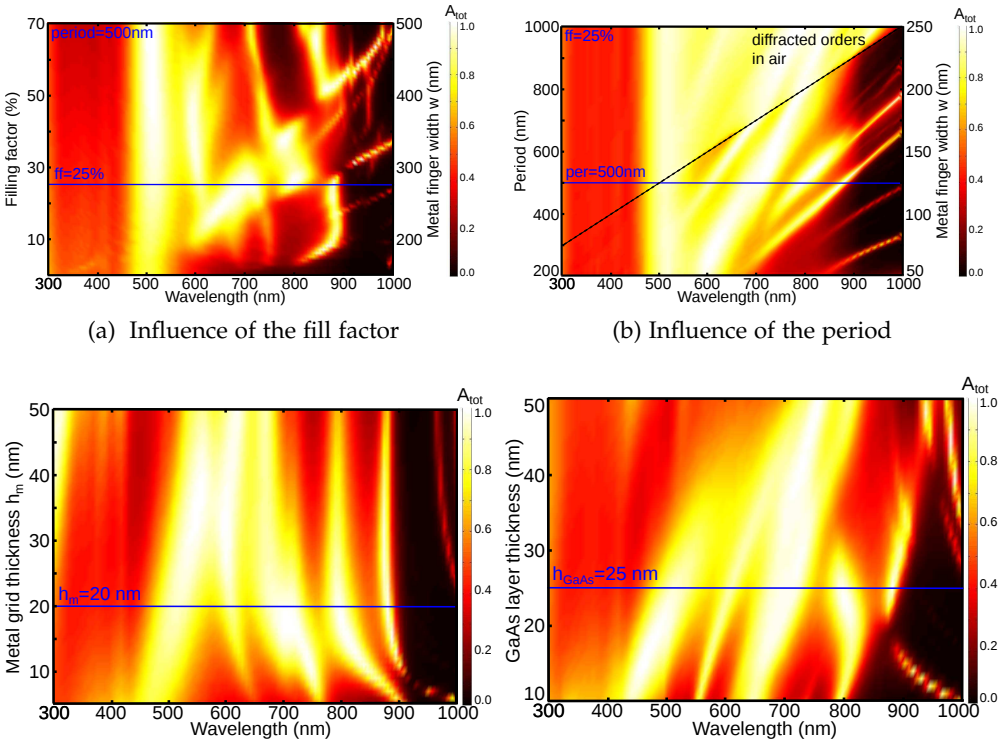

(a) Influence of the fill factor

(b) Influence of the period

(c) Influence of the metal thickness

(d) Influence of the GaAs layer thickness

Figure 76: Total absorption for the structure defined in the inset of Fig. 74 as a function of the grid fill factor (a) /grid period (b)/grid thickness h_m (c)/GaAs layer thickness (d) and the excitation wavelength at normal incidence. The values corresponding to the nominal structure ($h_1 = 80$ nm, $h_{GaAs} = 25$ nm, $p = 500$ nm, $w = 125$ nm and $h_m = 20$ nm) are shown with blue lines.

It is worth noticing that resonance c (for $p = 500$ nm and $w = 125$ nm) does not depend on the geometry of the grid. For all the other peaks, the resonance wavelength depends strongly on the geometry of the nanogrid (period p, grid width w).

8.5.2.2 *Metal thickness*

The total absorption as a function of the metal thickness and the wavelength is shown in Fig. 76c. Our nominal structure relies on a 20 nm-thick metal grid. For this particular thickness, the absorption spectrum includes five peaks. For thicker grids, the absorption spectrum is globally similar but exhibits a shrinking of the main absorption band from $450 - 750$ nm for $h_m = 20$ nm to $400 - 700$ nm for $h_m = 40$ nm. Furthermore, we see that for very thin metal grids ($h_m < 20$ nm), the metal thickness has a strong influence on both the intensity and the spectral position of all the peaks. In particular, the long wavelength peaks observed at 800 and 880 nm for $h_m = 20$ nm exhibit a strong spectral shift towards long wavelengths when the metal thickness decreases.

8.5.3 *Influence of the GaAs layer*

So far, we have focused on a design with a GaAs layer thickness fixed to 25 nm. As displayed in Fig. 76d, we have investigated the influence of the GaAs layer thickness on the total absorption for thicknesses between 10 and 50 nm. The nominal value ($h_{GaAs} = 25$ nm) is shown with a blue line. The absorption spectrum depends strongly on the GaAs layer thickness. For layers thicker than 35 nm, the absorption band is limited, probably because the GaAs thickness is then higher than twice the surface plasmon decay length in GaAs. Therefore, on this thickness range, the surface plasmons at the two GaAs/Ag interfaces are no longer coupled.

8.6 STUDY OF THE ANGULAR DEPENDENCE

We have investigated the evolution of the total absorption in the structure as a function of the angle of incidence (plane of incidence xz) and the excitation wavelength. Results are shown in Fig. 77 for TE (Fig. 77a) and TM (Fig. 77b) polarizations.

High intensity absorption bands are confined between 500 and 900 nm approximately. We see that below 850 nm, the spectral position of the absorption peaks is independent from the angle of incidence for both polarizations. However, for increasing incidence angles, some absorption peaks suffer from an intensity loss because of light diffraction in the air. We have plotted the curve corresponding to diffracted orders in Air for both polarizations (dashed black line). Above this line, the absorption intensity drops in particular for a transverse magnetic polarized light.

It is noteworthy that some of the absorption peaks do not exist at normal incidence. For TM polarization, two peaks appear around 920 nm for $\theta > 0°$.

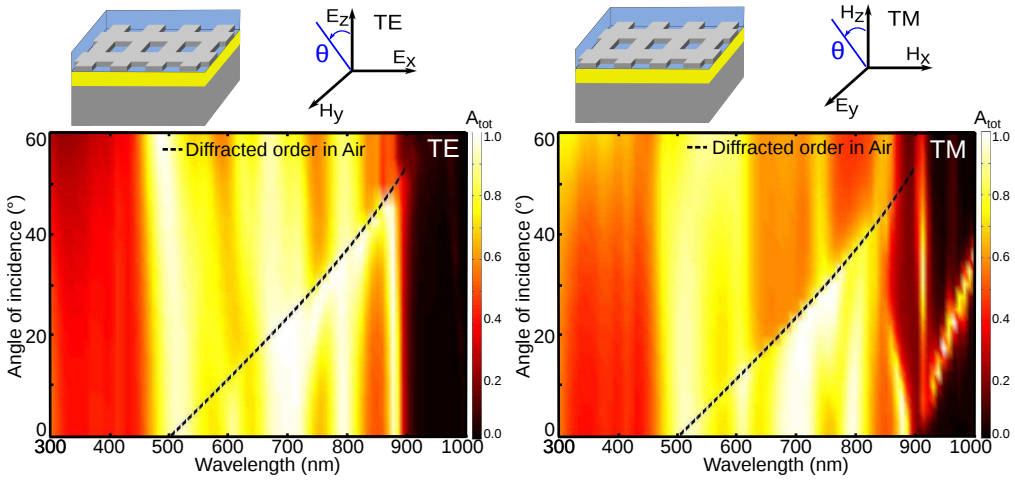

(a) TE polarization (b) TM polarization

Figure 77: Total absorption in the structure as a function of the angle of incidence and the wavelength for TE (a) and TM (b) polarizations. The domain where diffraction orders in air exist is shown with a dashed black curve. The definition of transverse electric (TE) and transverse magnetic (TM) polarizations is reminded in inset.

One of them shows a strong dependence on the angle of incidence. Likewise, the absorption peak observed at 880 nm exhibits a shift towards short wavelengths when the angle increases. The behaviour of these three peaks for TM polarization resembles the dispersion of surface modes in a square array of holes. As previously studied in our group [118, 163, 164], a metallic substrate with square apertures exhibits surface modes due to coupling between surface plasmons propagating at the Metal/Air interface. Four branches exist corresponding to two symmetric modes (S_x and S_y) and two asymmetric modes (A_x and A_y).

In our case, the nature of these four modes is not completely understood yet. We can assume that they are modes propagating in the $Ag/SiN_x/Air$ guide. The symmetric modes give rise to absorption peaks that exist at normal incidence: in our case, the peaks observed around 880 nm for TE (Fig. 77a) and TM (Fig. 77b) polarizations. As for the asymmetric modes, they are not observed at normal incidence and they correspond to the peaks appearing around 920 nm for $\theta > 0°$ for TM polarization. The effective index of the guided mode at the resonance wavelength λ is given by:

$$n_{eff} = \frac{\lambda}{p}, \tag{36}$$

with p the grid period ($p = 500$ nm here). For instance, the symmetric modes ($\lambda \sim 880$ nm) have an effective index $n_{eff} \sim 1.8 < n_{SiN_x}$, which is consistent with the assumption of a propagation in the $Ag/SiN_x/Air$ guide. For a surface mode confined at the Ag/SiN_x interface, the effective index should be higher than the silicon nitride index.

The effective index of the modes depends on the thickness of the silicon nitride layer. When the thickness h_1 increases, the mode is more and more confined in the silicon nitride film, leading to a increase of the effective index of the mode. Using Eq. (36), we see that it induces a shift of the resonance towards longer wavelengths. It is consistent with the evolution of the absorption band g observed in Fig. 75. In addition, we see that these modes exist only for $h_1 > 60$ nm approximately. It suggests that these modes have a cut-off wavelength.

The effective index of the modes also depends on the thickness of metal grid h_m. If we reduce the metal thickness towards a value lower than the attenuation length in the metal, the mode is going to overlap with the GaAs layer, which should lead to an increase of the effective index of the mode. It could explain the spectral shift towards long wavelengths for very thin metal thicknesses observed previously in Fig. 76c.

In order to quantify the angular dependence of the structure, we have calculated the theoretical short-circuit current density as defined in Eq. (28) (see *chapter* 6, subsection 6.1.2) for an angle of incidence between 0 and 60° for TE (blue) and TM (red) polarizations. The current density value J_{th} for an unpolarized incident light is calculated as the average of the values for TE and TM polarizations. The result is shown in Fig. 42 in orange. The current density shows a low decrease when the angle of incidence increases: at 60° , J_{th} is still equal to 18.6 mA/cm^2, to be compared to 21.6 mA/cm^2 at normal incidence. Regarding the selectivity to light polarization, one should note that in TE polarization, light incoupling seems to be more efficient for angles between 20° and 40° than at normal incidence. In TM polarization, J_{th} drops for angles higher than 15°. As shown previously in Fig. 77b, the energy lost through diffracted orders in Air is particularly important in TM polarization, especially for wavelengths above 600 nm.

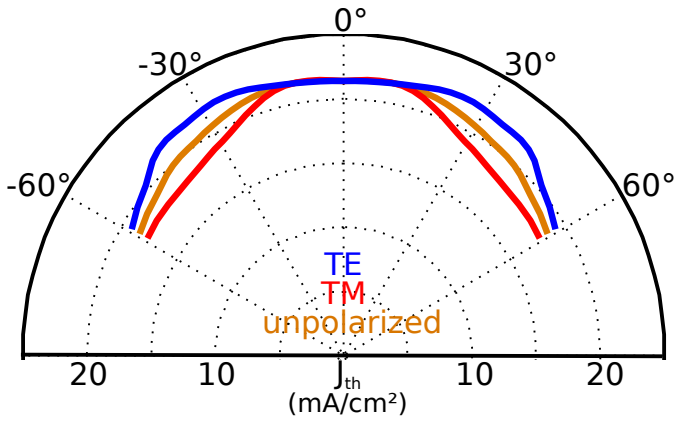

Figure 78: Theoretical short-circuit current density J_{th} as a function of the angle of incidence (plane of incidence xz) for a TE (blue), TM (red) and unpolarized light (orange).

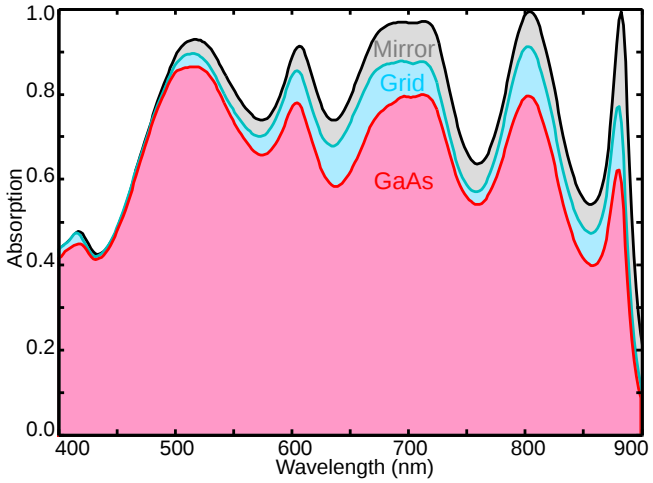

(a) SiN_x(Ag)/GaAs/Ag

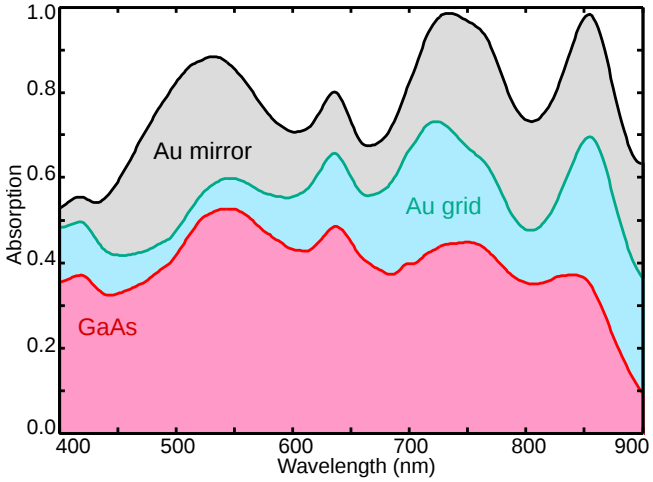

(b) SiN_x(Au)/GaAs/Au

Figure 79: Influence of the metal constituting the grid and the back mirror: absorption fraction in each material for a structure with silver (a) and gold (b).

8.7 SILVER VERSUS GOLD

So far, we have used silver as the metal for both the patterned grid and the back mirror. The question of the metal choice is a fundamental issue for plasmonic structures, in particular to limit the parasitic absorption losses. Figure 79 shows the absorption fraction in each material of the structure (grid, GaAs, back mirror) in the case of silver (Fig. 79a) and gold (Fig. 79b)[5]. The red area represents the absorption only in the GaAs layer, i.e the absorption useful for current generation. The blue and grey areas represent the absorption losses in the front metal grid and back mirror respectively.

In the case of silver, for the shorter wavelength resonance (520 nm), the absorption fraction lost in the metal is quite low (5 %). However, losses in the metal (grid + mirror) increase with the excitation wavelength: losses are below

5 Optical constants for both metals are taken from Johnson and Christy [143].

10 % at 517 nm and reach 62 % at 880 nm. Intuitively, we would expect the light trapping mechanism to be more efficient at longer wavelengths because of the higher reflectivity of the back mirror. Thus, total absorption equal to 1 is reached at 800 and 880 nm as seen in Fig. 79a. Because of increased losses, the global trend is a decrease of the absorption in GaAs as the wavelength increases. We suggest that it is due to the fact that long wavelength photons need to travel back and forth in the GaAs layer more times than for blue photons and that absorption losses are induced every time the light strikes a GaAs/Ag interface.

In the case of gold, there is not such a striking trend. However, it should be noted that absorption losses are much more important for a structure with gold. For instance, nearly 40 % of absorbed light is lost in the metallic parts at 530 nm to be compared to 5 % in silver on the same wavelength range. It may be partly due to the fact that reflectivity on the GaAs/Ag interface is much higher than on GaAs/Au at short wavelengths: at 500 nm, $R_{Ag} = 0.95$ while $R_{Au} = 0.52$. Light-trapping is thereby more efficient in the case of silver at short wavelengths. Above 700 nm, both metals have a very high reflectivity, which explains the perfect total absorption for the long wavelength resonances in both cases.

The performances of the structure have also been compared in the case of silver and gold metal/GaAs/metal designs. For gold, the theoretical short-circuit current density is 13.3 mA/cm^2 at normal incidence for unpolarized light. The use of silver is therefore much more favorable because of increased absorption losses in the gold mirror and lower gold reflectivity at short wavelengths.

8.8 CONCLUSION

In this chapter, we have presented a proof-of-concept design to enhance light absorption in an ultra-thin GaAs layer (thickness = 25 nm). A two-dimensional metal grid is patterned onto the GaAs layer and embedded in a silicon nitride layer. We have achieved a broadband multi-resonant absorption independent from light polarization at normal incidence. A theoretical short-circuit current density value of $J_{th} = 21.6\,mA/cm^2$ has been predicted numerically at normal incidence for the 25 nm-thick GaAs layer. We have also shown the low angular dependence of the absorption in the GaAs layer. Our design represents a potential fortyfold thickness reduction compared to the current record for a single-junction GaAs solar cell with a limited drop in the conversion efficiency. Besides, a theoretical value of $J_{th} = 19\,mA/cm^2$ has been shown previously in our group for the complementary structure (2D silver nanoparticles) with an additional ZnO:Al top contact (total ZnO:Al thickness = 55 nm). In the 2D grid design, the grid can be used as an alternative front contact. We have thus replaced the ZnO:Al top contact by a silicon nitride layer. Optical losses in the front contact are reduced thereby leading to an increase of the short-circuit current density. In addition, the embedded metallic grid should increase the lateral conductance: reduced electrical losses are expected.

A more detailed study of the absorption mechanism is needed to understand the influence of all the parameters. In particular, the impact of the anti-reflection coating layer material is not trivial. Furthermore, we have compared the performances of the structure for gold and silver metal/GaAs/metal designs. To date, we have considered only structures with the same metal for the grid and the back mirror. In fact, we have an additional degree of freedom because the grid metal and the mirror could be different. We could imagine choosing a metal with a high reflectivity as silver on the rear side and a metal with a lower absorption cross-section on the front side.

In this chapter, we have presented a design of a 2D patterned resonant front contact for ultra-thin (25 nm) GaAs layers. This concept shows very promising results that could pave the way towards ultra-thin and highly efficient photovoltaic devices. The designed structures are too thin to integrate a p-n junction and therefore to be photovoltaic devices. However, the concept of nanopatterned front contact can be applied to thicker ($\sim$ 100 nm) GaAs devices with a p-n junction.

8.9 SUMMARY

A design for absorption enhancement in ultra-thin GaAs layers is presented. A 2D metal grid is patterned onto a 25 nm-thick GaAs layer on a back mirror. The metal grid is embedded in a silicon nitride layer to constitute an alternative front contact.

The proposed design combines vertical Fabry-Perot resonances and guided modes. The dimensions of the metal grid and the silicon nitride thickness can be varied to tune the resonances. We have demonstrated numerically that the theoretical current density of our design is only 1.4 times lower than the current experimental record while the GaAs thickness has undergone a fortyfold reduction.

This design can be applied to thicker devices in order to fully design patterned GaAs solar cells.

9

FABRICATION OF ULTRA-THIN AU/GAAS/AU DEMONSTRATORS

Contents

In *chapter* 8, we have proposed a design to confine light efficiently in an ultra-thin GaAs layer (thickness = 25 nm). In this chapter, we present our first demonstrators with 2D metal nanogrids. For practical reasons, we have fabricated Au/GaAs/Au structures instead of the Ag/GaAs/Ag designs we have studied numerically. As shown previously, we expect a slight modification of the total absorption spectrum as well as more important metal losses. We first describe the fabrication process stage by stage. We then show the results of the optical characterization performed on the demonstrators. As a conclusion, the main results and perspectives of our work will be discussed.

9.1 FABRICATION PROCESS

Our aim has been to fabricate the $SiN_x(Au)$/GaAs/Au depicted in Fig. 80. We use crystalline GaAs which is epitaxially grown on a GaAs substrate. The fabrication of the demonstrators first requires a transfer of the GaAs layer on a gold mirror. The 2D gold grid is then patterned by electron beam lithography onto the GaAs layer. Finally, the metal grid is embedded in a silicon nitride film. Each step of the process is detailed in the following.

9.1.1 *Description of the layer transfer process*

The layer transfer process is done in four main steps:

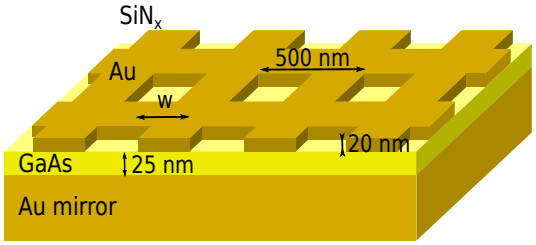

Figure 80: Schematic of the fabricated structure: a 25 nm-thick GaAs layer on gold mirror with a 2D grid of gold nanowires ($h_m = 20$ nm, $p = 500$ nm, varying width w). A 60 nm-thick silicon nitride layer is deposited on top of the structure.

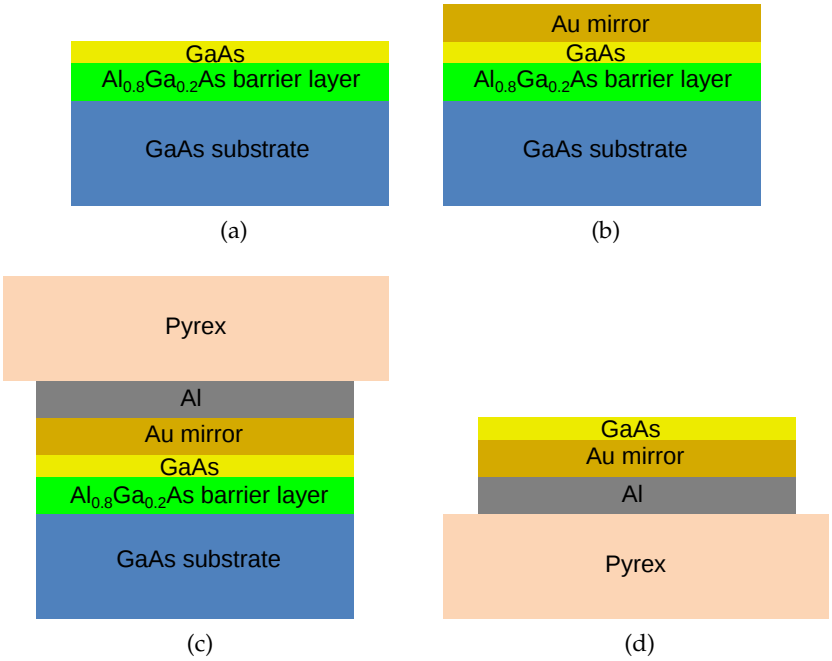

Figure 81: Overview of the layer transfer process.

A. Epitaxy growth of the GaAs layer on a GaAs substrate with an AlGaAs etch-stop layer (Fig. 81a)

B. Deposition of the back mirror (Fig. 81b)

C. Anodic bonding to Pyrex substrate (Fig. 81c)

D. Removal of the substrate and the AlGaAs etch-stop layer (Fig. 81d).

9.1.1.1 *Gallium arsenide layer epitaxy*

We use crystalline GaAs layers grown by Molecular Beam Epitaxy on a GaAs substrate with a 300 nm-thick $Al_{0.8}Ga_{0.2}As$ etch-stop layer. The nominal thickness of the GaAs layers is 25 nm in our case. The grown GaAs layer is non intentionally doped.

9.1.1.2 *Deposition of the back mirror*

A 200 nm-thick gold layer is deposited onto the GaAs layer by electron-beam assisted evaporation. Prior to gold deposition, a deoxidation of the GaAs surface is performed in a hydrochloric (HCl) solution (concentration = 20 % of the commercial solution) for one minute.

9.1.1.3 *Transfer of GaAs on gold by anodic bonding*

In order to transfer the ultra-thin crystalline GaAs layer on a mirror, we need to bond the mirror on a host substrate and then remove the initial substrate. The resulting surface must be perfectly planar in order to carry out patterning of a gold layer by electron beam lithography (EBL) and obtain the desired 2D grid. At LPN, we use a bonding technique called anodic bonding or "field assisted sealing". Anodic bonding technique was patented in 1968 by Pomerantz [165] and described further in another publication [166]. In the literature, this technique is mostly used to perform metal-to-glass or semiconductor-to-glass bonding. A process has been developed in our group to bond Al to glass at low temperature with successful results (See Ref. 167, p. 105-117).

Anodic bonding relies on the electrostatic force created between the Al layer and the Pyrex substrate by increasing the temperature and applying a high voltage. The Al layer is connected to the anode and the Pyrex substrate to the cathode. Pyrex glass is a sodium-rich glass, it contains sodium oxides (Na_2O) that can release sodium (Na^+) and oxygen (O^{2-}) ions. When the temperature increases, the mobility of the sodium ions Na^+ rises. The migration of sodium ions towards the cathode induces a depletion region close to the Al/Pyrex interface. All of the applied voltage is dropped in this space charge region. The high electric field created increases the electrostatic pressure applied on the two surfaces to be bonded. Once the surfaces are in contact under a high electrostatic force, chemical bonds are created leading to the strong anodic bonding between Al and Pyrex. The electrostatic force intensity depends on the temperature, applied voltage and sodium content in the Pyrex substrate.

At first, because of the non perfect planarity and the roughness of the surfaces, only a few contact points exist between Al and Pyrex. In these particular points, high electrostatic pressure is created leading to a local bonding of the surfaces as mentioned above. The electrostatic pressure also induces a local surface deformation. The contact area increases and the bonding propagates until the whole area is sealed.

Anodic bonding process constitutes of three steps:

1. 200 nm of Al are deposited by electron beam assisted evaporation on the gold mirror. A 20 nm-thick titanium layer is used as a barrier layer to avoid diffusion between gold and aluminium during bonding.

2. Anodic bonding requires very clean surfaces with a low roughness. The sample surface is cleaned before bonding in trichloroethylene, acetone

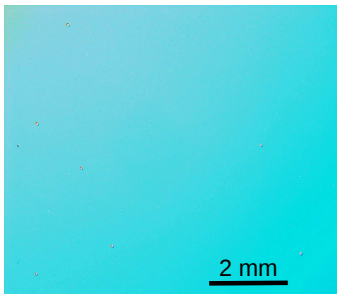

Figure 82: Photograph of the GaAs surface after layer transfer on a Au/Al/Pyrex substrate, taken with an optical microscope.

and isopropyl alcohol baths, two minutes each in sequence. The Pyrex substrate is cleaned with a Piranha solution ($H_2SO_4 : H_2O_2$, 2 : 1) for 15 minutes. The substrate is then cleaned with the same sequence and blow dried with nitrogen.

3. The anodic bonding is performed with a substrate bonder (SUSS MicroTec). The bonding of Al to Pyrex is done at 1700 V for 80 minutes at a maximum temperature of 210°C.

After bonding, the quality of the bonding can be checked by looking through the Pyrex substrate. For successful bondings, the Al surface appears homogeneous.

9.1.1.4 *Substrate removal*

The last step of layer transfer is the removal of the initial GaAs substrate with a wet etching technique (Fig. 81d). Because of the very low thickness (25 nm) of the GaAs active layer, it is critical to control the etching depth. An $Al_xGa_{1-x}As$ layer is therefore used as an etch-stop layer (in our case, $x = 0.8$). The ammonium hydroxide/hydrogen peroxide (NH_4OH/H_2O_2) solution is a standard etching solution for selective etching of GaAs/$Al_xGa_{1-x}As$ systems. The selectivity of this etch solution, defined as the ratio of the etching rates of GaAs to AlGaAs, is around 30 [168], which means that the AlGaAs etch-stop layer is etched at a rate of only 10 nm/min. Given the thickness of the AlGaAs layer (300 nm), this etch process has a selectivity sufficient in our case to ensure a controlled etching of the GaAs substrate without damaging the 25 nm-thick GaAs layer.

The AlGaAs layer is then etched with hydrofluoric acid (HF, 10 %) for a few seconds. Figure 82 displays a photograph of the GaAs surface obtained after anodic bonding and substrate removal. The GaAs layer appears blue with a very clean surface. The color is uniform on the whole surface, which shows that the GaAs thickness is constant on the entire film.

9.1.2 *Patterning of the 2D metallic grid*

We have fabricated 2D gold grids with a 500 nm period but a varying width (w = 105, 115 and 125 nm). The nanopatterning was done with electron beam lithography on a PMMA resist (30 g/L). After resist development, a gold film (thickness = 20 nm) was deposited with a 1 nm-thick germanium nucleation layer. More details on the patterning process by EBL are provided in *chapter 7* of the thesis. In the particular case of 2D grids, the resist lift-off is difficult because the areas to be lifted are closed surfaces. Therefore, we have used a thicker resist layer than in the case of the 1D gratings presented in *chapter 7* and use an ultrasonic bath to make the lift-off easier.

SEM images of 2D grids are shown in Fig. 83. We have measured the dimensions (grid width and period) of the grid on the whole patterned area. As shown in Figs. 84a and 84b, the period of the grid is constant over the whole area. However, we observe a 10 nm variation in the grid width between the centre of the patterned area and the edges. It is a direct consequence of the proximity effect (see *chapter 7*, subsection 7.1.4). The electron scattering in the different layers during electron beam exposure, i.e a wider pattern, leads to a higher exposure dose in the centre of the patterned area.

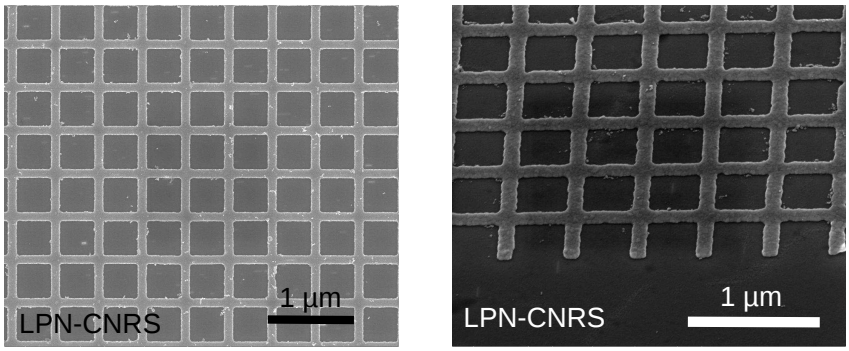

(a) (b)

Figure 83: SEM images of 2D gold grids patterned on a 25 nm-thick GaAs layer on a gold mirror. Fig. 83b is taken with a tilt angle of 45°.

9.1.3 *Deposition of the anti-reflection layer*

The final step of the fabrication process is to embed the metal grid in a silicon nitride layer. The top silicon nitride layer is deposited with a PLASSYS MP 800S sputtering reactor. The nominal thickness of the SiN_x layer is 60 nm, as modeled in the numerical calculations presented in *chapter 8*. The profile of the silicon nitride layer is discussed in the following.

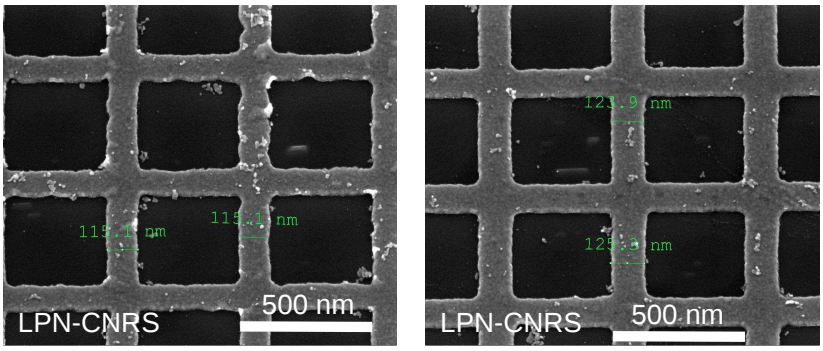

(a) (b)

Figure 84: Measurement of the width of 2D gold grids ($p = 500$ nm, nominal width $= 125$ nm) patterned on a 25 nm-thick GaAs layer on a gold mirror. SEM images taken on (a) the edges and (b) the center of the patterned area. The measured grid width is 115 nm on the edges and around 125 nm in the middle of the pattern.

9.2 OPTICAL CHARACTERIZATION OF THE AU/GAAS/AU STRUCTURE

We have carried out reflectivity measurements in order to estimate the optical performances of the patterned structures. The measurements were performed on a SENTECH reflectometer. The reflectivity at normal incidence is measured and normalized with respect to a reference sample. The total absorption is then obtained assuming no light transmission through the substrate[1]. In this section, we present the measurements done on the Au/GaAs/Au structure before SiN_x deposition. We then discuss in the next section the optical response of the complete SiN_x(Au)/GaAs/Au structure and show the effect of the additional anti-reflection coating layer.

9.2.1 *Optical response of the planar GaAs/Au structure*

We have measured the optical response of the unpatterned GaAs/Au structure. The measurement of this planar reference structure allows us to highlight the light-trapping effect of the gold grid. It is also used to adjust our model for the numerical calculations. In particular, we will discuss the effective thickness of the GaAs layer and the choice of gold optical constants.

Figure 85a shows the measured total absorption spectrum (black curve) of the GaAs/Au depicted in the inset. In an Air/GaAs/Au stack, only one absorption peak is observed at $\lambda \sim 650$ nm due to vertical Fabry-Perot resonances in the GaAs layer. The nominal thickness of the GaAs layers is 25 nm. We have calculated the total absorption in a GaAs/Au stack with a varying GaAs thickness (h_s) between 22 and 25 nm (colored curves). The optical constants of GaAs and

1 Doing so, we neglect light scattering due to surface inhomogeneities as well as light diffraction in free space that can occur at short wavelengths.

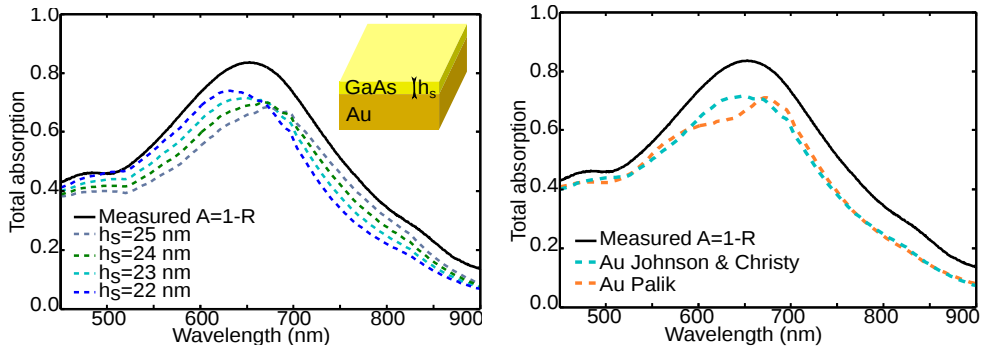

Figure 85: Total absorption spectrum of a plane GaAs/Au structure (black curve in Figs. a and b) compared with numerical calculations. (a) The GaAs thickness h_s of the modeled structure varies betwen 22 and 25 nm. Inset: schematic of the structure. (b) Comparison of the absorption spectrum calculated with gold data from Johnson and Christy [143] (blue dashed line) and Palik [116] (orange dashed line).

Au[2] used in the calculations here are taken from Refs. 116 and 143 respectively. We see that the resonance wavelength shifts towards long wavelengths when h_s increases, as expected for a Fabry-Perot resonance. If we take the position of the main peak ($\lambda \sim 650$ nm) as the fitting criterion, the best fit is obtained for $h_s = 23$ nm. In the following, all the calculations will be done for a 23 nm-thick GaAs layer.

As shown in Fig. 85b, we have also compared the calculated response obtained with gold data from Johnson and Christy [143] (orange dashed line) and Palik [116] (blue dashed line). Both curves have been calculated with a GaAs layer thickness of 23 nm. The shape of the curve obtained with Johnson and Christy agrees better with the experimental data. Palik's data give rise to a splitting of the main absorption peak observed on the measured spectrum in two distinct features at 600 and 675 nm. In the following, all the calculations will be done with gold optical constants taken from Johnson and Christy [143]. Note that for the feature at short wavelengths ($\lambda \sim 480$ nm), data from Palik give a more accurate estimation of the peak position.

9.2.2 *Measured absorption spectrum of the patterned Au/GaAs/Au structure*

Figure 86 displays the measured total absorption spectrum of a patterned Au/-GaAs/Au structure (red curve) with $w = 125$ nm. The response of the flat GaAs/Au structure (black curve) is shown for the sake of comparison. A schematic of the 2D patterned Au/GaAs/Au structure is given in the inset.

When we add a patterned gold layer onto the planar GaAs layer, the broad Fabry-Perot peak is splitted in two peaks at $\lambda_1 \sim 600$ nm and $\lambda_2 \sim 671$ nm. The

2 We have considered similar optical constants for the grid and the back mirror. A more in-depth model could use different data for the front and back gold elements to take into account the metal alteration during the fabrication process.

Fabry-Perot resonances in the Air/GaAs/Au and the Au/GaAs/Au cavities do not have the same phase shift, thereby leading to different values of the resonance wavelength. With the gold grid, we achieve nearly perfect absorption ($A_{tot} \sim 0.98$) at $\lambda_2 \sim 671$ nm. We see that the 2D grid leads to an absorption enhancement on the $520 - 775$ nm range with respect to the planar GaAs/Au structure. Note that the addition of the 2D grid does not affect the spectral width of the absorption band.

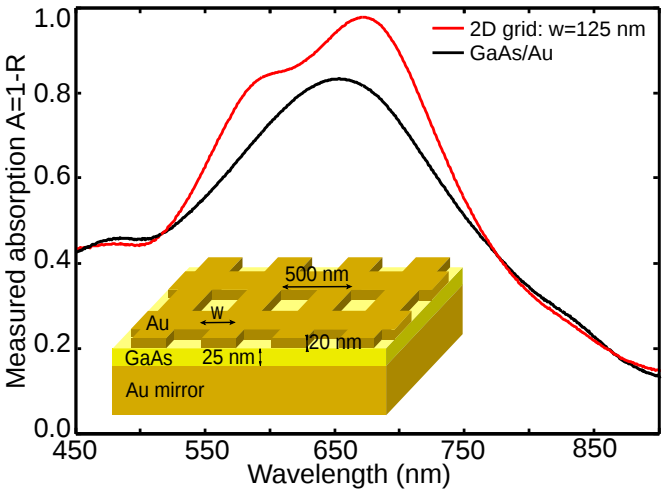

Figure 86: Measured absorption spectra of a structure with a 2D gold grid ($h_m = 20$ nm, $p = 500$ nm, $w = 125$ nm) (red curve) and a planar GaAs/Au structure (black curve). Inset: schematic of the patterned Au/GaAs/Au structure.

9.2.3 *Influence of the grid width*

We have fabricated structures with a varying width of the grid: $w = 105$, 115 and 125 nm. Figure 87 shows the effect of the grid width on the measured (Fig. 87a) and calculated (Fig. 87b) absorption spectra. The evolution of both experimental and calculated spectra when the width w varies are in good agreement.

On the one hand, the absorption peak at $\lambda_1 \sim 600$ nm blueshifts when the grid width increases. We can note that both the measured wavelength resonance and absorption intensity of the peaks are lower than expected with the calculations. On the other hand, the peak at $\lambda_2 \sim 671$ nm shifts towards long wavelengths for a wider grid, i.e for a higher grid fill factor. The evolution of peaks 1 and 2 seen in Fig. 87 shows that splitting of the Fabry-Perot peak increases when the fill factor increases, which is consistent with the results already discussed in *chapter* 8. Note that the calculated absorption spectrum exhibits an additional peak at $\lambda_3 \sim 830$ nm which is not resolved experimentally.

It is notheworthy that the wavelength gap between the two peaks is larger in the case of the experimental results: for $w = 125$ nm, we measure $\lambda_2 - \lambda_1 = 81$ nm whereas the calculations give $\lambda_2 - \lambda_1 = 65$ nm. It may be due to the fact that we have modeled a 2D grid with the nominal fill factor which may be lower than the effective value. For instance, as shown previously in Fig. 84, in the case of a grid with a nominal fill factor value of 0.25 ($p = 500$ nm and $w = 125$ nm),

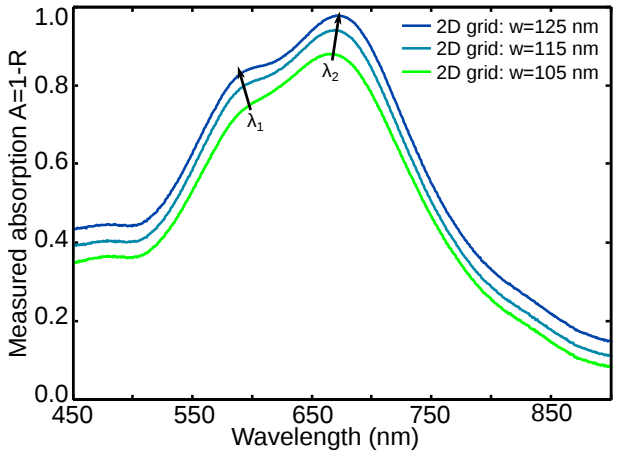

(a)

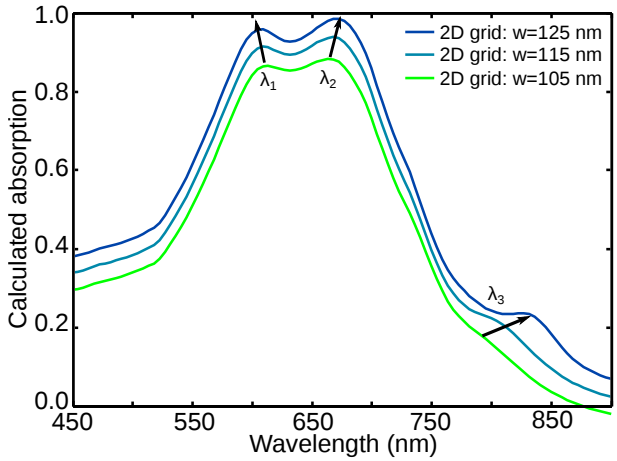

(b)

Figure 87: Comparison of the measured (a) and calculated (b) absorption spectra of a 23 nm-thick GaAs layer on gold with a 2D gold grid ($h_m = 20$ nm, $p = 500$ nm, varying width w). In each figure, two of the curves ($w = 105$ and 115 nm) have been downshifted vertically (of 0.04 for $w = 105$ nm and 0.085 for $w = 115$ nm) to ensure a good reading of the peak position.

the measured grid width varies between 125 nm in the center and 115 nm on the edges because of the proximity effect. The mean value of the measured grid width is 120 nm, which leads to an effective fill factor value of 0.24. The reduction of the grid width compared to the nominal value induces a decrease of the phase shift due to reflection on the top GaAs/Au interface, leading to a lower resonance wavelength than for the calculated spectrum. Note that it has an impact only on the resonances in the Au/GaAs/Au cavity, thereby on the first peak at short wavelengths. The position of the second peak ($\lambda_2 \sim 671$ nm for $w = 125$ nm) is well predicted by the calculations.

In order to provide a better understanding of the absorption mechanism at stake, we have studied the spatial distribution of the electric field. Figure 88 displays the calculated maps of the electric field intensity $|E|^2$ for a 2D gold

grid (h_m = 20 nm, p = 500 nm, w = 125 nm) at the three main resonance wavelengths (λ = 600, 671 and 831 nm). The orientation of the magnetic field H is shown as an inset.

At 600 nm, the electric field is strongly confined in the GaAs layer below the gold wires. It is consistent with the attribution of the peak to a Fabry-Perot resonant mode in Au/GaAs/Au cavities. At 671 nm, the distribution of the electric field is more complex. Still, we see that within the GaAs layer, the electric field intensity exhibits a minimum below the metal wires, which means that absorption occurs mainly below the grid holes.

For an excitation at $\lambda_3 \sim 830$ nm, the four maxima of the electric field located in the Au/GaAs/Au cavities are the signature of a third-order Metal/Insulator/Metal (MIM) resonance [87]. The coupling of surface plasmons propagating at the two GaAs/Au interfaces leads to an increase of the effective index of the plasmonic mode. This system can be modeled as an horizontal Fabry-Perot cavity with a size equal to the width of the metallic wires w. For this resonance, the peak position strongly depends on the grid width w: the absorption peak shifts of 40 nm towards long wavelengths when w increases from 105 to 125 nm as can be seen in Fig. 87b. As discussed previously (Fig. 84), the width of the wires is not uniform on the whole patterned area. This variation could explain the fact that we cannot see the third peak in the measured absorption spectra.

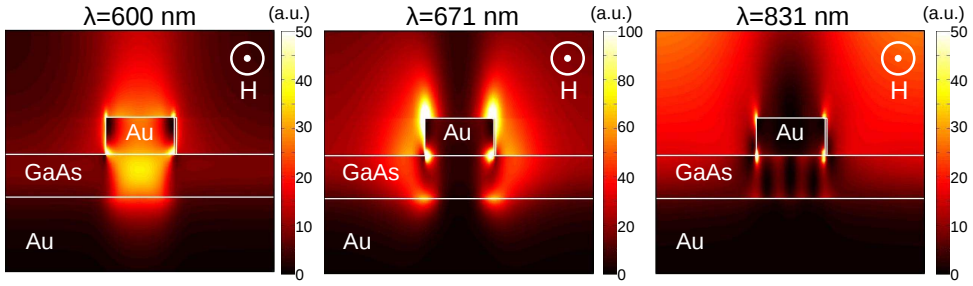

Figure 88: Maps of the electric field intensity $|E|^2$ at the three main resonance wavelengths (λ = 600, 671 and 831 nm) for the Au/GaAs/Au structure with a 2D gold grid (h_m = 20 nm, p = 500 nm, w = 125 nm). Excitation at normal incidence, the magnetic field H is perpendicular to the cross-section as shown in inset. All the intensity maps have the same unit.

9.3 ADDITION OF AN ANTI-REFLECTION COATING LAYER

The metallic array is embedded in a transparent anti-reflection coating layer in order to:

- protect the metal grid, in particular in the case of silver metal
- reduce reflection at short wavelengths
- broaden the absorption spectrum with additional peaks.

We have deposited a 60 nm-thick silicon nitride (SiN_x) layer by RF magnetron sputtering onto the Au/GaAs/Au structure discussed previously. The total absorption spectrum measured for the SiN_x(Au)/GaAs/Au structure (Fig. 80) is

shown in Fig. 89a. We see that the optical response is dramatically improved compared to the Au/GaAs/Au structure.
First, we report a reflection lower than 20 % at 450 nm. It represents a threefold reduction compared to the Au/GaAs/Au structure which exhibits a reflection of 60 % at 450 nm (Fig. 86). Second, we see that a broad and nearly flat absorption band (absorption intensity higher than 80 %) is achieved between 450 and 830 nm thanks to the combination of four absorption peaks. For $\lambda > 850$ nm, the absorption efficiency drops in accordance with the increased absorption depth of bulk GaAs.

In order to understand the measured absorption spectrum, we have calculated numerically the response of the fabricated $SiN_x(Au)/GaAs/Au$ structure. A SEM image of the gold grid after conformal deposition of the SiN_x layer is displayed in Fig. 89b. We have taken into account this surface profile in the numerical calculations following the schematic given in Fig. 89d. As shown in Fig. 89c, the calculations exhibit the same number of absorption peaks than the measurements and the peak positions predicted by the numerical calculations are in good accordance with the experimental results. A slight spectral shift is evidenced for the resonances at long wavelengths. This may be due to the difference between the real dimensions and the nominal width used in the calculations.

Note that the measured absorption is the total absorption in the structure, i.e it includes also the parasitic absorption losses in the metallic parts, which are non negligible in the case of gold. The absorption fraction lost in the grid and the back mirror can be estimated from the calculated absorption spectrum. For this structure, we find that 51 % of absorbed photons are lost in the metallic parts (grid + back mirror). As shown in *chapter* 8, we expect much better performances with $SiN_x(Ag)/GaAs/Ag$ structures partly because of reduced parasitic absorption losses in the metal.

9.4 CONCLUSION

In this chapter, we have reported the fabrication of ultra-thin Au/GaAs/Au structures with 2D gold nanogrids on 25 nm of crystalline GaAs transferred on a gold mirror. We have demonstrated experimentally that we could achieve a broadband total absorption spectrum with absorption over 80 % between 450 and 830 nm at normal incidence. This is better than the results reported by Aydin et al. [86] (average total absorption at normal incidence of 0.71 between $400 - 700$ nm) and very close to Söndergard et al. [169] (total absorption over 87 % on $450 - 850$ nm).

Furthermore, in the approaches cited above, the light is absorbed entirely in the metal. In order to integrate plasmonic structures into efficient photovoltaic devices, light should be absorbed mainly in the active semiconductor layer. Our experimental study shows that using our 2D grid design, light absorption can be confined in a semiconductor layer in a subwavelength volume while keeping

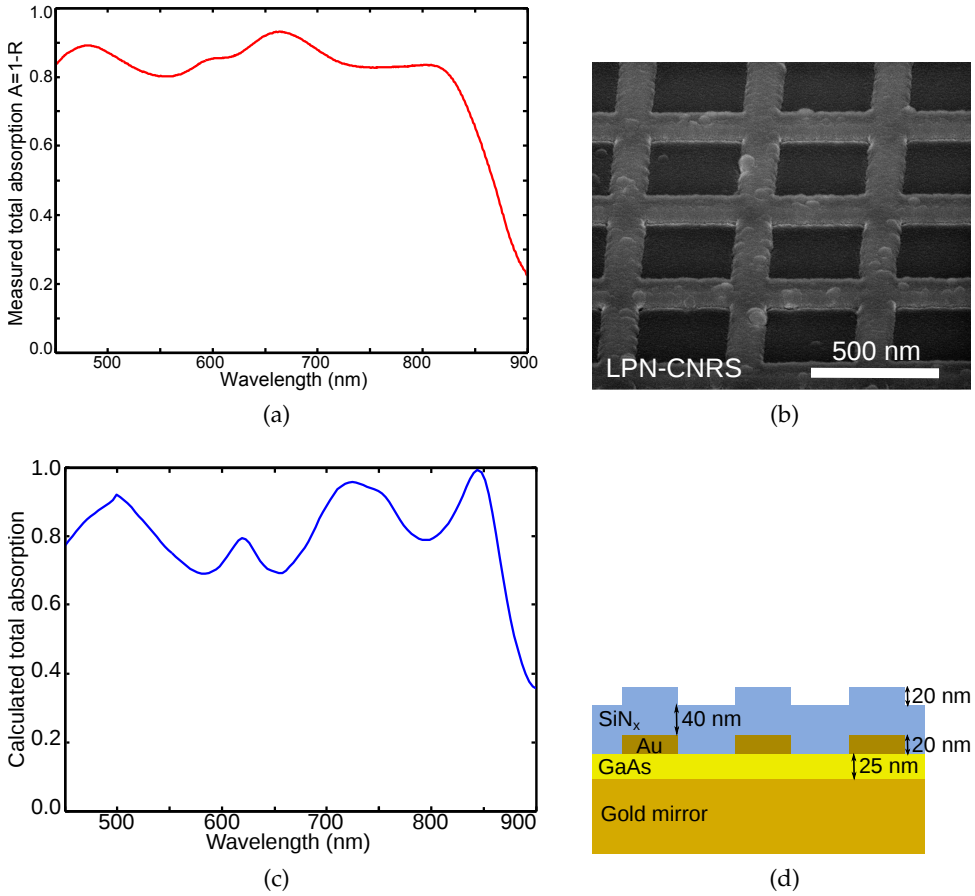

Figure 89: Measured (a) and calculated (c) total absorption spectra of a 23 nm-thick GaAs layer on gold with a 2D grid of gold nanowires ($h_m = 20$ nm, $p = 500$ nm, $w = 125$ nm) embedded in a 60 nm-thick silicon nitride layer. (b) SEM image of the 2D gold grid after SiN_x deposition. (d) Schematic of the modeled structure, taking into account the profile of the top SiN_x layer.

good performances[3]. As a matter of fact, to our knowledge, this is the broadest absorption band reported for such an ultra-thin semiconductor layer.

Our experimental study confirms the potential of the nanopatterned resonant front contact for ultra-thin GaAs devices. A short-term perspective of this work is to fabricate devices to carry out photocurrent measurements. The fabrication process that has already been developed and presented in this chapter could be used with additional steps to etch mesa and deposit metallic pads to collect the current in the front side.

3 In *chapter* 8, we have shown that we could predict a short-circuit current density of $J_{th} = 21.6$ mA/cm^2 for a 25 nm-thick GaAs layer.

9.5 SUMMARY

We have developed a fabrication process to realize demonstrators. Ultra-thin (thickness = 25 nm) crystalline GaAs layers have been transferred on metallic mirrors before being patterned with a 2D metallic grid.

Structures with a 2D gold grid embedded in a silicon nitride layer have been optically characterized. The fabricated structures evidence the combination of Fabry-Perot resonances in the GaAs layer and surface modes due to the metallic grid.

The measured absorption spectra exhibit a broad absorption band ($A_{tot} > 80\,\%$ between 450 and 830 nm) in good agreement with the numerical calculations. We have shown the potential of the 2D grid design to confine light in a very thin semiconductor layer. It paves the way towards the realization of high-efficient ultra-thin GaAs devices.

Part IV

LIGHT-TRAPPING IN ULTRA-THIN CRYSTALLINE SILICON SOLAR CELLS

10

INTRODUCTION TO EFFICIENT ULTRA-THIN CRYSTALLINE SILICON SOLAR CELLS

Contents

Parts 2 and 3 of the thesis have been focused on light-trapping strategies for thin-film solar cells (a-Si:H and GaAs). However, the potential of nanophotonics to confine and control light in very small volumes is also applicable to other photovoltaic materials. In particular, advanced light-trapping strategies, such as photonic crystals or plasmonic nanostructures, could allow a thickness reduction of silicon wafers of a factor 20 to 100 with respect to commercial wafers, which would represent a breakthrough in the c-Si technology. My work on thin film silicon solar cells has been done in the framework of the ANR project NATHISOL. In this chapter, we first introduce the motivations towards ultra-thin c-Si solar cells before presenting the objectives of the NATHISOL project. Two main challenges of the project are to produce thin films of high quality c-Si material and implement light-trapping schemes adapted to thin films (thickness of a few microns). In the following, we address these two issues and give an overview of the solutions proposed in literature.

10.1 MOTIVATIONS TOWARDS ULTRA-THIN C-SI SOLAR CELLS

Despite the development of thin-film technologies, crystalline silicon technology still dominates the photovoltaics market with a share of 85 % in 2010. In an article published in 2009, Martin Green [22] reviews all the improvements made since the first silicon solar cell fabricated in 1941 towards the current efficiency record of 25 %. The main advantages of crystalline silicon, compared to thin film silicon technologies are:

1. the use of an abundant and non-toxic material
2. the huge knowledge and know-how on the silicon-based technology
3. a high minority-carrier lifetime responsible for the high conversion efficiency and long-term stability of the modules.

However, there is still a strong potential for further cost reduction. In particular, the production cost of c-Si solar cells is dominated by two factors: the substrate cost and the energy costs (due to high temperature processes). On the other hand, thin-film technologies, such as amorphous or microcrystalline silicon solar cells, benefit from a reduced amount of raw material and large-area deposition methods on inexpensive substrates. Their competitiveness is limited by their conversion efficiency which is much lower than crystalline silicon solar cells because of increased defect density (current a-Si:H record: $\eta \sim 10.1\,\%$ [162]). In the case of amorphous silicon, the Staebler-Wronski effect strongly reduces the long-term stability of the photovoltaic devices.

With the ability to control light absorption at a very small scale, the emerging of the field of nanophotonics has opened new possibilities to achieve high efficiencies with a reduced crystalline silicon layer thickness. Therefore, current research on thin-film crystalline silicon solar cells is driven by the opportunity of finding a "meet-in-the-middle" that would combine the best of both technologies, as defined by Dross et al. in a review article published in 2012 [170]. In particular, the thin-film c-Si technology should allow to produce thin c-Si films with a large-area and low temperature deposition process while keeping a high crystalline quality for the material. Another challenge is to be able to produce thin c-Si solar cells on low-cost substrates. Several layer transfer processes have already been proposed in literature as will be presented in *chapter 11*.

10.2 DESCRIPTION OF THE ANR PROJECT NATHISOL

The ANR project NATHISOL (NAnophotonics for THIn film crystalline silicon SOLar cells) has started in November 2012. The project is done between four partners:

- Nanotechnology Institute of Lyon (INL)
- Laboratory for Photonics and Nanostructures (LPN)
- Laboratory of Physics of Interfaces and Thin Films (LPICM)
- TOTAL Energies Nouvelles[1].

The aim of the project is to reach a conversion efficiency of 13.5 % with 2 µm-thick crystalline silicon solar cells. As described in this chapter, several strategies have been developed in literature to obtain thin crystalline silicon films.

1 TOTAL Energies Nouvelles R&D, Tour Michelet 24 cours Michelet - La Défense 10 92069 Paris La Défense Cedex

The project is based on epitaxial thin ($2-5$ µm) crystalline silicon films deposited with low temperature ($< 200°C$) PECVD at LPICM. As developed in subsection 10.3.2, this deposition technique leads to thin c-Si solar cells with high crystalline quality and high fill factor values but limited short-circuit current density because of the reduced thickness of the c-Si layer.

Our approach relies on the transfer of the epitaxial layer on a host substrate in order to integrate light trapping strategies going from a simple metallic back reflector to advanced photonic and plasmonic structures. The first milestone of the project is depicted in Fig. 90. The technological developments and first experimental results obtained will be presented in the following chapter.

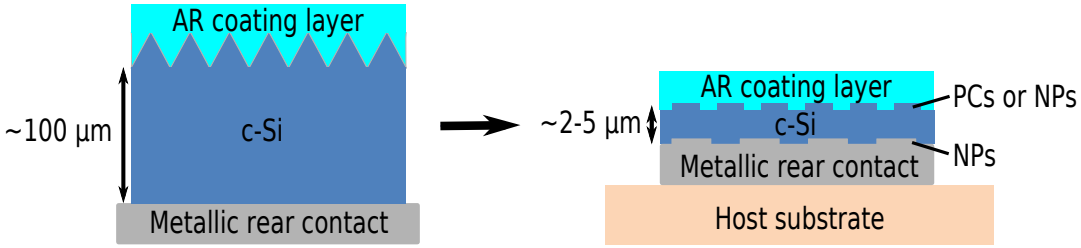

Figure 90: Towards thin crystalline silicon cells: from wafer-based cells to high-efficient thin film c-Si cells. The aimed structure is based on thin epitaxial c-Si films transferred on a low-cost substrate which allows the integration of light trapping strategies such as photonic crystals (PCs) or plasmonic nanoparticles (NPs).

10.3 FABRICATION OF HIGH-QUALITY CRYSTALLINE SILICON THIN FILMS

10.3.1 *Overview of the existing technologies*

As presented in Ref. 170, several approaches have been developed to produce thin c-Si films.

The first way is to use a kerf-free wafering method as an alternative to conventional sawing of wafers. Standard kerf wafering leads to an average material loss of $40-50\,\%$ [170]. Several methods have been developed to reduce material losses during the sawing process: light ion implantation, laser wafer cutting, electrochemical cutting. Another strategy called stress-induced lift-off method (SLiM-Cut process) has been proposed at IMEC to slice and transfer very thin wafer-based films (thickness $= 30-50$ µm). To date, they have demonstrated a $10\,\%$ efficiency [171] but are still working on reducing the process temperature to improve the material quality [170].

The second approach relies on the production of epitaxially-grown silicon foils on glass. Most of the developed technologies are based on a layer-transfer process: the silicon film is first grown on a wafer substrate and then detached and transferred on a host substrate. A weak layer (silicon oxide or porous silicon layer) is used as a sacrificial layer. The current record for this technology is hold by Solexel [21]: a $20.1\,\%$ conversion efficiency has been reported for a 43 µm-thick transferred c-Si layer. The major drawback of this technology is the

need of a high-throughput epitaxy reactor. IMEC has developed an alternative approach to produce ultra-thin c-Si foils without epitaxy [172, 173]. Nanocavities (size $\sim$ 550 nm) are formed at a controlled depth of a silicon wafer using reactive ion etching. The wafer is then annealed in order to merge all the cavities into a single void. The resulting structure is a thin silicon film that can be separated from the wafer substrate by breaking the cavity. To date, their best result is a 4.2 %-conversion efficiency for an heterojunction solar cell based on a 1 µm-thick silicon layer [172]. This "Epifree" approach has also been upscaled to large area and thicker foils (up to 2.4 µm).

The third route available is to deposit directly crystalline silicon on glass. The techniques giving the best results so far are solid phase crystallization (SPC) and aluminium-induced crystallization (AIC). In both cases, silicon material with low crystallographic quality (amorphous silicon or microcrystalline silicon) is deposited on non-silicon substrates. It is then recrystallized into a material called polycrystalline silicon (pc-Si). To date, the highest conversion efficiency reported is 10.5 % obtained by CSG Solar for a thin-film c-Si submodule composed of 20 cells [174]. Each cell is made of ultra-thin polycrystalline silicon films (thickness $= 1 - 2$ µm) produced by SPC on borosilicate glass. IMEC has worked on pc-Si cells fabricated using the AIC technique. They demonstrated 8.5 % of efficiency for pc-Si deposited by CVD on a seed layer grown with AIC on an alumina-ceramic substrate [175, 176].

The ANR project NATHISOL aims at producing crystalline silicon solar cells with thicknesses of a few microns ($2 - 5$ µm). To date, kerf-free wafering cannot be used to obtain silicon films thinner than 10 µm. As for the other techniques (Epifree and direct deposition of pc-Si on glass), the produced micron-thick thin films suffer from low crystalline quality which limits the conversion efficiency of the cell. The NATHISOL project is therefore focused on the application of the thin-film PECVD technique developed at LPICM to produce high quality epitaxial crystalline silicon films as presented in the following subsection.

10.3.2 *Epitaxial crystalline silicon films grown by PECVD*

Pere Roca i Cabarrocas and his group have demonstrated the possibility to grow high quality silicon material with PECVD with a various crystallinity from amorphous to microcrystalline and even crystalline silicon, while keeping temperature below 200°C [148, 150, 177–179]. The deposition of the c-Si epitaxial layers (epi-layers) is done using the same RF-PECVD reactor as for a-Si:H deposition (see description in *chapter* 7, subsection 7.1.3). The structural properties of the deposited epi-layers have been investigated using Raman spectroscopy [178], spectroscopic ellipsometry [178, 179] and transmission electron microscopy measurements.

In particular, Cariou et al. [179] have reported in a recent article the growth of epitaxial intrinsic c-Si layers obtained by PECVD at 165°C on p-doped (100) c-Si substrates. Spectroscopic ellipsometry measurements have been performed to check the thickness and crystallinity of the deposited epi-layers. As shown in Fig. 91a, the good agreement between the Im(ε) ellipsometric spectrum of

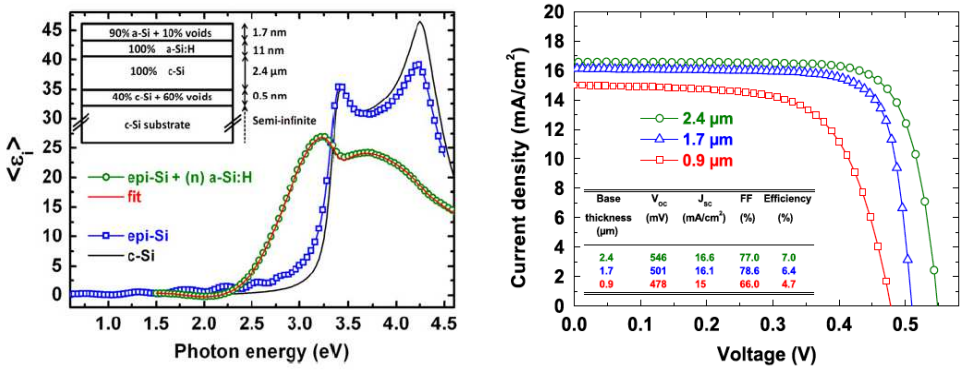

(a) (b)

Figure 91: Properties of thin crystalline silicon solar cells deposited at LPICM [179]. (a) Ellipsometric spectra of a monocrystalline wafer (black line), an epitaxial layer (blue squares) and an heterojunction solar cell (n^+ a-Si:H/epi Si/p^{++}wafer) (green circles). The red line is a fit of the data to the model shown in the inset. (b) Current-voltage characteristics of solar cells based on epitaxial c-Si films with various thicknesses.

an epitaxial layer and the spectrum of the bare c-Si wafer suggests that the epi-layer has the same structural composition and crystalline quality as the wafer. The amplitude of the peak at 4.2 eV reflects the c-Si surface quality and the presence of a thin oxide layer on the surface [180]. Moreno et al. [180] have fitted ellipsometry measurements with a model of an epitaxial c-Si layer with a surface roughness of 2 nm (± 1 nm depending on the sample) and a thin oxide layer ($0 - 5$ nm) due to oxidation after deposition. The spectrum of the epitaxial layer exhibits also oscillations at low energies due to interferences between light reflecting on the epi Si/air and epi Si/wafer interfaces. The period of the oscillations is in agreement with the thickness of the epitaxial layer of 2.4 µm. As a matter of fact, Moreno and Roca i Cabarrocas [178] have shown that if the growth of the Si epi-layer is performed at high hydrogen dilution, a thin porous interface layer (up to 9 nm) is formed between the epi-layer and the substrate. The resulting oscillations allow us to determine precisely the thickness of the epitaxial film deposited. This fragile interface is also used to peel the epi-layer off the wafer and transfer it on a host substrate [178].

In order to assess the electronic quality of the epi-layers, they are used as absorbers in heterojunction cells (n^+a-Si:H/epi Si/p^{++}wafer). A n^+ doped a-Si:H layer is deposited on the non intentionally doped epi layer in the same PECVD reactor without breaking the vacuum. The measured ellipsometry spectrum of an heterojunction with a 2.4 µm-thick epitaxial intrinsic c-Si layer is shown in Fig. 91a and fitted with a model described in the inset. The fit of the stack (red curve) shows a very good agreement with the experimental spectrum, thus validating the model of a 2.4 µm-thick c-Si layer with a 100 % crystallinity separated from the wafer by a porous interface (thickness = 0.5 nm and porosity = 60 % in the model). The performance of the cells has been measured for epi-layers with a thickness between 0.9 and 2.4 µm. The results are shown in Fig.

91b. The best cell ($\sim$ 2.4 µm) corresponds to $V_{OC} = 0.546\,V$ and $FF = 0.77$, which leads to a conversion efficiency of 7 %[2]. Let us compare these results to another epitaxy technique called hot wire chemical vapor deposition (HWCVD) [182, 183]. Alberi et al. have reported 2 µm-thick c-Si films grown by HWCVD with a conversion efficiency of $\eta \sim 6.3\,\%$ ($V_{OC} = 0.57\,V$ and $FF = 0.725$) [183]. We see that the films obtained by PECVD exhibit better characteristics and in particular, higher fill factor values.

EQE experiments (not shown here, see Ref. 179) have been performed on the cells with the 2.4 µm-thick epi layer in order to check the crystalline quality. At long wavelengths ($\lambda > 600$ nm), the EQE is low (equal to 25 % at 800 nm) because of the low absorption in c-Si on this wavelength range. At short wavelengths, light absorption in c-Si is strong, however the measured EQE is only 20 % at 400 nm. Given that short wavelength EQE is sensitive to surface passivation, it is thought that the poor EQE in this wavelength range reflects a rough interface with high defect density between the a-Si:H emitter layer and the epi c-Si layer. In the middle of the visible range, a maximum value of 75 % is reported around 580 nm. In this wavelength range, the collection efficiency being close to 1, the epitaxial c-Si layers have a crystalline quality sufficient to realize photovoltaic devices.

However, in order to compete with wafer-based silicon solar cells, thin-film silicon solar cells should aim at a conversion efficiency higher than 15 %. The conversion efficiency of the epitaxial layers obtained by PECVD is limited by the low short-circuit current density value (the latest results report a value of $J_{SC} = 20\,\mathrm{mA/cm^2}$ for 3.4 µm [181]). The generated photocurrent stems from the photons absorbed in a single pass of light in the 2 µm-thick absorber layer. A possible solution to increase the efficiency is to integrate light trapping solutions in the thin film c-Si solar cell. In the following section, we will give an overview of the solutions developed to enhance light absorption in thin crystalline silicon films.

10.4 OVERVIEW OF LIGHT TRAPPING SOLUTIONS FOR THIN-FILM CRYSTALLINE SILICON SOLAR CELLS

10.4.1 *Introduction*

The current 25 % efficiency record has been obtained for a monocrystalline silicon solar cell by the University of New South Wales, Australia in 1998 with a passivated emitter rear locally diffused cell (PERL cell) [22, 184]. The record cell exhibits a short-circuit current density of $J_{SC} = 42.7\,\mathrm{mA/cm^2}$. The red response has been improved compared to the last record thanks to light trapping features as can be seen in Fig. 92. In the front surface, a double layer anti-reflection coating is used to reduce reflection losses. A rear aluminum reflector and an inverted pyramid texturation of the surface increase the optical path length of long wavelength photons that are not absorbed in a single pass through the

2 Cariou et al. have recently reported improved results with a 8.5 % efficiency for 3.4 microns of epitaxial crystalline silicon [181].

absorber. As for the blue response, a lightly doped n surface is used to improve the performances of the cell in this wavelength range [22].

In the following, we describe further the conventional light trapping techniques used in wafer-based Si solar cells (anti-reflection coating layer and surface texturing) and we present innovative approaches from literature using diffraction gratings and nanostructures to enhance light absorption in thin crystalline silicon solar cells.

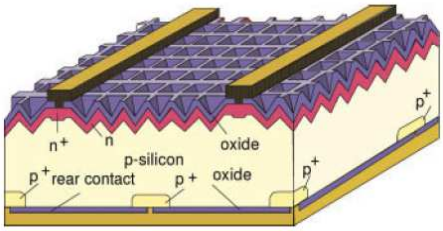

Figure 92: Schematic of the record crystalline silicon PERL cell [22].

10.4.2 *Anti-reflection coating layers*

A standard bare silicon surface reflects more than 35 % of incoming light at 600 nm. The easiest way to reduce reflection on the front surface of the cell is to use an anti-reflection coating (ARC) layer, i.e to deposit a thin layer of dielectric material on the silicon surface. ARC layers are commonly used to coat displays and windows or optical components such as lenses. For instance, in the everyday life, eyeglasses are coated in order to eliminate reflections of light from the front and back surfaces of lenses.

Let us consider a single ARC layer (thickness e, refractive index n). As shown in Fig. 93a, the incoming light gives rise to multiple reflected rays due to reflection at the air/dielectric (reflected ray R_1) and dielectric/silicon (reflected ray R_2) interfaces. These reflected waves interfere with each other because of the path difference $d = \frac{2ne}{\cos r}$ between R_1 and R_2, with r the refracted angle in the dielectric layer. In our case, we want the total reflected light on the cell to be

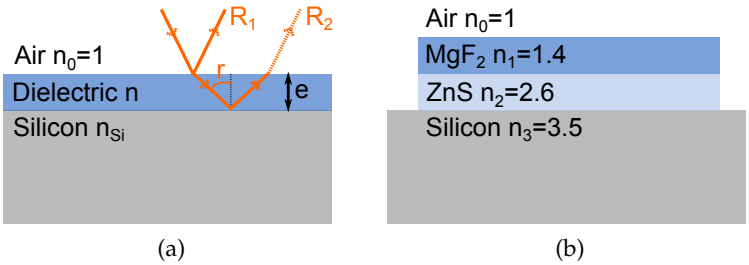

Figure 93: (a) Description of a basic anti-reflection coating layer. (b) Schematic of a standard double layer anti-reflection coating. The refractive index values of the materials are given for $\lambda = 600$ nm.

zero: the interferences between R_1 and R_2 should be destructive. The thickness and refractive index of the ARC layer are therefore chosen so that:

1. the phase shift between the waves R_1 and R_2 is equal to π
2. R_1 and R_2 have the same amplitude.

These two conditions lead respectively to $e = \frac{\lambda}{4n}$ and $n = \sqrt{n_{Si} \times n_0}$, with n_0 the refractive index of air, in the case of normal incidence ($r = 0$). Note that the ARC layer is then optimized to achieve $R = 0$ for one specific wavelength at normal incidence. Usually, R is minimized where the incoming photon flux is maximal, i.e $\lambda \sim 650$ nm. For instance, the standard thickness for an ITO ARC layer is $e = 80 - 100$ nm for a refractive index of $n = 1.8$ at 650 nm.

The major drawback of ARC layers is that their efficiency is limited to narrow wavelength band and angular range. In order to increase the anti-reflection effect, improved designs use a double layer anti-reflection coating (as for the PERL cell). A standard example is the combination of MgF_2 and ZnS as described in Fig. 93b. The variation of the refractive index changes more gradually between the air index ($n \sim 1$) and the silicon index ($n_{Si} \sim 3.5$). It allows to broaden the wavelength range where the reflection is minimized.

In the framework of the thesis, the architecture considered is a heterojunction cell (c-Si/a-Si:H). In this case, because of the low conductivity of doped amorphous silicon (see *chapter* 5, subsection 5.2.2), we cannot apply directly a dielectric as an ARC. The use of a transparent conductive oxide is required to ensure the current collection at the front contact.

10.4.3 *Front surface texturing*

Another conventional technique used for industrial crystalline silicon solar cells to reduce light reflection is the texturation of the front silicon surface. Most monocrystalline silicon-based solar cells combine ARC layers and a surface texturation to minimize reflection losses on the front surface. In the case of monocrystalline silicon, a random pyramid texturation is easy to achieve with low-cost and large-area fabrication processes. Anisotropic wet etching of (100) silicon substrate, usually performed with potassium hydroxide (KOH) or tetramethylammonium hydroxide (TMAH), leads to a selective etching along the (111) crystallographic planes. The resulting surface presents randomly spaced and sized pyramids as shown in Fig. 94b.

Regular arrays of inverted pyramids are also a standard surface texturing of silicon solar cells. In this case, the pyramids are etched down into the silicon surface. The areas to be etched are defined using a patterned grid as an etching mask. Fig. 94c shows a SEM picture of 500 nm-large inverted pyramids fabricated at LPN.

Front surface texturing also allows us to increase the cell's effective optical thickness. Long wavelength photons that are weakly absorbed and reflected towards the surface can be trapped due to total internal reflection on the front texturation. Therefore, surface texturing is often combined with a rear metallic mirror such as in the case of the PERL cell (Fig. 92). The use of a metallic

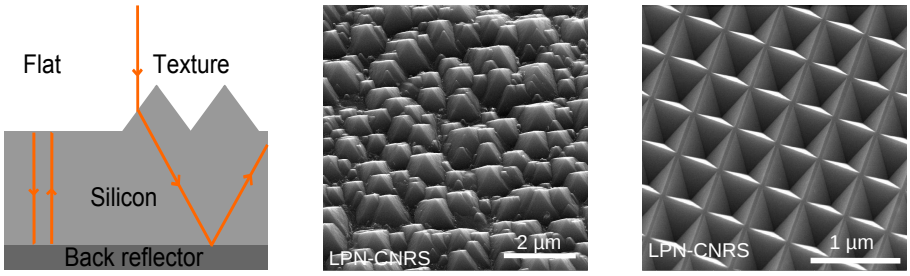

(a) (b) (c)

Figure 94: (a) Schematic of path length enhancement mechanism due to front surface texturing. (b) SEM picture of a random pyramid texturation obtained by anisotropic etching of c-Si with a mixture of potassium hydroxide and isopropanol at LPN. (c) SEM picture of inverted nanopyramids obtained by KOH wet etching of c-Si at LPN.

rear reflector in a flat cell doubles the optical path length of the photons in the cell. If combined with a front texturation, the photons can be trapped for multiple passes in the cell as shown in Fig. 94a. For instance, Mavrokefalos et al. have shown that 10 µm-thick crystalline silicon layers could exhibit absorption values similar to 300 µm-thick Si substrates [185].

Our aim is a thickness of crystalline silicon of the order of a few microns ($2-5$ µm). In this thickness range, standard solutions presented previously are not sufficient as a twofold enhancement of the short-circuit current density is needed to reach the 15 % power conversion. Advanced strategies combining a broadband anti-reflection effect and a strong absorption enhancement are required. Among the proposed solutions, we focus in the next subsection on innovative designs with:

- photonic crystals (PCs) or diffractive gratings (DGs)
- nanoparticles (metallic or dielectric).

These light trapping strategies have already been introduced in the first chapter of this thesis. Here, we will focus on designs adapted for thin ($2-5$ µm) crystalline silicon films.

10.4.4 *Photonic crystals and diffraction gratings*

Both photonic crystals and diffraction gratings schemes have been developed for applications to thin film silicon solar cells. Many designs have been adapted to with:

- 1D or 2D patterns
- various shapes: rectangular-shaped gratings [49, 186], circular holes [49], nanocones [187], nanopillars [186, 188] or nanopyramids [186]
- front side and/or back side structuration.

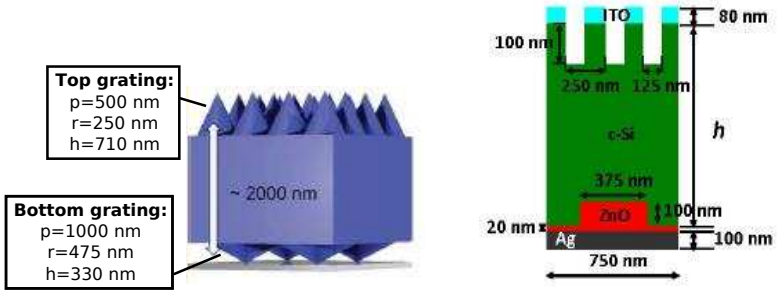

(a) (b)

Figure 95: Photonic approaches for light trapping in thin c-Si cells. (a) Double-sided nanocone gratings proposed by Wang et al. [187]. (b) Cross-section view of the combined front and back 1D gratings design proposed by Meng et al. [49].

Front side structures (PCs or DGs) are aimed at decreasing light reflection on the front surface and improve light coupling in the cell. When placed at the back side, they are often combined with back metallic reflectors in order to increase the optical path length in the cell. The most promising designs are double-sided structures as numerically shown by Wang et al. [187] and Meng et al. [49] in recent articles.

In Ref. 187, Wang et al. proposed a design with nanocone gratings both on the front and back sides of a 2 µm-thick silicon layer, as displayed in Fig. 95a. The cone geometry induces a smooth index transition from air to silicon on the front side leading to broadband anti-reflection effect. On the back side, the long wavelength photons are diffracted on the grating and coupled to waveguide modes. The grating period is optimized to ensure an efficient light trapping close to the bandgap of crystalline silicon, i.e in the $800 - 1100$ nm wavelength range. The back side grating is combined with a silver mirror. A 2 µm-thick silicon dioxide spacer layer is used to reduce the parasitic absorption losses in the metallic mirror. In this configuration, the nanocone grating is too far away from the back mirror to observe excitation of surface plasmons which would lead to enhaced absorption in the metal. They predict a very promising short-circuit current value of nearly $34\,\mathrm{mA/cm^2}$ for 2 microns of crystalline silicon, which is close to the Yablonovitch limit ($J_{SC} = 35.5\,\mathrm{mA/cm^2}$ for the same structure) [187]. However, doped and contact layers have not been included in their model. Additional losses are thus expected leading to a degradation of the predicted current density value. The proposed design also sets technological challenges that have not been answered yet.

As for Meng et al., they have numerically optimized diffraction gratings for a complete c-Si solar cell with a 1.2 µm-thick absorber layer, as described in Ref. 49. They have obtained a short-circuit current density value of $30.3\,\mathrm{mA/cm^2}$ for 2D patterns on both the front and the back sides of the cell. It corresponds to a 65 % relative increase compared to a flat unpatterned cell. This value is very close to the performances demonstrated by Wang et al. with a more simple and technologically feasible design. Even though no patterned solar cells have been

done yet, first samples with double 1D gratings were processed using laser holographic lithography and reactive ion etching as described in Meng's PhD thesis, Ref. 4 p. 118-121 (Fig. 95).

Both numerical works rely on the structuration of the active layer which may also degrade the electronic properties. In a recently published article, Trompoukis et al. [189] reported on the fabrication of 2D periodic photonic nanopatterns on a 1 µm-thick c-Si layer using nanoimprint lithography and RIE. The measured short-circuit current density of the cell is increased by 23% thanks to the 2D nanopatterning. However, the overall increase in the conversion efficiency compared to unpatterned cells (0.4%) is limited by a decrease of both the open-circuit voltage and the fill factor. The increase of surface area leads to a rise of the surface recombination. It has also been shown that reactive ion etching induced permanent carrier lifetime degradation [190]. A solution to limit the surface degradation is to combine two etching processes to achieve a better surface passivation. For instance, Oh et al. [191] have presented an approach where wafer-based silicon solar cells are nanostructured with a metal-assisted etch followed by an anisotropic wet tetramethylammonium hydroxide etch. Their best cells exhibit a 18.2 %-efficiency without an anti-reflection coating layer. Alternative designs to avoid these detrimental effects use dielectric or metallic nanostructures to increase light absorption instead of etching the active material. We will describe these approaches in the following.

10.4.5 *Nanostructures on the front surface*

10.4.5.1 *Plasmonic nanostructures*

We have previously described the integration of plasmonic structures in thin film solar cells (a-Si:H (PART 2) and GaAs (PART 3)). To date, only few works have been done on plasmonics for thin film crystalline silicon solar cells. Schaadt et al. [192], Beck et al. [193], Catchpole and Polman [194] and Diukman and Orenstein [195] have studied the effect of metal particles deposited on the front side of wafer-based silicon cells. In this configuration, the main light trapping mechanism relies in light scattering by the metallic particles. As introduced in *chapter* 2, section 2.3, metal nanoparticles placed in an electromagnetic field behave as dipoles. At the dipole resonance, i.e the plasmon resonance, the polarizability of the particle is enhanced, thereby leading to an increased scattering cross-section according to Eq. (14). The scattering process efficiency is increased compared to dielectric particles because of the larger scattering cross-section of metallic particles. For instance, Catchpole and Polman [194] have shown numerically that using silver hemispheres, the path length enhancement in a silicon layer could be as high as 28 close to the plasmon resonance wavelength. The scattering efficiency depends on the nature of the metal, the shape and the size of the nanoparticles as studied by Catchpole and Polman [194].

Theoretical studies have also been done on front metallic gratings to enhance absorption in very thin silicon layers ($t \sim 50$ nm) [154, 196]. In particular, Pala et al. [154] have shown that strong absorption increase could be achieved thanks to localized plasmonic resonances and the excitation of guided modes. How-

ever, the effect of the metal grating in this design is limited to specific wavelengths and strongly depends on light polarization. In addition, the proposed design is based on localized field enhancement in a very thin c-Si layer. A very low conversion efficiency is expected for the resulting cells.

Let us now consider realistic thin film silicon cells with a few microns thickness. Pillai et al. [197] studied experimentally the effect of silver nanoparticles integrated in 1.25 µm-thick silicon-on-insulator cells. They showed that localized surface plasmon resonances on the nanoparticles led to a photocurrent enhancement for wavelengths close to the bandgap of silicon. The particle size is critical: small particles lead to lower performances but increase absorption in the visible range. Larger particles induce absorption enhancement on the long wavelength range (near infrared) as well as parasitic losses at short wavelengths. A 33 % increase of the photocurrent was measured for the smallest silver particles (12 nm mass thickness). In addition to this study, a recent work from El Daif et al. [73] was published with the purpose of showing experimentally the absorption enhancement due to silver nanodisks patterned randomly on thin silicon ($2-10$ µm) epitaxial solar cells. The epi Si layer is grown on a highly doped wafer in order to avoid light transmission through the substrate. They report absorption enhancement due to light scattering on the nanoparticles. This surface plasmon resonance can be tuned by varying the diameter ($40-100$ nm) and height ($30-50$ nm) of the disks. However, the performances of the patterned thin silicon solar cells are showed to be lower than flat cells coated with a 100 nm-thick SiO_2 layer. The absorption gain is compensated by parasitic losses in the silver nanoparticles [73]. They conclude that metallic nanostructures integrated in thin silicon solar cells should be placed on the rear surface so that they interact only with long wavelength photons that are weakly absorbed in the active layer. The absorption decrease observed by El Daif et al. [73] at short wavelengths is consistent with the work of Pillai et al. [197] since they used larger silver particles.

10.4.5.2 *Dielectric nanostructures*

A major problem of plasmonic approaches is parasitic absorption loss in the metal particles. In order to circumvent this problem, theoretical [186] and experimental works [188, 198] have been done on light trapping designs with dielectric nanostructures. Dielectric structures also allow to avoid a texturing of the active silicon layer and can be applied to the finished cell with large-area patterning techniques such as nanoimprint lithography.

The first approach is to use similar structures as the surface texturing obtained by silicon etching (pyramides, binary gratings,...). Chong et al. [186] demonstrated numerically that TiO_2 nanostructures lead to a J_{SC} enhancement but with lower performances than silicon structures because of the lower refractive index of the dielectric material. Titanium dioxide is more attractive than silicon dioxide because of its higher refractive index ($n_{TiO_2} \sim 2.6 > n_{Si0_2} \sim 1.5$ at 600 nm). Wang et al. [188] have fabricated silicon solar cells with TiO_2 nanopillars on the rear side showing a J_{SC} enhancement of 37 % compared to flat cells. Päivänranta et al. [198] have used a periodic array of silicon dioxide nanopyra-

Approach	Metallic particles	Dielectric particles
Light trapping effect	Scattering or near-field enhancement	Scattering or impedance matching
Advantages	Large scattering cross section	Surface passivation
Drawbacks	Parasitic absorption losses Recombination centers for carriers	Limited enhancement

Table 9: Comparison of the properties of metal and dielectric particles for light-trapping in thin film crystalline silicon solar cells.

mids patterned on the front surface to achieve a reflectance below 0.45 % on a wide spectral (380–760 nm) and angular range ($0 - 40°$).

Finally, Lee et al. [199] have proposed to use high-refractive index dielectric nanoparticles (TiO_2 and Al_2O_3) as a back reflector on thin ($t \sim 2.5$ µm) epitaxial c-Si cells deposited on glass. They have shown experimentally a 40 % conversion efficiency enhancement compared to cells without any back reflector. Titanium dioxide nanoparticles give very promising results, better than standard white paints used as back reflectors.

10.4.5.3 *Metal vs dielectric*

Both metal and dielectric approaches are considered to enhance the performances of silicon solar cells. The metal versus dielectric question does not have a clear answer yet. In order to conclude this section on the proposed light-trapping nanostructures in literature, we have summarized the advantages and drawbacks of metallic and dielectric particles as shown in Table 9. It is noteworthy that some recently developed approaches combine both strategies. Santbergen et al. from Delft University have worked on a back reflector combining silver nanoparticles and a white reflector made of titanium dioxide particles [200]. Doing so, the back reflector should exhibit a high internal reflectance because of the dielectric particles and a broad angular distribution thanks to the large scattering cross-section of metallic nanoparticles. They have shown experimentally that a back reflector with silver nanoparticles and white paint combines high reflectivity ($0.90 - 0.95$) and high diffuseness (half width half maximum of the angular intensity distribution $= 30 - 50°$). Through optical simulations, a relative short-circuit current density gain of 20 % compared to a standard white paint reflector is predicted for 2 µm-thick nanocrystalline silicon cells.

10.5 SUMMARY

Crystalline silicon solar cells technology suffers from high production cost. The use of ultra-thin low temperature grown high quality monocrystalline silicon layers is a promising solution to address this issue, provided that we overcome the low short-circuit current density associated with thin absorber layers.

We propose to integrate light trapping solutions to improve the absorption of light in heterojunction aSi/cSi cells based on ultra-thin ($2-5$ µm) c-Si absorber layers. Our approach relies on:

1. the use of c-Si epitaxial layers grown by PECVD at low temperature ($<$ 200°C)
2. the transfer of the epitaxial layer on a low-cost host substrate
3. light trapping structures integrated in the front and/or rear surfaces of the cell.

11

THIN FILM SILICON SOLAR CELLS TRANSFERRED ON LOW-COST SUBSTRATE

Contents

As mentioned in *chapter 10*, the purpose of the ANR project NATHISOL is to fabricate ultra-thin crystalline silicon solar cells on low-cost substrate. The first milestone of the project has been to detach an epitaxial ultra-thin crystalline silicon film from the wafer substrate and transfer it on a host substrate. In this chapter, we will first give an overview of state-of-the-art silicon layer transfer processes. We will then present the lift-off process we have developed and the characterization of the first transferred thin films. The second purpose of the project is to implement light-trapping nanostructures in ultra-thin c-Si solar cells. In particular, the fabrication of periodic nanostructures (photonic crystals) either by wet etching or plasma etching is considered. In this thesis, as a first step, technological developments carried out to achieve controlled texturation of nanopyramids in epitaxial crystalline silicon solar cells are presented in the following. As a conclusion, we will summarize the first experimental achievements of the project and give an outlook of the perspectives.

11.1 TRANSFER OF THE EPITAXIAL LAYER ON A METALLIC MIRROR

11.1.1 *State-of-the-art of silicon layer transfer processes*

The transfer of silicon layers on a host substrate allows to use a low-cost substrate with additional functionalities. For instance, plastic can be used for flexible applications or metallic reflectors for light-trapping purposes. Most of the silicon layer transfer processes that have been developed rely on the use of a porous silicon layer as reviewed by Solanki et al. in an article published in 2004 [201]. The porous layer can arise from ion implantation in the wafer or porosification before epitaxy of the c-Si layer [170].

In most processes, a double porous layer is made between the epitaxial layer and the silicon wafer. The top layer, with a low porosity, is used as a seed layer for the epitaxial growth. The highly porous bottom layer plays the role of a sacrificial layer in order to detach the epitaxial c-Si film. The highest efficiency value is 20.1 % as demonstrated by Solexel for a transferred 43 µm-thick silicon layer in 2012 [162].

It has to be noted that some layer transfer processes without a porous layer already exist at a commercial scale, as the Smart-Cut process from SOITEC. This process, originally developed at CEA-Leti [202], combines ion implantation (to create an in-depth cleavage zone) and wafer bonding in order to produce silicon-on-insulator (SOI) wafers.

Other approaches have been developed to transfer thinner silicon films. Stephen Bedell and his co-workers of the IBM Thomas J. Watson Research Center have recently proposed a novel technique called "controlled spalling technology" [203]. It allows to achieve a kerf-free removal of thin c-Si, Ge and III-V layers at room temperature. A metal layer is deposited on the top of the layer to be detached in order to induce stress and to fracture the substrate. The fracture depth is controlled by adjusting the stress in the metal tensile layer (thickness, deposition conditions). A flexible adhesive film is deposited on the metal surface and used to i) assist the spalling process and ii) handle the detached layer during transfer towards the host substrate. For instance, they have reported the lift-off and transfer of InGaP/InGaAs/Ge and InGaP/InGaAs tandem cells with final efficiencies over 28 % [204, 205].

Another strategy uses thermal treatment to induce the detachment of thin silicon layers. The "Stress-induced Lift-off Method" (SLiM-Cut) has been developed at IMEC to produce wafers with a thickness around 50 µm and a size up to 50 cm^2 [171, 173]. Moreno and Roca i Cabarrocas have used a similar technique to detach and transfer epitaxial films obtained by PECVD with a thickness below 1 µm. In this case, the lift-off is enabled by a thin porous layer between the epi layer and the wafer. We will describe further this thermal lift-off process in the next subsection.

Finally, an epitaxy-free process has been proposed by IMEC [170, 172, 173]. The first step of the "Epifree" technique is based on the formation of an array of regular pores (size $\sim$ 550 nm) in a silicon wafer using deep UV lithography

and reactive ion etching. The sample is then annealed at 1150° C in order to produce a single void underlaying a thin silicon film. The c-Si film is then bonded to a low-cost substrate and detached from the wafer. So far, they have demonstrated a conversion efficiency of 4.2 % for an heterojunction solar cell based on a 1 µm-thick silicon layer [172].

11.1.2 *Thermal lift-off process*

11.1.2.1 *Thermal stress and strain*

Our approach follows the work of Moreno and Roca i Cabarrocas [178] on epi layer transfer using thermally induced stress. In the first step, we deposit a metal layer (aluminium in our case) on the epi Si/wafer stack. A rapid annealing step of a few seconds is then done to induce stress in the silicon substrate. Upon heating, the epitaxial c-Si layer is detached from the wafer substrate. The mechanism of the thermal lift-off leading to this layer is not fully understood yet. In Fig. 96, we present the mechanism expected from our experimental observations.

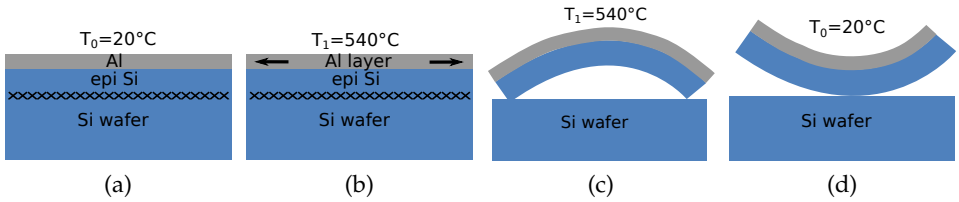

Figure 96: Thermal lift-off process. (a) Deposition of a thin aluminium layer. (b) Rapid thermal annealing to induce stress in the metal layer. (c) Peeling of the epi Si layer attached to the Al tensile layer. (d) Cooling of the epi Si/Al stack.

The stress created upon annealing is due to the mismatch between the thermal expansion coefficients of Al ($a_{Al} = 23.1 \times 10^{-6}$ °C^{-1}) and Si ($a_{Si} = 2.6 \times 10^{-6}$ °C^{-1}). If we consider a material with a length l_0 at temperature T_0 and a thermal expansion coefficient a, its length at temperature T is given by:

$$l(T) = l_0(1 + a \times (T - T_0)). \tag{37}$$

At ambient temperature ($T_0 = 20°C$), Al and Si layers have the same length ($l_0 = 1$ cm for instance). Using Eq. (37), we can calculate the expansion of the Al and Si layers after an annealing step at $T_1 = 540°C$: $\Delta l_{Al} = 9.9$ µm and $\Delta l_{Si} = 1.1$ µm respectively. The Al layer thus tends to be longer than the Si layer. As mentioned previously (see *chapter* 10, subsection 10.3.2), the deposition conditions of the epi Si layer lead to the creation of a porous fragile interface between the epitaxial layer and the wafer substrate (black crosses in Fig. 96b) at the beginning of the epitaxy. Upon sufficient stress, a fracture can initiate and propagate at the porous interface. If the adhesion between the Al and the epi Si layers is strong, the thin epitaxial layer peels off with the metal thereby relieving the stress in the substrate. During our experiments, we have observed that the epi layer peeled off on the whole surface in a really short time. It

seems consistent with the configuration shown in Fig. 96c. Upon cooling down towards ambient temperature, the detached film rolls on itself as illustrated in Fig. 96c and observed experimentally in Fig. 97a. Figure 97a shows a picture of a 2.5 µm-thick epi layer detached from a wafer using thermal lift off.

Figure 97b displays a SEM image of a 1 µm-thick epi layer starting to peel off. The wafer substrate can be in principle reused for deposition of other epitaxial Si layers.

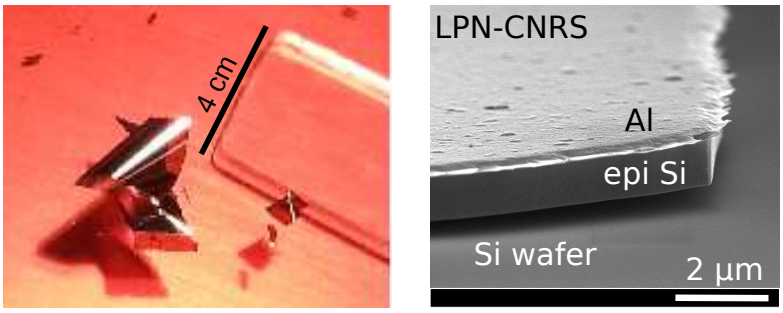

(a) (b)

Figure 97: Thermal lift-off of epi c-Si layers. (a) Picture of a 2.5 µm-thick epi layer detached from the wafer substrate. (b) SEM image of a 1 µm-thick epi layer starting to peel off.

11.1.2.2 *Description of the lift-off process*

As described previously, the epitaxial silicon layer is peeled off from the substrate using thermal lift off. A host substrate is required to handle the epitaxial layer after lift-off. In our approach, the layer is then transferred on a PDMS/-glass substrate. PDMS (polydimethylsiloxane) is the most widely-used silicon-based organic polymers. PDMS is a flexible polymer which can be easily used as a glue between the sample and a glass substrate. The flexibility of PDMS is a critical point because the handling layer should enable the relaxation of the thermally induced stress without creating cracks in the Al/epi Si stack.

As described in Fig. 98, the transfer of the epi layer on a host substrate is done as follows:

A. Deposition of a thin epitaxial silicon layer by PECVD on a (100)-oriented silicon substrate (Fig. 98a). The interface between the epi layer and the wafer substrate is made of a very thin porous layer. The native silicon oxide layer (thickness $\sim$ 1.5 nm) on the front surface of the epi layer is removed by ammonium fluoride (AF) wet etching (30 seconds).

B. Deposition of a 200 nm-thick Al layer by electron beam assisted evaporation (Fig. 98b). Cleavage of the sample with a diamond scraper[1].

C. Sticking of the sample on a glass substrate with PDMS (Fig. 98c). The two surfaces to be bonded together (aluminum layer and glass) are cleaned

1 In some cases, the epi-layer surface is shorter than the substrate. The Al film is then deposited over the epi-layer/substrate interface, thus preventing the epi-layer lift-off.

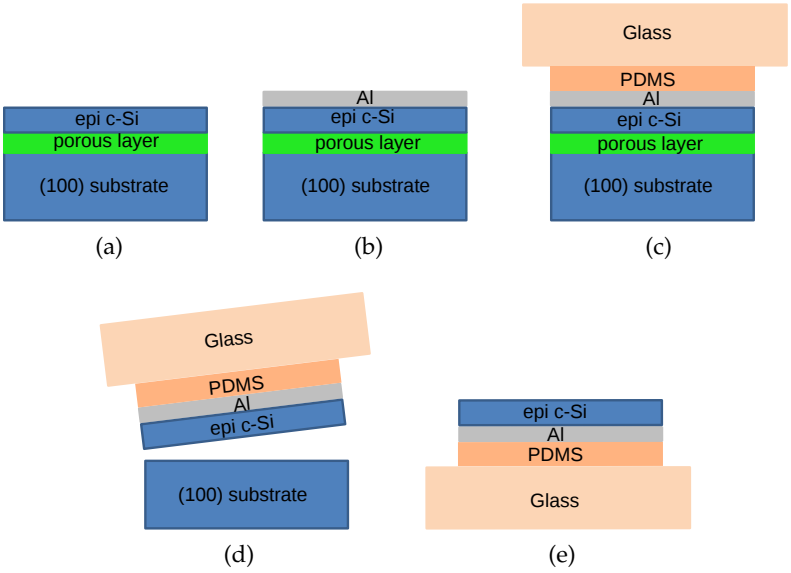

Figure 98: Description of the thermal lift-off process step by step.

by a short oxygen plasma treatment before spin coating of the PDMS on glass and sticking. After bonding, the sample is thermally annealed (two hours on a hot plate at 60 °C then 80 °C) in order to cure the polymer.

D. Thermal annealing at 540 °C on a hot plate, the wafer substrate side being in contact with the hot plate. The epi layer peels off after a few seconds 98d. Even if the effect of thermal annealing on the PDMS polymer is not clear yet, we have not observed any deformation of the PDMS surface upon heating so far.

E. We obtain an epi Si/Al/PDMS/glass stack at the end of the process.

The first advantage of the thermal lift-off process that we have developed is that it is easily carried out. Compared to the SLiM-Cut process, the peeling off requires a very short thermal treatment (a few seconds) at a moderate temperature. Furthermore, the tensile aluminium layer used in our thermal lift-off process can also play the role of a back reflector.

11.1.3 *Characterization of the transferred epitaxial layers quality*

At first, we have used the process described above to transfer intrinsic (non intentionally doped) epitaxial silicon layers with thicknesses between 2 and 6 microns.

Figure 99a displays a picture of a 2.5 µm-thick epi c-Si layer transferred on PDMS/glass on the left and the wafer substrate on the right. The epi layer has peeled off on the whole area of the sample ($\sim 0.6\,cm^2$). Raman spectroscopy has been carried out on this layer in order to characterize the crystalline quality of the epitaxial material after lift-off. The result of the characterization is displayed in Fig. 99b. Raman spectroscopy relies on the analysis of the inelastic scattering

of light by the vibrational modes of the material. The energy shift due to the interaction of incoming photons with the bond vibrations reflects the material structure and in particular, its crystallinity. The Raman spectrum displays the intensity of the scattered light as a function of the Raman shift expressed as a wavenumber, as shown in Fig. 99b. The sharp peak exhibited at 520 cm^{-1} (full width at half maximum (FWHM) = 5.3 cm^{-1}) is a feature of monocrystalline silicon. In amorphous silicon, a broad diffuse feature should appear at shorter wavenumbers because of the variation of bond angles, strength and energy.

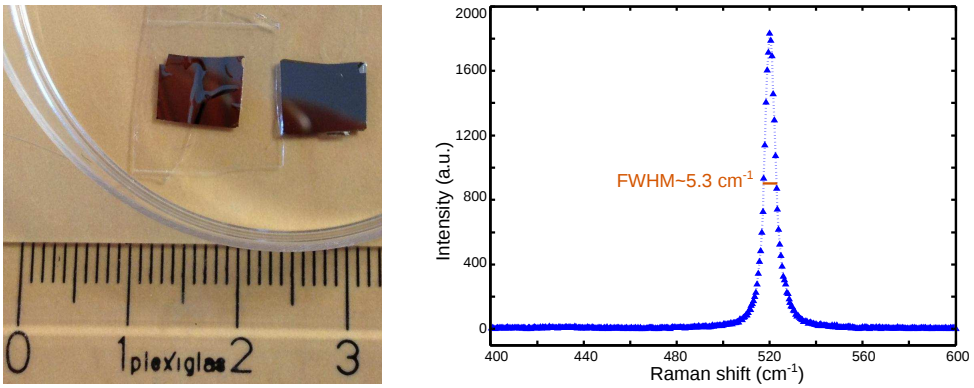

(a) (b)

Figure 99: Epitaxial lift-off of a 2.5 µm-thick c-Si layer. (a) Picture of the epi layer transferred on PDMS/glass (left) and the initial wafer substrate (right). (b) Measured Raman spectrum.

Additional ellipsometry measurements and AFM have been performed on a 6 µm-thick epi layer after lift-off as shown in Fig. 100. The measured RMS roughness is 1.3 nm (Fig. 100a), showing that the surface quality is still very good after the lift-off process. Figure 100b displays the $\mathrm{Im}(\epsilon)$ spectrum of the epi Si layer measured after lift-off (red curve) compared to the spectrum of bulk silicon taken from Ref. 206 (black curve). The $\mathrm{Im}(\epsilon)$ spectrum of the detached epi c-Si layer exhibits two peaks characteristic of crystalline silicon. The peak at 4.2 eV corresponds to the E2 transition and the peak around 3.4 eV to the E'0 and E1 transitions [207]. As already mentioned in *chapter 10*, subsection 10.3.2, the peak E2 probes the surface of the epitaxial layer. The intensity drop at 4.2 eV compared to the bulk silicon spectrum may be due the presence of an oxide layer on the surface and to the surface rugosity. The ellipsometry measurements have suggested that there were no variations of the crystalline quality as well as the epi layer thickness ($t \sim 6$ µm) during the lift-off process. The next step of the project was to demonstrate experimentally transferred devices, as developed in the next section.

11.1.4 *First transferred epitaxial silicon diode*

One of the intrinsic epi Si layer (thickness = 2.5 µm) transferred on an Al/PDMS/glass substrate has been used to make a diode. The ANR project NATHISOL is based on heterojunction cSi/a-Si solar cells with an epitaxial c-Si absorber

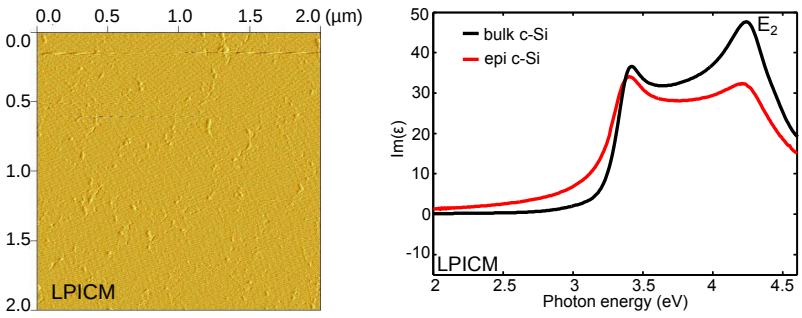

(a) (b)

Figure 100: Characterization of a 6 µm-thick epi layer after lift-off : (a) AFM image. (b) Ellipsometry Im(ϵ)) spectrum of a 6 µm-thick epi layer after lift-off (red curve) compared to the bulk c-Si spectrum (black curve).

layer and an a-Si:H emitter (i/n stack), which are more efficient than homojunction c-Si cells. In order to obtain such a structure, intrinsic and n-doped a-Si:H layers have been deposited by PECVD at LPICM on the transferred epi c-Si layer. The front contact is then made of a sputtered ITO layer and an aluminium grid. Figure 101a displays a photograph of the resulting diode (area $\sim 3\,\mathrm{mm}^2$). Note that there is no p-doped layer in the structure.

Current-voltage measurements have been performed as shown in Fig. 101b. The I-V curve of the transferred sample is characteristic of a rectifier behaviour. It represents a first promising step towards the realization of solar cells based on transferred thin epitaxial silicon films. The next step should be to integrate the epi c-Si layer within a whole p-i-n heterojunction in order to test its electrical performances. Furthermore, so far, we do not have any information on the density of defects created during the lift-off process. Further measurements, for instance carrier lifetime measurements, are needed to fully characterize the crystalline quality of the epitaxial c-Si after layer transfer.

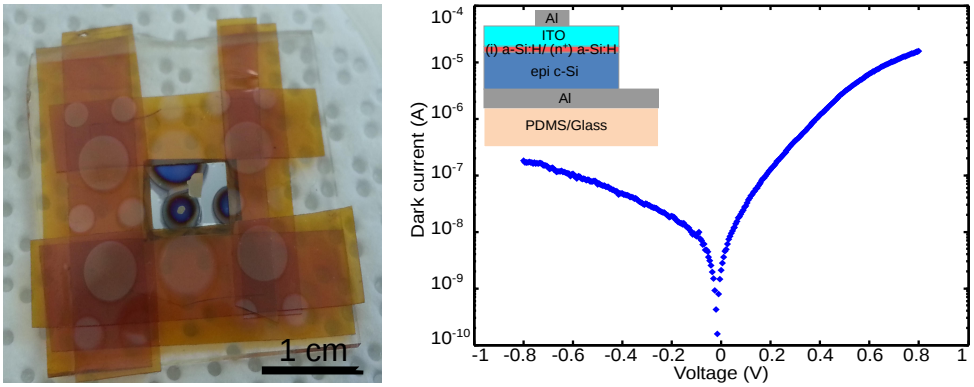

(a) (b)

Figure 101: First diode based on a thin epitaxial silicon film transferred on a PDMS/glass substrate. (a) Photograph of the fabricated diode. The blue areas correspond to the ITO front contacts. (b) Measured I-V curve (no illumination) on a $3\,\mathrm{mm}^2$ area. Inset: schematic of the diode.

11.2 TRANSFER OF P/I STACKS

We have showed previously that we could detach and transfer intrinsic epi c-Si layers. We have reported a first diode based on a PECVD deposited epi c-Si layer but a whole junction is needed to test the I-V characteristics. The first strategy we have considered to achieve transferred c-Si cells is based on three steps:

- the deposition of a p/i silicon stack by PECVD at LPICM
- the lift-off and transfer of the stack onto a PDMS/glass substrate
- the deposition of i and n doped a-Si:H layers in order to complete the junction[2].

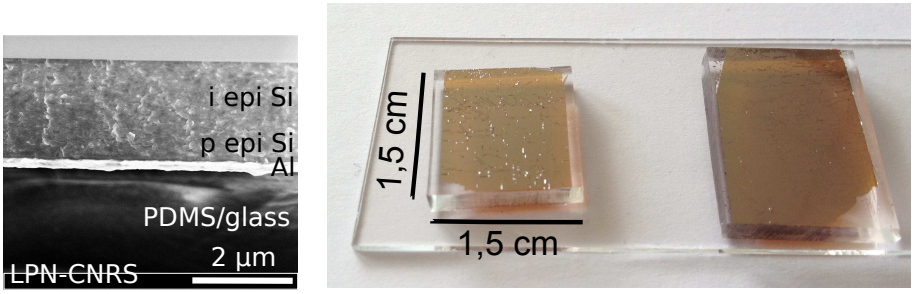

(a) (b)

Figure 102: Transfer of a 2.1 µm-thick p/i epi c-Si stack. (a) SEM image of a p/i stack transferred on Al/PDMS/glass. (b) Picture of p/i layers transferred on PAA/thick PDMS. A glass slide is used to ease the handling of the samples.

Several lift-offs and transfers were carried out on 2 µm-thick epi layers. Figure 102a displays a SEM image of a p/i stack transferred on an Al/PDMS/glass host substrate with the thermal lift-off process described previously. It shows that the lift-off is done keeping clean interfaces and a constant thickness over the sample. However, once transferred, the surface of the i epi layer appears altered, with many fractures. The deposition of the p-layer may have increased the strain in the stack, thus leading to spontaneous fracture of the samples.

We have also observed an ageing of the samples with a p/i stack: after a few weeks, the epi layers would peel off spontaneously. We have tried to transfer p/i stacks without using a metal layer to induce stress. A thick slab of PDMS has been used instead of a PDMS/glass host substrate. PAA polymer has been deposited on the p/i epi stack before spin coating of PDMS. PAA (polyacrylic acid) is a water soluble polymer that can be used as a sacrificial layer in a layer-transfer process. We have managed to transfer p/i stacks on large areas ($\sim 2-3$ cm^2) on PAA/PDMS substrate as displayed in Fig. 102b. These transferred layers still exhibit fractures on the surface with mm-sized domains.

2 The purpose of using an intrinsic amorphous silicon layer within the heterojunction is to ensure the passivation of the c-Si surface.

As a consequence, another strategy is needed to avoid spontaneous fracture of the epitaxial layer. A possible alternative is to deposit only an intrinsic epitaxial layer and to perform a double layer transfer in order to deposit doped p and n a-Si:H layers. This approach circumvents the problems we have encountered with p doped epi c-Si layers. Besides, the double layer-transfer technique offers additional degrees of freedom for the integration of light-trapping structures.

11.3 SURFACE TEXTURATION FOR LIGHT TRAPPING

In the previous section, we have demonstrated that the transfer of thin ($2-5$ µm) epitaxial crystalline silicon films on a host substrate was feasible. As discussed in *chapter 10*, another aspect of the project is to integrate advanced light-trapping strategies to increase light absorption in these thin c-Si films. As a first step, we have started with standard strategies such as texturing of upright and inverted pyramids to reduce reflection losses. The first objective of this study has been to develop a fabrication process in order to achieve controlled nanopatterning of crystalline silicon with the nanofabrication tools available at LPN. The second goal has been to perform surface texturation on PECVD deposited epitaxial c-Si films, which has not been done before. First experimental results are presented in this section.

11.3.1 *Anisotropic KOH wet etching*

Anisotropic etching of silicon is conventionally done with hydroxides such as KOH, NaOH or TMAH ($(CH_3)_4NOH$). The equation of silicon hydroxide etching reaction is given by:

$$Si + 2\,OH^- + 4\,H_2O \rightarrow Si\,(OH)_2^{++} + 2\,H_2 + 4\,OH^- \,.$$

It is a redox reaction based on silicon oxidation and water reduction. The etch rate of crystalline silicon with hydroxide etching depends strongly on the crystallographic orientation [32]:

$$v_{(110)} > v_{(100)} > v_{(111)} \,.$$

Table 10 relates silicon KOH etch rates to the crystallographic orientations for a KOH concentration of 30 % and a temperature of 70 °C [208]. The (111) crystallographic planes are very slow etching planes because of their high atomic packing density [32]. Therefore, the (111) planes are stop planes for the etching process. The intersections of these planes with the planar bottoms thus define the etching structures.

Depending on the shape and orientation of the etch mask, a wide variety of textures can be achieved. In our case, we will focus on pyramidal shapes obtained by anisotropic etching of (100) substrates. A schematic of such a structure is displayed in Fig. 103. The angle α between the pyramid and the horizontal plane for a (100)-oriented substrate is constant and equal to 54.7°. The relation between the etching depth h and the pyramid width w is therefore given by:

Crystallographic orientation	(100)	(110)	(111)
KOH etch rate (µm/min)	0.797	1.455	0.005

Table 10: KOH etch rates of crystalline silicon as a function of the crystallographic orientation for a KOH concentration of 30 % and a temperature of 70 °C. Values taken from Ref. 208.

$$h = w \times \tan \alpha \,. \tag{38}$$

The etch rate depends also strongly on the temperature and the etchant concentration. In the following, we will first present the patterning of pyramids on wafer c-Si substrates and then on epitaxial silicon layers deposited by PECVD.

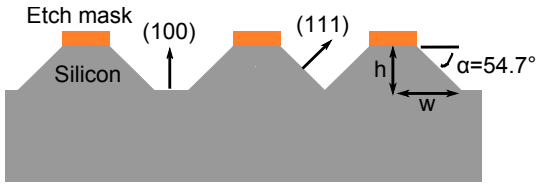

Figure 103: Schematic of inverted pyramids etched in a (100)-oriented silicon wafer. The height h and the width w of the pyramids are related through the angle α.

11.3.2 *Patterning of inverted pyramids in wafer crystalline silicon*

As introduced in *chapter 10*, subsection 10.4.3, a regular array of inverted pyramids manage a more efficient light trapping than random pyramids. We have worked with two patterning processes depending on the scale of the etched structures. The process is done in four main steps:

1. Patterning of the etch mask with lithography (UV photolithography or e-beam lithography)
2. AF etching of the native oxide layer
3. Anisotropic KOH etching at a constant temperature
4. Wet etching mask removal.

11.3.2.1 *Process A: micron-scaled inverted pyramids*

We have first patterned micron-scaled structures with a process adapted from Ref. 198. A chromium etch mask was obtained using UV photolithography. KOH wet etching was then carried out followed by a chemical removal of the mask. The mask used was an array of chromium squares. By varying the period of the array, we have obtained various shapes of inverted pyramids[3] (Fig. 104a)

3 The SEM image in Fig. 104a shows the sample before the Cr mask removal. Wet etching of the Cr mask also improves the surface quality (not shown here).

or faceted micropyramids (Fig. 104b) with this simple and large-area patterning process. However, the size of the etched structures is about a few microns. For instance, the inverted pyramids shown in Fig. 104a are 3 µm-wide. The etching depth in silicon, obtained from Eq. (38), is 2 microns. A sub-micron scaled texturing is therefore required for application to thin film epitaxial crystalline silicon films.

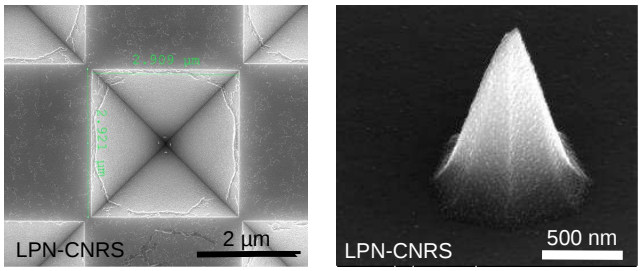

(a) (b)

Figure 104: SEM images of (a) inverted pyramids and (b) faceted pyramids obtained by KOH etching of wafer c-Si with a micropatterned Cr etch mask.

11.3.2.2 *Process B: inverted nanopyramids*

In order to obtain inverted nanopyramids, we have to define a 2D grid etch mask. The width of the grid corresponds to the spacing between two inverted pyramids. Our aimed structure was an array of inverted pyramids with a size of 300 nm[4] and a spacing between the pyramids as small as possible.

We have developed a patterning process using an HSQ (hydrogen silsesquioxane) resist patterned by EBL as an etch mask. HSQ is a negative electron-sensitive resist. The main advantages of HSQ are its very high resolution for e-beam lithography (< 10 nm) and its ability to be converted in silica after annealing. After crosslink under e-beam exposure, the HSQ cage structure converts in a silica type structure that is insoluble in alkali hydroxide solutions. A post-baking treatment at 400 °C induces a network redistribution of its chemical structure and increases the resistance of the HSQ mask. After electron beam lithography, resist development and annealing, we obtain an HSQ grid as shown in Fig. 105a.

Before KOH etching, the native oxide layer is removed by an AF etching. The HSQ etching mask is also etched by AF. Therefore, this step is critical and the cleaning step duration must be controlled precisely to obtain the optimal width of the grid. The sample is then etched in a KOH solution (concentration = 20 %). The KOH etch rate is controlled by placing the beaker in a constant temperature bath. After KOH etching, we obtain well defined inverted pyramids as displayed in Fig. 105b. The patterning is homogeneous on the whole patterned area ($\sim$ mm^2). The HSQ mask is then removed with AF leaving a

4 The patterning process developed here to achieve a 300 nm-size is easily applicable to wider inverted pyramids.

clean surface. In order to improve the anti-reflection effect of the pyramids, we deposited a silicon nitride anti-reflection coating layer (thickness = 80 nm) by PECVD (Fig. 105c).

It is noteworthy that the patterning of the etch mask can also be done with nanoimprint lithography. In the case of this study, electron-beam lithography was a valuable tool to optimize the fabrication process. Indeed, several areas can be patterned with a varying period or grid width on the same sample.

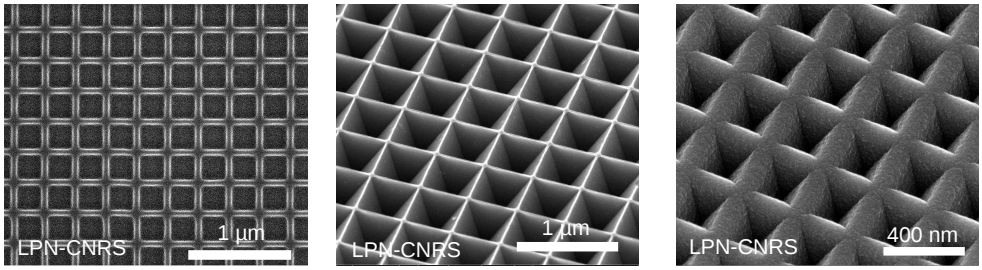

(a) (b) (c)

Figure 105: Patterning of inverted pyramids in wafer crystalline silicon with HSQ process. (a, b) SEM images of a c-Si wafer before (a) and after (b) KOH etching (pyramid size = 300 nm, spacing = $20 - 30$ nm). (c) SEM image of inverted pyramids after deposition of an anti-reflection coating SiN_x layer (thickness = 80 nm). Images b and c are tilted with an angle of 45° and 30° respectively.

We have performed reflectivity measurements at normal incidence with a SENTECH reflectometer in order to quantify the improvement due to the patterning of the front surface. Figure 106 shows the reflectivity spectrum measured on a sample with inverted pyramids at normal incidence[5]. The response of several areas with the same period ($p = 300$ nm) but different pyramid sizes between 240 (blue curve) and 280 nm (orange curve) with a step of 10 nm is shown with colored curves. Reflectivity of an unpatterned area was also measured as a reference (black curve). We see that the patterned areas exhibit an overall lower reflectivity than the planar substrate with SiN_x. The table in inset shows the measured reflectivity values at short (450 nm) and long (850 nm) wavelengths extracted from the planar silicon wafer (black) and best inverted pyramids (orange) curves. On both wavelength ranges, the best inverted pyramids array (orange curve) exhibits at least a two-fold reflectivity decrease compared with the wafer substrate.

Our structure is made of an array of inverted pyramids etched in c-Si with a 300 nm period, which is therefore sub-wavelength over the whole visible range. This inhomogeneous layer can be modeled as an effective homogeneous medium with a graded index between the air index ($n_{Air} = 1$) and the silicon index ($n_{Si} = 3.5 - 5$ on the visible range). The impedance matching is therefore much more efficient than in the case of a simple silicon nitride anti-reflection

5 Here, we measure only specular reflectivity. Because we do not take into account scattering, the reflectivity of the textured samples is probably underestimated.

coating layer. It is noteworthy that the pyramidal shape leads to an efficient broadband anti-reflection effect ($R < 10\,\%$ on $500 - 900$ nm range).

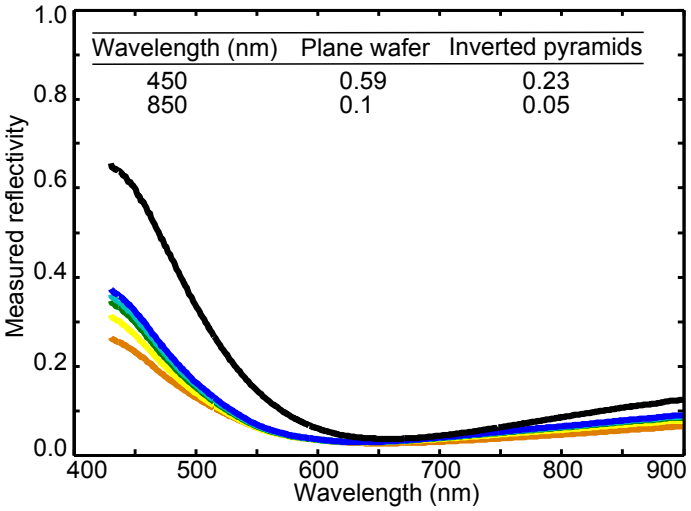

Figure 106: Reflectivity measurements on silicon wafer (black curve) and patterned inverted pyramids with varying size (colored curves) (nominal size $\sim$ 300 nm), all coated with a 80 nm-thick silicon nitride layer. Inset: measured reflectivity values at short (450 nm) and long (850 nm) wavelengths extracted from the plane silicon wafer (black) and best inverted pyramids (orange) curves.

If we integrate the absorption $A = 1 - R$ and weight it with the solar spectrum, we predict a short-circuit current density value of 30.6 mA/cm^2 for the best pyramid pattern, to be compared to 28 mA/cm^2 for the unpatterned SiN_x/Si stack. The next step is therefore to apply this fabrication process to epitaxial crystalline silicon layers.

11.3.3 *Texturation of epitaxial crystalline silicon layers*

The first idea was to pattern inverted nanopyramids in epitaxial crystalline silicon layers using the processes presented in the previous section. We have tried to pattern epi c-Si layers with a thickness of $\sim$ 1.6 µm with the process A. The obtained etching structures were not well defined, the anisotropic etching seemed to occur in localized clusters. It is attributed to the fact that the epi layer was too thin to ensure a sufficient crystalline quality. Regarding process B, the first tries were not successful either. We suggest that it is due to the epitaxial layers used.

As a consequence, we have decided to carry out KOH wet etching of epi c-Si layers without any etch mask. Anisotropic KOH etching of wafer crystalline silicon is very well-known. However, here, we deal with a novel material, epitaxial c-Si deposited at low temperature by PECVD, and achieving this wet etching dependent from the crystallographic orientation is not trivial.

We have added isopropyl alcohol to the hydroxide etching solution in order to improve the anisotropic etching of c-Si. As published by Zubel and Kramkowska [209], isopropyl alcohol addition leads to smoother etched sur-

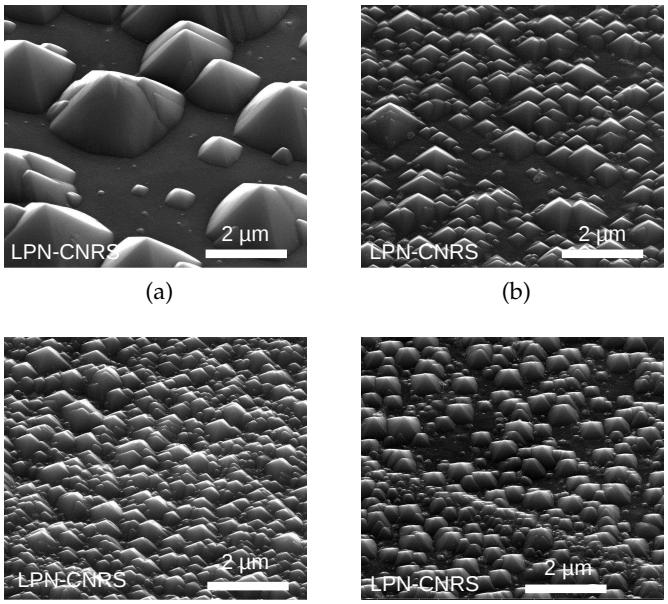

Figure 107: KOH wet etching of random pyramids on PECVD deposited epi c-Si layers (thickness = 3 µm) for a varying etching time: 3 min (a), 4 min (b), 5 min (c) and 6 min (d). In Fig. 107d, a line with denser and smaller pyramids is shown in green. All SEM figures have the same magnification.

faces and a better morphology of the pyramid patterns. Here, the KOH wet etching has been performed at a constant temperature of 80 °C and with a magnetic stirring. A deoxidation step (few seconds in AF solution) is done prior to KOH etching in order to remove the native oxide layer. Figure 107 shows SEM images of the sample surface (thickness = 3 µm) for a varying etch time between 3 and 6 minutes. No etch mask is used this time, the obtained texturing is made of random pyramids.

If we compare Figs. 107a, 107b and 107c, we find that the pyramid density increases with the etch time. The sample which has undergone a 5 min-long etch (Fig. 107c) exhibits more numerous but smaller pyramids than the 3 min-long etch (Fig. 107a). It is noteworthy that the pyramid density and size is not homogenous on the whole surface in spite of the magnetic stirring as shown in Fig. 107d. In particular, we can distinguish a line with denser and smaller pyramids (shown in green in Fig. 107d). The spatial distribution of the pyramids reflects the structure of the crystalline material. Nitrogen bubbling could be used to improve the homogeneity of KOH etching on these samples.

We have shown that we could pattern random pyramids on epi c-Si layers using anisotropic etching. It is an additional evidence of the crystalline nature of PECVD deposited c-Si. However, this texturing is not adapted for light-trapping in ultra-thin c-Si solar cells for two reasons. First, light-trapping is more efficient with regular arrays of inverted pyramids. Second, for the 3 min etch, the etch depth is already 1.4 µm. It means that after 6 minutes, the whole epitaxial layer is etched. For our purpose of using ultra-thin c-Si layers, we need a patterning

of nanopyramids as the process B presented in the previous section. Controlled patterning of inverted nanopyramids in epi c-Si layers is in progress.

11.4 CONCLUSION

11.4.1 *Transfer layer of epitaxial micron-thick c-Si films*

We have developed a transfer layer process based on thermal lift-off. Epitaxial c-Si layers with thicknesses between 2 and 6 µm have been detached and transferred on a host PDMS/glass substrate. It has been shown that Raman and ellipsometry spectra of the transferred layers were not affected by the lift-off process. We have also reported the fabrication of a diode from a transferred epi c-Si layer and a rectifier behavior was demonstrated. It is very encouraging regarding the quality of the deposited epi c-Si material. Additional electrical characterizations on a whole p-i-n junction should give more information about the properties of this material for photovoltaic applications.

So far, the quantity of available epi layers and the discrepancies in the properties of these layers have limited the reproducibility of the layer transfer process. A systematic study of influence of the parameters (temperature, nature of the metal, epi c-Si thickness) is needed to fully understand the lift-off mechanism.

11.4.2 *Nanopatterning of epitaxial c-Si films*

As described in this chapter, we have adapted a well-known texturation process of c-Si to perform a controlled patterning of inverted nanopyramids on c-Si wafers. The KOH wet etching process has led to clean and well defined patterns with a good homogeneity on large areas. The measured reflectivity has shown promising reflectivity decrease on the whole solar spectrum ($R < 10\,\%$ on $500 - 900$ nm range).

So far, we have not been able to fabricate arrays of inverted nanopyramids on epitaxial c-Si layers. However, we have reported selective KOH etching of random upright pyramids on 3 µm-thick epitaxial c-Si layers, thereby giving an additional evidence that this material is crystalline. Patterning periodic arrays of nanopyramids is only a step away from this study.

Furthermore, this first study of surface texturing of epitaxial c-Si layers deposited by PECVD paves the way towards more advanced light-trapping strategies such as photonic crystals [49] and plasmonic structures. It enables to address some issues that are common to all texturation approaches. For instance, it is crucial to optimize the passivation of the textured surface in order to prevent increase of surface recombination.

We have also shown that nanofabrication techniques (such as electron beam lithography) conventionally associated with thin film materials could be applied to crystalline silicon.

11.5 SUMMARY

We have developed a process to transfer PECVD deposited epi c-Si layers on a host substrate. It is based on a thermal lift-off of the epi layer from the wafer substrate. Epitaxial crystalline silicon layers (thickness between 2 and 6 µm) have been transferred and characterized, without showing any variation of the crystalline quality. A first diode based on a transferred epi i-layer has been fabricated and characterized. A double layer-transfer technique is considered in order to obtain thin-film c-Si cells with transferred epi c-Si layers.

As a first step, a patterning process to fabricate upright nanopyramids on epitaxial c-Si layers with a wet etching technique has been implemented. A patterned technique for regular arrays of inverted nanopyramids has also been developed with promising results on silicon wafers. This study open novel perspectives for the realization of double-sided nanopatterned ultra-thin c-Si solar cells.

CONCLUSION AND PERSPECTIVES

GENERAL CONCLUSION

Within the context of thesis, we have studied the design and fabrication of light-trapping structures for ultra-thin solar cells. As introduced in *chapter 1*, reducing the absorber thickness towards ultra-thin layers could open the way towards more efficient and cheaper photovoltaic devices and relieve the limitation on scarce materials. However, this breakthrough requires to achieve high photocurrents in very small semiconductor volumes. As reviewed in *chapter 2*, the research field of light-trapping strategies for solar cells has expanded dramatically over the last few years. Our study has been partly motivated by the ability of plasmonic structures to confine and control light within very thin layers down to the subwavelength scale. In addition, metallic nanostructures could also be used as alternative transparent electrodes to replace conventional transparent conductive oxides (ITO, ZnO:Al...) as introduced in *chapter 3*. The characterization tools necessary to the study of patterned solar cells, which I have partly developed within my thesis, have been described in *chapter 4*.

Design of resonant ultra-thin a-Si:H solar cells

In this thesis, we have proposed an original approach to design ultra-thin a-Si:H solar cells using plasmonic nanostructures with a nanopatterned resonant front contact. The one-dimensional front metal grating used as a light-trapping scheme is integrated in the front electrode of the solar cell. We have first chosen amorphous silicon as the material to test this concept because of its low cost and the possibility to deposit a-Si:H on various substrates. We have presented in *chapter 6* the optical optimization of the design for ultra-thin a-Si:H solar cells. Using numerical calculations, we have shown that the proposed design of a 90 nm-thick a-Si:H solar cell exhibits multi-resonant broadband absorption (absorption $> 60\,\%$ on $400 - 700$ nm) because of the combination of multiple electromagnetic modes (Fabry-Perot resonances and guided modes). Two main properties of the one-dimensional metallic light-trapping structure are i) its low sensitivity to incident polarization and angle and ii) the limited absorption losses in the metal ($< 10\,\%$) despite the presence of the grating on the front surface of the cell. A theoretical short-circuit current density J_{th} of 14.6 $\mathrm{mA/cm^2}$ has been calculated for 90 nm of a-Si:H, which is similar to state-of-the-art works with thicker absorber layers. Furthermore, in our approach, the light-trapping structure is in the front surface of the cell. The a-Si:H absorber layer is thus deposited on a flat back mirror. In most light-trapping strategies for ultra-thin cells, the material is grown on a patterned substrate which leads to a degradation of the open-circuit voltage and the fill factor of the device.

We have reported the fabrication of nanopatterned ultra-thin a-Si:H demonstrators in *chapter 7*. The experimental study has two main conclusions. First, the optical characterizations of the samples has shown a good agreement with the numerical analysis of the absorption mechanism. Absorption enhancement due to Fabry-Perot resonances and the excitation of guided modes thanks to the metal grating has been evidenced. Second, it has also highlighted the necesity

to perform optical simulations hand in hand with advanced material characterization. The experimental devices have shown several differences with the structure optimized numerically, thereby leading to a measured optical response with limited performances. In particular, the optical constants of a-Si:H (refractive index and extinction coefficient) strongly depend on the deposition conditions. In the case of the fabricated samples, the bandgap wavelength was lower than expected in the model and most of the light-trapping effects due to the metallic grating were confined in a spectral range above the material bandgap.

Design of broadband and omnidirectional ultra-thin GaAs absorbers

The main purpose of the work presented in PART 3 of this manuscript has been to demonstrate that we could achieve a broadband and omnidirectional absorption with only 25 nm of GaAs as presented in *chapter* 8. We have numerically studied a Ag/GaAs/Ag structure with a 25 nm-thick GaAs layer, the top silver layer being a nanopatterned grid. The calculated absorption spectrum exhibits multiple resonances leading to a broad absorption band. A theoretical short-circuit current density value of $J_{th} = 21.6$ mA/cm^2 has been predicted numerically at normal incidence with a low dependence on the angle of incidence. Our approach resembles metal/insulator/metal strategies but in our case, we achieve not only high total absorption but also high absorption in the GaAs film, as shown by the predicted short-circuit current density value. This design represents a potential fortyfold thickness reduction compared to the current record for a single-junction GaAs solar cell with a limited drop in the conversion efficiency. We have fabricated and optically characterized Au/GaAs/Au demonstrators as shown in *chapter* 9. We have demonstrated a broadband total absorption spectrum with absorption over 80 % between 450 and 830 nm at normal incidence, in very good agreement with the numerical calculations. We have thus shown better performances than state-of-the-art superabsorbers with metal/insulator/metal structures.

In this study, we have shown through the design of a proof-of-concept structure the potential of nanopatterned metal films to confine light absorption within ultra-thin semiconductor films. It is a first step towards complete ultra-thin GaAs solar cells including a whole junction and barrier layers.

Layer transfer and nanopatterning of epitaxial thin crystalline silicon films

In PART 4, we have presented preliminary results obtained in collaboration with LPICM in the framework of the ANR project NATHISOL, aiming at integrating nanophotonics in ultra-thin c-Si solar cells. As discussed in *chapter* 10, the integration of light-trapping strategies to achieve high short-circuit current density in ultra-thin c-Si films would represent a breakthrough for the c-Si technology. Within this thesis, we have worked on technological developments in order to fulfill the first milestones of the project NATHISOL as presented in *chapter* 11. Our approach is to use micron-thick epitaxial c-Si films deposited by PECVD at low temperature at LPICM, and then transfer the c-Si layer on a back metallic

reflector. We have developed a layer transfer process based on thermal lift-off and transferred successfully epitaxial films with varying thicknesses ($2-6$ µm). We have validated the first milestone of the project NATHISOL, which was to transfer an intrinsic epi layer on a back mirror. The realization of a transferred diode from the transfer of an intrinsic epitaxial c-Si layer has also been reported and the first measured I-V curve exhibits a rectifier behaviour. Ellipsometry and Raman measurements provide encouraging evidence that the detached epi layers have a good quality. As a first step towards nanostructured cells, a patterning process to fabricate inverted nanopyramids in c-Si with a wet etching technique has been developed. The results displayed in *chapter 11* open promising perspectives for the realization of double-sided nanopatterned ultra-thin c-Si films.

PERSPECTIVES

Towards advanced optimization of ultra-thin solar cells

First, the numerical study presented in PART 2 on ultra-thin a-Si:H solar cells could be developed further. In this thesis, our study of the patterned a-Si:H solar cell has been limited to the optical point of view. Optical study should be coupled with electrical simulations in order to understand better the effect of the metallic nanostructures on the efficiency of the cell. Knowing the electric field intensity spatial distribution, the carrier generation rate can be calculated in the whole cell. These additional information could be used to optimize further the design. Indeed, one should favor light absorption through optical modes that lead to an efficient collection of the generated carriers. In particular, as suggested in a recent work from Deceglie et al. [210], coupling optical and electrical optimization could help reducing the absorption losses in the doped layers. The generation rates can also be used as an input of simulation softwares in order to predict the I-V curves and ultimately the potential conversion efficiency of the device. Furthermore, the design proposed in PART 2 includes ITO and ZnO:Al buffer layers. We have already studied the influence of the thickness of these layers on the short-circuit current density. We have also shown that the ZnO:Al layer between the a-Si:H layer and the back mirror could be used to reduce parasitic losses in the metal. A recent work suggests that the spacing layers could also decrease the absorption losses in the doped layers [145]. In this thesis, we could not take into account the buffer layers and the p-doped and n-doped a-Si:H layers simultaneously in the calculations. Further developments in the calculation tools could allow to investigate this point. Regarding the buffer layers, all the calculations have been done with the same optical constants. The doping level of these layers is an additional degree of freedom that has not been investigated yet. Using lower doping levels would reduce parasitic absorption losses in these layers and therefore increase the short-circuit current density.

Second, despite encouraging numerical results, through this study, we have seen the limits of a-Si:H for plasmonic light-trapping. Light-trapping effects

occur mainly in the long wavelength range. Because of the low bandgap wavelength of a-Si:H, the potential of plasmonic nanostructures for absorption enhancement in ultra-thin a-Si:H solar cells is thus limited. However, the concept of nanopatterned resonant front contact proposed within this study is applicable to other photovoltaic materials as well as more efficient photovoltaic systems as tandem a-Si:H/μc-Si solar cells.

From broadband absorbers to ultra-thin GaAs solar cells

As shown in PART 3, our results on ultra-thin metal/GaAs/metal absorbers are very promising. Nevertheless, some points in the numerical and experimental studies still remain unanswered. First, the numerical results have shown that the absorption mechanism is complex and the influence of the different parameters is not well understood yet. In particular, in this design, a dielectric layer (here silicon nitride) is used to broaden the absorption spectrum and to prevent the ageing of the silver grid. We have already studied the effect of this layer thickness on the absorption but it is still to be analyzed in detail. Further developments include a more advanced modeling of the air/dielectric interface because so far, we have only modeled this layer as having a planar top surface. The shape of the air/dielectric interface has a strong impact of the response at short wavelengths. In particular, a textured interface should exhibit a lower front reflection. Furthermore, the nature of the dielectric material impacts on the effective index of the optical modes and therefore on the optical response. Our numerical study should be completed by a comparison of several dielectric materials. Second, we have fabricated Au/GaAs/Au demonstrators with a broadband total absorption as presented in *chapter* 9. However, absorption losses in the metal are expected to be around 40 % on average, as discussed in *chapter* 8. We have shown numerically that parasitic losses in the metal could be reduced by replacing gold by silver. A short-term perspective of this study is to fabricate Ag/GaAs/Ag demonstrators and validate the numerical results presented in this thesis. The detailed analysis of the absorption mechanism in this structure also requires to perform more advanced optical characterization, in particular to study the angular dependence of the structure. Third, the two-dimensional metallic grid can also be used as a front electrode in order to perform photocurrent measurements on metal/GaAs/metal samples. It would allow to confirm there is high photocurrent on a broad spectral range.

We have proposed in this study to combine a top 2D metallic grid with a back metallic mirror in order to achieve high light confinement in a very thin absorber layer (thickness = 25 nm). From this proof-of-concept, realistic GaAs solar cell can be designed by taking into account a p-n junction and barrier layers in order to ensure a high conversion efficiency. The metallic grid would play the role of an alternative electrode as well as a resonant light-trapping structure. As shown in this thesis, its geometrical parameters should be chosen to optimize the short-circuit current density of the cell. This approach opens novel perspectives towards ultra-thin GaAs solar cells with a thickness of 100 − 200 nm.

Ultra-thin crystalline silicon solar cells: perspectives of the ANR project NATHISOL

In PART 4, we have shown that nanostructures are not limited to applications to thin film materials but could also be of main importance for the development of the crystalline silicon technology. The final aim of the NATHISOL project is to implement nanophotonic structures (photonic crystals and/or plasmonic structures) within ultra-thin ($2-5$ µm) crystalline silicon solar cells. For instance, an aimed structure of the project is an heterojunction aSi/cSi cell based on an epitaxial c-Si absorber layer. The cell would include a front light-trapping structure such as photonic crystals and a plasmonic nanostructured mirror on the back side. In order to be competitive with existing technologies, such a cell should have a short-circuit current density of 30 mA/cm^2 for an epi c-Si layer between 2 and 5 µm. The results presented in this thesis, i.e the developments of a layer transfer process and the nanopatterning of pyramids, represent a first step towards this long-term objective.

In the short term, further experiments are needed to confirm the potential of epitaxial c-Si deposited by PECVD for ultra-thin c-Si solar cells. First, the layer transfer process is not completely understood yet. In particular, we have not performed a systematic study of the influence of each parameter because of the few epitaxial layers available and the discrepancies in the properties of each layer. An in-depth analysis of the influence of the porous layer (thickness and porosity) on the lift-off would provide useful information on the lift-off mechanism. The importance of the metal is still to be investigated in detail. A proper engineering of the porous layer could allow to detach the epitaxial layer without requiring any metal layer to induce stress. Another road for further work is to reduce the temperature of the lift-off. Additional characterizations are also needed to confirm that transferred epitaxial layers have a sufficient quality to realize photovoltaic device. For instance, carrier lifetime measurements should provide information on the defect density within the material. The transferred layers should also be tested within a complete heterojunction. Second, regarding the structuration, we have already developed a process for patterning of inverted nanopyramids in c-Si wafers. The application to micron-thick epitaxial c-Si layers is still to be performed.

As a general conclusion, this thesis has been the result of the encounter between nanophotonics and photovoltaics. We have proposed a novel design with a very thin nanopatterned metallic layer used as a resonant front contact of an ultra-thin solar cell. The idea of using a metallic grid as an alternative electrode has already emerged in the field of organic photovoltaics a few years ago. In this study, we have shown promising results for a-Si:H and GaAs absorber layers. This concept could be extended further to other thin film materials such as CdTe or CIGS and why not to ultra-thin crystalline silicon cells?

As a matter of fact, with the research of the ultimate low-cost and high-efficiency photovoltaic device, the boundaries between the different photovoltaics technologies are getting more and more blurred. Within this thesis, we have already studied the application of nanofabrication techniques conventionally

associated to thin film technologies to monocrystalline silicon. Whatever the considered technology, this thesis has shown that the efficient implementation of advanced light-trapping structures requires a synergy between numerical design, material science and nanofabrication techniques.

Part V

APPENDIX

A

RETICOLO CODE

All numerical calculations discussed in this thesis have been performed with the "Reticolo" code. The purpose of Reticolo code is to analyze diffraction by stacks of lamellar 1D and 2D crossed gratings. It has been developed by Philippe Lalanne (LP2N, Institute of Optics Graduate School) and Jean-Paul Hugonin (Institute of Optics Graduate School) and operates under MATLAB. Within my thesis, I have used a version of Reticolo provided by Philippe Lalanne and Christophe Sauvan for our application to nanostructured solar cells.

In this appendix, we first present the principle of Reticolo code, then we give the parameters used as inputs of the calculations and discuss the applications of this code.

A.1 PRINCIPLE OF RETICOLO CODE

A standard problem solved by Reticolo code is a multilayer system with periodic gratings as illustrated in Fig. 108. The grating is defined by a stack of N layers in the z direction. Each layer can be structured or not. All structured layers must have identical periods p in the x direction and must be invariant in the y direction. Incident light strikes the structure on the top surface as shown in Fig. 108.

Reticolo software relies on the exact determination of electromagnetic fields from Maxwell equations. It implements the Rigorous Coupled wave Analysis (RCWA) method developed by Moharam and Gaylord [211, 212]. The eigenmodes of all the layers in the structure are determined using a Fourier decomposition. Once the eigenmodes are known, the mode amplitudes in the different layers are calculated using a scattering matrix approach. Let us call O and I the matrices for the output fields and input fields of the system respectively. Then these two matrices are related through the scattering matrix S by:

$$O = S \times I \,. \tag{39}$$

We can calculate recursively the field amplitudes in all the layers in the system. Reticolo code thus gives the absorption fraction in each layer of the system but it also provides electromagnetic field calculations [213].

A.2 INPUT PARAMETERS

Performing a numerical calculation with Reticolo code requires to define a certain amount of input parameters. Among these, one can distinguish parameters defining the structure and parameters of the computation.

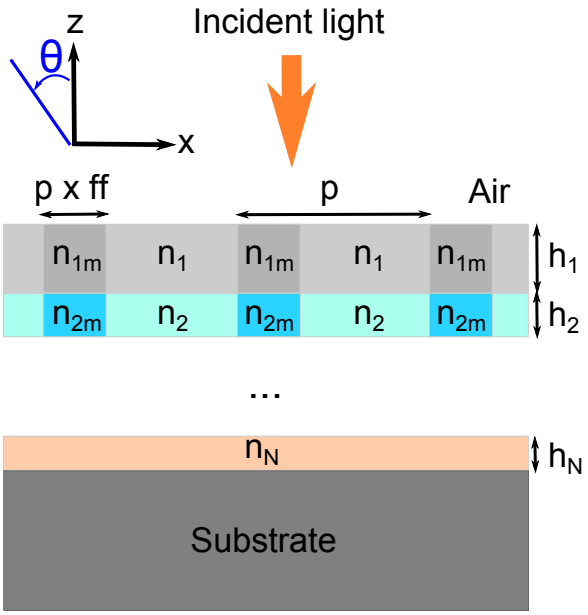

Figure 108: Schematic of the diffraction problem.

A.2.1 *Definition of the structure*

Figure 108 shows an example of a multilayer structure that can be simulated with Reticolo. The first parameter needed is the number of layers N in the stack. For the version of Reticolo code used during this thesis, N was limited between 1 and 6. Once the number of layers is defined, we have to give the thickness of each layer in the stack (h_1, h_2,...,h_N).

As illustrated in Fig. 108, some layers of the stack can be structured and others can be uniform. This is defined through the optical constants of the different materials. In the example of Fig. 108, the first and second layers are structured. Let us consider the first layer (thickness h_1). It is based on a material with a refractive index n_1 and includes a grating with a refractive index n_{1m}. If the layer is uniform (as in the case of the N layer in Fig. 108), $n_{Nm} = 0$.

The grating is also characterized by its geometry (1D or 2D) and its geometrical parameters (period p and fill factor ff). As shown in Fig. 108, the fill factor of the structure is defined as the ratio of width of the grating over the grating period. If $ff = 0$, there is no structuration ($n_{1m} = 0$) and if $ff = 1$, $n_1 = n_{1m}$. Note that all the structured layers have the same period and are invariant along the y axis.

Note that we can model 1D and 2D gratings (as presented in the thesis) but calculations for 2D structures are much longer because a Fourier decomposition is needed along both x and y axes.

A.2.2 *Parameters of the calculation*

First, we have to define the vector containing the wavelength values. If we want to calculate the absorption in each layer of the structure, we define the

boundaries of the spectral range and the number of points needed for one spectrum. If it is a calculation of the electromagnetic field, the computation is performed for a specific wavelength value that needs to be precised.

Second, we choose the incident polarization (TE or TM) and the angle of incidence. In TE polarization, the electric field is parallel to the y direction. In TM polarization, the magnetic field is parallel to the y direction. The angle of incidence θ in the (xz) plane of incidence is defined as shown in Fig. 108.

Third, we have to give the number of Fourier harmonics along x (M_x) and y (M_y) axes retained for the computation. This parameter is very important in particular for 2D structures where more Fourier modes are required to ensure a convergence of the computation. For 2D systems, the calculations done during this thesis have shown that at least 20 Fourier modes are needed to achieve convergence for the long wavelength resonances, i.e the ones that depend the most on the metallic grating. A modified RCWA method has been developed by Philippe Lalanne and his coworkers in order to improve the convergence while reducing the calculation time. All the calculations presented in this thesis have been done with this modified RCWA method.

A.3 APPLICATIONS OF RETICOLO CODE FOR OUR STUDY

In the context of this thesis, we have used Reticolo code in different ways to model solar cells with nanostructured metallic layers. The most standard calculation is to determine the absorption in each layer of the stack. In particular, it allows us to know the absorption fraction within the semiconductor absorber layer and to calculate the predicted short-circuit current density of the cell. The values of the absorption fraction in each material of the system also enables an analysis of the absorption losses in the solar cell and to distinguish the different sources of losses: spacing layers, doped layers, metallic grating, back mirror,...

We have also used Reticolo code to calculate the field maps giving the spatial distribution of the electric and magnetic fields in the structure. Using these data, we can know where light absorption and thus carrier generation preferentially occurs. Knowing the value of the electric field in each point of the structure could be used to deduce the maps of carrier generation rates and thus couple optical and electrical simulations of the solar cell.

B

OPTICAL CONSTANTS USED IN THE NUMERICAL SIMULATIONS

In this appendix, we give the optical constants used in the numerical simulations presented in PARTS 2 and 3 of this thesis. For each material, the reference is given as well as a plot of the real and imaginary parts of the refractive index.

B.1 OPTICAL CONSTANTS OF TRANSPARENT CONDUCTIVE OXIDES

B.1.1 *Indium tin oxide (ITO)*

The optical constants of ITO displayed in Fig. 109 have been obtained by ellipsometry measurements performed at LPICM.

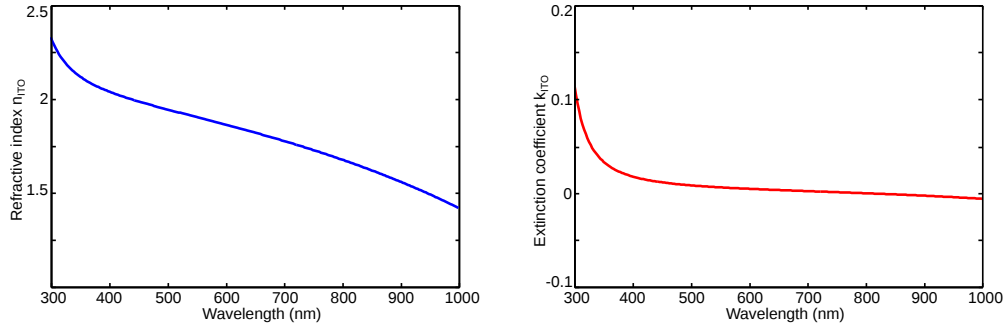

(a) (b)

Figure 109: Real (a) and imaginary (b) parts of the refractive index of ITO.

B.1.2 *Aluminium doped zinc oxide (ZnO:Al)*

The optical constants of ZnO:Al displayed in Fig. 110 have been obtained by ellipsometry measurements performed at LPICM.

B.1.3 *Non doped zinc oxide (ZnO)*

The optical constants of ZnO displayed in Fig. 111 have been obtained by ellipsometry measurements performed at LPICM.

B.2 OPTICAL CONSTANTS OF GAAS

The optical constants of GaAs used in the numerical calculations and displayed in Fig. 112 are taken from Palik [116], p. 429 – 443.

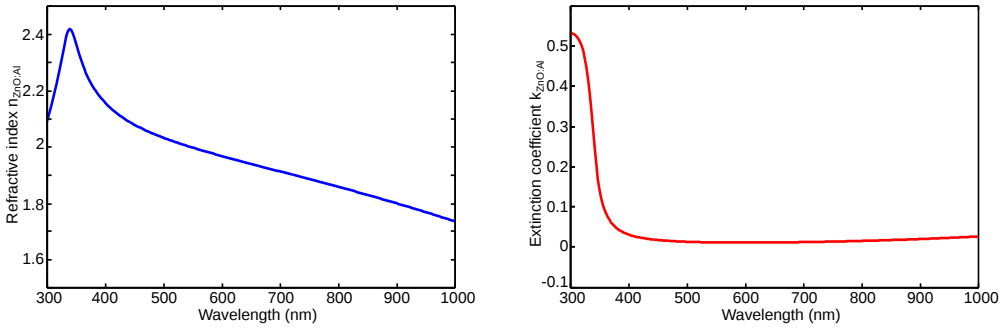

(a) (b)

Figure 110: Real (a) and imaginary (b) parts of the refractive index of ZnO:Al.

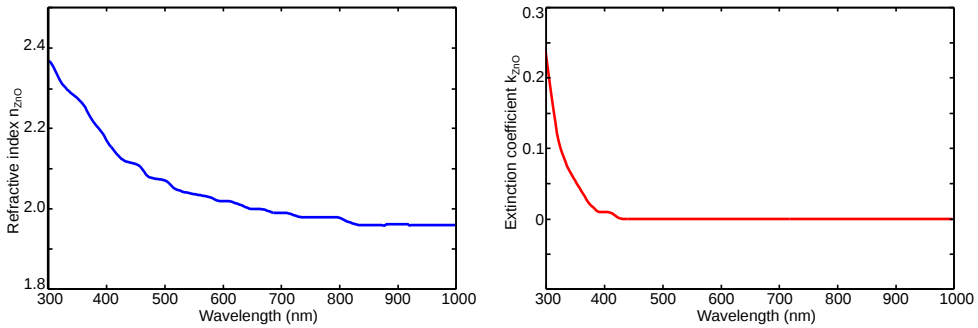

(a) (b)

Figure 111: Real (a) and imaginary (b) parts of the refractive index of ZnO.

B.3 OPTICAL CONSTANTS OF SiN_x

The optical constants of silicon nitride used in the numerical calculations and displayed in Fig. 113 are taken from Palik [116], p. 771 – 774. It should be noted that the data from Palik refer to the particular case of Si_3N_4.

B.4 OPTICAL CONSTANTS OF SILVER

In this thesis, we have used two sources for the optical constants of silver: Palik [116] p. 350 – 357 and Johnson and Christy [143]. Both data are shown in Fig. 114.

B.5 OPTICAL CONSTANTS OF GOLD

In this thesis, we have used two sources for the optical constants of gold: Palik [116] p. 286 – 295 and Johnson and Christy [143]. Both data are shown in Fig. 115.

In *chapter* 9, subsection 9.2.1, we have used both references to fit our experimental measurements. We have shown that data from Johnson and Christy [143] seemed to adjust better our experimental results.

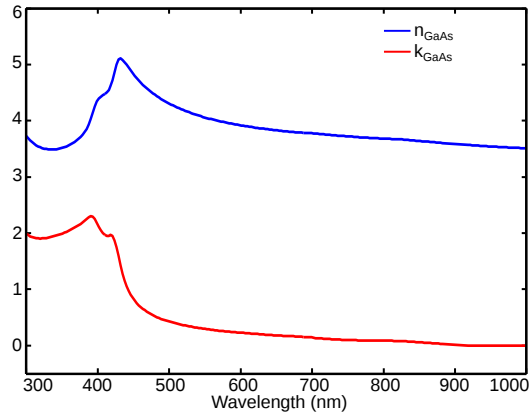

Figure 112: Real (blue) and imaginary (red) parts of the refractive index of GaAs.

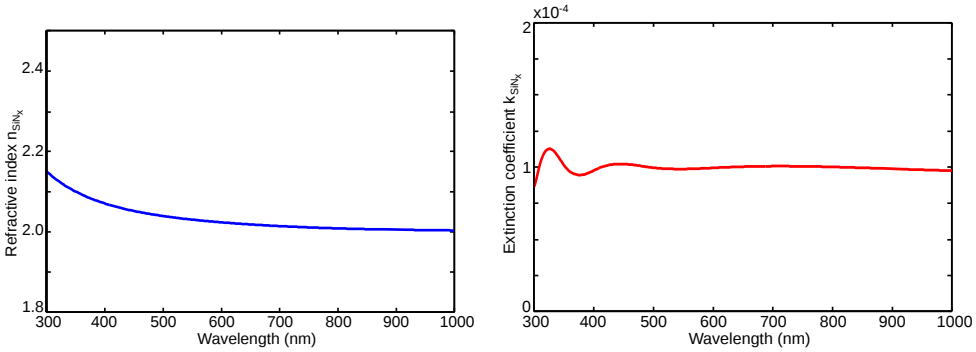

(a) (b)

Figure 113: Real (a) and imaginary (b) parts of the refractive index of Si_3N_4.

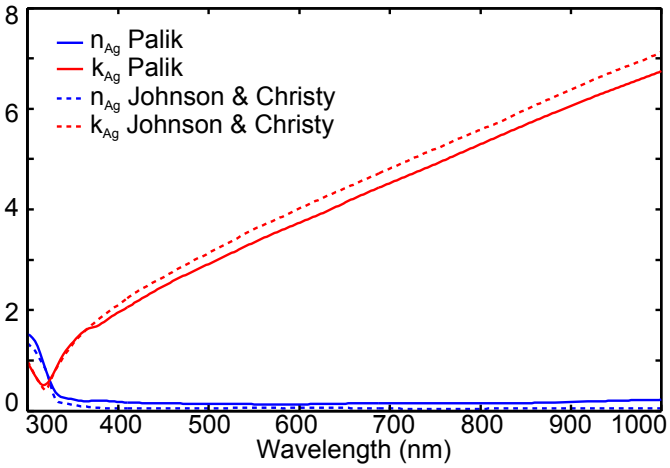

Figure 114: Real (blue) and imaginary (red) parts of the refractive index of Au taken from Refs. 116 (plain line) and 143 (dashed line).

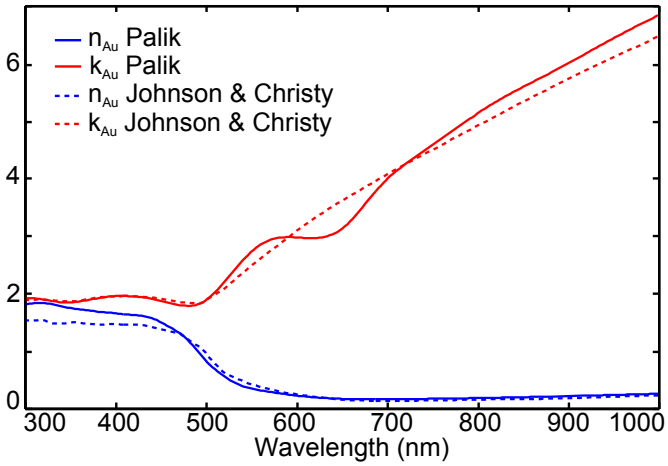

Figure 115: Real (blue) and imaginary (red) parts of the refractive index of Au taken from Refs. 116 (plain line) and 143 (dashed line).

C

RÉSUMÉ EN FRANÇAIS

INTRODUCTION

Un des plus grands défis posés actuellement est de trouver comment subvenir aux besoins croissants en énergie dus d'une part à la croissance démographique globale et d'autre part, au développement des pays émergents. Le marché énergétique actuel est dominé par les énergies fossiles (pétrole, charbon et gaz) qui représentent plus de 80 % de la production d'énergie en 2012. Ce système est cependant menacé. Les ressources limitées en énergies fossiles et le changement climatique dû aux émissions de gaz à effets de serre rendent nécessaire la réorganisation du marché énergétique. Les énergies renouvelables et en particulier le solaire photovoltaïque, sont des alternatives prometteuses aux énergies fossiles. Elles permettent l'accès à une source d'énergie abondante, sûre et propre. Malgré la découverte de l'effet photoélectrique, c'est-à-dire la conversion d'énergie lumineuse en énergie électrique par Edmond Becquerel en 1839, il a fallu attendre les crises pétrolières des années 1970 pour qu'une utilisation à large échelle de l'énergie photovoltaïque soit envisagée. Cependant, les investissements dans le solaire photovoltaïque connaissent une croissance importante depuis 10 ans, jusqu'à représenter plus de la moitié des investissements dans les énergies renouvelables en 2012. Selon l'Agence Internationale de l'Energie (IEA), l'énergie solaire devrait occuper une place importante au sein du futur marché énergétique. Ainsi, un tiers de la demande globale en énergie pourrait être fournie par l'énergie d'origine solaire en 2060 [3].

Plusieurs filières photovoltaïques existent déjà à l'échelle industrielle. Néanmoins, la recherche dans le domaine du photovoltaïque est encore motivée par la possibilité de réduire le coût de production et d'améliorer l'efficacité de conversion des cellule solaires. En particulier, réduire l'épaisseur de matériau actif nécessaire est crucial pour la plupart des technologies que ce soit une question de coût (filières silicium cristallin (c-Si) et arsenure de gallium (GaAs) par exemple), de rareté des éléments chimiques utilisés (indium, tellurium ou sélénium) ou de stabilité du dispositif (silicium amorphe (a-Si:H)). Cependant, réduire la quantité de matériau absorbant utilisé signifie aussi réduire la quantité de photons absorbés, et ce particulièrement aux grandes longueurs d'onde. En conséquence, ces dernières années ont vu émergé un certain nombre de stratégies pour piéger les photons dans des couches absorbantes ultra-fines. Parmi les approches développées, il a déjà été montré que l'utilisation de cristaux photoniques [4] ou de contacts métalliques nanostructurés [5–7] permettait de confiner l'absorption de la lumière dans des couches très fines ($100 - 200$ nm). Ces deux approches reposent néanmoins sur la structuration de la couche active, ce qui entraîne une augmentation des recombinaisons en surface. Dans le cas de la deuxième approche, le dépôt du métariau actif sur un substrat nanos-

tructuré est aussi responsable de la création de zones poreuses et riches en défauts qui peuvent être à l'origine de courants de fuite dans la cellule. Dans les deux cas, l'amélioration de l'absorption due au piégeage optique est donc limitée par des dégradations de la tension de circuit-ouvert et du fill factor de la cellule solaire.

Dans cette thèse, nous proposons une stratégie originale de piégeage optique dans des cellules solaires ultra-fines basée sur des nanostructures métalliques placées en face avant de la cellule afin de conserver une couche d'absorbeur plane. D'autre part, dans notre approche, nous suggérons de donner une double fonctionnalité aux nanostructures métalliques. Elles servent à la fois à confiner la lumière dans un volume d'absorbeur réduit et à assurer le rôle d'électrode alternative. Nous avons ainsi travaillé sur trois matériaux différents (a-Si, GaAs et c-Si) avec le même objectif de réduire l'épaisseur d'absorbeur vers des couches ultra-fines, c'est-à-dire 100 nm pour les matériaux couches minces et $2-5$ µm pour le silicium cristallin. Le manuscrit est structuré en quatre parties.

La PARTIE 1 fournit une introduction au travail effectué dans cette thèse: en particulier, les notions de cellules ultra-fines et de contacts avants nanostructurés sont introduites dans les *chapitres 1* et *3*. Un aperçu de l'état de l'art sur les techniques de piégeage optique pour les cellules ultra-fines est présenté dans le *chapitre 2*. Enfin, le *chapitre 4* décrit la plateforme de caractérisation adaptée pour l'étude de cellules nanostructurées dont j'ai développée une partie importante pendant ma thèse.

La PARTIE 2 est dédiée à la conception de cellules solaires ultra-fines en silicium amorphe avec une épaisseur d'absorbeur inférieure à 100 nm. Nous présentons une approche originale avec un réseau métallique unidimensionnel en face avant de la cellule. Les simulations numériques sont discutées dans le *chapitre 6* et les fabrication et caractérisation optique de démonstrateurs sont décrites dans le *chapitre 7*.

L'objectif de la PARTIE 3 est de présenter une preuve-de-concept en amont de la réalisation de cellules ultra-fines en GaAs. Nous proposons une architecture dans laquelle une grille métallique bidimensionnelle est couplée avec une couche ultra-fine de GaAs et un miroir arrière. Les performances théoriques de cette structure sont discutées dans le *chapitre 8*. Le *chapitre 9* présente la fabrication d'absorbeurs large bande Au/GaAs/Au.

Enfin, l'objet de la PARTIE 4 est les cellules ultrafines en silicium cristallin. Le travail présenté dans cette partie a été effectué dans le cadre du projet ANR NATHISOL, qui vise à réaliser des cellules c-Si ultrafines à partir de couches épitaxiées par PECVD à basse température. Le *chapitre 10* introduit le contexte du projet ainsi que ses motivations. Dans le *chapitre 11*, nous présentons les développements technologiques effectués en collaboration avec le LPICM afin de i) transférer des couches de c-Si epitaxiées d'épaisseur micrométrique et ii) de fabriquer des réseaux de nanopyramides inversées dans du silicium cristallin.

L'objet de ce résumé est de rassembler les résultats majeurs de cette étude, l'ensemble du travail de thèse pouvant être trouvé dans la version en anglais.

INTRODUCTION AU PHOTOVOLTAÏQUE ET MOTIVATIONS DE L'ÉTUDE

Le premier défi à relever par le marché de l'énergie actuel est la croissance de la demande énergétique pour répondre au développement économique et social. Ainsi, l'Agence internationale de l'énergie a rapporté une valeur de 150.000 TWh (TWh= térawatts-heures) pour la consommation mondiale d'énergie pour l'année 2010 et une valeur de 175.000 TWh est prévue à l'horizon 2020. Comment allons-nous répondre à cette demande croissante en énergie? Le marché énergétique actuel, basé à 80 % sur les énergies fossiles, est remis en question par la nécessité de limiter l'augmentation de température due au réchauffement climatique. Le dernier rapport de l'IEA [10] montre que la réduction des émissions liées à l'énergie ne peut se faire qu'à la condition que les sources d'énergie renouvelables (énergie éolienne, énergie solaire, biomasse, géothermie, hydroélectricité, énergie océanique) occupent une part plus importante dans le mix énergétique mondial (27 % en 2020). La production renouvelable d'électricité est un secteur très dynamique qui en dépit du contexte économique difficile, a montré une croissance remarquable de 8 % en 2012, pour atteindre une production d'énergie renouvelable totale de 4860 TWh [10]. Les énergies renouvelables ont un bel avenir devant elles, mais des politiques à long terme et des mesures incitatives sont nécessaires afin de permettre un développement à large échelle.

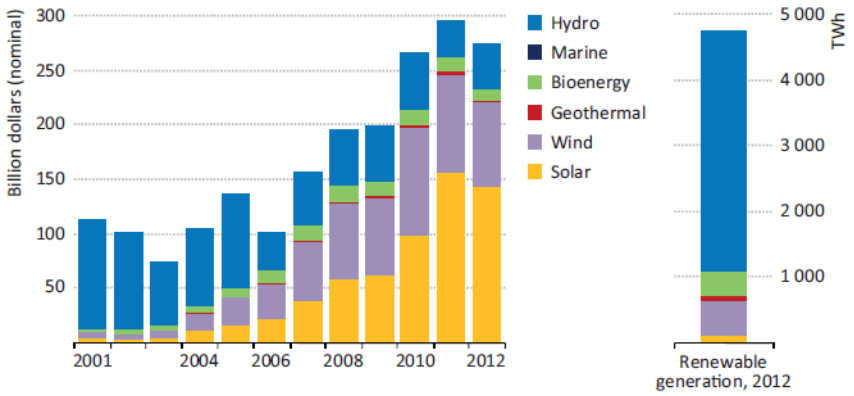

Figure 2: (gauche) Répartition des investissements mondiaux par secteur de production d'énergie renouvelable. (droite) Répartition de la production d'énergie renouvelable d'électricité totale en 2012. Figure extraite de la Ref. 10.

Figure 2 (droite) montre la répartition de la production d'énergie renouvelable en 2012. L'électricité provenant de l'énergie solaire représente une très faible fraction de la production mondiale d'électricité. Cependant, sur la figure 2 (à gauche), nous pouvons noter que les investissements dans l'énergie solaire ont considérablement augmenté depuis 2001. En 2012, le secteur de l'énergie solaire a représenté plus de la moitié des investissements mondiaux. L'énergie solaire a un potentiel énorme comme source d'électricité. En effet, elle est la plus grande ressource d'énergie sur Terre. La puissance lumineuse frappant la Terre en 90 min est suffisante pour subvenir aux besoins énergétiques de la planète pendant une année entière [3]! L'énergie solaire est exploitée sous deux

formes: le solaire photovoltaïque (PV) et l'énergie solaire à concentration. Dans cette thèse, nous nous focaliserons sur le solaire photovoltaïque, c'est-à-dire la conversion directe de l'énergie solaire en électricité.

Le marché du photovoltaïque a connu une croissance très impressionnante depuis 2003 avec un taux de croissance moyen de 40 % jusqu'en 2009 [3]. Une capacité de production de plus de 40 GW a été atteinte en 2010 avec un déploiement dans plusieurs pays, l'Allemagne étant le premier marché du photovoltaïque depuis 2001. En raison de l'augmentation des capacités de production, le prix de l'électricité photovoltaïque produite a chuté de façon spectaculaire dans la dernière décennie. La parité réseau est déjà atteinte dans plusieurs pays d'Europe (Italie, Espagne, Portugal, Allemagne, Danemark) [12], ce qui signifie que l'électricité produite par les installations photovoltaïques a le même prix que celle achetée à partir du réseau. La production d'électricité à partir de l'énergie solaire photovoltaïque est donc un objectif réalisable.

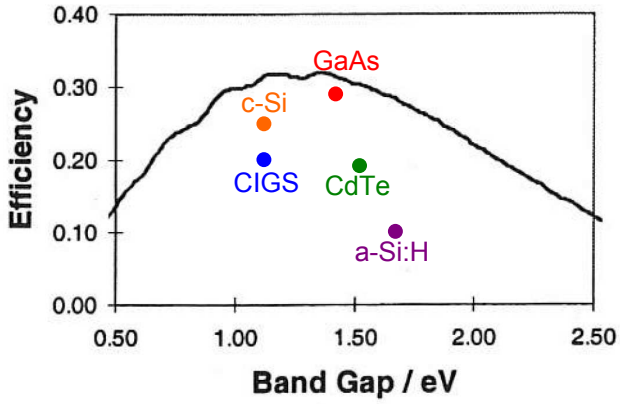

Figure 3: Limite théorique de l'éfficacité de conversion (courbe noire) en fonction de l'énergie de bande interdite du matériau pour une cellule solaire à simple jonction sous une illumination avec le spectre AM1.5G (figure extraite de Ref. 17). Les efficacités records des différentes filières technologiques sont aussi montrées.

Le marché du photovoltaïque repose sur plusieurs filières technologiques qui s'organisent notamment autour de deux groupes: la filière silicium cristallin et les filières couches minces. La figure 3 montre les records d'efficacité pour les principales filières ainsi que l'énergie du gap du matériau correspondant. À l'heure actuelle, 80 % de l'industrie photovoltaïque est encore basée sur la technologie silicium cristallin (monocristallin ou polycristallin). Le silicium est un matériau abondant et non toxique et il a une énergie de bande interdite presque optimale (1.1 eV) pour les cellules solaires. Les cellules solaires en silicium actuelles utilisent des wafers avec une épaisseur de 100 à 200 µm. La technologie de silicium cristallin est limitée par son coût: autour de 50 % du coût du module est dû au coût du matériau et à la purification nécessaire pour obtenir une qualité suffisante pour les cellules solaires. En outre, le silicium cristallin a un coefficient d'absorption faible du fait de son gap indirect. Par conséquent, une deuxième génération de cellules solaires à base de matériaux à gap direct (GaAs, a-Si:H, CdTe, CIGS) a été développée avec des cellules solaires d'une

épaisseur de quelques microns. Les technologies couches minces se sont considérablement développées jusqu'à atteindre des efficacités talonnant les 20 % pour les filières CdTe et CIGS ou dépassant même le silicium cristallin comme la filière GaAs (28.8 %). Malgré son faible coût de production, le développement de la filière silicium amorphe est limité par les faibles efficacités de conversion: le record actuel dépasse à peine les 10 % [24].

Les technologies couches minces ont été la première étape vers des dispositifs photovoltaïques plus efficaces et moins coûteux. Le point de départ de cette thèse est de concevoir des cellules solaires efficaces à partir d'absorbeurs ultrafins. Pour les matériaux en couches minces, notre objectif est de descendre en dessous de 100 nm pour l'épaisseur de la couche absorbante. Quels seraient les avantages d'aller plus loin dans la réduction de l'épaisseur des cellules vers des cellules solaires ultra-fines? Cela permettrait de réduire les coûts de production tout en augmentant le rendement de conversion grâce à une meilleure efficacité de collection. Cependant, la conception des cellules solaires ultra-minces n'a d'intérêt que si on parvient à générer un photocourant élevé à partir de couches de semiconducteur ultra-fines. En conséquence, la recherche de techniques avancées de piégeage de la lumière pour les cellules solaires ultrafines a connu un véritable essor au cours des dernières années. Parmi les stratégies proposées, les nanostructures métalliques montrent un fort potentiel pour confiner l'absorption de la lumière. Dans cette thèse, nous avons donc choisi de nous focaliser sur des nanostructures métalliques intégrées en face avant de la cellule solaire. Cette approche offre l'avantage de conserver une couche active plane.

D'autre part, nous avons aussi étudié la possibilité de donner une double fonctionnalité à la structure métallique utilisée pour piéger la lumière. Les électrodes conductrices transparentes à base de films métalliques sont une alternative intéressante aux électrodes conventionnelles de type oxyde transparent conducteur (ITO, ZnO:Al). En effet, elles possèdent à la fois une grande transparence optique et une grande conductivité et offrent des applications possibles dans le marché du photovoltaïque flexible. De façon standard, les performances des conducteurs transparents sont évaluées à partir de deux figures de mérite proposées par Haacke et Jain. Nous avons suggéré que ces figures de mérite ne sont pas adaptées à des applications photovoltaïques parce qu'elles considèrent les propriétés de l'électrode indépendamment de la cellule solaire. Dans le cas des contacts avant nanostructurés résonants qui sont l'objet de cette étude, nous proposons d'utiliser comme figure de mérite le gain de densité de courant de court-circuit ΔJ par rapport à une cellule de référence, par exemple une cellule classique sans dispositif de piégeage de lumière. Il convient de noter que la cellule de référence doit être définie très soigneusement afin de fournir une estimation précise des performances de l'électrode transparente. Cette figure de mérite permet de prendre en compte à la fois la perte de densité de courant dans le contact métallique et le gain de densité de courant dû au piégeage de la lumière.

CONCEPTION DE CELLULES SOLAIRES ULTRA-FINES EN SILICIUM AMORPHE

Potentiel et limites du silicium amorphe comme matériau photovoltaïque

La technologie silicium amorphe offre des avantages non négligeables malgré des performances électroniques inférieures au silicium cristallin. Les procédés de déposition bas coût et grande surface permettent un plus haut rendement de production et un coût de fabrication réduit. De plus, comme on peut le voir sur la figure 4a, beaucoup de progrès technologiques ont été réalisés depuis la première cellule simple jonction en silicium amorphe réalisée en 1976 par Carlson and Wronski [123] pour atteindre une efficacité de conversion supérieure à 10 % comme démontré par Benagli et al. [24] en 2009. Cependant, a-Si:H est un matériau avec une densité importante de défauts. L'efficacité de conversion des cellules solaires en silicium amorphe est limitée par la dégradation induite par l'exposition à la lumière, autrement connue sous le nom d'effet Staebler-Wronski. Cette dégradation peut aller jusqu'à une perte de 30 % de l'efficacité de conversion après illumination. Comme on peut le voir sur la figure 4b, une solution pour limiter les effets négatifs de l'effet Staebler-Wronski est de réduire l'épaisseur de la couche intrinsèque de silicium amorphe. Absorber efficacement la lumière dans des couches ultra-fines est donc de première importance pour la filière silicium amorphe.

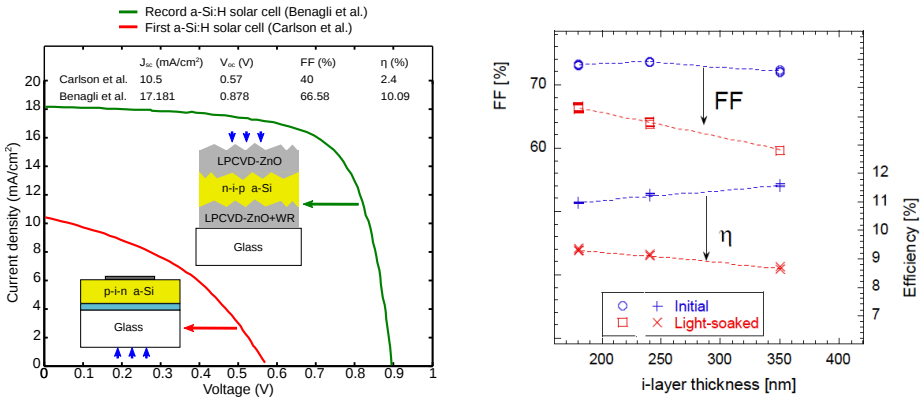

(a) (b)

Figure 4: (a) Progrès technologiques effectués dans la filière silicium amorphe depuis la première cellule démontrée par Carlson and Wronski [123] en 1976 jusqu'au record actuel démontré par Benagli et al. [24] en 2009. (b) Valeurs initiales et stabilisées du fill factor et de l'efficacité de conversion d'une cellule simple jonction en a-Si:H en fonction de l'épaisseur de la couche intrinsèque (figure extraite de Ref. 24).

Conception d'un contact résonant

Notre approche est basée sur une couche métallique nanostructurée encapsulée dans une couche de diélectrique en face avant de la cellule pour obtenir un

spectre d'absorption multi-résonant.
Nous avons défini plusieurs conditions que notre structure doit remplir:

1. une couche absorbante plane et ultra-mince (< 100 nm)
2. une large bande d'absorption (absorption $> 80\,\%$ sur $400 - 700$ nm)
3. une faible dépendance à la polarisation
4. une faible dépendance à l'angle d'incidence.

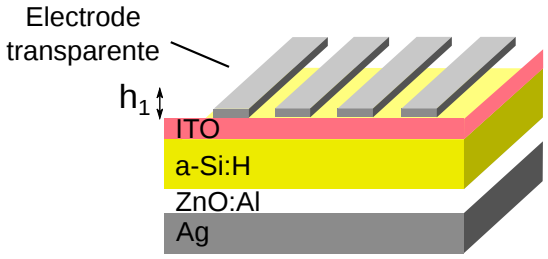

Figure 5: Schéma de la cellule solaire Si_3N_4(Ag)/ITO/a-Si:H/ZnO:Al/Ag considérée avec une couche d'a-Si:H de 90 nm d'épaisseur. L'électrode avant est constituée d'un réseau 1D d'argent (épaisseur de métal = 20 nm, largeur de trait = 80 nm et période 2 = 00 nm) encapsulée dans unce couche de matériau non absorbant (nitrure de silicum). Les autres paramètres géométriques sont: $h_1 = 60$ nm, $h_{ITO} = 10$ nm, $h_{ZnO:Al} = 15$ nm.

Notre proposition pour remplir ces critères est décrite sur la figure 5. La couche active est composée d'une jonction a-Si:H, l'influence du dopage sur l'indice de réfraction du matériau est négligée dans les calculs numériques. Deux couches d'espacement supplémentaires sont insérées au-dessus (ITO) et en dessous (ZnO:Al) de la couche d'a-Si:H pour empêcher la diffusion de métal dans la couche absorbante. Nous proposons d'utiliser la grille métallique pour jouer le rôle d'une électrode transparente conductrice en face avant de la cellule. Le contact supérieur est formé par la fine couche d'ITO et la grille métallique, ce qui entraîne une réduction de l'absorption optique dans les couches supérieures de la structure aux faibles longueurs d'onde par rapport aux contacts standards constitués d'une couche de 80 nm d'ITO ou de ZnO:Al.

La réponse optique de cette structure est étudiée par des calculs numériques avec le code Reticolo développé par Philippe Lalanne et ses collègues à IOGS. Il est basé sur une méthode Rigorous Coupled Wave Analysis (RCWA) et permet déterminer la réponse optique d'empilements de structures lamellaires. Les paramètres d'entrée des calculs sont les suivants:

- les épaisseurs des différentes couches de l'empilement
- les paramètres géométriques de la grille (w, p)
- les constantes optiques (n, k) de chaque matériau (ici, ZnO:Al, a-Si:H et Ag).

La réponse optique calculée numériquement de la cellule est montrée sur la figure 6a pour une polarisation TE (vert) et TM (orange) à incidence normale. Elle est comparée avec la réponse d'une structure de référence non structurée TCO/a-Si:H/ZnO:Al/Ag (mêmes épaisseurs d'a-Si:H et de ZnO:Al , $h_{TCO} =$

$h_1 + h_{ITO} = 70$ nm, aucun réseau). On remarque que l'utilisation de l'électrode transparente alternative conduit à une amélioration de l'absorption aux courtes ($300 - 380$ nm) et grandes ($600 - 700$ nm) longueurs d'onde. Aux courtes longueurs d'onde, le remplacement de l'oxyde transparent conducteur par un matériau non absorbant (nitrure de silicium) permet de réduire les pertes par absorption dans l'électrode avant. Dans le cas de la structure de référence avec une électrode TCO conventionnelle (ZnO:Al ou ITO), il existe un compromis entre la conductivité requise et la transparence de l'électrode. L'utilisation d'une couche de TCO fortement dopée conduit à des pertes d'absorption parasites dues à l'absorption des porteurs libres. L'électrode alternative relève cette contrainte, ce qui permet la diminution des pertes aux courtes longueurs d'onde tout en conservant une conductivité élevée. Dans la partie rouge du spectre, l'amélioration de l'absorption est due aux effets de piégeage de la lumière près de la bande interdite du silicium amorphe. De façon plus précise, nous avons analysé le mécanisme d'absorption en étudiant l'influence des différents paramètres de la structure. Le résumé de cette analyse est présenté dans le tableau 11.

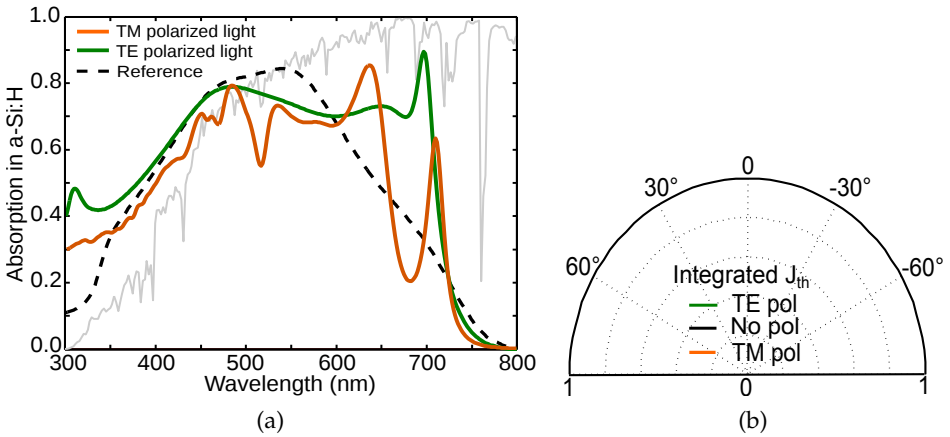

(a) (b)

Figure 6: (a) Absorption dans la couche d'a-Si:H pour la cellule solaire illustrée sur la figure 5 pour une polarisation TE (vert) et TM (orange) à incidence normale. Le spectre solaire AM1.5G normalisé est représenté pour référence (courbe grise). Courbe pointillée: spectre d'absorption de la structure de référence non structurée TCO/a-Si:H/ZnO:Al/Ag (mêmes épaisseurs d'a-Si:H et de ZnO:Al , $h_{TCO} = h_1 + h_{ITO} = 70$ nm, aucun réseau). Le gap du a-Si:H est représenté en gris. (b) Dépendance angulaire de l'intensité de court-circuit intégrée pour la structure représentée sur la figure 5. Les valeurs de J_{th} sont normalisées par rapport à la valeur maximale de J_{th} sous polarisation TE (égale à 15.97 mA/cm^2 pour $\theta = 10°$).

Nous avons estimé la densité théorique de court-circuit pour la structure optimisée. Nous montrons que l'utilisation du réseau métallique/diélectrique comme une électrode transparente alternative conduit à un J_{th} de 14.6 mA/cm^2 pour 90 nm d'a-Si:H. Une valeur de 14 mA/cm^2 a été calculée pour la structure de référence. Cette amélioration de la densité de courant de court-circuit par rapport à la structure de référence peut être attribuée à:

Paramètre géométrique	Type de résonance	Gamme spectrale
Epaisseur de diélectrique h_1	Rés. F-P dans la couche supérieure	$450 - 500$ nm
Epaisseur d'a-Si:H	Rés. F-P dans la couche d'a-Si:H	$600 - 650$ nm
Période du réseau p	Excitation de modes guidés	$650 - 750$ nm

Table 11: Résumé de l'analyse du mécanisme d'absorption. "Rés. F-P" signifie "Résonance de Fabry-Pérot".

- la réduction des pertes d'absorption aux courtes longueurs d'onde ($300 - 380$ nm) en raison du remplacement du TCO par du nitrure de silicium
- l'amélioration de l'absorption à proximité de la bande interdite de a-Si:H (600 à 700 nm) en raison de résonances Fabry-Perot dans la couche d'a-Si et du couplage à des modes guidés.

Nous avons aussi étudié la dépendance en angle des performances de la structure comme montré sur la figure 7b. Pour les deux polarisations (TE et TM), la dépendance angulaire est faible.

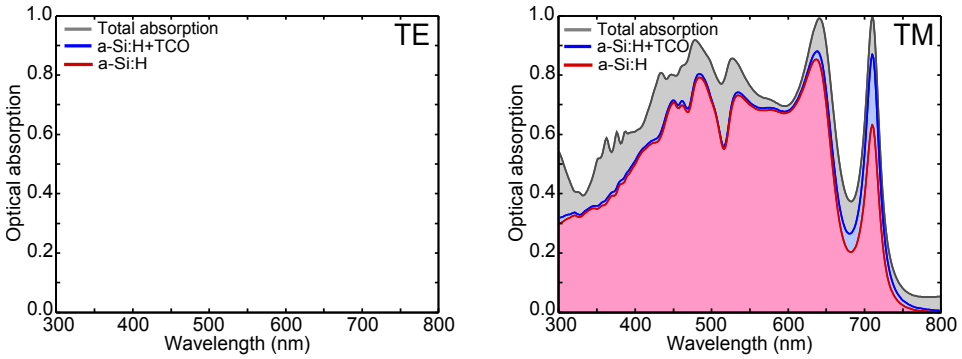

Figure 7: Absorption calculée numériquement dans chaque matériau de la cellule ultrafine en a-Si:H pour une excitation avec une polarisation TE (a) et TM (b) à incidence normale (courbe rouge: absorption dans a-Si:H; courbe bleue: absorption dans a-Si:H et les couches tampons d'ITO et de ZnO:Al; courbe grise: absorption totale). Le gap du a-Si:H est représenté en gris.

Il est important de rappeler que seuls les photons absorbés dans la couche d'a-Si:H contribuent à la génération de photocourant. La partie restante des photons incidents est soit réfléchie soit absorbée dans le métal (réseau + miroir arrière) ou les couches tampons. Sur les figures 7a et 7b, nous montrons la proportion de l'absorption dans chaque matériau constituant la cellule solaire pour les polarisations TE (Fig. 7a) et TM (Fig. 7b). En particulier, nous avons évalué la fraction de photons absorbés dans les deux contacts métalliques définis comme le rapport de l'absorption dans le métal (réseau + miroir) (en gris sur les figures) sur l'absorption totale dans la structure. Nous avons constaté que les pertes parasites dans le métal sont inférieures à 10 % des photons incidents

(pour une excitation avec une lumière non polarisée en incidence normale). Ce résultat contredit l'idée répandue que placer des structures métalliques en face avant de la cellule conduit à des pertes très importantes par absorption parasite dans le métal.

A travers cette étude numérique, nous avons montré que la combinaison de résonances de Fabry-Pérot verticales et du couplage à des modes guidés conduit à un spectre d'absorption large bande avec une faible dépendance par rapport à la polarisation et l'angle d'incidence. Nous avons ainsi montré que notre structure vérifiait les critères que nous avions fixés précédemment. Cette approche versatile peut être appliquée à différents matériaux et géométries de l'électrode. Elle ouvre de nouvelles possibilités pour les électrodes transparentes à haute conductivité et transparence optique.

Fabrication et caractérisation de cellules solaires ultra-fines en silicium amorphe

Des cellules solaires ultra-fines en a-Si:H avec des couches d'argent nanostructurées ont été fabriquées comme montré sur la figure 8a. Les échantillons ont ensuite été caractérisés avec le montage présenté dans le *chapitre* 4. La figure 8b montre l'absorption totale à $\theta = 5°$ (plan d'incidence perpendiculaire aux fils) d'une cellule de 4 mm^2 avec un réseau 1D en argent (épaisseur $= 20$ nm, période $= 500$ nm, facteur de remplissage $= 0,38$) pour une lumière polarisée en TE (vert) et TM (orange). La réponse mesurée d'une cellule de référence non structurée est représentée en pointillés noirs pour comparaison. Sans aucune structuration, seuls deux pics d'absorption (P_1 and P_2) sont visibles, ils sont dus à des résonances de Fabry-Pérot verticales dans l'empilement. Ces pics P_1 and P_2 sont également mis en évidence pour la cellule structurée. En outre, les spectres de la cellule structurée présentent dans les deux polarisations TE et TM plusieurs pics d'absorption attribués au piégeage de la lumière aux grandes longueurs d'onde. Malheureusement, nous constatons que la plupart de ces pics sont situés au-delà de la longueur d'onde de bande interdite (en gris sur la figure 8b) et donc ne contribuent pas à la génération de porteurs dans la cellule.

Nous avons utilisé le montage GonioVISIR décrit au *chapitre* 4 pour étudier l'évolution du spectre d'absorption en fonction de l'angle d'incidence. Des mesures de réflectivité ont été effectuées sur la même cellule que précédemment (épaisseur $= 20$ nm, période $= 500$ nm, facteur de remplissage $= 0,38$) pour un angle d'incidence entre 5 et 60 degrés, avec un pas de 5 degrés. Les résultats sont montrés sur la figure 9. Nous avons aussi mené des caractérisations optiques sur le second montage MicroVISIR. Nous avons ainsi étudié l'évolution de la réponse optique en fonction de l'angle d'incidence mais aussi des paramètres géométriques du réseau métallique. Nous avons attribué les pics d'absorption à des résonances de Fabry-Pérot ainsi qu'à l'excitation de modes guidés se propageant dans la couche d'a-Si:H et à des résonances localisées de plasmons de surface. Cette étude expérimentale confirme donc l'approche multi-résonante que nous avons considérée dans cette thèse.

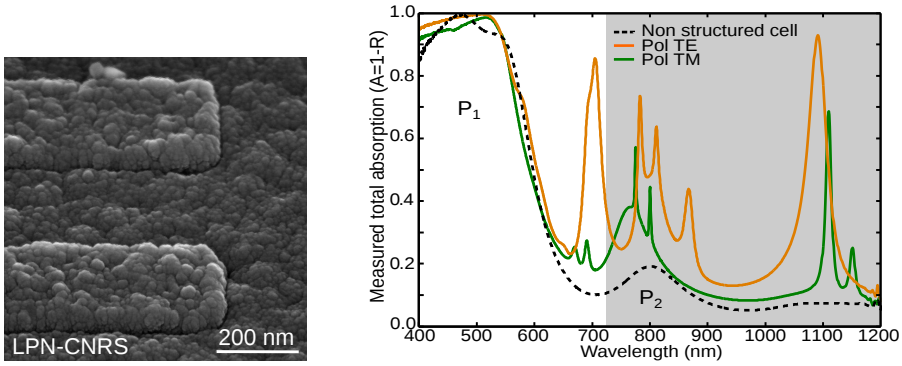

(a) (b)

Figure 8: (a) Image MEB d'un réseau unidimensionnel d'argent après encapsulation avec un contact avant en ITO. (b) Absorption totale mesurée de cellules en a-Si:H avec un réseau 1D d'argent ($p = 500$ nm, $ff = 0.38$) pour une excitation à $\theta = 5°$ avec une lumière polarisée en TE (vert) et TM (orange) par rapport à la réponse de cellules non structurées (courbe en pointillés noirs). Le gap du a-Si:H est représenté en gris.

La caractérisation de ce système particulier a mis en évidence la complémentarité des deux montages expérimentaux que nous avons développés et présentés dans le *chapitre* 4. Le montage GonioVISIR a permis de mettre en évidence le couplage à des ordres diffractés grâce à la haute résolution des pics observés. Malgré sa résolution spectrale inférieure, la configuration MicroVISIR a permis de caractériser même les plus petites structures et ainsi de fournir des informations sur l'influence des paramètres du réseau sur la réponse optique.

Enfin, la structure fabriquée ne correspond pas à la structure optimisée avec les calculs numériques et étudiée dans le *chapitre* 6. En particulier, les constantes optiques de l'a-Si:H déposé expérimentalement étaient différentes des valeurs utilisées dans les calculs. En conséquence, la plupart des résonances observées ont été déplacées au-delà de la longueur d'onde de bande interdite du matériau. Ce travail montre que le contrôle des propriétés du matériau déposé est crucial pour réaliser un piégeage efficace de la lumière. Il est essentiel d'effectuer des simulations optiques en forte synergie avec la caractérisation avancée des matériaux.

APPLICATION À L'ARSENURE DE GALLIUM: VERS DES CELLULES SOLAIRES ULTRA-FINES À HAUTE EFFICACITÉ

Conception d'absorbeurs large bande ultra-fins en GaAs avec une grille métallique sub-longueur d'onde

Dans cette partie, nous nous intéressons à l'application du concept de contact métallique nanostructuré résonant pour la conception de cellules solaires ultra-fines en GaAs. Considérons ainsi le cas d'une couche de GaAs ultra-mince avec une épaisseur de 25 nm. La quantité de photons absorbés dans la couche peut être visualisée à partir du calcul de l'absorption simple passage dans la

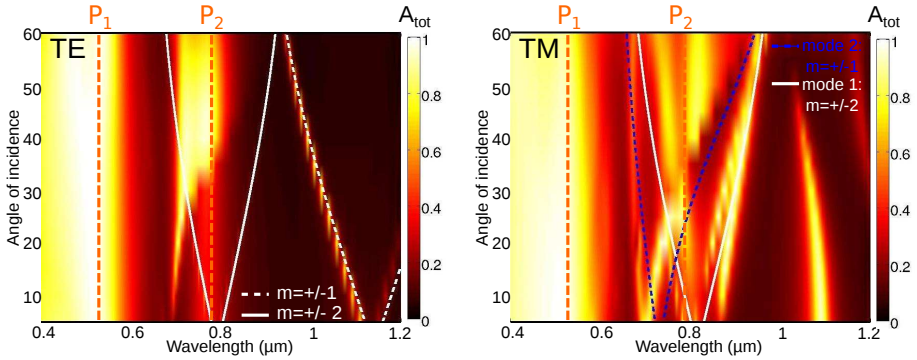

Figure 9: Absorption totale mesurée de cellules en a-Si:H avec un réseau 1D en argent ($p = 500$ nm, $ff = 0.38$) en fonction de la longueur d'onde pour une excitation à $\theta = 5°$ avec une lumière polarisée en TE (gauche) et TM (droite). Les principaux pics d'absorption sont attribués à des résonances de Fabry-Pérot (orange pointillé) et modes guidés dans la couche d'a-Si:H (ligne de couleur blanche et pointillée pour la polarisation TE; ligne de couleur blanche et ligne pointillée bleue pour la polarisation TM).

couche, c'est-à-dire la fraction de photons absorbés après un seul passage à travers la couche. Figure 10b affiche l'absorption simple passage pour 25 nm de GaAs (courbe bleue). A 500 nm, seulement 20 % de la lumière incidente est absorbée dans la couche de GaAs. La façon la plus simple d'augmenter le nombre de photons absorbés dans la couche de GaAs est d'ajouter un miroir arrière métallique. L'absorption dans une couche de GaAs d'épaisseur 25 nm sur un miroir d'argent est représentée sur la figure 10b (courbe verte). Entre 470 et 920 nm, l'absorption est augmentée grâce à des résonances de Fabry-Pérot dans la cavité Air/GaAs/Ag. Un large pic d'absorption est ainsi mis en évidence avec une intensité atteignant 65 % à 620 nm. Cependant, la bande d'absorption obtenue est restreinte (largeur à mi-hauteur de 250 nm) et l'intensité trop faible.

Nous proposons ainsi une structure avec une grille métallique bidimensionnelle pour obtenir un spectre d'absorption multi-résonant et large bande. Notre approche est décrite dans la figure 10a. Une grille d'argent 2D (période p, largeur de traits w et épaisseur de métal h_m) est déposée sur une couche de GaAs d'épaisseur 25 nm sur un miroir d'argent. La grille d'argent est encapsulée dans une couche anti-réfléchissante avec une épaisseur totale h_1. Quand $h_1 = h_m$, le matériau diélectrique remplit exactement les trous de la grille métallique. Nous avons choisi le nitrure de silicium (SiN_x) comme matériau diélectrique en raison de son indice optique (environ 2) entre celui du GaAs (entre 3.5 et 5.1) et celui de l'air.

Nous avons calculé numériquement l'absorption intégrée dans la couche de GaAs entre 400 et 900 nm en fonction des différents paramètres de la structure variable (h_1, p, w, h_m). Le meilleur résultat est obtenu pour $h_1 = 80$ nm, $p = 500$ nm, $w = 125$ nm et $h_m = 20$ nm. Nous avons représenté le spectre d'absorption correspondant à la structure optimale sur la figure 10c. Pour cette épaisseur de nitrure de silicium, on obtient cinq pics d'absorption. Un spectre d'absorption très large est obtenu grâce à ces multiples résonances. Notez que cette réponse est indépendante de la polarisation de la lumière incidente en incidence nor-

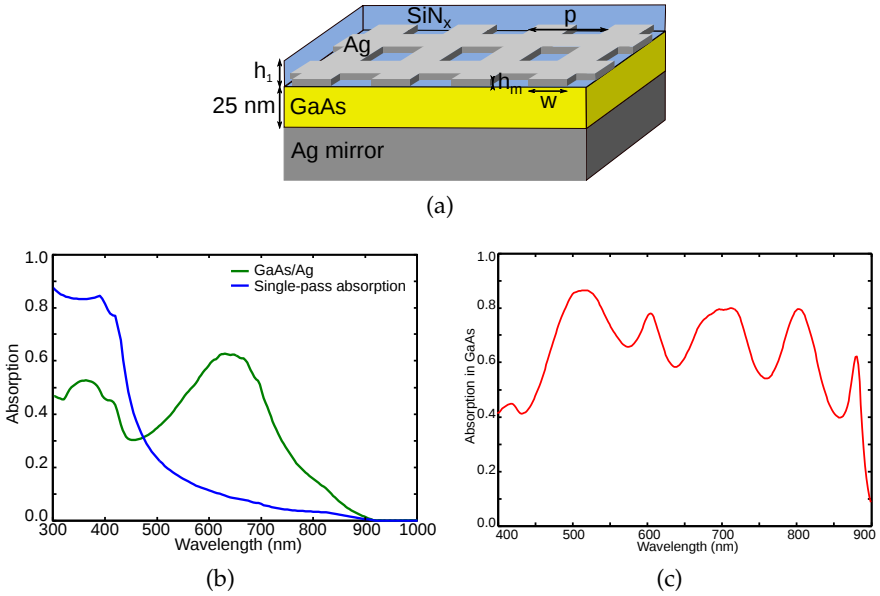

Figure 10: (a) Schéma de la structure proposée pour un absorbeur large bande ultrafin (épaisseur de 25 nm) à base de GaAs. (b) Absorption en un simple passage dans une couche de 25 nm de GaAs (courbe bleue) comparée à l'absorption pour la même couche déposée sur un miroir d'argent (courbe verte). (c) Spectre d'absorption dans la couche de GaAs pour la structure suivante: $h_1 = 80$ nm, $h_{GaAs} = 25$ nm, $p = 500$ nm, $w = 125$ nm et $h_m = 20$ nm.

male grâce à la bidimensionnalité de la structure. Nous avons évalué les performances de cette structure en calculant la densité de courant théorique J_{th} pour la courbe montrée sur la figure 10c. Une valeur de $J_{th} = 21.6$ mA/cm^2 a été obtenue pour une excitation à incidence normale. Par souci de comparaison, le record actuel expérimental pour une cellule solaire GaAs simple jonction est un rendement de conversion de 28.8 % obtenu par Alta Devices en 2012 [21]. La densité de courant de court-circuit mesurée est $J_{SC} = 29.68$ mA/cm^2 pour une épaisseur de GaAs de 1 µm. Dans notre approche, la densité de courant de court-circuit théorique n'est donc réduite que d'un facteur 1.4 par rapport au record expérimental tandis que l'épaisseur de GaAs a subi une réduction d'un facteur 40. En raison de la couche absorbante ultrafine, nous nous attendons également à une meilleure collection des porteurs et une tension en circuit ouvert plus importante.

Nous avons aussi étudié la dépendance de la réponse de la structure en fonction de l'angle d'incidence, comme présenté sur la figure 11. La densité de courant montre une faible diminution lorsque l'angle d'incidence augmente: à 60°, J_{th} est toujours égale à 18.6 mA/cm^2, à comparer à la valeur de 21.6 mA/cm^2 pour une incidence normale.

Grâce à une analyse numérique du mécanisme d'absorption, nous avons montré que cette structure combinait des résonances de Fabry-Pérot verticales dans la couche de GaAs et des modes guidés par couplage avec la grille métallique. Les dimensions de la grille métallique et l'épaisseur de la couche de nitrure de silicium permettent d'ajuster la position et l'intensité des résonances.

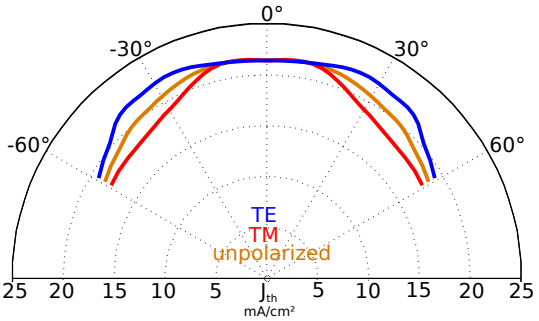

Figure 11: Densité de courant de court-circuit théorique en fonction de l'angle d'incidence pour une polarisation TE (bleu), TM (rouge) et pour une lumière non polarisée (orange). La structure considérée est la suivante: $h_1 = 80$ nm, $h_{GaAs} = 25$ nm, $p = 500$ nm, $w = 125$ nm et $h_m = 20$ nm.

Pour l'instant, la structure proposée n'est qu'une preuve-de-concept, la couche de GaAs étant trop fine pour intégrer une jonction p-n et donc pour réaliser une cellule solaire. Cependant, ce concept montre des résultats très prometteurs. Il peut être appliqué à des dispositifs plus épais ($100 - 200$ nm) comprenant une jonction p-n et des couches barrière, ouvrant ainsi la voie à des dispositifs photovoltaïques ultra-minces et très efficaces (efficacité > 20 %).

Fabrication et caractérisation de démonstrateurs Au/GaAs/Au

Nous avons développé un procédé de fabrication pour réaliser des absorbeurs large bande à base de couches ultra-fines (épaisseur nominale de 25 nm) de GaAs. Nous utilisons du GaAs cristallin obtenu par croissance épitaxiale sur un substrat de GaAs. La fabrication de démonstrateurs nécessite d'abord un transfert de la couche de GaAs épitaxiée depuis le substrat initial de GaAs sur un miroir d'or. Une grille bidimensionnelle d'or est ensuite structurée par lithographie électronique sur la couche de GaAs. Enfin, la grille métallique est encapsulée dans une couche de nitrure de silicium.

La figure 12c montre une image MEB d'une grille à la fin du procédé de fabrication. Nous avons mesuré la réflectivité à incidence normale de ces structures et déduit l'absorption totale comme montré sur la figure 12a. Le spectre d'absorption mesuré présente une large bande d'absorption ($A_{tot} > 80\,\%$ entre 450 et 830 nm) en bon accord avec les calculs numériques (figure 12b). L'analyse des résultats expérimentaux montre que le spectre d'absorption multi-résonant provient de la combinaison de résonances Fabry-Pérot dans la couche de GaAs et de modes guidés dus à la grille métallique.

Il est important de noter que dans la plupart des approches de type plasmonique existantes pour réaliser des absorbeurs large bande, la lumière est absorbée entièrement dans le métal. Afin d'intégrer les structures plasmoniques dans des dispositifs photovoltaïques efficaces, la lumière doit être absorbée principalement dans la couche de semi-conducteur active. Dans le cadre de notre étude, nos calculs montrent des valeurs de densité de courant de court-circuit importantes, comme mentionné plus haut. Cette étude expérimentale

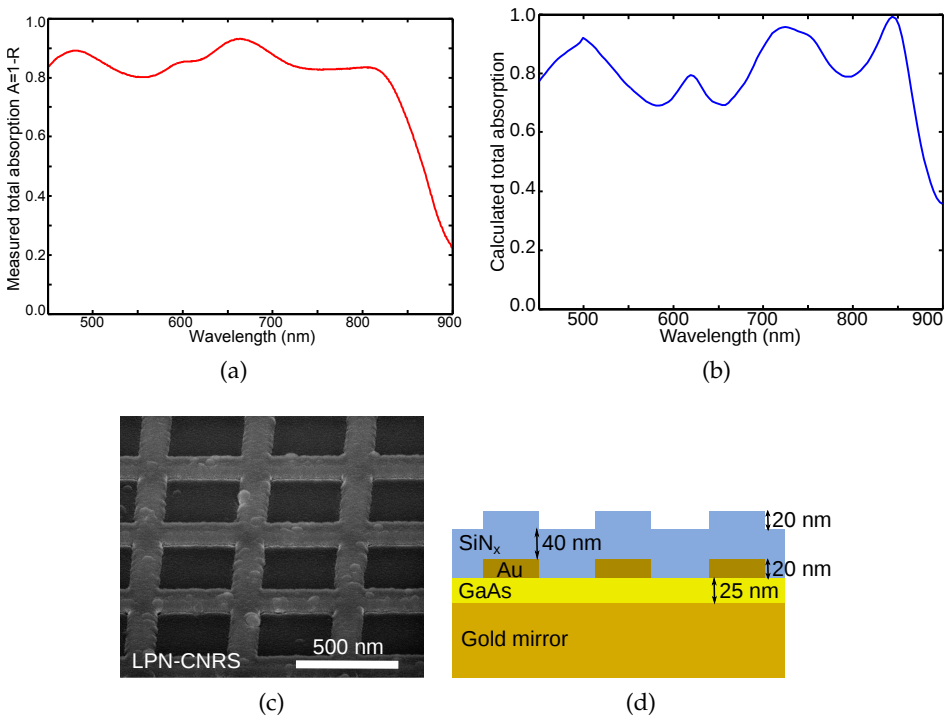

Figure 12: Absorption totale mesurée (a) et calculée (b) pour une couche de GaAs de 23 nm transférée sur un miroir d'or avec une grille bidimensionnelle d'or (épaisseur = 20 nm, période = 500 nm, largeur des traits = 125 nm) encapsulée dans une couche de nitrure de silicium de 60 nm. (c) Image MEB d'une grille bidimensionnelle d'or après dépôt de la couche de SiN_x. (d) Schéma de la structure modélisée dans les simulations, prenant en compte un profil non plan pour la couche supérieure de SiN_x.

confirme donc le potentiel de la grille 2D non seulement pour obtenir une absorption totale importante mais surtout pour confiner la lumière dans une couche semi-conductrice dans un volume sub-longueur d'onde tout en conservant de bonnes performances.

CONFINER LA LUMIÈRE DANS DES CELLULES SOLAIRES ULTRA-FINES EN SILICIUM CRISTALLIN

Contexte et motivations du projet ANR NATHISOL

Les PARTIES 2 et 3 de la thèse portent sur le piégeage de la lumière dans les cellules solaires couches minces (a-Si:H et GaAs). Le potentiel de la nanophotonique pour confiner l'absorption de la lumière dans de très petits volumes est également applicable à d'autres matériaux photovoltaïques. En particulier, l'utilisation de stratégies avancées de piégeage de lumière pourraient permettre une réduction de l'épaisseur des cellules en silicium cristallin d'un facteur 20 à 100 par rapport aux cellules commerciales, ce qui représenterait une formidable avancée pour cette filière. Mon travail sur les cellules solaires silicium couches

minces a été effectué dans le cadre du projet ANR NATHISOL comme présenté dans la PARTIE 4. L'objectif du projet est d'atteindre un rendement de conversion de 13.5 % pour des cellules solaires en silicium cristallin avec une épaisseur entre 2 et 5 microns. Comme décrit sur la figure 13, la structure visée repose sur l'utilisation de couches minces de c-Si épitaxiées par PECVD à basse température au LPICM et ensuite transférées sur un substrat à faible coût. Cette technique de dépôt produit des couches fines de c-Si de bonne qualité cristalline mais la densité de courant de court-circuit est limitée en raison de la faible épaisseur de la couche de c-Si. Notre approche repose également sur le transfert de la couche épitaxiale sur un substrat hôte afin d'intégrer des stratégies de piégeage de lumière allant du simple réflecteur arrière à des structures photoniques et plasmoniques avancées.

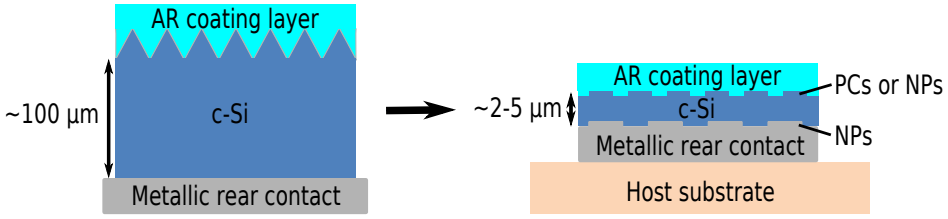

Figure 13: Vers des cellules en silicium cristallin ultra-fines. PCs = cristaux photoniques; NPs = nanoparticules métalliques

Fabrication de cellules solaires ultra-fines en silicium cristallin transférées sur substrat bas coût

Nous avons développé un procédé pour transférer des couches minces de c-Si épitaxiées par PECVD d'un substrat wafer à un substrat hôte bas coût grâce à un détachement thermique de la couche épitaxiale. Des couches en silicium cristallin épitaxié (épaisseur entre 2 et 6 µm) ont été détachées et transférées sur un substrat hôte PDMS/verre suivant ce procédé (figure 14a). Elles ont ensuite été caractérisées par spectroscopie Raman (figure 14b) et par ellipsométrie (figure 14c). Les résultats sont très encourageants et semblent montrer qu'il n'y a pas de variation de la qualité cristalline lors du détachement et du transfert. Nous avons également fabriqué une diode à partir d'une couche de c-Si epitaxiée transférée et complétée par une couche d'a-Si:H dopée n pour créer une hétérojonction. Un comportement redresseur a été démontré par des mesures I-V sous illumination (figure 14d). Des caractérisations électriques supplémentaires avec une jonction p-i-n complète devraient fournir davantage d'informations sur les propriétés de ce matériau pour les applications photovoltaïques. Jusqu'à présent, la quantité de couches disponibles et les variations dans les propriétés de ces couches ont limité la reproductibilité du procédé de transfert. Une étude systématique de l'influence des paramètres (température, nature du métal, épaisseur de la couche de c-Si épitaxiée) est nécessaire pour mieux comprendre le mécanisme de détachement.

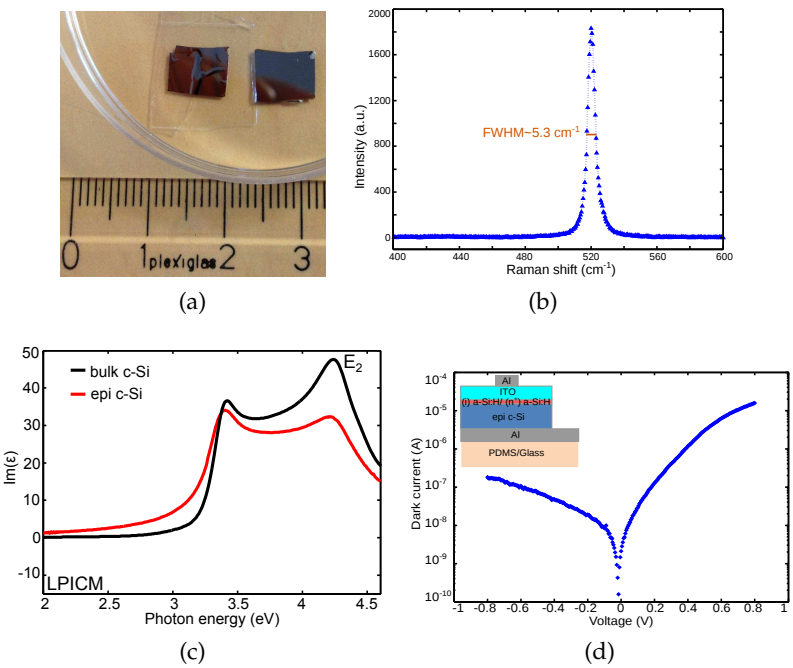

Figure 14: Caractérisation de couches intrinsèques de c-Si épitaxiées par PECVD (a) Photographie d'une couche epi de 2.5 µm transférée sur substrate hôte PDMS/verre (gauche) et du substrat wafer initial (droite). (b) Spectre Raman de la couche epi de 2.5 µm. (c) Courbe de Im(ffl) mesurée par ellipsométrie sur une couche epi de 6 µm après détachement (courbe rouge) comparée au spectre du silicium cristallin massif. (d) Courbe I-V mesurée sous illumination (surface = 3 mm^2) sur une diode réalisée à partir d'une couche epi de 2.5 µm transférée sur substrate hôte PDMS/verre.

Le deuxième objectif du projet est de mettre en œuvre des nanostructures de piégeage de lumière dans des cellules solaires en c-Si ultra-minces. En particulier, la fabrication de nanostructures périodiques (des cristaux photoniques par exemple) soit par gravure humide ou gravure plasma est considérée. Dans cette thèse, nous présentons les premiers développements technologiques en vue de réaliser une nanotexturation contrôlée de cellules solaires en silicium cristallin épitaxié. Ainsi, nous avons adapté un procédé de texturation de c-Si bien connu (gravure anisotropique humide avec du KOH) pour effectuer une structuration contrôlée de nanopyramides inversées dans des wafers de c-Si. Ce procédé conduit à des motifs propres et bien définis, avec une bonne homogénéité sur de grandes surfaces, comme on peut le voir sur la figure 15a après dépôt d'une couche anti-reflet de nitrure de silicium. La réflectivité mesurée (figure 15b) a montré une diminution de la réflectivité sur l'ensemble du spectre solaire très prometteuse ($R < 10\,\%$ entre 500 et 900 nm). Jusqu'à présent, nous n'avons pas été en mesure de fabriquer des réseaux de nanopyramides inversées sur des couches de c-Si épitaxiées par PECVD. Cependant, nous avons rapporté la gravure de pyramides aléatoires sur des couches de c-Si épitaxiées de 3 µm d'épaisseur. Ceci apporte une preuve supplémentaire que

le matériau déposé est cristallin. La structuration de réseaux périodiques de nanopyramides semble être rapidement réalisable.

Par ailleurs, cette première étude de texturation de surface des couches de c-Si épitaxiées par PECVD ouvre la voie à des stratégies de piégeage de lumière plus avancées que les pyramides. Elle peut aussi permettre de répondre à des problématiques communes à toutes les approches de texturation. Par exemple, il est essentiel d'optimiser la passivation de la surface texturée pour empêcher l'augmentation des recombinaisons de surface.

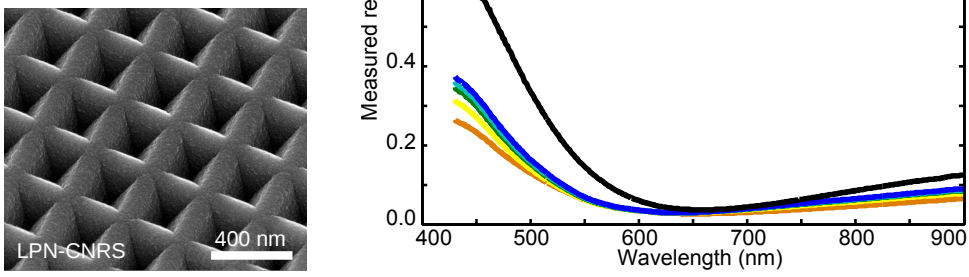

(a) (b)

Figure 15: Nanostructuration de pyramides inversées dans du silicium cristallin massif avec un process avec un masque de gravure en résine HSQ. (a) Image prise au MEB de pyramides inversées après déposition d'une couche anti-reflet en nitrure de silicium (épaisseur = 80 nm). (b) Mesures de réflectivité sur un substrat de silicium plan (courbe noire) et des pyramides inversées (courbes colorées) avec une période constante de 300 nm et une taille variable entre 240 (courbe bleue) et 280 nm (courbe orange). Dans les deux cas, l'échantillon a une couche anti-reflet en nitrure de silicium (épaisseur = 80 nm). Insert: valeurs de la réflectivité à 450 et 850 nm extraites des courbes noire et orange.

CONCLUSION ET PERSPECTIVES DE L'ÉTUDE

En conclusion générale, cette thèse s'est présentée comme le fruit de la rencontre entre la nanophotonique et le domaine du photovoltaïque. En effet, la réduction de l'épaisseur de l'absorbeur vers des couches ultra-minces pourrait ouvrir la voie vers des dispositifs photovoltaïques plus efficaces et moins coûteux et soulager la contrainte pesant sur les matériaux rares. Cependant, cette avancée technologique n'a lieu d'être que s'il est possible de générer un photocourant élevé dans de très petits volumes de semi-conducteurs. Dans ce but, nous avons proposé une nouvelle structure avec une très fine couche métallique nanostructurée pour concentrer la lumière dans la cellule solaire ultra-mince mais également pour constituer un contact avant alternatif. L'idée d'utiliser une grille métallique comme une électrode alternative a déjà été développée dans

le domaine du photovoltaïque organique depuis plusieurs années. Dans cette thèse, nous avons montré des résultats prometteurs pour l'application de ce concept à d'autres matériaux que sont le silicium amorphe et l'arsenure de gallium. Pourquoi ne pas étendre cette approche dans un premier temps à d'autres matériaux couches minces tels que CdTe ou CIGS et dans un deuxième temps aux cellules ultra-fines en silicium cristallin ?

De fait, la recherche des cellules photovoltaïques ultimes à faible coût et à haut rendement brouille les frontières entre les différentes filières technologiques. Par exemple, dans cette thèse, nous avons déjà étudié l'application de techniques de nanofabrication classiquement associées aux technologies couches minces à la structuration du silicium monocristallin. Plus globalement, quelle que soit la technologie considérée, cette thèse a montré que la mise en œuvre efficace de structures avancées de piégeage optique nécessite une forte synergie entre la conception numérique, la science des matériaux et les techniques de nanofabrication.

D

LIST OF PUBLICATIONS

JOURNAL CONTRIBUTIONS

1. **I. Massiot**, C. Colin, N. Péré-Laperne, P. Roca i Cabarrocas, C. Sauvan, P. Lalanne, J-L. Pelouard and S. Collin, *Nanopatterned front contact for broadband absorption in ultra-thin amorphous silicon solar cells*, Applied Physics Letters, Vol. 101, p. 163901 (2012).
2. **I. Massiot**, C. Colin, C. Sauvan, P. Lalanne, P. Roca i Cabarrocas, J-L. Pelouard and S. Collin, *Multi-resonant absorption in ultra-thin silicon solar cells with metallic nanowires*, Optics Express, Vol. 21, Issue S3, p. A372-A381 (2013).

CONFERENCE PROCEEDINGS AS FIRST AUTHOR

1. **I. Massiot**, S. Collin, C. Colin, N. Péré-Laperne, N. Bardou, C. Dupuis, P. Roca i Cabarrocas and J-L. Pelouard, *Conception of ultra-thin amorphous silicon solar cells*, In Proceedings of the 26th European Photovoltaic Solar Energy Conference, 1DV.1.28, p. 398-401, Hamburg, Germany (2011).
2. **I. Massiot**, C. Colin, P. Roca i Cabarrocas, N. Bardou, C. Dupuis, C. Sauvan, P. Lalanne, J-L. Pelouard and S. Collin, *Nanopatterned front contact for multi-resonant absorption in ultra-thin amorphous silicon solar cells*, In Proceedings of the 27th European Photovoltaic Solar Energy Conference, 3AO.6.5, p. 2132-2136, Frankfurt, Germany (2012).
3. **I. Massiot**, C. Colin, N. Vandamme, N. Bardou, P. Roca i Cabarrocas, C. Sauvan, P. Lalanne, J-L. Pelouard and S. Collin, *Towards high-efficiency ultra-thin solar cells with nanopatterned metallic front contact*, In Proceedings of the 39th IEEE Photovoltaic Specialists Conference, Tampa, United States (2013).

CONFERENCE PROCEEDINGS AS CO-AUTHOR

1. S. Collin, C. Sauvan, C. Colin, **I. Massiot**, F. Pardo, N. Bardou, P. Lalanne and J-L. Pelouard, *High-efficient ultra-thin solar cells*, In Proceedings of the 25th European Photovoltaic Solar Energy Conference, 1CO.8.4, p. 265-268, Valencia, Spain (2010).
2. C. Colin, S. Collin, N. Péré-Laperne, **I. Massiot**, G. Dagher, N. Quach-Vu, N. Bardou, C. Dupuis, J-F. Guillemoles, J-L. Pelouard, *Ultrathin CIGS*

solar cells with metallic nanoparticles, In Proceedings of the 26th European Photovoltaic Solar Energy Conference, 3*DV*.1.24, p. 2863-2866, Hamburg, Germany (2011).

3. C. Colin, A. Cattoni, **I. Massiot**, J.F. Guillemoles, N. Bardou, C. Dupuis, J-L. Pelouard, D. Mercier, I. Gérard, A. Etcheberry, Z. Jehl, D. Lincot, N. Naghavi, S. Collin, *Broadband light trapping in ultra-thin nano-structured* $Cu(In,Ga)Se_2$ *solar cells,* In Proceedings of the 27th European Photovoltaic Solar Energy Conference, 3*CO*.4.6, p. 2244-2248, Frankfurt, Germany (2012).

4. C. Colin, **I. Massiot**, A. Cattoni, N. Vandamme, C. Dupuis, N. Bardou, I. Gérard, N. Naghavi, J-F. Guillemoles, J-L. Pelouard, S. Collin, *Broadband light-trapping in ultra-thin nano-structured solar cells*, In Proceedings of SPIE, Vol. 8620 , p. 86200C (2013).

BIBLIOGRAPHY

[1] IEA. *Key world energy statistics* 2012. 2012.

[2] E. Becquerel. Mémoire sur les effets électriques produits sous l'influence des rayons solaires. *Comptes Rendus*, 9:561–567, 1839.

[3] IEA. *Solar Energy Perspectives*. 2011.

[4] X. Meng. *Conception et réalisation de cristaux photoniques et réseaux de diffraction pour les cellules photovoltaïques silicium en couches ultra-minces*. PhD thesis, Ecole Centrale de Lyon, 2012.

[5] K. Söderström, F-J. Haug, J. Escarré, O. Cubero, and C. Ballif. Photocurrent increase in n-i-p thin film silicon solar cells by guided mode excitation via grating coupler. *Applied Physics Letters*, 96:213508, 2010.

[6] V. E. Ferry, M. A. Verschuuren, H. B. T. Li, E. Verhagen, R. J. Walters, R. E. I. Schropp, H. A. Atwater, and A. Polman. Light trapping in ultrathin plasmonic solar cells. *Optics Express*, 18:A237–A245, 2010.

[7] J. Zhu, C. Hsu, Z. Yu, S. Fan, and Y. Cui. Nanodome solar cells with efficient light management and self-cleaning. *Nano Letters*, 10:1979–1984, 2010.

[8] IPCC. *Renewable energy sources and climate change mitigation*. 2011.

[9] B. Meyssignac and A. Cazenave. Sea level: A review of present-day and recent-past changes and variability. *Journal of Geodynamics*, 58:96–109, 2012.

[10] IEA. *World Energy Outlook Special Report - Redrawing the energy-climate map*. 2013.

[11] OECD. URL http://www.oecd.org.

[12] H. Ossenbrink, A. Jäger-Waldau, T. Huld, and N. Taylor. New opportunities for PV systems. In *Proceedings of 27th European Photovoltaic Solar Energy Conference, Frankfurt, Germany*, pages 3727–3730, 2012.

[13] Solar Aid. URL www.solar-aid.org.

[14] Renewable World. URL http://www.renewable-world.org.

[15] P. Würfel. The chemical potential of radiation. *Journal of Physics C - Solid State Physics*, 15:3967–3985, 1982.

[16] P. Würfel. *Physics of Solar Cells - From Basic Principles to Advanced Concepts*. Wiley, 2009.

[17] J. Nelson. *The physics of solar cells*. Imperial College Press, 2003.

[18] S. R. Wenham, M. A. Green, M. E. Watt, R. Corkish, and A. Sproul. *Applied Photovoltaics*. Earthscan, 2012.

[19] W. Shockley and H. J. Queisser. Detailed balance limit of efficiency of p-n junction solar cells. *Journal of Applied Physics*, 32:510, 1961.

[20] I. Tobias and A. Luque. Ideal efficiency of monolithic, series-connected multijunction solar cells. *Progress in Photovoltaics: Research and Applications*, 10:323–329, 2002.

[21] M. A. Green, K. Emery, Y. Hishikawa, W. Warta, and E. D. Dunlop. Solar cell efficiency tables (version 42). *Progress in Photovoltaics: Research and Applications*, 21:827–837, 2013.

[22] M. A. Green. The path to 25% silicon solar cell efficiency: History of silicon cell evolution. *Progress in Photovoltaics: Research and Applications*, 17:183–189, 2009.

[23] X. Deng and E. A. Schiff. *Handbook of Photovoltaic Science and Engineering*, chapter 12, pages 505–565. John Wiley & Sons, 2003.

[24] S. Benagli, D. Borrello, E. Vallat-Sauvain, J. Meier, U. Kroll, J. Hoetzel, J. Bailat, J. Steinhauser, M. Marmelo, G. Monteduro, and L. Castens. High-efficiency amorphous silicon devices on LPCVD-ZnO prepared in industrial KAI-M R&D reactor. In *Proceedings of 24th European Photovoltaic Solar Energy Conference, Hamburg, Germany*, pages 2293–2298, 2009.

[25] T. M. Razykov, C. S. Ferekides, D. Morel, E. Stefanakos, H. S. Ullal, and H. M. Upadhyaya. Solar photovoltaic electricity: current status and future prospects. *Solar Energy*, 85:1580–1608, 2011.

[26] C. Colin, A. Cattoni, I. Massiot, J-F. Guillemoles, N. Bardou, C. Dupuis, J-L. Pelouard, D. Mercier, I. Gérard, A. Etcheberry, Z. Jehl, D. Lincot, N. Naghavi, and S. Collin. Broadband light trapping in ultra-thin nano-structured $Cu(In,Ga)Se_2$ solar cells. In *Proceedings of the 27th European Photovoltaic Solar Energy Conference, Frankfurt, Germany*, pages 2244–2248, 2012.

[27] M. Paire. *Highly efficient solar cells in low dimensionality based on $Cu(In,Ga)Se_2$ chalcopyrite materials*. PhD thesis, Université Pierre et Marie Curie, 2012.

[28] J. Kalowekamo and E. Baker. Estimating the manufacturing cost of purely organic solar cells. *Solar Energy*, 83:1224–1231, 2009.

[29] M. Bernardi, M. Palummo, and J. C. Grossman. Extraordinary sunlight absorption an one nanometer thick photovoltaics using two-dimensional monolayer materials. *Nano Letters*, 13:3664–3670, 2013. doi: 10.1021/nl401544y.

[30] E. Yablonovitch and G. D. Cody. Intensity enhancement in textured optical sheets for solar cells. *IEEE Transactions on Electron Devices*, 29:300–305, 1982.

[31] S. Mokkapati and K. R. Catchpole. Nanophotonic light trapping in solar cells. *Journal of Applied Physics*, 112:101101, 2012.

[32] K. Bean. Anisotropic etching of silicon. *IEEE Transactions on Electron Devices*, 25:1185–1193, 1978.

[33] P. Campbell and M. A. Green. Light trapping properties of pyramidally textured surfaces. *Journal of Applied Physics*, 62:243–249, 1987.

[34] E. Vazsonyi, K. De Clercq, R. Einhaus, E. Van Kerschaver, K. Said, J. Poortmans, J. Szlufcik, and J. Nijs. Improved anisotropic etching process for industrial texturing of silicon solar cells. *Solar Energy Materials and Solar Cells*, 57:179–188, 1999.

[35] M. Python, O. Madani, D. Dominé, F. Meillaud, E. Vallat-Sauvain, and C. Ballif. Influence of the substrate geometrical parameters on microcrystalline silicon growth for thin-film solar cells. *Solar Energy Materials and Solar Cells*, 93:1714–1720, 2009.

[36] S. Hänni, D. T. L. Alexander, L. Ding, G. Bugnon, M. Boccard, C. Battaglia, P. Cuony, J. Escarré, G. Parascandolo, S. Nicolay, M. Cantoni, M. Despeisse, F. Meillaud, and C. Ballif. On the interplay between microstructure and interfaces in high-efficiency microcrystalline silicon solar cells. *IEEE Journal of Photovoltaics*, 3:11–16, 2013.

[37] H. Sai, Y. Kanamori, and M. Kondo. Flattened light-scattering substrate in thin film silicon solar cells for improved infrared response. *Applied Physics Letters*, 98:113502, 2011.

[38] K. Söderström, G. Bugnon, R. Biron, C. Pahud, F. Meillaud, F-J. Haug, and C. Ballif. Thin-film silicon triple-junction solar cell with 12.5% stable efficiency on innovative flat light-scattering substrate. *Journal of Applied Physics*, 112:114503, 2012.

[39] C. Battaglia, C-M. Hsu, K. Söderström, J. Escarré, F-J Haug, M. Charrière, M. Boccard, M. Despeisse, D. T. L. Alexander, M. Cantoni, Y. Cui, and C. Ballif. Light trapping in solar cells: can periodic beat random? *ACS Nano*, 6:2790–2797, 2012.

[40] C. Heine and R. H. Morf. Submicrometer gratings for solar energy applications. *Applied Optics*, 34:2476–2482, 1995.

[41] O. Isabella, A. Campa, M. C. R. Heijna, W. Soppe, R. van Erven, R. H. Franken, H. Borg, and M. Zeman. Diffraction gratings for light-trapping in thin-film silicon solar cells. In *Proceedings of the 23th PVSEC Conference, Valencia, Spain*, pages 2320–2324, 2008.

[42] H. Sai, H. Fujiwara, and M. Kondo. Back surface reflectors with periodic textures fabricated by self-ordering process for light-trapping in thin-film microcrystalline silicon solar cells. *Solar Energy Materials and Solar Cells*, 93:1087–1090, 2009.

[43] C. Battaglia, J. Escarré, K. Söderström, L. Erni, L. Ding, G. Bugnon, A. Billet, M. Boccard, L. Barraud, S. De Wolf, F-J. Haug, M. Despeisse, and C. Ballif. Nanoimprint lithography for high-efficiency thin-film silicon solar cells. *NanoLetters*, 11:661–665, 2011.

[44] C. Battaglia, J. Escarré, K. Söderström, M. Charrière, M. Despeisse, F-J. Haug, and C. Ballif. Nanomoulding of transparent zinc oxide electrodes for efficient light trapping solar cells. *Nature Photonics*, 5:535–538, 2011.

[45] Z. Yu, A. Raman, and S. Fan. Fundamental limit of nanophotonic light-trapping in solar cells. *PNAS*, 107:17491–17496, 2010.

[46] K. Jäger, O. Isabella, L. Zhao, and M. Zeman. Light scattering properties of surface-textured substrates. *Physica Status Solidi C: Conferences and Critical Reviews*, 7:945–948, 2010.

[47] V. E. Ferry, M. A. Verschuuren, C. van Lare, R. E. I. Schropp, H. A. Atwater, and A. Polman. Optimized spatial correlations for broadband light trapping nanopatterns in high efficiency ultrathin a-Si:H solar cells. *Nano Letters*, 11:4239–4245, 2011.

[48] X. Meng, G. Gomard, O. El Daif, E. Drouard, R. Orobtchouk, A. Kaminski, A. Fave, M. Lemiti, A. Abramov, P. Roca i Cabarrocas, and C. Seassal. Absorbing photonic crystals for silicon thin-film solar cells: Design, fabrication and experimental investigation. *Solar Energy Materials and Solar Cells*, 95:32–38, 2011.

[49] X. Meng, E. Drouard, G. Gomard, R. Peretti, A. Fave, and C. Seassal. Combined front and back diffraction gratings for broad band light trapping in thin film solar cells. *Optics Express*, 20:A560–A571, 2012.

[50] X. Meng, V. Depauw, G. Gomard, O. El Daif, C. Trompoukis, E. Drouard, C. Jamois, A. Fave, F. Dross, I. Gordon, and C. Seassal. Design, fabrication and optical characterization of photonic crystal assisted thin film monocrystalline-silicon solar cells. *Optics Express*, 20:A465–A475, 2012.

[51] E. R. Dedman, D. N. Sharp, A. J. Turberfield, C. F. Blanford, and R. G. Denning. Photonic crystals with a chiral basis by holographic lithography. *Photonics and Nanostructures - Fundamentals and applications*, 3:79–83, 2005.

[52] O. El Daif, E. Drouard, G. Gomard, A. Kaminski, A. Fave, M. Lemiti, S. Ahn, S. Kim, P. Roca i Cabarrocas, H. Jeon, and C. Seassal. Absorbing one-dimensional planar photonic crystal for amorphous silicon solar cell. *Optics Express*, 18:A293–A299, 2010.

[53] G. Gomard, X. Meng, E. Drouard, K. El Hajjam, E. Gerelli, R. Peretti, A. Fave, R. Orobtchouk, M. Lemiti, and C. Seassal. Light harvesting by planar photonic crystals in solar cells: the case of amorphous silicon. *Journal of Optics*, 14:024011, 2012.

[54] Y. Park, E. Drouard, O. El Daif, X. Letartre, P. Viktorovitch, A. Fave, A. Kaminski, M. Lemiti, and C. Seassal. Absorption enhancement using photonic crystals for silicon thin film solar cells. *Optics Express*, 17: 14312–14321, 2009.

[55] R. B. Wehrspohn and J. Üpping. 3D photonic crystals for photon management in solar cells. *Journal of Optics*, 14:024003, 2012.

[56] M. Vanecek, O. Babchenko, A. Purkrt, J. Holovsky, N. Neykova, A. Poruba, Z. Remes, J. Meier, and U. Kroll. Nanostructured three-dimensional thin film silicon solar cells with very high efficiency potential. *Applied Physics Letters*, 98:163503, 2011.

[57] J. Zhu, Z. Yu, G-F. Burkhard, C-M. Hsu, S-T. Connor, Y. Xu, Q. Wang, M. D. McGehee, S. Fan, and Y. Cui. Optical absorption enhancement in amorphous silicon nanowire and nanocone arrays. *Nano Letters*, 9:279–282, 2009.

[58] L. Zeng, Y. Yi, C. Hong, J. Liu, N. Feng, X. Duan, L. C. Kimerling, and B. A. Alamariu. Efficiency enhancement in Si solar cells by textured photonic crystal back reflector. *Applied Physics Letters*, 89:111111, 2006.

[59] A. Abass, K. Q. Lee, A. Alù, M. Burgelman, and B. Maes. Dual-interface gratings for broadband absorption enhancement in thin-film solar cells. *Physical Review B*, 85:115449, 2012.

[60] S. A. Maier. *Plasmonics - fundamentals and applications*. Springer, 2007.

[61] A. Polman. Plasmonics applied. *Science*, 322:868, 2008.

[62] H. A. Atwater and A. Polman. Plasmonics for improved photovoltaic devices. *Nature Materials*, 9:205–213, 2010.

[63] S. Pillai and M. A. Green. Plasmonics for photovoltaic applications. *Solar Energy Materials and Solar Cells*, 94:1481–1486, 2010.

[64] V. E. Ferry, J. N. Munday, and H. A. Atwater. Design considerations for plasmonic photovoltaics. *Advanced Materials*, 22:4794–4808, 2010.

[65] M. A. Green and S. Pillai. Harnessing plasmonics for solar cells. *Nature Photonics*, 6:130–132, 2012.

[66] Q. Gan, F. J. Bartoli, and Z. H. Kafafi. Plasmonic-enhanced organic photovoltaics: breaking the 10% efficiency barrier. *Advanced materials*, 25:2385–2396, 2013.

[67] C. F. Bohren and D. R. Huffman. *Absorption and scattering of light by small particles*. John Wiley & Sons, 1983.

[68] H. R. Stuart and D. G. Hall. Absorption enhancement in silicon-on-insulator waveguides using metal island films. *Applied Physics Letters*, 69:2327–2329, 1996.

[69] H. R. Stuart and D. G. Hall. Island size effect in nanoparticle-enhanced photodetectors. *Applied Physics Letters*, 73:3815–3817, 1998.

[70] H. Tan, R. Santbergen, A. H. M. Smets, and M. Zeman. Plasmonic light-trapping in thin-film silicon solar cells with improved self-assembled silver nanoparticles. *Nano Letters*, 12:4070–4076, 2012.

[71] U. W. Paetzold, E. Moulin, D. Michaelis, W. Böttler, C. Wächter, V. Hagemann, M. Meier, R. Carius, and U. Rau. Plasmonic reflection grating back contact for microcrystalline silicon solar cells. *Applied Physics Letters*, 99: 181105, 2011.

[72] H. Fredriksson, Y. Alaverdyan, A. Dmitriev, C. Langhammer, D. S. Sutherland, M. Zäch, and B. Kasemo. Hole-mask colloidal lithography. *Advanced Materials*, 19:4297–4302, 2007.

[73] O. El Daif, L. Tong, B. Figeys, K. Van Nieuwenhuysen, A. Dmitriev, P. Van Dorpe, I. Gordon, and F. Dross. Front side plasmonic effect on thin silicon epitaxial solar cells. *Solar Energy Materials and Solar Cells*, 104: 58–63, 2012.

[74] D. Derkacs, S. H. Lim, P. Matheu, W. Mar, and E. T. Yu. Improved performance of amorphous silicon solar cells via scattering from surface plasmon polaritons in nearby metallic nanoparticles. *Applied Physics Letters*, 89:093103, 2006.

[75] P. Matheu, S. H. Lim, D. Derkacs, C. McPheeters, and E. T. Yu. Metal and dielectric nanoparticle scattering for improved optical absorption in photovoltaic devices. *Applied Physics Letters*, 93:113108, 2008.

[76] M. van Lare, F. Lenzmann, M. A. Verschuuren, and A. Polman. Mode coupling by plasmonic surface scatterers in thin-film silicon solar cells. *Applied Physics Letters*, 101:221110, 2012.

[77] K. Nakayama, K. Tanabe, and H. A. Atwater. Plasmonic nanoparticle enhanced light absorption in GaAs solar cells. *Applied Physics Letters*, 93: 121904, 2008.

[78] N. P. Hylton, X. Li, V. Giannini, K-H. Lee, N. J. Ekin-Daukes, J. Loo, D. Vercruysee, P. Van Dorpe, H. Sodabanlu, M. Sugiyama, and S. A. Maier. Al nanoparticle arrays for broadband absorption enhancements in GaAs devices. In *Proceedings of 39th IEEE PVSC Conference, Tampa, United States*, 2013.

[79] D. Derkacs, W. V. Chen, P. M. Matheu, S. H. Lim, P. K. L. Yu, and E. T. Yu. Nanoparticle-induced light scattering for improved performance of quantum-well solar cells. *Applied Physics Letters*, 93:091107, 2008.

[80] L. Novotny and N. van Hulst. Antennas for light. *Nature Photonics*, 5: 83–90, 2011.

[81] C. Hägglund, M. Zäch, and B. Kasemo. Enhanced charge carrier generation in dye sensitized solar cells by nanoparticle plasmons. *Applied Physics Letters*, 92:013113, 2008.

[82] F.-J. Haug, T. Soderström, O. Cubero, V. Terrazzoni-Daudrix, and C. Ballif. Influence of the ZnO buffer on the guided mode structure in Si/ZnO/Ag multilayers. *Journal of Applied Physics*, 106:044502, 2009.

[83] M-G. Kang, T. Xu, H. J. Park, X. Luo, and L. J. Guo. Efficiency enhancement of organic solar cells using transparent plasmonic Ag nanowire electrodes. *Advanced Materials*, 22:4378–4383, 2010.

[84] V. E. Ferry, L. A. Sweatlock, D. Pacifici, and H. A. Atwater. Plasmonic nanostructure design for efficient light coupling into solar cells. *Nano Letters*, 8:4391–4397, 2008.

[85] N. N. Lal, H. Zhou, M. Hawkeye, J. K. Sinha, P. N. Bartlett, G. A. J. Amaratunga, and J. J. Baumberg. Using spacing layers to control metal and semiconductor absorption in ultrathin solar cells with plasmonic substrates. *Physical Review B*, 85:245318, 2012.

[86] K. Aydin, V. E. Ferry, R. M. Briggs, and H. A. Atwater. Broadband polarization-independent resonant light absorption using ultrathin plasmonic super absorbers. *Nature communications*, 2:1–7, 2011.

[87] A. Cattoni, P. Ghenuche, A-M. Haghiri-Gosnet, D. Decanini, J. Chen, J-L. Pelouard, and S. Collin. $\lambda^3/1000$ plasmonic nanocavities for biosensing fabricated by soft UV nanoimprint lithography. *NanoLetters*, 11:3557–3563, 2011.

[88] M. W. Rowell, M. A. Topinka, and M. D. McGehee. Organic solar cells with nanotube network electrodes. *Applied Physics Letters*, 88:233506, 2006.

[89] S. Pang, Y. Hernandez, X. Feng, and K. Müllen. Graphene as transparent electrode material for organic electronics. *Advanced Materials*, 23:2779–2795, 2011.

[90] Y. H. Kim, C. Sachse, M. L. Machala, C. May, L. Müller-Meskamp, and K. Leo. Highly conductive PEDOT:PSS electrode with optimized solvent and thermal post-treatment for ITO-free organic solar cells. *Advanced Functional Materials*, 21:1076–1081, 2011.

[91] S. Vedraine, A. El Hajj, P. Torchio, and B. Lucas. Optimized ITO-free trilayer electrode for organic solar cells. *Organic Electronics*, 14:1122–1129, 2013.

[92] M-G. Kang and L. J. Guo. Nanoimprinted semitransparent metal electrodes and their application in organic light-emitting diodes. *Advanced Materials*, 19:1391, 2007.

[93] M-G. Kang, M-S. Kim, J. Kim, and L. J. Guo. Organic solar cells using nanoimprinted transparent metal electrodes. *Advanced Materials*, 20:4408–4413, 2008.

[94] W. E. I. Sha, W. C. H. Choy, Y. Wu, and W. C. Chew. Optical and electrical study of organic solar cells with a 2D grating anode. *Optics Express*, 20: 2572–2580, 2012.

[95] K-S. Lee, I. Kim, C. B. Yeon, J. W. Lim, S. J. Yun, and G. E. Jabbour. Thin metal electrodes for semitransparent organic photovoltaics. *ETRI Journal*, 35:587–593, 2013.

[96] J. C. Scott, J. H. Kaufman, P. J. Brock, R. DiPietro, J. Salem, and J. A. Goitia. Degradation and failure of MEH-PPV light-emitting diodes. *Journal of Applied Physics*, 79:2745–2751, 1996.

[97] K. Ellmer. Past achievements and future challenges in the development of optically transparent electrodes. *Nature Photonics*, 6:809–817, 2012.

[98] D. S. Hecht, L. Hu, and G. Irvin. Emerging transparent electrodes based on thin films of carbon nanotubes, graphene, and metallic nanostructures. *Advanced Materials*, 23:1482–1513, 2011.

[99] H. Han, N. D. Theodore, and T. L. Alford. Improved conductivity and mechanism of carrier transport in zinc oxide with embedded silver layer. *Journal of Applied Physics*, 103:013708, 2008.

[100] J. Chen, H. Bi, S. Sun, Y. Tang, W. Zhao, T. Lin, D. Wan, F. Huang, X. Zhou, X. Xie, and M. Jiang. Highly conductive and flexible paper of 1D silver-nanowire-doped graphene. *ACS Applied Materials and Interfaces*, 5(4):1408–1413, 2013.

[101] P. Grosse, R. Hertling, and T. Müggenburg. Design of low emissivity systems based on a three-layer coating. *Journal of Non Crystalline Solids*, 218:38–43, 1997.

[102] L. Hu, H. Wu, and Y. Cui. Metal nanogrids, nanowires, and nanofibers for transparent electrodes. *MRS Bulletin*, 36:760–765, 2011.

[103] T. Gao and P. W. Leu. Copper nanowire arrays for transparent electrodes. *Journal of Applied Physics*, 114(6):063107, 2013.

[104] R. G. Gordon. Criteria for choosing transparent conductors. *MRS Bulletin*, 25:52–57, 2000.

[105] K. H. Choi, J. Y. Kima, Y. S. Leeb, and H. J. Kima. ITO/Ag/ITO multilayer films for the application of a very low resistance transparent electrode. *Thin Solid Films*, 341:152, 1999.

[106] I. Crupi, S. Boscarino, V. Strano, S. Mirabella, F. Simone, and A. Terrasi. Optimization of ZnO:Al/Ag/ZnO:Al structures for ultra-thin high-performance transparent conductive electrodes. *Thin Solid Films*, 520: 4432–4435, 2012.

[107] A. Kim, Y. Won, K. Woo, C-H. Kim, and J. Moon. Highly transparent low resistance ZnO/Ag nanowire/ZnO composite electrode for thin-film solar cells. *ACS Nano*, 7(2):1081–1091, 2013.

[108] T. Akter and W. S. Kim. Reversibly stretchable transparent conductive coatings of spray-deposited silver nanowires. *ACS Applied Materials and Interfaces*, 4:1855–1859, 2012.

[109] J-A. Jeong, J. Kim, and H-K. Kim. Ag grid/ITO hybrid transparent electrodes prepared by inkjet printing. *Solar Energy Materials and Solar Cells*, 95:1974–1978, 2011.

[110] T. M. Barnes, M. O. Reese, J. D. Bergeson, B. A. Larsen, J. L. Blackburn, M. C. Beard, J. Bult, and J. van de Lagemaat. Comparing the fundamental physics and device performance of transparent conductive nanostructured networks with conventional transparent conducting oxides. *Advanced Energy Materials*, 2:353–360, 2012.

[111] B. O' Connor, C. Haughn, K-H. An, K. P. Pipe, and M. Shtein. Transparent and conductive electrodes based on unpatterned thin metal films. *Applied Physics Letters*, 93:223304, 2008.

[112] P. B. Catrysse and S. Fan. Nanopatterned metallic films for use as transparent conductive electrodes in optoelectronic devices. *NanoLetters*, 10: 2944, 2010.

[113] G. Haacke. New figure of merit for transparent conductors. *Journal of Applied Physics*, 47:4086–4089, 1976.

[114] D. B. Fraser and H. D. Cook. Highly conductive, transparent films of sputtered $In_{2-x}Sn_xO_{3-y}$. *Journal of Electrochemical Society*, 119:1368, 1972.

[115] V. K. Jain and A. P. Kulshreshtha. Indium-tin-oxide transparent conducting coatings on silicon solar cells and their "figure of merit". *Solar Energy Materials and Solar Cells*, 4:151–158, 1981.

[116] E. D. Palik. *Handbook of Optical Constants of Solids*. Academic, 1985.

[117] J. van de Groep, P. Spinelli, and A. Polman. Transparent conducting silver nanowire networks. *Nano Letters*, 10:2944–2949, 2012.

[118] C. Billaudeau, S. Collin, C. Sauvan, N. Bardou, F. Pardo, and J-L. Pelouard. Angle-resolved transmission measurements through anisotropic two-dimensional plasmonic crystals. *Optics Letters*, 33:165–167, 2008.

[119] R. C. Chittick, J. H. Alexander, and H. F. Sterling. The preparation and properties of amorphous silicon. *Journal of the Electrochemical Society*, 116: 77–81, 1969.

[120] P. G. Le Comber and W. E. Spear. Electronic transport in amorphous silicon films. *Physical Review Letters*, 25:509–511, 1970.

[121] W. E. Spear and P. G. Le Comber. Substitutional doping of amorphous silicon. *Solid State Communications*, 17:1193–1196, 1975.

[122] W. E. Spear, P. G. Le Comber, S. Kinmond, and M. H. Brodsky. Amorphous silicon p-n junction. *Applied Physics Letters*, 28:105–107, 1976.

[123] D. E. Carlson and C. R. Wronski. Amorphous silicon solar cell. *Applied Physics Letters*, 28:671–673, 1976.

[124] I-S. Chen and C. R. Wronski. Internal photoemission on a-Si:H Schottky barrier structures revisited. *Journal of Non Crystalline Solids*, 190:58–66, 1995.

[125] M. Stutzmann, W. B. Jackson, and C. C. Tsai. Light-induced metastable defects in hydrogenated amorphous silicon: a systematic study. *Physical Review B*, 32:23–47, 1985.

[126] M. Stutzmann, D. K. Biegelsen, and R. A. Street. Detailed investigation of doping in hydrogenated amorphous silicon and germanium. *Physical Review B*, 35:5666–5701, 1987.

[127] R. A. Street. Doping and the Fermi energy in amorphous silicon. *Physical Review Letters*, 49:1197–1190, 1982.

[128] B. Rech and H. Wagner. Potential of amorphous silicon for solar cells. *Applied Physics A*, 69:155–167, 1999.

[129] M. Zeman. *Thin films solar cells - Fabrication, Characterization and Applications*, chapter Advanced Amorphous Silicon Solar Cell Technologies, pages 173–236. John Wiley & Sons, 2006.

[130] A. V. Shah, H. Schade, M. Vanecek, J. Meier, E. Vallat-Sauvain, N. Wyrsch, U. Kroll, C. Droz, and J. Bailat. Thin-film silicon solar cell technology. *Progress in Photovoltaics: Research and Applications*, 12:113–142, 2004.

[131] D. L. Staebler and C. R. Wronski. Reversible conductivity changes in discharge-produced amorphous Si. *Applied Physics Letters*, 31:292, 1977.

[132] D. L. Staebler and C. R. Wronski. Optically induced conductivity changes in discharge produced hydrogenated amorphous silicon. *Journal of Applied Physics*, 51:3262–3268, 1980.

[133] M. Stutzmann, W. B. Jackson, and C. C. Tsai. Kinetics of the Staebler-Wronski effect in hydrogenated amorphous silicon. *Applied Physics Letters*, 45:1075–1077, 1984.

[134] R. Biron, S. Hänni, M. Boccard, C. Pahud, G. Bugnon, L. Ding, S. Nicolay, G. Parascandolo, F. Meillaud, M. Despeisse, F-J. Haug, and C. Ballif. Optimization of the asymmetric intermediate reflector morphology for high stabilized efficiency thin n-i-p micromorph solar cells. *IEEE Journal of Photovoltaics*, 3:41–45, 2013.

[135] K. Söderström, J. Escarré, O. Cubero, F-J Haug, S. Pérregaux, and C. Ballif. UV-nano-imprint lithography technique for the replication of back reflector for n-i-p thin film silicon solar cells. *Progress in Photovoltaics: Research and Applications*, 19:202–210, 2011.

[136] K. Söderström, F-J Haug, J. Escarré, C. Pahud, R. Biron, and C. Ballif. Highly reflective nanotextured sputtered silver back reflector for flexible high-efficiency n-i-p thin film silicon solar cells. *Solar Energy Materials and Solar Cells*, 95:3585–3591, 2011.

[137] K. Söderström, G. Bugnon, F-J Haug, S. Nicolay, and C. Ballif. Experimental study of flat light-scattering substrates in thin-film silicon solar cells. *Solar Energy Materials and Solar Cells*, 101:193–199, 2012.

[138] L. Ding, M. Boccard, G. Bugnon, M. Benkhaira, S. Nicolay, M. Despeisse, F. Meillaud, and C. Ballif. Highly transparent ZnO bilayers by LP-MOCVD as front electrodes for thin-film micromorph silicon solar cells. *Solar Energy Materials and Solar Cells*, 98:331–336, 2012.

[139] I. Massiot, C. Colin, N. Péré-Laperne, P. Roca i Cabarrocas, C. Sauvan, P. Lalanne, J-L. Pelouard, and S. Collin. Nanopatterned front contact for broadband absorption in ultra-thin amorphous silicon solar cells. *Applied Physics Letters*, 101:163901, 2012.

[140] I. Massiot, C. Colin, C. Sauvan, P. Lalanne, P. Roca i Cabarrocas, J-L. Pelouard, and S. Collin. Multi-resonant absorption in ultra-thin silicon solar cells with metallic nanowires. *Optics Express*, 21:A372–A381, 2013.

[141] V. E. Ferry, A. Polman, and H. A. Atwater. Modeling light trapping in nanostructured solar cells. *ACS Nano*, 5:10055–10064, 2011.

[142] W. B. Berry, K. A. Emery, A. B. Swartzlander, and A. J. Nelson. Low temperature diffusivity for aluminum and silver in amorphous silicon. In *In Proceedings of the IEEE PVSC Conference, Las Vegas, United States*, pages 262–266, 1988.

[143] P. B. Johnson and R. W. Christy. Optical constants of the noble metals. *Physical Review B*, 6:4370–4379, 1972.

[144] N. Naqavi, K. Söderström, F-J Haug, V. Paeder, H. P. Scharf, T. Herzig, and C. Ballif. Understanding of photocurrent enhancement in real thin film solar cells: towards optimal one-dimensional gratings. *Optics Express*, 19:128–140, 2011.

[145] K. Söderström. *Coupling light into thin silicon layers for high-efficiency solar cells*. PhD thesis, Ecole Polytechnique Fédérale de Lausanne, 2013.

[146] T. Söderström, V. Haug, F.-J.and Terrazzoni-Daudrix, and C. Ballif. Optimization of amorphous silicon thin film solar cells for flexible photovoltaics. *Journal of Applied Physics*, 103:114509, 2008.

[147] P. Roca i Cabarrocas, J. B. Chevrier, J. Huc, A. Lloret, J. Y. Parey, and J. P. M. Schmitt. A fully automated hot-wall multiplasma-monochamber reactor for thin film deposition. *Journal of Vacuum Science and Technology A*, 9:2331, 1991.

[148] P. Roca i Cabarrocas, R. Cariou, and M. Labrune. Low temperature plasma deposition of silicon thin films: from amorphous to crystalline. *Journal of Non Crystalline Solids*, 358:2000–2003, 2012.

[149] A. Hadjadj, N. Pham, P. Roca i Cabarrocas, O. Jbara, and G. Djellouli. Ellipsometry investigation of the amorphous-to-microcrystalline transition in a-Si:H under hydrogen-plasma treatment. *Journal of Applied Physics*, 107:083509, 2010.

[150] P. Roca i Cabarrocas, K.H. Kim, R. Cariou, M. Labrune, E.V. Johnson, M. Moreno, A. Torres Rios, S. Abolmasov, and S. Kasouit. Low temperature plasma synthesis of nanocrystals and their application to the growth of crystalline silicon and germanium thin films. *MRS Proceedings*, 1426: 319–329, 2012.

[151] Z. Cui. *Nanofabrication: principles, capabilities and limits*, chapter Nanofabrication by charged beams, pages 89–106. Springer, 2008.

[152] M. A. Mohammad, M. Muhammad, S. K. Dew, and M. Stepanova. *Nanofabrication: Techniques and Principles*, chapter Fundamentals of Electron Beam Exposure and Development, pages 11–41. Springer, 2012.

[153] V. J. Logeeswaran, N. P. Kobayashi, M. Saif Islam, W. Wu, P. Chaturvedi, N. X. Fang, S-Y. Wang, and R. Stanley Williams. Ultrasmooth silver thin films deposited with a germanium nucleation layer. *NanoLetters*, 9:178–182, 2009.

[154] R. A. Pala, J. White, E. Barnard, J. Liu, and M. L. Brongersma. Design of plasmonic thin-film solar cells with broadband absorption enhancements. *Advanced Materials*, 21:1–6, 2009.

[155] C. Liu, V. Kamaev, and Z. V. Vardeny. Efficiency enhancement of an organic light-emitting diode with a cathode forming two-dimensional periodic hole array. *Applied Physics Letters*, 86:143501, 2005.

[156] Y-M. Chi, H-L. Chen, Y-S. Lai, H-M. Chang, Y-C. Liao, C-C. Cheng, S-H. Chen, S-C. Tseng, and K-T. Lin. Optimizing surface plasmon resonance effects on finger electrodes to enhance the efficiency of silicon-based solar cells. *Energy & Environmental science*, 6:935–942, 2013.

[157] T. W. Ebbesen, H. J. Lezec, H. F. Ghaemi, T. Thio, and P. A. Wolff. Extraordinary optical transmission through sub-wavelength hole arrays. *Nature*, 391:667, 1998.

[158] W. L. Barnes, A. Dereux, and T. W. Ebbesen. Surface plasmon subwavelength optics. *Nature*, 424:824, 14 August 2003.

[159] C. Genet and T. W. Ebbesen. Light in tiny holes. *Nature*, 445:39–46, 2007.

[160] C. Colin. *Metallic nano-structures for light-trapping in ultra-thin GaAs and CIGS solar cells*. PhD thesis, Université Paris Sud 11, 2013.

[161] S. Collin, C. Sauvan, C. Colin, I. Massiot, F. Pardo, N. Bardou, P. Lalanne, and J-L. Pelouard. High-efficient ultra-thin solar cells. In *Proceedings of 25th European Photovoltaic Solar Energy Conference, Valencia, Spain*, pages 265–268, 2010.

[162] M. A. Green, K. Emery, Y. Hishikawa, W. Warta, and E. D. Dunlop. Solar cell efficiency tables (version 41). *Progress in Photovoltaics: Research and Applications*, 21:1–11, 2013.

[163] C. Billaudeau. *Guidage optique dans les cristaux plasmoniques* 1*D et* 2*D*. PhD thesis, Université Paris-Sud 11, 2007.

[164] S. Collin, C. Sauvan, C. Billaudeau, F. Pardo, J. C. Rodier, J-L. Pelouard, and P. Lalanne. Surface modes on nanostructured metallic surfaces. *Physical Review B*, 79:165405, 2009.

[165] D. I. Pomerantz. Anodic bonding, US patent 3,397,278, 1968.

[166] G. Wallis and D. I. Pomerantz. Field assisted glass-metal sealing. *Journal of Applied Physics*, 40:3946, 1969.

[167] H. Elfatimi. *Etude et réalisation de transistors bipolaires à hétérojonction InP/GaAsSb/InP reportés sur substrat hôte pour application à la puissance*. PhD thesis, Université de Limoges, 2008.

[168] J. J. LePore. An improved technique for selective etching of GaAs and $Ga_{1-x}Al_xAs$. *Journal of Applied Physics*, 51(12):6441–6442, 1980.

[169] T. Søndergaard, S. M. Novikov, R. L. Holmgaard, T.and Eriksen, J. Beermann, Z. Han, K. Pedersen, and S. I. Bozhevolnyi. Plasmonic black gold by adiabatic nanofocusing and absorption of light in ultra-sharp convex grooves. *Nature Communications*, 3:969, July 2012.

[170] F. Dross, K. Baert, T. Bearda, J. Deckers, V. Depauw, O. El Daif, I. Gordon, A. Gougam, J. Govaerts, S. Granata, R. Labie, X. Loozen, R. Martini, A. Masolin, B. O' Sullivan, Y. Qiu, J. Vaes, D. Van Gestel, J. Van Hoeymissen, A. Vanleenhove, K. Van Nieuwenhuysen, S. Venkatachalam, M. Meuris, and J. Poortmans. Crystalline thin-foil silicon solar cells: where crystalline quality meets thin-film processing. *Progress in Photovoltaics: Research and Applications*, 20:770–784, 2012.

[171] F. Dross, J. Robbelein, B. Vandevelde, E. van Kerschaver, I. Gordon, G. Beaucarne, and J. Poortmans. Stress-induced large-area lift-off of crystalline Si films. *Applied Physics A*, 89:149–152, 2007.

[172] V. Depauw, Y. Qiu, K. Van Nieuwenhuysen, I. Gordon, and J. Poortmans. Epitaxy-free monocrystalline silicon thin film: first steps beyond proof-of-concept solar cells. *Progress in Photovoltaics: Research and Applications*, 19: 844–850, 2011.

[173] I. Gordon, F. Dross, V. Depauw, A. Masolin, Y. Qiu, J. Vaes, D. Van Gestel, and J. Poortmans. Three novel ways of making thin-film crystalline-silicon layers on glass for solar cell applications. *Solar Energy Materials and Solar Cells*, 95:S2–S7, 2011.

[174] M. J. Keevers, T. L. Young, U. Schubert, and M. A. Green. 10% efficient CSG minimodules. In *Proceedings of 22nd European Photovoltaic Solar Energy Conference, Milan, Italy*, 2007.

[175] I. Gordon, L. Carnel, D. Van Gestel, G. Beaucarne, and J. Poortmans. Fabrication and characterization of highly efficient thin-film polycrystalline-silicon solar cells based on aluminium-induced crystallization. *Thin Solid Films*, 516:6984–6988, 2008.

[176] Y. Qiu, O. Kunz, S. Venkatachalam, D. Van Gestel, R. Egan, I. Gordon, and J. Poortmans. 8.5% efficiency for thin-fim polycrystalline silicon solar cells: a study of hydrogen plasma passivation. In *Proceedings of 25th European Photovoltaic Solar Energy Conference, Valencia, Spain*, pages 3633–3637, 2010.

[177] J. Damon-Lacoste and P. Roca i Cabarrocas. Toward a better physical understanding of a-Si:H/c-Si heterojunction solar cells. *Journal of Applied Physics*, 105:063712, 2009.

[178] M. Moreno and P. Roca i Cabarrocas. Ultra-thin crystalline silicon films produced by plasma assisted epitaxial growth on silicon wafers and their transfer to foreign substrates. *EPJ Photovoltaics*, 1:1–6, 2010.

[179] R. Cariou, M. Labrune, and P. Roca i Cabarrocas. Thin crystalline silicon solar cells based on epitaxial films grown at 165°C by RF-PECVD. *Solar Energy Materials and Solar Cells*, 95:2260–2263, 2011.

[180] M. Moreno, G. Patriarche, and P. Roca i Cabarrocas. Fine-tuning of the interface in high-quality epitaxial silicon films deposited by plasma-enhanced chemical vapor deposition at 200°C. *Journal of Materials Research*, 28:1626–1632, 2013.

[181] R. Cariou, R. Ruggeri, P. Chatterjee, J.-L. Gentner, and P. Roca i Cabarrocas. Silicon epitaxy below 200°C: towards thin crystalline solar cells. In *Proceedings SPIE*, number 84700B, 2012.

[182] H. M. Branz, C. W. Teplin, M. J. Romero, I. T. Martin, Q. Wang, D. L. Young, K. Alberi, and P. Stradins. Hot-wire chemical vapor deposition of epitaxial film crystal silicon for photovoltaics. *Thin Solid Films*, 519: 4545–4550, 2011.

[183] K. Alberi, I. T. Martin, M. Shub, C. W. Teplin, M. J. Romero, R. C. Reedy, E. Iwaniczko, A. Duda, P. Stradins, H. M. Branz, and D. L. Young. Material quality requirements for efficient epitaxial film silicon solar cells. *Applied Physics Letters*, 96:073502, 2010.

[184] J. Zhao, A. Wang, P. Altermatt, and M. A. Green. Twenty-four percent efficient silicon solar cells with double layer antireflection coatings and reduced resistance loss. *Applied Physics Letters*, 66:3636, 1995.

[185] A. Mavrokefalos, S. Eon Han, S. Yerci, M. S. Branham, and G. Chen. Efficient light trapping in inverted nanopyramid thin crystalline silicon membranes for solar cell applications. *Nano Letters*, 12:2792–2796, 2012.

[186] T. K. Chong, J. Wilson, S. Mokkapati, and K. R. Catchpole. Optimal wavelength scale diffraction gratings for light trapping in solar cells. *Journal of Optics*, 14:024012, 2012.

[187] K. X. Wang, Z. Yu, V. Liu, Y. Cui, and S. Fan. Absorption enhancement in ultrathin crystalline silicon solar cells with antireflection and light-trapping nanocone gratings. *Nano Letters*, 12:1616–1619, 2012.

[188] E-C. Wang, S. Mokkapati, T. P. White, T. Soderstrom, S. Varlamov, and K. R. Catchpole. Light trapping with titanium dioxide diffraction gratings fabricated by nanoimprinting. *Progress in Photovoltaics: Research and Applications*, 2012.

[189] C. Trompoukis, O. El Daif, V. Depauw, I. Gordon, and J. Poortmans. Photonic assisted light trapping integrated in ultrathin crystalline silicon solar cells by nanoimprint lithography. *Applied Physics Letters*, 101:103901, 2012.

[190] S. Z. Ngwe, A. Blakers, and K. Weber. RIE-induced carrier lifetime degradation. *Progress in Photovoltaics: Research and Applications*, 18:214–220, 2010.

[191] J. Oh, H. C. Yuan, and H. M. Branz. An 18.2%-efficient black-silicon solar cell achieved through control of carrier recombination in nanostructures. *Nature Nanotechnology*, 7:743–748, 2012.

[192] D. M. Schaadt, B. Feng, and E. T. Yu. Enhanced semiconductor optical absorption via surface plasmon excitation in metal nanoparticles. *Applied Physics Letters*, 86:063106, 2005.

[193] F. J. Beck, A. Polman, and K. R. Catchpole. Tunable light trapping for solar cells using localized surface plasmons. *Journal of Applied Physics*, 105(11):114310, 2009.

[194] K. R. Catchpole and A. Polman. Design principles for particle plasmon enhanced solar cells. *Applied Physics Letters*, 93:191113, 2008.

[195] I. Diukman and M. Orenstein. How front side plasmonic nanostructures enhance solar cell efficiency. *Solar Energy Materials and Solar Cells*, 95: 2628–2631, 2011.

[196] M. B. Dühring, N. A. Mortensen, and O. Sigmund. Plasmonic versus dielectric enhancement in thin-film solar cells. *Applied Physics Letters*, 100: 211914, 2012.

[197] S. Pillai, K. R. Catchpole, T. Trupke, and M. A. Green. Surface plasmon enhanced silicon solar cells. *Journal of Applied Physics*, 101:093105, 2007.

[198] B. Päivänranta, T. Saastamoinen, and M. Kuittinen. A wide-angle antireflection surface for the visible spectrum. *Nanotechnology*, 20:375301, 2009.

[199] B. G. Lee, P. Stradins, D. L. Young, K. Alberi, T-K. Chuang, J. G. Couillard, and H. M. Branz. Light trapping by a dielectric nanoparticle back reflector in film silicon solar cells. *Applied Physics Letters*, 99:064101, 2011.

[200] R. Santbergen, J. Blanker, A. Dhathathreyan, H. Tan, A. H. M. Smets, and M. Zeman. Towards lambertian internal light scattering in solar cells using coupled plasmonic and dielectric nanoparticles as back reflector. In *Proceedings of IEEE PVSC 39th Conference*, 2013.

[201] C. S. Solanki, R. R. Bilyalov, J. Poortmans, J. Nijsw, and R. Mertensz. Porous silicon layer transfer processes for solar cells. *Solar Energy Materials and Solar Cells*, 83:101–113, 2004.

[202] M. Bruel, B. Aspar, and A-J. Auberton-Hervé. Smart-cut: a new silicon on insulator material technology based on hydrogen implantation and wafer bonding. *Japanese Journal of Applied Physics*, 36:1636–1641, 1996.

[203] S. W. Bedell, D. Shahrjerdi, B. Hekmatshoar, K. Fogel, P. A. Lauro, J. A. Ott, N. Sosa, and D. Sadana. Kerf-less removal of Si, Ge, and III-V layers by controlled spalling to enable low-cost PV technologies. *IEEE Journal of Photovoltaics*, 2:141–147, 2012.

[204] D. Shahrjerdi, S. W. Bedell, C. Ebert, C. Bayram, B. Hekmatshoar, K. Fogel, P. A. Lauro, M. Gaynes, T. Gokmen, J. A. Ott, and D. K. Sadana. High-efficiency thin-film InGaP/InGaAs/Ge tandem solar cells enabled by controlled spalling technology. *Applied Physics Letters*, 100:053901, 2012.

[205] D. Shahrjerdi, S. W. Bedell, C. Bayram, C. C. Lubguban, K. Fogel, P. A. Lauro, J. A. Ott, M. Hopstaken, M. Gaynes, and D. Sadana. Ultralight high-efficiency flexible InGaP/(In)GaAs tandem solar cells on plastic. *Advanced Energy Materials*, 3(5):566–571, 2013. ISSN 1614-6840.

[206] C. M. Herzinger, B. Johs, W. A. McGahan, J. A. Woollam, and W. Paulson. Ellipsometric determination of optical constants for silicon and thermally

grown silicon dioxide via a multi-sample, multi-wavelength, multi-angle investigation. *Journal of Applied Physics*, 83:3323, 1998.

[207] P. Lautenschlager, M. Garriga, L. Viña, and M. Cardona. Temperature dependence of the dielectric function and interband critical points in silicon. *Physical Review B*, 36:4821–4830, 1987.

[208] K. Sato, M. Shikida, Y. Matsushima, T. Yamashiro, K. Asaumi, Y. Iriye, and M. Yamamoto. Characterization of orientation-dependent etching properties of single-crystal silicon: effects of KOH concentration. *Sensors and Actuators A: Physical*, 64:87–93, 1988.

[209] I. Zubel and M. Kramkowska. The effect of isopropyl alcohol on etching rate and roughness of (100) Si surface etched in KOH and TMAH solutions. *Sensors and Actuators A: Physical*, 93(2):138 – 147, 2001. ISSN 0924-4247.

[210] M. G. Deceglie, V. E. Ferry, A. P. Alivisatos, and H. A. Atwater. Design of nanostructured solar cells using coupled optical and electrical modeling. *Nano Letters*, 12:2894–2900, 2012.

[211] M. G. Moharam, E. B. Grann, D. A. Pommet, and T. K. Gaylord. Formulation for stable and efficient implementation of the rigorous coupled-wave analysis of binary gratings. *Journal of the Optical Society of America A*, 12: 1068–1076, 1995.

[212] P. Lalanne and G. M. Morris. Highly improved convergence of the coupled-wave method for tm polarization. *Journal of the Optical Society of America A*, 13:779–784, 1996.

[213] P. Lalanne and M. P. Jurek. Computation of the near-field pattern with the coupled-wave method for transverse magnetic polarization. *Journal of Modern Optics*, 45:1357, 1998.